CRANFIELD UNIVERSITY

ABUDUREHEMAN BILALE (BILAL ABDURAHMAN)

STATE RELATIVITY AND SPEED-ALLOCATED LINE-OF-SIGHT COURSE CONTROL FOR PATH-FOLLOWING OF UNDERWATER VEHICLES

SCHOOL OF AEROSPACE, TRANSPORT AND MANUFACTURING
Aerospace

PhD
Academic Year: 2014–2018

Supervisors: Dr Al Savvaris, Prof Antonios Tsourdos
13 April 2018

CRANFIELD UNIVERSITY

SCHOOL OF AEROSPACE, TRANSPORT AND MANUFACTURING
Aerospace

PhD

Academic Year: 2014–2018

ABUDUREHEMAN BILALE (BILAL ABDURAHMAN)

State Relativity and Speed-Allocated Line-Of-Sight Course Control for Path-Following of Underwater Vehicles

Supervisors: Dr Al Savvaris, Prof Antonios Tsourdos
13 April 2018

This thesis is submitted in partial fulfilment of the requirements for the degree of PhD.

Abstract

Path-following is a primary task for most marine, air or space crafts, especially during autonomous operations. Research on autonomous underwater vehicles (AUV) has received large interests in the last few decades with research incentives emerging from the safe, cost-effective and practical solutions provided by their applications such as search and rescue, inspection and monitoring of pipe-lines ans sub-sea structures. This thesis presents a novel guidance system based on the popular line-of-sight (LOS) guidance law for path-following (PF) of underwater vehicles (UVs) subject to environmental disturbances. Mathematical modeling and dynamics of (UVs) is presented first. This is followed by a comprehensive literature review on guidance-based path-following control of marine vehicles, which includes revised definitions of the track-errors and more detailed illustrations of the general PF problem. A number of advances on relative equations of motion are made, which include an improved understanding of the fluid FLOW frame and expression of its motion states, an analytic method of modeling the signs of forces and moments and the proofs of passivity and boundedness of relative UV systems in 3-D. The revision in the relative equations of motion include the concept of state relativity, which is an improved understanding of relativity of motion states expressed in reference frames and is also useful in incorporating environmental disturbances. In addition, the concept of drift rate is introduced along with a revision on the angles of motion in 3-D. A switching mechanism was developed to overcome a drawback of a LOS guidance law, and the linear and nonlinear stability results of the LOS guidance laws have been provided, where distinctions are made between straight and curved PF cases. The guidance system employs the unique formulation and solution of the speed allocation problem of allocat-

ing a desired speed vector into x and y components, and the course control that employs the slip angle for desired heading for disturbance rejection. The guidance system and particularly the general course control problem has been extended to 3-D with the new definition of vertical-slip angle. The overall guidance system employing the revised relative system model, course control and speed allocation has performed well during path-following under strong ocean current and/or wave disturbances and measurement noises in both 2-D and 3-D scenarios. In 2-D and 3-D 4 degrees-of-freedom models (DOF), the common sway-underactuated and fully actuated cases are considered, and in 3-D 5-DOF model, sway and heave underactuated and fully actuated cases are considered. Stability results of the LOS guidance laws include the semi-global exponential stability (SGES) of the switching LOS guidance and enclosure-based LOS guidance for straight and curved paths, and SGES of the loolahead-based LOS guidance laws for curved paths. Feedback sliding mode and PID controllers are applied during PF providing a comparison between them, and simulations are carried out in MatLab.

Keywords

Guidance systems; line-of-sight guidance; path-following control; underwater vehicles; kinematics; dynamics and modelling; marine systems; ocean currents.

Contents

List of Figures

List of Tables

List of Abbreviations

AUV	Autonomous Underwater Vehicle
CB	Centre of Buoyancy
CBR	Constant Bearing
CC	Centre of Current
CF	Centre of FLow
CFD	Computational Fluid Dynamics
CG	Centre of Gravity
CO	Centre of Origin
DOF	Dgree of Freedom
DP	Dynamic Positioning
ELOS	Enclosure-based Line-Of-Sight
GNC	Guidance, Navigation and Control
GPS	Global Positioning System
HROV	Hybrid-Remotely Operated Vehicle
I-AUV	Intervention Autonomous Underwater Vehicle
ILOS	Integral Line-Of-Sight
KF	Kalman Filter
LFC	Lyapunov Function Candidate
LHS	Left Hand Side
LLOS	Lookahead-based Line-Of-Sight

LOS	Line-Of-Sight
PID	Proportional-Integral-Derivative
LQR	Linear Quadratic Regulator
MSV	Marine Surface Vehicle
NED	North-East-Down
PF	Path-Following
PMM	Planar Motion Mechanism
PP	Pure-Pursuit
RHS	Right Hand Side
ROV	Remotely Operated Vehicle
SELOS	Switching Enclosure-based Line-Of-Sight
SGES	Globally Semi-Exponentially Stable (or Stability)
SNAME	Society of Naval Architects and Mechanical Engineers
SSS	Side-Scan Sonar
TMS	Tether Management System
TT	Trajectory Tracking
UAV	Unmanned Ariel Vehicle
GS	Globally Stable (or Stability)
GAS	Globally Asymptotically Stable (or Stability)
GES	Globally Exponentially Stable (or Stability)
LES	Locally Exponentially Stable (or Stability)
UUV	Unmanned Underwater Vehicle
UV	Underwater Vehicle
VF	Vector Field

List of Publications

Abdurahman, B., Savvaris, A. & Tsourdos, A. (2017). A switching LOS guidance with relative kinematics for path-following of underactuated underwater vehicles. In *Proceedings of 20th IFAC World Congress* (Vol. 50, p. 2290-2295). Touluse, France.

Abdurahman B., Savvaris, A. & Tsourdos, A. (2017). A comparison between guidance laws for AUVs using relative kinematics. *OCEANS 2017 - Aberdeen*, Aberdeen, p. 1-6.

Abdurahman, B., Savvaris, A. & Tsourdos, A. (2018). Switching LOS Guidance and Vertical Course Control with Speed Allocation for Path-Following of Unmanned Underwater Vehicles. *Manuscript submitted to Ocean Engineering*.

Acknowledgements

I would like to thank my supervisors Dr Al Savvaris and Prof Antonios Tsourdos for their kind supervision and assistance during the work. I also would like to thank my parents for their love and support, external advisor Dr Hyo-Sang Shin for his constructive comments, the reviewers for their positive feedback, my friends and colleagues for their support during the course of the project. It would not be possible to complete the work without them.

Chapter 1

Introduction

Underwater Vehicles (UVs) have found numerous applications at sea and have seen growing research interest in the past decades. Their applications including Autonomous Underwater Vehicles (AUVs) are required in various fields and mainly include oceanographic and military tasks such as subsea surveying and mapping, searching for downed aircrafts, tracking of pipelines, and inspections of subsea structures (Seto, Paull, & Saeedi, 2013). Wit the exponential growth and cost and size reductions in electronic systems, the potential of their applications are also growing tremendously. A primary task of these applications are the path-following problem, which will require the design and application of guidance, navigation and control (GNC) techniques. This chapter will present a brief background and state-of-the-art Unmanned UV technologies and their application spectrum along with introductions to GNC. The thesis aims and objectives and contributions to knowledge are also presented at the end.

1.1 Background

AUVs are untethered submersible vehicle, unlike Remotely Operated Vehicles (ROVs) that are connected with a tether (an umbilical cord) to a surface vessel that provides the vehicle with power and communications. Both vehicles belong to the category of Unmanned Underwater Vehicle (UUV). AUV developments began in the 1960s with appli-

cations limited to specific missions such as data gathering. Publications regarding these efforts were limited. In the 70s AUV developments entered a phase of exploration of their potentials. A number of testbeds were developed during this phase such as the UARS and SPURV developed by the University of Washington APL and the EAVE vehicle (an open space-frame AUV) by the Autonomous Undersea Systems Institute in conjunction with an effort undertaken at the US Navy's facility in San Diego. This was a time of experimentations with hopes of identifying potential of AUVs. Technological advances outside the AUV community in the 1980s reinforce AUV development efforts and development of proof of concept prototypes. The decrease in size and power consumptions in computers and memory devices made complex guidance and control algorithms affordable for implementations on AUVs. Research programs began in the USA providing substantial funding to develop proof of concept prototypes. Efforts at Draper Labs which led to the development of two large AUVs used as testbeds for a number of Navy programs was the most published program. First generation of operational AUVs started to appear in the 90s with vehicles able to accomplish defined tasks. Funding in the technology has grown internationally and organizations worldwide took part in development works aimed at achieving various tasks. Practical commercial products only started to become available from the beginning of this century (Blidberg, 2001).

1.2 UUV State of the Art

During the last two decades AUVs have become a standard technology for mapping the sea floor by means of optical and acoustic sensor modalities, being used in applications such as dam inspection, marine geology and underwater archaeology to name a few. Few autonomous platforms are available in the market with mostly the capabilities to perform Side-Scan Sonar (SSS) and bathymetric multi-beam surveys. Capabilities mostly related to optical mapping, e.g. 2-D photo-mosaicking are not yet available from off-the-shelf applications, although there had been numerous in-field demonstrations by a number of

research institutions. Another major forefront of the research is 3-D optical mapping, with available implementations based on monocular structure from motion, stereo and laser scanners (Ridao, Tiano, El-Fakdi, Carreras, & Zirilli, 2004).

Many applications such as the maintenance of permanent observatories, submerged oil wells or pipes need the use of work-class ROVs deployed from Dynamic Positioning (DP) vessels, making them costly. DP refers to the technique of maintaining the position of a vehicle by using only its thrusters and actuators. The increased demand for autonomy in underwater intervention systems led to the leading research works in the 90s with OTTER, ODIN, UNION and AMADEUS. However, field demonstrations only started to appear in the first decade of this century. Hybrid ROV/AUV concepts are among the successful approaches such as the SWIMMER project, where an AUV shuttle transporting a ROV autonomously homes and docks onto a seabed docking station. The ROV connected to a remote operation station through a docking device is then tele-operated for intervention tasks, avoiding the use of a DP vessel and resulting in savings. Another hybrid concept, HROVs (Hybrid ROVs), have recently arrived, which are essentially AUVs reconfigurable as ROVs when tethered through an ultra-light optical fibre umbilical that could be operated from vessels without DPs. They behave as conventional ROVs when connected and also possess the ability to detach the cable before surfacing autonomously. However, these both systems require control input from a human operator (Ridao et al., 2004).

1.2.1 Intervention Vehicles

Recent field operations with UUVs in applications such as marine rescue require intervention capabilities to perform the desired tasks. These interventions are mainly undertaken by manned vehicles or ROVs equipped with manipulator arms. The first fully autonomous subsea intervention was demonstrated by the ALIVE project, in which a hovering capable AUV was able to perform homing and docking into a subsea intervention panel, which was achieved using hydraulic grasps and an imaging sonar as visual feedback. The ve-

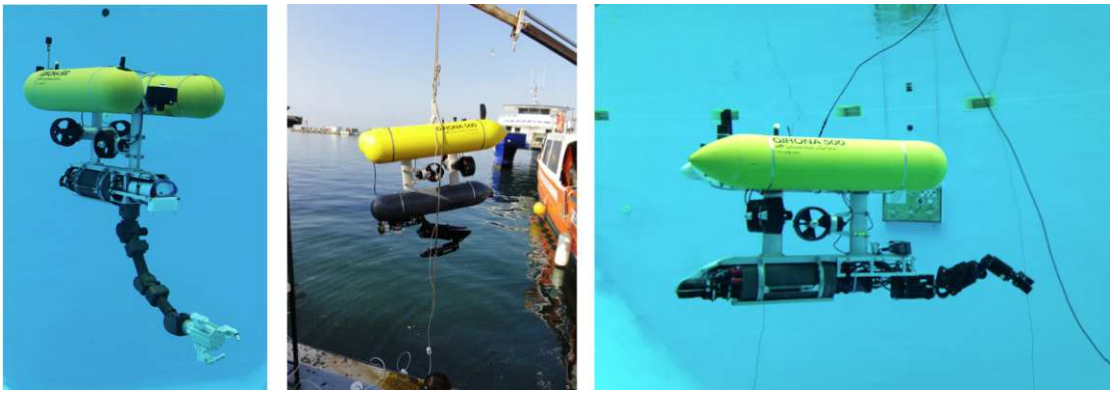

Figure 1.1: Girona 500 I-AUV: Left) TRIDENT configuration; Middle) RAUVI/TRITON configuration; Right) PANDORA configuration.

Figure 1.2: Autonomous Inspection Vehicle (AIV) by Subsea7

hicle was then able to perform basic manipulations to open or close a valve after the vehicle was attached to the panel. The earliest object manipulation from a floating platform was achieved in 2009 in SAUVIM project, where the vehicle located and hooked an object with approximate position known a priori with a recovery device while hovering. Multi-purpose object search and recovery strategy was first demonstrated in the TRIDENT project in 2012. In it, combination of a down-looking camera and photomosaicking technique in a water tank were used to search the object first and then autonomously hooking it (Ridao et al., 2004).

The drawbacks associated with these vehicles include reduced operation time, putting humans in a hostile underwater environment and huge costs associated with the need of expensive oceanographic vessels for operations. Work class ROVs are better suited for deep water interventions, which can be remotely operated for days without any problems.

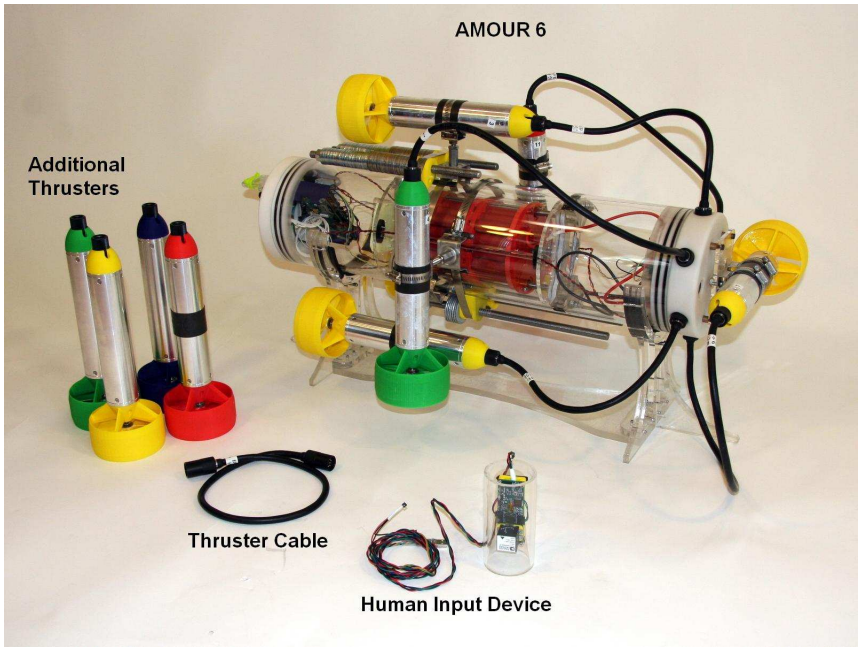

Figure 1.3: AMOUR 6 micro-AUV developed at MIT

Nevertheless, they need an expensive vessel with a heavy crane, an automatic Tether Management System (TMS) and a DP system. Another drawback is the cognitive fatigue of the ROV pilot, who has to deal with the umbilical cord and the ROV while cooperating with the operator controlling the robotic arms. These factors led the researchers to the idea of the Intervention AUVs (I-AUVs). I-AUVs could lead to a huge reduction in cost since they do not require a TMS or a DP vessel and can be deployed and operated from cheap vessels of opportunities (Ridao et.al. 2014). Figure 1.1 shows the intervention vehicle Girona 500 I-AUV developed by the University of Girona in different configurations for different projects (Ridao et al., 2004). Other types of modern AUVs are shown in Figures 1.2 (Mainwaring, 2001) and 1.3 (DRL, 2010).

1.2.2 Application Spectrum

The importance of developing technologies for gathering and processing of ocean data may not be overemphasized (Fryxell, Oliveira, Pascoal, & Silvestre, 1994). UUVs have a variety of demands for applications that can be found in industries such as offshore oil and gas industry, search and rescue missions, deepwater archaeology, and scientific research.

Offshore Energy and Renewables Industries

The oil and gas industry stands as one of the primary users of underwater robotics technology and uses work-class intervention ROVs for routine inspections and repairing of submerged infrastructures. AUVs have entered this market recently, but already being used to perform geophysical surveys prior to pipe installations and for their inspection afterwards. Hovering type AUVs are also under consideration by the research community, for inspection of infrastructures, e.g. submerged oil wells, chains, risers. They represent major challenges for current research capabilities, and thus are still in a research (Ridao et al., 2004).

The application of UUVs in the offshore energy market is not limited to the oil and gas sector. Trending topics in the offshore energy and renewables market include developments in Wave Energy Converters, and Tidal Energies using current turbines as one of the most exciting emerging forms of renewables. The maintenance operations of these sub-sea infrastructures can also be costly and not suitable to direct human intervention and thus the use of UUVs is more cost effective and a safer alternative.

Search and Recovery

I-AUV can be simply deployed from commercial airplanes or inexpensive marine vessels of opportunity and this can make them very effective in quick search and recovery of lost objects such as black-boxes. After localizing and constraining the intervention area by acoustic techniques, these I-AUVs could be deployed fast and the recovery could be achieved autonomously at a lower cost (Ridao et al., 2004).

Deep Water Archaeology

The continental shelf was wider than what it is now about a million years ago and the sea levels were about 130 m lower, which was attractive for human settlements. These areas are now drowned underwater together with important heritages that could reveal critical historical information. This makes high resolution seafloor mapping very attractive to

underwater archaeologists who are keenly interested in gathering information about these sites. Deep water excavations were undertaken on few occasions using adhoc hardware or ROV operations, which mostly end up with high costs. Most of the archaeologists only have access to small boats, which are not suitable for deep sea interventions. Hence, this makes light Hybrid ROVs and I-AUVs highly attractive to them (Ridao et al., 2004).

Science

Permanent observatories located on the seabed are artificial infrastructures that require periodic maintenance including tasks such as downloading great volumes of data, connecting or disconnecting cables, replacing batteries, and placing and recovering sensor packages. These tasks could be closely associated with the capabilities of I-AUVs and benefit from their reduced cost of operations (Ridao et al., 2004).

1.3 Modelling, Guidance, Navigation and Control

The ability of a system, either marine or space crafts, to maneuver accurately along a desired geometrical trajectory is a principle objective for most applications. This objective is commonly achieved by solving tracking control problems through design and implementation of GNC systems. The invention of the gyro-compass in 1908, was the start of the first model-based ship control, which made available a reliable yaw angle feedback. The gyro-compass was the initial basic instrument in the feedback control systems design for heading control and these devices are known as autopilots. Figure 1.4 shows a block diagram representing a GNC signal flow.

Development of local positioning systems was the next milestone, while satellite navigation systems were first made available in 1994. Advances in local area positioning systems and new results in feedback control have contributed to the development of DP systems. The global use of DP systems is improved by the commercialization of satellite navigation systems and GPS receivers are standard devices in way-point tracking control

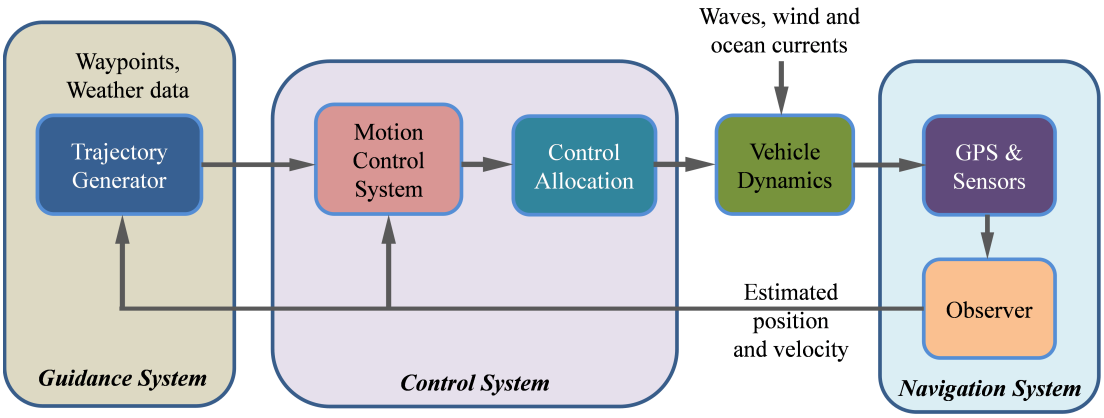

Figure 1.4: GNC signal block with a closed-loop guidance system.

and ship positioning systems (T. Fossen, 2011). The GNC systems are briefly introduced here and are discussed in detail in chapter 3.

1.3.1 Modelling

GNC techniques rely on a model of the vehicle which are identified either using first principles or empirical methods e.g. neural-networks, in order to calculate, control or estimate the system states since models will describe the system behavior and thus the evolution of states. This concerns the modeling of the dynamics of the vehicle, which consists of the kinetics and kinematics. Vehicle kinetics are commonly described by Newton-Euler formulations of the equations of motion, and sometimes using Lagrangian methods. Kinetic modeling of UVs in 6-DOF are non-trivial and time-consuming since it requires large number of hydrodynamic parameters. Kinematics usually concerns with the representation and transformation of states in coordinate systems or reference frames, which are usually the body-fixed reference frame BODY that is fixed to the vehicle which moving along with it, and an inertial reference frame that describes the position and orientation of the vehicle with respect to a certain reference on Earth, such as the North East Down (NED) frame. Kinematics is also thus important from the perspective of modeling environmental disturbances such as ocean currents and waves and of describing their interaction with the vehicle.

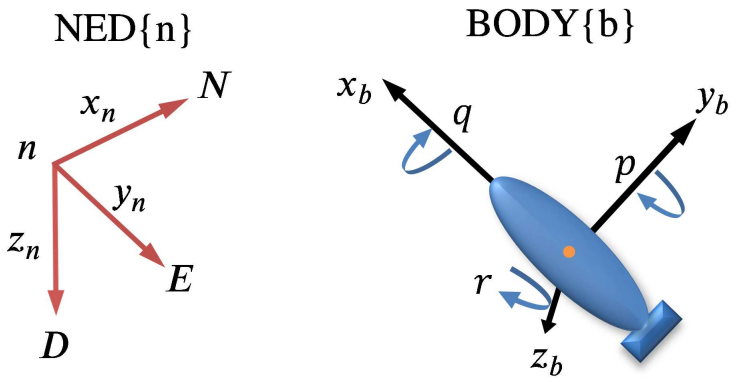

Figure 1.5: BODY and NED reference frames

1.3.2 Kinematics

For mathematical models of UV, the following notations adopted by SNAME (T. Fossen, 1994) are used to describe the vehicle motion (Table 1.1).

DOF	Motion	Forces and moments	Linear and angular velocity	Position and Orientation
1	Surge (motion in x-axis)	$X(N)$	$u(m/s)$	$x(m)$
2	Sway (motion in y-axis)	$Y(N)$	$v(m/s)$	$y(m)$
3	Heave (motion in z-axis)	$Z(N)$	$w(m/s)$	$z(m)$
4	Roll (rotation about x-axis)	$K(Nm)$	$p(rad/s)$	$\phi(rad)$
5	Pitch (rotation about y-axis)	$M(Nm)$	$q(rad/s)$	$\theta(rad)$
6	Yaw (rotation about z-axis)	$N(Nm)$	$r(rad/s)$	$\psi(rad)$

Table 1.1: Notations for motion of marine vehicles.

The reference frames describing these motions are shown in Figure 1.5. Further discussions on vehicle dynamics and modeling are presented in Chapter 2.

1.3.3 Guidance

Guidance systems are responsible for generating reference trajectories such as desired states for the vehicle to track. They can also use joysticks, keyboards, external inputs (such as weather data, wind and wave disturbances, digital charts etc.) and the state vectors estimated from navigation and sensors systems. These data are further processed in order to generate a feasible trajectory for motion control. The *guidance law* can be

interpreted as the method of computing at least the desired heading angle and/or turning rate which the vehicle is required to track in order to converge to the desired path.

Popular guidance laws in both marine and aerospace communities are the Lookahead-based and Enclosure-Baed Line-Of-Sight (LLOS and ELOS), Pure-Pursuit, and Vector Field guidance laws (Nelson, Barber, McLain, & Beard, 2005; T. Fossen, 2011; Caharija, Pettersen, Calado, & Braga, 2015). Guidance laws are further discussed and reviewed in chapter 3.

1.3.4 Navigation

Navigation concerns with the problem of knowing the vehicle states of motion, and thus deals with estimating the vehicle states such as position, orientation, and linear and angular velocity and acceleration. Vehicles or systems are equipped with a state estimator to process the raw sensor and navigation data. The measurements are sent to a computer which is able to filter noise, predict and reconstruct unmeasured states. The most popular state estimation algorithm is the Kalman Filter (KF) and its variations, which was introduced in the 1960s. Other algorithms based on the passivity and nonlinear theory have also been developed later (T. Fossen, 2011).

The navigation problem is more challenging for underwater platforms due mainly to the principle issues of attenuation of higher frequency signals and the unstructured nature of the undersea environment, which makes the vehicle to rely heavily on acoustic signals. The acoustic signals present a number of shortcomings, such as noisier and slower travel speed compared to light, which will make it difficult to achieve fast and accurate measurements for state estimation and positioning (Paull, Saeedi, Seto, & Li, 2014).

1.3.5 Control

Control systems are designed to achieve specific control objectives, and is here associated with motion control (T. Fossen, 2011). The approach to control system can be divided into two main categories depending on whether or not they use feedback of actual system

states: open-loop or feedback control. The aim of control systems are either to stabilize an unstable system or to render the system to behave in a desired manner so that the errors between the actual and some desired states are minimized. In control literature the following classifications are typically used for motion control scenarios (T. Fossen, 2011):

- **Set-point regulation** (point stabilization): A special case where the desired position and attitude are constants.
- **Trajectory tracking (TT) control**: Objective is to render the system output $y(t) \in R^m$ to track a desired output $y_d(t) \in R^m$.
- **Path-following (PF) control**: Following a time-invariant predefined path without spatial constraints.

Once control objectives are identified a motion control system is designed to meet these objectives.

Motion control of marine vehicles has been an active field of research since the first mechanical autopilot was invented in 1911. Modern control systems are based on various design methods such as the widely-known proportional-integral-derivative (PID) control, linear quadratic optimal and stochastic control, feedback-linearization and backstepping techniques, H_∞ control, fuzzy systems, neural networks and nonlinear control theory, to name some (T. Fossen, 2011). Further discussion on PF control for AUVs is presented in Chapter 3, along with the reason why the PF strategy is considered in this thesis for its flexibility over TT.

PF Course Control

The term course control in PF (e.g. (T. Fossen, 2011; A. Lekkas & Fossen, 2013; T. Fossen & Pettersen, 2014)) refers to controlling the course angle of the vehicle which incorporates sideways motion into the computation of the heading angle through the sideslip angle. The sideways motion is induced in sway direction of the vehicle, which will produce a non-zero sideslip angle that has to be taken into account for full position control

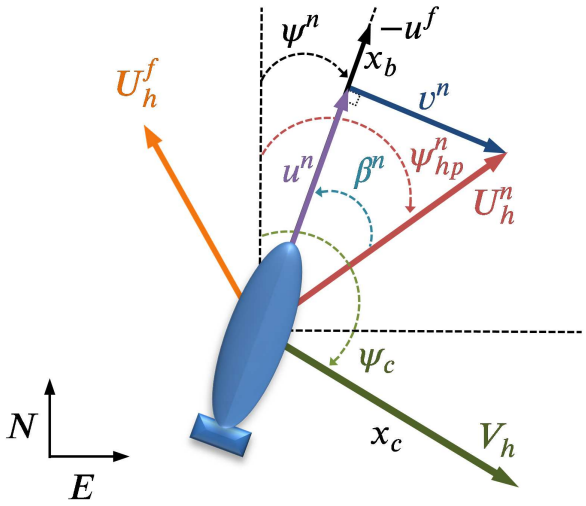

Figure 1.6: Geometry of LOS guidance law with vehicle heading ψ^n, sideslip angle β^n, surge, sway velocities and total horizontal speed u^n, v^n, U_h^n, resp., in NED frame. The rest of the vectors are introduced later accordingly.

using heading control. This will be made more clear in Chapter 3. Without taking into account this sideslip angle, it will be obvious to see that the actual displacement of the vehicle cannot be controlled accurately through heading control, especially during . This sideslip angle exists w/ or w/o external disturbances since its function is dependent on sway velocity. Thus, it is important to take into account the sideslip in PF control systems, i.e. to design a course control system that helps control the actual displacement of the vehicle, despite the existence of external disturbances.

The course angle is the combination of the vehicle heading angle and *sideslip angle* that is caused by vehicle non-zero sway motion. Thus, controlling course angle is the accurate approach in PF since it can control the actual displacement of the vehicle in an inertial frame rather than just controlling its heading. Especially, the difference in accuracy of the PF using course control and heading control is more stark when there are environmental disturbances which cause larger sway motion and thus larger sideslip angles, which is only taken into account in the course control problem. Therefore, the course control is more important in guidance-based PF.

The PF problem for straight-line with sideslip angle is shown in Figure 1.6.

Speed Allocation in Course Control

In PF course control, it is natural to only have a desired total vehicle speed at the kinematic level, which is then required to be correctly distributed to three linear speeds in vehicle surge, sway and heave DOFs, due to the definition of the total speed. In 2-D, this problem reduces the design of desired surge and sway speeds (or desired state trajectory generation for surge and sway) given the desired horizontal speed of the vehicle. This problem is conventionally solved by directly making the desired surge speed approximately equal to the desired horizontal speed assuming the sway velocity of marine craft to be negligible (e.g. (A. Lekkas & Fossen, 2012; T. Fossen, 2011; T. Fossen & Pettersen, 2014; Caharija et al., 2016)). Børhaug, Pavlov, and Pettersen (2008); Caharija, Candeloro, Pettersen, and Sørensen (2012); Caharija et al. (2016) have also designed the desired surge speed as a cosine component of the desired total horizontal speed. This is referred as speed allocation in this thesis as the problem of allocating the desired speed vector into x and y directions of at the BODY level.

1.4 Thesis Aims and Objectives

Research on UVs has been considerably active in the last few decades due to a number of factors as mentioned earlier such as the need for automation which will ultimately minimize the cost, enabling of deep-water missions whcih are dangerous for humans. The literature on UV modelling and control shows that achieving a model that can accurately describe the vehicle motion and its interactions with the surrounding fluid is not easy due to the non-trivial hydrodynamic modelling of UV in 6 DOF (T. Fossen, 2011), unmodelled thruster-hull and thruster-thruster interactions (Caccia, Indiveri, & Veruggio, 2000), simplifications in vehicle and nonlinear actuator models. In addition, as discussed earlier, there are challenges in UV navigation problem due to unavailability of high-frequency signals for state estimation and vast oceans without reference systems for localization and changing currents (Paull et al., 2014). One of the primary objectives of UV control and

autonomy is the efficient, safe and accurate execution of a path-following tasks, since any motion control scenario requires the vehicle to follow a desired trajectory. Between TT and PF strategies, the PF provides a more flexible and robust alternative to TT since it does not impose any temporal constraints (Børhaug & Pettersen, 2005), among other advantages which are discussed in chapter 3. Therefore, the aim of this thesis is to develop an efficient and robust guidance system for PF of UVs. In order to achieve the thesis aim, the following objectives are summarized:

1. A literature review on modeling and guidance for UV PF.
2. Derivation of a 6-DOF mathematical model of UVs incorporating environmental disturbances.
3. Design of a novel guidance system for UV PF.
4. Performance and stability analysis.

The TT or PF problem is a primary task for any mobile systems including aircraft, spacecraft, ground robots, and not just marine craft.

1.5 Contribution to Knowledge

The contributions to knowledge of the thesis with respect to the state of current literature can be summarized into two main topics: Relativity and Expression of States in Reference Frames, and PF control and Stability of LOS Guidance Laws.

1.5.1 Relativity and Expression of States in Reference Frames

The essential contribution to knowledge of this thesis pivots around an improved understanding in expression of motion states in reference frames. This is based on a distinction whether a state is *relative to* and *expressed in* a reference frame, as first described in (Encarnação & Pascoal, 2000a). Compared to current literature, this is expended to describe the motion states of the FLOW reference frame along with an improved definition

of the FLOW frame. Particularly, it is shown in this thesis which reference frame the FLOW states are expressed in. This provides an updated relationship between the BODY, FLOW and NED motion states, which is referred as the relationship of relativity.

Inspired by Newton's 3rd Law, the theory of *state relativity* has been presented to describe the relativity between two objects represented by reference frames, which provides a mathematical basis for incorporating environmental disturbances into the relative equations of motion. Newton's 3rd Law is also rephrased using reference frames, which makes it easier to apply it more accurately. In relation, a complete model of 3-D ocean current and/ro wave is modeled in a simpler and more intuitive manner compared to the only such model in (T. Fossen, 2012), which also requires an improved understanding coordinate transformations between reference frames. The PF problem in general has also been revisited and the general definitions of track-errors are provided in an inertial frame NED w/o requiring a reference rotation as commonly done in the literature (T. Fossen, 2011; T. Fossen & Pettersen, 2014; T. Fossen & Lekkas, 2015).

1.5.2 LOS PF control and Stability of LOS Guidance Laws

Regarding LOS guidance law, a simple and effective tuning mechanism for the ELOS guidance law is presented, which will guarantee to provide virtual reference points on the path even when the cross-track error is larger than the fixed tuning radius. This tuning modification is easier and more effective compared to previous approaches proposed for ELOS guidance laws as in (Moreira, Fossen, & Soares, 2007; Khaled & Chalhoub, 2013). A comparison between the resulting guidance law, and the other two schemes of the LOS guidance and Vector Field guidance has also been provided for course control.

Course control is applied in the PF control problem, which is an improtant PF control technique due to its ability to incorporate sideway motion (sideslip) into the desired heading angle (T. Fossen, 2011; A. Lekkas & Fossen, 2013; T. Fossen & Pettersen, 2014). Course control is further investigated and extended to the vertical plane in this thesis with a new definition of the vertical-slip angle different to the only existing one in (A. Lekkas

& Fossen, 2013). Its disturbance rejection ability is also clearly shown in comparison. The unique formulation and solution of the speed allocation problem has been presented and employed in the guidance system. Its ability in further disturbance rejection and reduction in fluctuation in the path tracking error has also been illustrated. The speed allocation also provides interesting design options in sway full actuation that did not exist before since it does not assume the sway velocity to zero.

Guidance laws have the property of stabilizing the cross-track error at the kinematic level that can describe their robustness (Pettersen, 2017), which is independent of course control. The stability properties of the guidance laws in cross-track course control is limited to SGES of the conventional lookahead-based LOS (LLOS) guidance law (see (T. Fossen & Pettersen, 2014; Wigg, Caharija, Krogstad, & Pettersen, 2016) for SGES stability of LLOS guidance law). The stability results in this thesis show SGES of the ELOS and the new switching ELOS (SELOS) guidance laws, particularly with a distinction between straight-line and curved-path PF scenarios.

It can be seen that the main contribution to knowledge of the work is based on:

- an improved understanding of relativity and expression of motion states in reference frames.

1.5.3 Other Contributions

Other contributions include an analytic method to improve the modeling of forces and moments in the equations of motions based on the stability of unforced vehicle system. The method is derived by integrating Newton's 1st Law with Lyapunov stability. It helps in modeling the signs of hydrodynamic forces and moments in the equations of motion, particularly on the difference between the signs of the added mass and damping terms in the models in the literature.

The concept of *drift rate* has been presented, which is a simple and effective method of calculating relative velocities through lookup tables.

Finally, the formal proofs of passivity and boundedness of relative UV system has

been provided. They are essential properties of robotic systems in analyzing their stability and design of passivity based controllers, and have been treated as realistic assumptions in the literature without formal proofs (Børhaug et al., 2008; Caharija et al., 2012, 2016; Wigg et al., 2016). Note that however, an informal proof of passivity of marine vehicles has been suggested in (Sagatun & Fossen, 1991) w/o a formal proof. The formal proof of passivity and boundedness of marine vehicles is only limited to 2-D as provided by (Breivik & Fossen, 2005). In 3-D, the formal proofs require an analysis of the gravitational and restoring forces and moments vector. Hence, they are explicitly provided in this thesis under the assumption of hydro-static neutrality for convenience in future research.

Most of these contributions are based on identifying and trying to address potential gaps in the initial topic of research and a result of continuous improvement on these works. For example, the whole process of coming up with the latest complete version of the ocean CURRENT in 3-D has been over a year. Note that these problems are inherently challenging in the literature.

1.5.4 Organization of the Thesis

The thesis is organized as follows. Chapter 2 presents an introduction to dynamics, hydrodynamic modeling, and equations of motion of UVs.

Chapter 3 presents a literature review about state-of-the-art and discussions on current topics on guidance-based path-following control, popular guidance laws and the LOS guidance schemes. The topics on GNC have been revisited with a brief review on control techniques for UV flight control and integrated GNC approaches.

The advances related to relativity and expression of motion states and discussions on 3-D angles of motion are presented in Chapter 4 with a revision on the lift force. The unforced stability of equations of motion are analyzed here for understanding the meaning of the signs of forces and moments in the relative equations of motion in terms of stability theory. The concept of state relativity is presented which builds a mathematical analysis on incorporating the environmental disturbances. Newton's 3rd Law is also expressed in

terms of reference frames. The proofs of passivity and boundedness and the new model of ocean current are also derived in this chapter.

Chapter 5 focuses on performance and stability analysis of the LOS and modified LOS guidance laws using the speed allocation. PF course control performance of full and sway-underactuated cases are also studied using nonlinear sliding mode and PID controllers at the kinetic level. The linear analysis of LOS guidance laws are also included in this chapter, along with a comparison between three popular guidance laws in course control with speed allocation.

Chapter 6 extends the LOS course control to 3-D, particularly with the vertical course control for pitch DOF with the vertical-slip angle. The 3-D problem is studied for vehicle models in 4 and 5-DOF with passively-stabilized roll DOF in full actuation. Underactuated cases include sway underactuation in 4-DOF and sway and heave underactuation in 5-DOF. When heave and pitch DOFs are actuated, planar speed assignment techniques are required to track the 3-D LOS vector simultaneously in both planes.

Finally, conclusion and discussions on future works are presented in Chapter 7.

Chapter 2

Modelling and Dynamics

This chapter will present the state-of-the-art literature and a review on UV modeling including environmental disturbances. These include vehicle kinematics and kinetics, and finally the representation and incorporation of ocean wave and current forces and moments into the equations of motion. It will also highlight some differences in the equations of motion presented in the literature.

2.1 Dynamics of UVs

Motion control of UV requires a dynamic mathematical model which can describe the system inputs, outputs and the relationship between them. This problem concerns with deriving the governing equations of motion of rigid-bodies through fluids and thus, the dynamics of UV. Aside from the rigid-body kinetics, the dynamics of UVs also includes the kinematics which concerns the the description and transformation of vehicle states in and between coordinate systems or reference frames.

Modelling of underwater vehicle motion in 6-DOF is a time-consuming and a non-trivial process by any means, mainly because it involves determining dozens of hydrodynamic coefficients which usually require experimental set-ups and facilities, such as the popular Planar Motion Mechanism (PMM) tests of the 1960s. The difficulty in achieving good overall models that can accurately describe the vehicle motion and its interaction

with the dynamic ocean environment is increased by the high nonlinearities and coupling in motion (T. Fossen, 2011), thruster-thruster and thruster-hull interactions (Caccia et al., 2000), and the combined uncertainties and unmodelled factors from simplifications in vehicle and actuator models, and measurement noises. The experimental tests are usually costly and some require a scale model. Advances in computer simulation techniques, such as Computational Fluid Dynamics (CFD), have also made possible their application in determining the hydrodynamic coefficients for vehicles with complex geometries. However, CFD-based methods are convenient and cost effective for preliminary stages of ship designs but may not produce accurate results for identification of manoeuvring models, and require a considerable amount of computational work (Clark & Horn, 1997). Another approach to modelling is through on-line system identification techniques using on-board sensors. These are advantageous in terms of not involving the time-consuming and costly process of experimental identifications or extensive CFD analysis, and are easily repeatable for changes in vehicle configurations (Caccia et al., 2000), which easily result from e.g. changes in vehicle payloads that are common in modular vehicle designs. They employ on-line parameter estimation techniques such as recursive least squares using data from on-board sensor (e.g. (Caccia et al., 2000; Mark, Frans, & Chryssostomos, 2006; David & Luis, 2003; Ridao et al., 2004; Pepijin, Johansen, Sørensen, Flanagan, & Toal, 2007; Avila, Décio, & Adamowski, 2013). The accuracy of on-line identification techniques commonly depend on the accuracy of the data collected from on-board sensors. Thus, it can be that identification capabilities off-line approaches such as availability of computational resources, larger volumes of data, higher precision sensors, and flexibility in experimental set-ups (e.g. uncoupled 1-DOF motion achieved in towing-tanks) can provide better model identifications since on-line identification approaches usually cannot provide such capabilities and procedures from on-board sensors alone.

Reference Frames

The vehicle states are describe within a defined reference frame or a coordinate system. These coordinate systems are also referred as reference frames in vehicle kinematics. The common coordinate systems for vehicle GNC purposes are the body-fixed BODY frame, the earth-fixed inertial NED frame, and the FLOW reference frame. Discussions on other reference frames like Earth-centred inertial (ECI) frame can be found in (T. Fossen, 2011).

BODY: The BODY frame is a moving reference frame fixed to the body of the vehicle, usually its centre of origin (CO). The x-axis points in the forward direction of the vehicle, the y-axis from port to starboard, and the z-axis from top to bottom. It is denoted by $\{b\} = \{x_b, y_b, z_b\}$. This orientation makes the BODY frame appropriate for expressing the vehicle velocities.

NED: The NED frame is an earth-fixed frame with x-axis pointing towards the true North, the y-axis pointing towards East, and the z-axis pointing downwards perpendicular to the surface of the sea. This reference frame is denoted by $\{n\} = \{x_n, y_n, z_n\}$, with its $\{n\}$ origin defined relative to Earth's reference ellipsoid (T. Fossen, 2011). This is a reference frame used in everyday life, which is defined by the plane tangent to the surface of the Earth and moving with the vehicle but axes pointing in different directions than BODY axes (T. Fossen, 2011). Way-points are generally defined with reference to a fixed point on Earth, which makes it convenient to carry out guidance and navigation tasks in this frame.

FLOW: The FLOW reference frame is used to describe hydrodynamic data. It is found by rotating the BODY axis to achieve a resulting x-axis that is parallel to the free-stream of the flow. The x-axis of FLOW points to the relative free-stream while its z-axis remains perpendicular to its x-axis, even when its rotated. The y-axis is the right-hand-side (RHS) of this right-handed reference frame (T. Fossen, 2011). The reason of using FLOW reference frame is because of its convenience in computing hydrodynamic forces. For example, the lift and drag forces are perpendicular and parallel to the relative FLOW axes, respectively(T. Fossen, 2011).

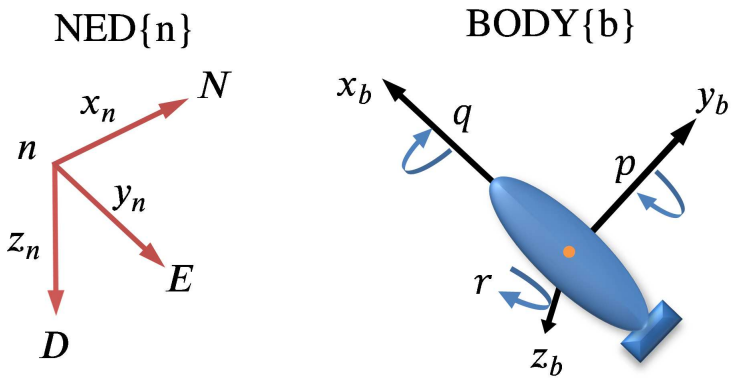

Figure 2.1: BODY and NED reference frames

The reference frames are depicted in Fig 2.1.

Coordinate Transformation Between Body and NED

The important element of the vehicle kinematics is the transformations between the reference frames, which will allow exchange of knowledge of vehicle states from one reference frame to the other. This is done by the traditional rotation matrix. The rotation of vehicle BODY velocities to vehicle NED velocities are achieved by the common rotation matrix:

$$\dot{\boldsymbol{\eta}} = \boldsymbol{J}(\boldsymbol{\Theta})\boldsymbol{\nu}, \tag{2.1}$$

where

$$\boldsymbol{\eta} \triangleq [x, y, z, \phi, \theta, \psi]^T \tag{2.2}$$

is the vector of position and Euler angles in the inertial frame NED,

$$\boldsymbol{\nu} \triangleq [u, v, w, p, q, r]^T \tag{2.3}$$

is the vehicle BODY vector of linear and angular velocities. $\boldsymbol{J}(\boldsymbol{\Theta})$ is the transformation matrix given by:

$$\boldsymbol{J}(\boldsymbol{\Theta}) = \begin{bmatrix} \boldsymbol{R}(\boldsymbol{\Theta}) & \mathbf{0}_{3x3} \\ \mathbf{0}_{3x3} & \boldsymbol{T}(\boldsymbol{\Theta}) \end{bmatrix} \tag{2.4}$$

where $\boldsymbol{\Theta} \triangleq [\phi, \theta, \psi]^T$ represents the vehicle orientation or Euler angles. The rotation matrices $\boldsymbol{R}(\boldsymbol{\Theta})$ and $\boldsymbol{T}(\boldsymbol{\Theta})$ are given by:

$$\boldsymbol{R}(\boldsymbol{\Theta}) = \begin{bmatrix} c(\psi)c(\theta) & -s(\psi)c(\phi)+c(\psi)s(\theta)s(\phi) & s(\psi)s(\phi)+c(\psi)c(\phi)s(\theta) \\ s(\psi)c(\theta) & c(\psi)c(\phi)+s(\phi)s(\theta)s(\psi) & -c(\psi)s(\phi)+s(\theta)s(\psi)c(\phi) \\ -s(\theta) & c(\theta)s(\phi) & c(\theta)c(\phi) \end{bmatrix} \tag{2.5}$$

$$\boldsymbol{T}(\boldsymbol{\Theta}) = \begin{bmatrix} 1 & s(\phi)t(\theta) & c(\phi)t(\theta) \\ 0 & c(\phi) & -s(\theta) \\ 0 & s(\phi)/c(\theta) & c(\phi)/c(\theta) \end{bmatrix} \tag{2.6}$$

Here, s, c and t represent $\sin, \cos$ and tan of the Euler angles. To avoid singularity in calculations, the Euler angles should be within these intervals or quaternions should be used instead:

$$-\pi < \phi \leq \pi; \quad -\pi/2 < \theta < \pi/2; \quad 0 \leq \psi < 2\pi. \tag{2.7}$$

Remark 2.1 Note that care should be given software simulations of coordinate systems and transformation where necessary since many software do not follow the right-hand convention, i.e. up is positive in software axes where Down is positive in NED.

2.2 Nonlinear Modeling of UV

UV dynamics are commonly represented by the equations of motion consisting of rigid-body kinetics that are derived using Newtonian or Lagrangian approaches (Yuh, 1990; T. Fossen, 1991; T. Fossen & Fjelstad, 1995). The equations of motion consider the motion of rigid-bodies through fluids. Earliest analysis of hydrodynamic forces and moments in a potential flow can be traced back to the extensive treatment of Lamb (1895). The first attempt of a mathematical model for ships can date back to the model of (Davidson & Schiff, 1946). Among the models that became popular models later are the nonlinear model of(Abkowitz, 1964), where hydrodynamic forces and moments are expressed us-

ing Taylor series expansion, and the steering model of Nomoto (Nomoto, Taguchi, Honda, & Hirano, 1957) which most model-based autopilot designs were based on (T. Fossen, 2011). Common models for autopilot designs also include the 1st and 2nd-order nonlinear extensions of Nomoto's model proposed by Norrbin (1963) and Bech and Smith (T. Fossen, 2011). The use of second-order modulus functions in the equations of motion was introduced by (Fedyaevsky & Sobolev, 1963). A simplified expression for Norbin's nonlinear model was also proposed by Blanke (1981). T. Fossen (1991) presented the use of robot-like vectorial representations to exploit the physical properties of both sea-keeping and manoeuvring models, with the linearized forms in (T. Fossen, 1994). The nonlinear damping forces were expressed using the theory of low-aspect ratio wings in the approach of Ross (2008).

Despite the emergence of simple and useful models based on Lagrangian or Newtonian methods that became common in the literature, such as those discussed and proposed in (T. Fossen, 2002, 2011), there is no standard models for ships and underwater vehicles. Thus, any contribution towards standardization is desirable. The essential different include the discrepancies in formulation of the hydrodynamics forces and moments Coriolis and centripetal forces, which is normal since there are inherently different ways to model them. However a notable difference exist on the signs of the hydrodynamics added mass and damping forces and moments, which do not have to exist under correct application of Newton's 2nd Law. This inconsistency will be highlighted later in this section.

The nonlinear model of (T. Fossen, 1991, 1994; T. Fossen & Fjelstad, 1995; T. Fossen, 2002, 2011) for marine vehicles in 6 degrees of motion (DOF) has become the common model in literature, and this model will be used here for modeling of UVs.

2.2.1 Rigid-Body Kinetics

The motion of a rigid-body w.r.p to a body-fixed rotating BODY frame, with a centre of origin $\{CO\}$ is given by Newton's Laws. This is represented in a compact form as in

(T. Fossen, 1991; T. Fossen & Fjelstad, 1995):

$$\boldsymbol{M}_{RB}\dot{\boldsymbol{\nu}} + \boldsymbol{C}_{RB}(\boldsymbol{\nu})\boldsymbol{\nu} = \boldsymbol{\tau}_{RB}, \tag{2.8}$$

where $\boldsymbol{M}_{RB} = \boldsymbol{M}_{RB}^T > 0$ is rigid-body mass-inertia matrix, $\boldsymbol{\nu} = [u, v, w, p, q, r]^T$ is the vehicle BODY-fixed vector of absolute/general velocities and angular rates, $\boldsymbol{C}_{RB} = -\boldsymbol{C}_{RB}^T$ is the rigid-body Coriolis and centripetal forces and moments, and $\boldsymbol{\tau}_{RB}$ is rigid-body forces and moments in respective DOFs. The 6×6 mass-inertia matrix $\boldsymbol{M}_{RB}$ is given by:

$$\boldsymbol{M}_{RB} = \begin{bmatrix} m & 0 & 0 & 0 & mz_g & -my_g \\ 0 & m & 0 & -mz_g & 0 & mx_g \\ 0 & 0 & m & my_g & -mx_g & 0 \\ 0 & -mz_g & my_g & I_x & -I_{xy} & -I_{xz} \\ mz_g & 0 & -mx_g & -I_{yx} & I_y & -I_{yz} \\ -my_g & mx_g & 0 & -I_{zx} & -I_{zy} & I_z \end{bmatrix}, \tag{2.9}$$

where $\boldsymbol{r}_g = [x_g, y_g, z_g]$ is the center of gravity (CG) w.r.t the CO of BODY, and $\boldsymbol{I}$ is the 3×3 inertia tensor with respect to CO given by:

$$\boldsymbol{I} = \begin{bmatrix} I_x & -I_{xy} & -I_{xz} \\ -I_{yx} & I_y & -I_{yz} \\ -I_{zx} & -I_{zy} & I_z \end{bmatrix}, \tag{2.10}$$

The skew-symmetric $\boldsymbol{C}_{RB}(\boldsymbol{\nu})$ is given by:

$$\boldsymbol{C}_{RB}(\boldsymbol{\nu}) = \begin{bmatrix} 0 & 0 & 0 \\ 0 & 0 & 0 \\ 0 & 0 & 0 \\ -m(y_g q + z_g r) & -m(y_g p + w) & m(z_g p - v) \\ m(x_g q - w) & -m(z_g r + x_g p) & m(z_g q + u) \\ m(x_g r + v) & m(y_g r - u) & -m(x_g p + y_g q) \end{bmatrix} \begin{bmatrix} m(y_g q + z_g r) & -m(x_g q - w) & -m(x_g r + v) \\ -m(y_g p + w) & m(z_g r + x_g p) & -m(y_g r - u) \\ -m(z_g p - v) & -m(z_g q + u) & m(x_g p + y_g q) \\ 0 & -I_{yz} q - I_{xy} p + I_z r & I_{yz} r + I_{xy} p - I_y q \\ I_{yz} q + I_{xz} p - I_z r & 0 & -I_{xz} r - I_{xy} q + I_x p \\ -I_{yz} r - I_{xy} p + I_y q & I_{xz} r + I_{xy} q - I_x p & 0 \end{bmatrix}. \tag{2.11}$$

2.2.2 Hydrodynamic Forces and Moments

The hydrodynamic forces and moments consist of the 6×6 hydrodynamic *added mass* matrix, added Coriolis and centripetal matrix, and damping/drag matrix.

Added Mass

The hydrodynamic added mass can be seen as the virtual mass added to the system mass as an accelerating body must displace some volume of fluid as it pass through it (T. Fossen,

2011). The added mass matrix is given by using the notations of (SNAME, 1950) as:

$$\boldsymbol{M}_A \triangleq -\begin{bmatrix} X_{\dot{u}} & X_{\dot{v}} & X_{\dot{w}} & X_{\dot{p}} & X_{\dot{q}} & X_{\dot{r}} \\ Y_{\dot{u}} & Y_{\dot{v}} & Y_{\dot{w}} & Y_{\dot{p}} & Y_{\dot{q}} & Y_{\dot{r}} \\ Z_{\dot{u}} & Z_{\dot{v}} & Z_{\dot{w}} & Z_{\dot{p}} & Z_{\dot{q}} & Z_{\dot{r}} \\ K_{\dot{u}} & K_{\dot{v}} & K_{\dot{w}} & K_{\dot{p}} & K_{\dot{q}} & K_{\dot{r}} \\ M_{\dot{u}} & M_{\dot{v}} & M_{\dot{w}} & M_{\dot{p}} & M_{\dot{q}} & M_{\dot{r}} \\ N_{\dot{u}} & N_{\dot{v}} & N_{\dot{w}} & M_{\dot{p}} & N_{\dot{q}} & N_{\dot{r}} \end{bmatrix}, \tag{2.12}$$

For example, the hydrodynamic added mass force Y_A along the x-axis due to an acceleration $\dot{u}$ in the x-direction is written as:

$$Y_A = Y_{\dot{u}}\dot{u}, \quad \text{where} \quad Y_{\dot{u}} \triangleq \frac{\partial Y}{\partial \dot{u}}. \tag{2.13}$$

The added mass matrix is generally assumed constant and has the following property (T. Fossen, 2011):

Property 2.1 (Hydrodynamic added mass matrix $\boldsymbol{M}_A$) *For a rigid body at rest or moving at a forward speed $U > 0$, the hydrodynamic system inertia matrix $\boldsymbol{M}_A$ is positive semi-definite:*

$$\boldsymbol{M}_A = \boldsymbol{M}_A^T \geq 0. \tag{2.14}$$

Proof. The proof is given in (T. Fossen, 2011). □

Remark 2.1 All 36 the elements of $\boldsymbol{M}_A$ may be distinct, but $\boldsymbol{M}_A \geq 0$. Experimentally identified values of $\boldsymbol{M}_A$ are usually in good agreement with their theoretical ones (T. Fossen, 2011). This is very intuitive since, by definition, added mass is also a "mass-inertia", and thus, should have the property of the mass of an object, which is positive.

The above property is based on the assumtion that $\boldsymbol{M}_A$ is independent of wave frequency, which is a good assumption for low frequency applications. Note that the hydrodynamic added mass-inertia and rigid-body mass-inerita matrices are the same in both Newtonian Lagrangian formulations (T. Fossen & Fjelstad, 1995).

The off-diagonal elements of the added mass matrix are usually small compared to their diagonal counter parts. For underwater vehicle applications at low speeds, the off-diagonal elements are generally neglected. This gives the following diagonal structure for $\boldsymbol{M}_A$ (T. Fossen & Fjelstad, 1995; T. Fossen, 2011):

$$\boldsymbol{M}_A \triangleq -diag\{X_{\dot{u}}, Y_{\dot{v}}, Z_{\dot{w}}, K_{\dot{p}}, M_{\dot{q}}, N_{\dot{r}}\}. \tag{2.15}$$

Added Coriolis and Centripetal matrix

The added Coriolis and centripetal matrix $\boldsymbol{C}_A$ is also simplified due to the diagonal structure of $\boldsymbol{M}_A$ above, and in this case is commonly given by (T. Fossen & Fjelstad, 1995):

$$\boldsymbol{C}_A \triangleq \begin{bmatrix} 0 & 0 & 0 & 0 & -Z_{\dot{w}}w & Y_{\dot{v}}v \\ 0 & 0 & 0 & Z_{\dot{w}}w & 0 & -X_{\dot{u}}u \\ 0 & 0 & 0 & -Y_{\dot{v}}v & X_{\dot{u}}u & 0 \\ 0 & -Z_{\dot{w}}w & Y_{\dot{v}}v & 0 & -N_{\dot{r}}r & M_{\dot{q}}q \\ Z_{\dot{w}}w & 0 & -X_{\dot{u}}u & N_{\dot{r}}r & 0 & -K_{\dot{p}}p \\ -Y_{\dot{v}}v & X_{\dot{u}}u & 0 & -M_{\dot{q}}q & K_{\dot{p}}p & 0 \end{bmatrix}, \tag{2.16}$$

Damping

The hydrodynamic damping/drag experience by rigid-bodies moving through fluids can be expressed by using the damping matrix $\boldsymbol{D}(\boldsymbol{\nu})$, which consists of the linear and nonlinear parts as:

$$\boldsymbol{D}(\boldsymbol{\nu}) = \boldsymbol{D}_l(\boldsymbol{\nu}) + \boldsymbol{D}_{nl}(\boldsymbol{\nu}) \tag{2.17}$$

where the nonlinear damping matrix $\boldsymbol{D}_{nl}(\boldsymbol{\nu})$ is usually modelled as the quadratic drag. The hydrodynamic damping is highly nonlinear and coupled in motion. However, under the assumption of low operating speeds for underwater vehicles, the off-diagonal terms

are negligible and the damping matrix is given by the diagonal form:

$$\begin{aligned}\boldsymbol{D}(\boldsymbol{\nu}) \triangleq & -diag\{X_u, Y_v, Z_w, K_p, M_q, N_r\} \\ & -diag\{X_{|u|u}|u|, Y_{|v|v}|v|, Z_{|w|w}|w|, K_{|p|p}|p|, M_{|q|q}|q|, N_{|r|r}|r|\}.\end{aligned} \tag{2.18}$$

The hydrodynamic damping matrix has the following dissipative property (T. Fossen, 2011).

Property 2.2 (Hydrodynamic Damping Matrix $\boldsymbol{D}(\boldsymbol{\nu})$) *For a rigid body moving through an ideal fluid, the hydrodynamic damping matrix $\boldsymbol{D}(\boldsymbol{\nu})$ is real, non-symmetric and strictly positive:*

$$\boldsymbol{D}(\boldsymbol{\nu}) > 0. \tag{2.19}$$

Restoring and Gravitational Forces and Moments

The restoring and gravitational forces and moments experience by the submerged body is given by:

$$\boldsymbol{g}(\boldsymbol{\eta}) = \begin{bmatrix} (W-B)s(\theta) \\ -(W-B)c(\theta)s(\phi) \\ -(W-B)c(\theta)c(\phi) \\ -(y_gW - y_bB)c(\theta)c(\phi) + (z_gW - z_bB)c(\theta)s(\phi) \\ (z_gW - z_bB)s(\theta) + (x_gW - x_bB)c(\theta)c(\phi) \\ -(x_gW - x_bB)c(\theta)s(\phi) + (y_gW - y_bB)s(\phi) \end{bmatrix} \tag{2.20}$$

where W and B are the weight and buoyancy of the vehicle, and $\boldsymbol{r}_b = [x_b, y_b, z_b]$ is the position of the center of buoyancy (CB) w.r.p the position of CG.

2.2.3 Nonlinear Equations of Motion

The nonlinear maneuvering equations of motion are then constructed by collecting all the forces and moments terms, which is then given by:

$$\boldsymbol{M}\dot{\boldsymbol{\nu}} + \boldsymbol{C}(\boldsymbol{\nu})\boldsymbol{\nu} + \boldsymbol{D}(\boldsymbol{\nu})\boldsymbol{\nu} + \boldsymbol{g}(\boldsymbol{\eta}) = \boldsymbol{\tau}_{act}, \tag{2.21}$$

where

$$\boldsymbol{M}\dot{\boldsymbol{\nu}} = \boldsymbol{M}_{RB}\dot{\boldsymbol{\nu}} + \boldsymbol{M}_{A}\dot{\boldsymbol{\nu}}, \tag{2.22}$$

$$\boldsymbol{C}(\boldsymbol{\nu})\boldsymbol{\nu} = \boldsymbol{C}_{RB}(\boldsymbol{\nu}) + \boldsymbol{C}_{A}(\boldsymbol{\nu})\boldsymbol{\nu}. \tag{2.23}$$

$\boldsymbol{\tau}_{act}$ is the actuator input matrix given by:

$$\boldsymbol{\tau}_{act} = [\tau_x, \tau_y, \tau_z, \tau_\phi, \tau_\theta, \tau_\psi]^T. \tag{2.24}$$

2.3 Environmental Disturbances

Environmental disturbances in marine applications consist of three components: wind, ocean waves and currents. For fully submerged underwater vehicles the effect of wind disturbance is neglected (T. Fossen, 1994).

2.3.1 Ocean Waves

Wave filtering is one of the most important issues in the design of ship control systems (T. Fossen, 1994). Extensive discussions on ocean waves on marine vehicles can be found in (T. Fossen, 2011) and in (Faltinsen, 2005) for highspeed vehicels. Underwater vehicles are influenced by wave loads if they are operating in the so-called wave zone. The definition for the depth of influence of the wave zone is $z < \lambda_w/2$, where λ_w is the wave length. The wave loads are divided into two forces in linear wave-frequency model (Faltinsen,

2005): wave excitation and wave reaction. They can be further separated into high and low frequency components. Forces exerted by the wave loads dissipate as the vehicle depth $z \to \infty$, which can be described by the scaling function (Faltinsen, 2005):

$$\sigma(k,z) = e^{-kz} \tag{2.25}$$

where k is the wave number.

Equations of Motion Including Ocean Waves

The forces and moments due to ocean waves are commonly incorporated into the equations of motion using the *priciple of linear superposition* such that (2.21) becomes (T. Fossen, 2012):

$$\boldsymbol{M}\dot{\boldsymbol{\nu}} + \boldsymbol{C}(\boldsymbol{\nu})\boldsymbol{\nu} + \boldsymbol{D}(\boldsymbol{\nu})\boldsymbol{\nu} + \boldsymbol{g}(\boldsymbol{\eta}) = \boldsymbol{\tau}_{act} + \boldsymbol{\tau}_{wave}, \tag{2.26}$$

where $\boldsymbol{\tau}_{wave}$ is the wave forces and moments in respective DOFs.

2.3.2 Ocean Currents

The ocean currents are perhaps the most important modelling aspect of underwater vehicles, and knowledge of of ocean current velocity are very useful for marine GNC since they allow estimation of the vehicle velocities. Ocean currents are described by the horizontal and verical circulation of the ocean waters generated by gravity, wind friction and variations in water density (T. Fossen, 2012). Ocean currents are mainly separated into 3 components, that is reduced from 6 in (T. Fossen, 1994):

- Local wind component.
- Component generated by nonlinear waves.
- Tidal component.

In coastal regions and fjords the tidal component of the current have been measured to reach $2-3m/s$ or more. Incorporation of the current speed into the equations of motion is done by replacing the vehicle generalized velocity with the relative velocity $\boldsymbol{\nu}_r$ given

by (Børhaug & Pettersen, 2005; T. Fossen, 2011, 2012; Caharija et al., 2012):

$$\boldsymbol{\nu}_r = \boldsymbol{\nu} - \boldsymbol{\nu}_c, \tag{2.27}$$

where $\boldsymbol{\nu}_c$ is the ocean current velocity rotated to BODY frame.

An *Irrotational fluid* is deined by (T. Fossen, 2012) and is given by only its linear components since its angular motion is zero (T. Fossen, 2012):

$$\boldsymbol{\nu}_c = [u_c, v_c, w_c, 0, 0, 0]^T, \tag{2.28}$$

and $\boldsymbol{\nu}_{c1} = [u_c, v_c, w_c]^T$ is the linear part which satisfies the following transformation from BODY to NED (T. Fossen, 2012):

$$\boldsymbol{\nu}_c^n = \boldsymbol{R}(\boldsymbol{\Theta})\boldsymbol{\nu}_{c1}, \tag{2.29}$$

where

$$\boldsymbol{\nu}_c^n = [V_x, V_y, V_z]^T, \tag{2.30}$$

is the linear part of ocean current velocity in NED.

An *irrotational constant ocean current* in NED $\boldsymbol{V}_c$ satisfies (T. Fossen, 2012):

$$\boldsymbol{V}_c = [V_x, V_y, V_z, 0, 0, 0]^T, \tag{2.31}$$

$$\dot{\boldsymbol{V}}_c = \boldsymbol{0}. \tag{2.32}$$

Heading, Course, and Sideslip Angles

The heading, course and sidelsip are important states in description of vehicle motion. The definitions of heading and course angles are sometimes used interchangeably in the literature. They are defined here according to conventions in (T. Fossen, 2011). First, the

vehicle speed in NED is defined as:

$$U = \sqrt{u^2 + v^2}. \tag{2.33}$$

which is conventional in SNAME (1950) notations. When the relative velocities are used, this becomes (T. Fossen, 2011):

$$U_r = \sqrt{(u - u_c)^2 + (v - v_c)^2} = \sqrt{{u_r}^2 + {v_r}^2}. \tag{2.34}$$

where u_c and v_c are the horizontal components of the ocean current expressed in BODY. The definitions of these angles are given as the following (T. Fossen, 2011).

Definition 2.1 (Heading (Yaw) Angle ψ) *The angle from x_n axis of $\{n\}$ to x_b axis of $\{b\}$ with positive rotation about z_n axis of $\{n\}$ by the right-hand screw convention.*

Definition 2.2 (Course Angle ψ_{crs}) *The angle from x_n axis of $\{n\}$ to the velocity vector of the craft, with positive rotation about z_n axis of $\{n\}$ by the right-hand screw convention.*

Definition 2.3 (Sideslip (Drift) Angle β) *The angle from x_b axis of $\{b\}$ to the velocity vector of the craft, with positive rotation about z_b axis of $\{b\}$ by the right-hand screw convention.*

According to (SNAME, 1950) and (Lewis, 1989), the sideslip angle for a marine craft is defined by:

$$\beta_{SNAME} \triangleq -\beta. \tag{2.35}$$

The definition of sideslip is adopted by the sign convention used in the aircraft community (T. Fossen, 2011). These definitions had the following relationship between these angles (T. Fossen, 2011):

$$\psi_{crs} = \psi + \beta. \tag{2.36}$$

where

$$\beta = \arcsin\left(\frac{v}{U}\right). \tag{2.37}$$

This can be extended to include the ocean current velocities by using the relative velocities such that (T. Fossen, 2011):

$$\beta = \arcsin\left(\frac{v_r}{U_r}\right). \tag{2.38}$$

Angle of Attack and Coordinate Transformation Between BODY and FLOW

The transformation between the FLOW and BODY axes are obtained using the *stability axes*. The stability axes is a coordinate system obtained by rotating the FLOW axes by a negative sideslip angel $-\beta$ about the z-axis. Then, the stability axes are rotated by a *positive* angle α about the new y-axis, where α is called *angle of attack* (T. Fossen, 2011).

The stability and *wind axes* are commonly used in aerodynamics to model lift and drag forces, which are nonlinear function of α, β and U. This convention has been adopted by the marine community and SNAME to describe the lift and drag forces on submerged bodies (SNAME, 1950; T. Fossen, 2011). For a marine craft, the *wind axes* corresponded to *flow axes* of FLOW (T. Fossen, 2011).

The transformations between BODY, STABILITY and FLOW axes are given by (T. Fossen, 2011, 2012):

$$\boldsymbol{v}^{stab} = \boldsymbol{R}(\alpha)\boldsymbol{v}^{b}, \tag{2.39}$$

$$\boldsymbol{v}^{flow} = \boldsymbol{R}(\beta)\boldsymbol{v}^{stab}, \tag{2.40}$$

where

$$\boldsymbol{R}(\alpha) = \begin{bmatrix} \cos(\alpha) & 0 & \sin(\alpha) \\ 0 & 1 & 0 \\ -\sin(\alpha) & 0 & \cos(\alpha) \end{bmatrix} \tag{2.41}$$

$$\boldsymbol{R}(\beta) = \begin{bmatrix} \cos(\beta) & \sin(\beta) & 0 \\ -\sin(\beta) & \cos(\beta) & 0 \\ 0 & 0 & 1 \end{bmatrix} \tag{2.42}$$

The rotation matrix from BODY to FLOW was then given by (T. Fossen, 2011, 2012):

$$\boldsymbol{R}_b^{flow} = \begin{bmatrix} \cos(\beta)\cos(\alpha) & \sin(\beta) & \cos(\beta)\sin(\alpha) \\ -\sin(\beta)\cos(\alpha) & \cos(\beta) & -\sin(\beta)\sin(\alpha) \\ -\sin(\alpha) & 0 & \cos(\alpha) \end{bmatrix} \tag{2.43}$$

The velocity transformation:

$$\boldsymbol{v}^{flow} = \boldsymbol{R}_b^{flow}\boldsymbol{v}^b, \tag{2.44}$$

was re-written as (T. Fossen, 2011):

$$\boldsymbol{v}^b = (\boldsymbol{R}_b^{flow})^T\boldsymbol{v}^{flow}, \tag{2.45}$$

$$\begin{bmatrix} u \\ v \\ w \end{bmatrix} = \boldsymbol{R}(\alpha)^T\boldsymbol{R}(\beta)^T \begin{bmatrix} U \\ 0 \\ 0 \end{bmatrix} \tag{2.46}$$

This was re-written in the component form as (T. Fossen, 2011):

$$\begin{bmatrix} u \\ v \\ w \end{bmatrix} = \begin{bmatrix} U\cos(\alpha)\cos(\beta) \\ U\sin(\beta) \\ U\sin(\alpha)\cos(\beta) \end{bmatrix} \tag{2.47}$$

The angle of attack for a marine craft is defined by (T. Fossen, 2011):

$$\alpha = \arctan\left(\frac{w}{u}\right). \tag{2.48}$$

When including ocean currents, the angle of attack (2.48), and velocity vector (2.47)

become (T. Fossen, 2011):

$$\begin{bmatrix} u_r \\ v_r \\ w_r \end{bmatrix} = \begin{bmatrix} U_r \cos(\alpha)\cos(\beta) \\ U_r \sin(\beta) \\ U_r \sin(\alpha)\cos(\beta) \end{bmatrix} \tag{2.49}$$

$$\alpha_r = \arctan\left(\frac{w_r}{u_r}\right). \tag{2.50}$$

where

$$u_r = u - u_c, \tag{2.51}$$

$$v_r = v - v_c, \tag{2.52}$$

$$w_r = w - w_c, \tag{2.53}$$

$$U_r = \sqrt{{u_r}^2 + {v_r}^2 + {w_r}^2}. \tag{2.54}$$

The state-space model of a marine craft can be transformed to FLOW axes using a transformation matrix, the general velocity vector $\boldsymbol{\nu}$ and the FLOW velocity vector defined by $\boldsymbol{\nu}^{flow}$ (T. Fossen, 2011):

$$\boldsymbol{\nu}^{flow} = [U, \alpha, \beta, p, q, r]. \tag{2.55}$$

This expression was said to be more intuitive to use from a hydrodynamic point of view, while control engineers prefer the absolute or general velocity vector $\boldsymbol{\nu}$ (T. Fossen, 2011).

Note that the velocity vector $\boldsymbol{\nu}^b$ and $\boldsymbol{\nu}$ were used here interchangeably (see (2.45) and (2.46)).

Models of Irrotational and Constant Ocean Currents

The ocean current velocity is modelled using the FLOW reference frame that describes the free-stream of ocean current in NED (T. Fossen, 2011, 2012). This is obtained by transforming the ocean current intensity V_c, its angle of attack α_c and heading ψ_c from

FLOW axes to NED axes as T. Fossen (2012):

$$\boldsymbol{\nu}_c^n = \begin{bmatrix} V_x \\ V_y \\ V_z \end{bmatrix} = \boldsymbol{R}(\alpha)^T \boldsymbol{R}(\beta)^T \begin{bmatrix} V_c \\ 0 \\ 0 \end{bmatrix} = \begin{bmatrix} V_c \cos(\alpha_c)\cos(\beta_c) \\ V_c \sin(\beta_c) \\ V_c \sin(\alpha_c)\cos(\beta_c) \end{bmatrix}, \tag{2.56}$$

This was then rotated to the BODY frame using the NED to BODY transformation matrix $\boldsymbol{R}(\boldsymbol{\Theta})$ to obtain $\boldsymbol{\nu}_{c1}$ as (T. Fossen, 2012):

$$\begin{bmatrix} u_c \\ v_c \\ w_c \end{bmatrix} = \boldsymbol{R}(\boldsymbol{\Theta}) \begin{bmatrix} V_c \cos(\alpha)\cos(\beta) \\ V_c \sin(\beta) \\ V_c \sin(\alpha)\cos(\beta) \end{bmatrix} = \begin{bmatrix} V_c(\cos\psi\cos\alpha_c\cos\beta_c + \sin\psi\sin\beta_c) \\ -V_c(\sin\psi\cos\alpha_c\cos\beta_c + \cos\psi\sin\beta_c) \\ V_c \sin\alpha_c\cos\beta_c \end{bmatrix} \tag{2.57}$$

where $\phi = \theta = 0$ in $\boldsymbol{R}(\boldsymbol{\Theta})$ and V_c is given by the speed convention (T. Fossen, 2011):

$$V_c = \sqrt{{u_c}^2 + {v_c}^2 + {w_c}^2}. \tag{2.58}$$

Børhaug et al. (2008) has shown that when the ocean current is only assumed constant and irrotational in the inertial frame, and thus, it has dynamics at the BODY frame. This gives the dynamics of $\boldsymbol{\nu}_{c1}$ by the time-derivative of (2.57) as (Børhaug et al., 2008):

$$\dot{\boldsymbol{\nu}}_{c1} = \frac{d}{dt}(\boldsymbol{\nu}_{c1}) = [\dot{u}_c, \dot{v}_c, \dot{w}_c]^T = [rv_c, -ru_c, 0]^T. \tag{2.59}$$

since $\dot{V}_c = \dot{\alpha}_c = \dot{\beta}_c = 0$ for constant ocean currents in NED.

In 2-D, the irrotational ocean current model is obtained from (2.57) by setting $\alpha_c = 0$, which is (T. Fossen, 2012):

$$u_c = V_h \cos(\beta_c - \psi) \tag{2.60}$$

$$v_c = V_h \cos(\beta_c - \psi). \tag{2.61}$$

where V_h denotes the current intensity in the horizontal plane. Similarly,

$$V_h = \sqrt{{u_c}^2 + {v_c}^2}. \tag{2.62}$$

The dynamics of the ocean current in BODY in 2-D is extracted from (2.59):

$$[\dot{u}_c, \dot{v}_c]^T = [rv_c, -ru_c]^T. \tag{2.63}$$

Note that u_c and v_c in (2.60)-(2.63) for 2-D are different to their counterparts in (2.57)-(2.59) for 3-D.

Relative Equations of Motion Including Ocean Currents

The ocean current velocities can be incorporated into the equations of motion by using the relative velocity, which is shown by (T. Fossen, 2012):

$$\dot{\boldsymbol{\eta}} = \boldsymbol{J}(\boldsymbol{\Theta})\boldsymbol{\nu}_r + \begin{bmatrix} \boldsymbol{\nu}_c^n \\ \mathbf{0} \end{bmatrix} \tag{2.64}$$

$$\boldsymbol{M}\dot{\boldsymbol{\nu}}_r + \boldsymbol{C}(\boldsymbol{\nu}_r)\boldsymbol{\nu}_r + \boldsymbol{D}(\boldsymbol{\nu}_r)\boldsymbol{\nu}_r + \boldsymbol{g}(\boldsymbol{\eta}) = \boldsymbol{\tau}_{act} + \boldsymbol{\tau}_{wave}. \tag{2.65}$$

The ocean current velocity is commonly incorporated at the kinematic level as in (2.64) (T. Fossen, 2011, 2012).

For low operating speed applications, such as DP, the ocean currents and damping can be modelled by three *current coefficients* C_X, C_Y and C_N. (T. Fossen, 2011) states that it is common in many textbooks that wind and current coefficients are defined relative to bow using a counter clock-wise rotation γ_c. The current forces acting on a marine craft at rest

in surge, sway and yaw in this case are given by (T. Fossen, 2011, 2012):

$$X_{current} \triangleq \frac{1}{2}\rho A_{Fc} C_X(\gamma_c) {V_c}^2, \tag{2.66}$$

$$Y_{current} \triangleq \frac{1}{2}\rho A_{Lc} C_Y(\gamma_c) {V_c}^2, \tag{2.67}$$

$$N_{current} \triangleq \frac{1}{2}\rho A_{Lc} L_{oa} C_N(\gamma_c) {V_c}^2, \tag{2.68}$$

where V_c is the speed of the current, A_{Fc} and A_{Lc} are the frontal projected currents areas, L_{oa} is the overall length, and ρ is the water density. The ocean current forces and moments can also be incorporated in the equations of motion using the *principle of superposition*, and thus, (2.65) becomes (T. Fossen, 2012):

$$\boldsymbol{M}\dot{\boldsymbol{\nu}}_r + \boldsymbol{C}(\boldsymbol{\nu}_r)\boldsymbol{\nu}_r + \boldsymbol{D}(\boldsymbol{\nu}_r)\boldsymbol{\nu}_r + \boldsymbol{g}(\boldsymbol{\eta}) = \boldsymbol{\tau}_{act} + \boldsymbol{\tau}_{wave} + \boldsymbol{\tau}_{current}, \tag{2.69}$$

where

$$\boldsymbol{\tau}_{current} \triangleq [X_{current}, Y_{current}, 0, 0, 0, N_{current}]^T. \tag{2.70}$$

is the current forces and moments in surge, sway and yaw. The current coefficients can be identified in wind tunnels by restraining the vehicle motion, i.e. by setting the total speed $U \approx 0$, and can be related to surge resistance, cross-flow drag and Munk moment used in manoeuvring theory. For vehicles in motion, i.e. $U > 0$, the quadratic damping can be embedded in current coefficients if relative velocity is used (T. Fossen, 2011, 2012).

Modeling the current moment in yaw as non-zero implies that the ocean current is not rotational in current yaw direction. Current forces and moments in other DOFs can also be modeled similarly if they are not assumed irrotational.

2.4 Actuator Modeling

The most common ways of providing actuation for marine vehicles electrically driven thrusters with propellers and rudders. Rudders are used as deflection plates that will

provide steering for the vehicle in both the vertical and horizontal plane. Rudders could be more efficient and less complex in their structure compared to thrusters for providing deflection since they can be fixed at desired bearings for steering action and thus do not require constant provision of actuation compared to steering with thrusters. This could be why rudders are also more common in torpedo-shaped long-range vehicles. However, thrusters also ideally provide steeper steering action such as vertical diving/climbing with vertical thrusters, and make them more suitable for confined spaces and tasks that require steeper turning in orientations.

2.4.1 Propeller Thrust

Accurate computation of thrust from a hydrodynamic thruster can also be a relatively complex procedure due to the fact that it depends on many parameters such as propeller size, motor speed, the motor shape, the blade pitch, the blade airfoil shape, the number of blades and the Raynolds number, density, flow speed and flow direction of the surrounding fluids.

For a hydrodynamically loaded propeller, the propeller thrust, torque and power consumed can be can be expressed by (Sørensen, Ruth, & Smogeli, 2005):

$$T_a = sgn(n)K_T\rho D_p^4 n^2, \tag{2.71}$$

$$Q_a = sgn(n)K_Q\rho D_p^5 n^2, \tag{2.72}$$

$$P_a = 2\pi n Q_a = sgn(n)2\pi K_Q\rho D_p^5 n^3, \tag{2.73}$$

being T_a the propeller thrust, Q_a the propeller load torque n the shaft speed, D_p the propeller diameter, K_T and K_Q strictly positive thrust and torque coefficients and P_a the propeller power. For a deeply submerged propeller its characteristics are given by thrust and torque coefficients as a function of the advance number J_a ((Sørensen et al., 2005)):

$$J_a = \frac{u_a}{nD}, \tag{2.74}$$

where u_a is referred as the advance velocity which describes the vehicle motion relative to an inertial frame.

2.4.2 Control Allocation

The output force from a single actuator unit can contribute to multiple DOF and desired forces therefore have to be efficiently distributed to all the thrusters. In practical applications, the vector of propulsion forces and moments τ acting on the vehicle can be described by:

$$\boldsymbol{\tau}_{act} = \boldsymbol{B}\boldsymbol{f}, \tag{2.75}$$

where $\boldsymbol{f} \in R^n$ is the vector of thrust with n equal to the number of thrusters, and $\boldsymbol{B}\boldsymbol{f}$ is the thruster configuration matrix, which depends on the thrusters layout on the vehicle.

2.5 Summary

The existing general 6-DOF mathematical modeling of UVs and the incorporation of environmental disturbances have been discussed and presented, which is not a trivial process and obtaining an accurate model which can also describe the motion of the vehicle relative to the surrounding fluid is difficult due to simplifications in thruster modeling and the thruster-thruster, and thruster-hull interactions. The models of irrotational and constant ocean currents and waves have also been presented. The equations of motion also includes the vehicle kinematics and definitions of heading and sideslip angles. A model of propeller thrust has also been provided to describe a conventional actuator model.

Chapter 3

Literature Review

This chapter focuses on further introduction and review on the state-of-the-art literature on marine guidance, navigation and control, and path-following of UVs. The contents include the difference between TT and PF approaches and how the PF problem is conventionally solved using guidance laws, which also include the revised definitions of the track errors in the inertial frame for the general PF. The discussions also include popular guidance laws and existing comparisons between them, AUV navigation and localization with state estimation, control techniques that are used for underwater flight vehicles, and the integrated approaches for GNC designs.

3.1 Guidance Systems

The guidance systems are required to generate the desired reference trajectories or orientations for the control systems so that the vehicle can fulfil the control objectives. For a linear system a feasible trajectory means that the dynamics of the reference model should be slower than the vehicle dynamics. For marine vehicles, the guidance and control problem can be divided into following two subsystems (T. Fossen, 2011):

- Attitude control system
- Path-following (PF) control system

The attitude control system is a heading autopilot, where its main function is to control

the vehicle in a desired attitude on the reference path. The aim of the path-following control is to maintain the vehicle on the reference path with some desired dynamics (T. Fossen, 2011).

3.1.1 Trajectory Tracking and Path-Following

The solution to render a subject system to converge to and follow a desired geometric path can thus be achieved by both trajectory tracking (TT) and path-following (PF) (Breivik & Fossen, 2005; T. Fossen, 2011). The common definition of trajectory tracking problem is given by (T. Fossen, 2011):

Definition 2.4 (Trajectory Tracking) *The trajectory tracking problem is defined by the problem of rendering a system output* $y(t) \in R^m$ *to track a desired output* $y_d(t) \in R^m$.

This definition is consistent with existing definitions in the literature (T. Fossen, 2011).

The TT and PF problems both can regarded as subsclasses of a tracking control problem. Their differences were explained using the notions of an *actual particle* and a *path particle*. The actual particle represents the position variables of the actual system whose goal is to converge to and follow a desired geometric path, while the path particle has its position variables belonging to the path and is restricted to move only along the path (Breivik & Fossen, 2005).

The TT scheme involves simultaneous generation of the geometric path and the dynamics behaviour of the path particle. This thus, combines the spacial and temporal assignments into as single task, which requires the subject system to be at a specific point in space at a specific, pre-assigned instant in time. The dynamic task is based on some a priori assumptions on the capabilities of the subject system, it must be re-assigned if the system capabilities are changed so that it can still fulfill the task (Breivik & Fossen, 2005).

On the other hand, the PF problem solves the tasks of path construction and dynamic assignment separately. It treats spacial localization as the primary objective, while considering the dynamic aspect as secondary in importance, which can be compromised if neces-

sary (Breivik & Fossen, 2005). In addition, the PF has the potential to offer smoother convergence properties and decreased actuator activity (Aguiar & Hespanha, 2007; De luca, Oriolo, & Samson, 1998). Hence, the PF scheme presents a better, more flexible, and robust choice over the TT scheme (Breivik & Fossen, 2005).

Target Tracking

Information about the trajectory to be tracked are not always available in advance, in which case the vehicle could be required to track a moving object as a target. This is referred as the ratget tracking problem and can be formulated in 3-D as(T. Fossen, 2011):

$$\lim_{t\to\infty} = [\boldsymbol{P}^n(t) - \boldsymbol{P}^n_t(t)] = \mathbf{0}, \tag{3.1}$$

where $\boldsymbol{P}^n(t) = [N, E, D]^T$ and $\boldsymbol{P}^n_t(t) = [N_t, E_t, D_t]^T$ denote the vehicle and target positions in NED, respectively. The target position $\boldsymbol{P}^n_t(t) = [N_t, E_t, D_t]^T$ is generally time-varying in the target tracking control problem.

Parametrized Path

The path or trajectories to be followed are a series of predefined waypoints in the simplest case, which can consist of straight-lines or curves paths. In more involved designs, an opticam trajectory can be dsgiend with given conditions, which will make it a constrained nonlinear optimization problem. In most applications, simple waypoints consisting of straight lines are used as the desired path for the vehicle to follow. However, it is also possible to define the path using path parametrization, which is used when following curved paths. The drawback of this apporahc is that the path must be known and parameterized in advance, which is not practicle in many cases, and simpler waypints consisting of straight lines are neccessary for path representation (T. Fossen, 2011). The following definition from (T. Fossen, 2011) is used to define a parametrized path, which was adopted from (Skjetne, Fossen, & Kokotovic, 2004):

Definition 2.5 (Parametrized Path) *A parametrized path is defined by a geometric curve* $\boldsymbol{\eta}_d(\mu) \in \mathbb{R}^q$ *with* $q \geq 1$ *parametrized by a continuous path variable* μ.

For a marine craft, this is usually a 3-D desired path represented by (T. Fossen, 2011):

$$\boldsymbol{p}_d(\mu) = [x_d(\mu), y_d(\mu), z_d(\mu)]^T \in \mathbb{R}^3. \tag{3.2}$$

3.1.2 Guidance-Based Path-Following

The path particle can be considered as the exact projection of the system particle on the desired path.The actual particle in this case requires a guidance law to converge to the path, which is why this PF strategy is referred as *guidance-based path-following* (Breivik & Fossen, 2005).

The initial works that essentially treat the guidance-based PF problems can be traced back to that of Samson (1992); Pettersen and Lefeber (2001); Lapierre, Soetanto, and A. (2003); Rysdyk (2003). The pioneering work of Samson (1992) treats wheeled mobile robots, Pettersen and Lefeber (2001) and (Lapierre et al., 2003) treat marine surface vehicles (MSV) and AUVs, respectively, and Rysdyk (2003) treats unmanned aerial vehicles (UAV). Research articles relevant to application aspects can be found in (Do & Pan, 2003; Encarnação & Pascoal, 2000a; del Rio, Jiménez, Sevillano, Vicente, & Balcells, 1999). A later review on the principles of guidance-based PF is provided in 2-D and 3-D is presented by Breivik and Fossen (2005).

The notions *system particle*, *system* or vehicle that are to be controlled will be used interchangeably with the term actual particle in the thesis.

The Manoeuvring Problem

The objective of guidance-based PF is to ensure that the system particle converges to and follows the desired geometric path, without any temporal constraints. The system particle is also required to satisfy a certain dynamic behaviour. The common approach to solve a PF problem is by solving the *manoeuvring problem*, where its objectives can be described

by the task classification scheme of Skjetne (2005). The manoeuvring problem is defined by the following two tasks (T. Fossen, 2011):

Definition 2.6 (Maneuvering Problem).

1. Geometric task: *To make the position of the actual particle or vehicle* $\boldsymbol{P}^n$ *converge to and follow a desired geometric path* $\boldsymbol{P}_d^n(\mu)$ *such that:*

$$\lim_{t\to\infty} = [\boldsymbol{P}^n(t) - \boldsymbol{P}_d^n(\mu)] = \mathbf{0}, \tag{3.3}$$

for a continuous function $\mu(t)$.

2. Dynamic task: *To make the speed of the actual particle converge to and track a desired speed assignment given by:*

$$U_d = \sqrt{{u_d}^2 + {v_d}^2 + {w_d}^2}. \tag{3.4}$$

These tasks make the manoeuvring problem to represent essential tasks in AUV applications, e.g. pipeline tracking, surveying or seabed mapping, and thus suitable for this thesis. Prior to (Skjetne, 2005), the manoeuvring problem has also been employed in (T. I. Fossen, Breivik, & Skjetne, 2003) in a case of path-following of surface vehicles.

Track Error

The common error variables in path-following problems are the cross-track and along-track errors. Let $\mu > 0$ be the path variable of a 2-D parametrized path $P_p(x_p, y_p) = (x_p(\mu), y_p(\mu))$. This is shown in Fig. 3.1, which is similar to the illustrations in (T. Fossen & Pettersen, 2014; T. Fossen & Lekkas, 2015). At any point $(x_p(\mu), y_p(\mu))$, the path-tangential reference frame is rotated by an angle,

$$\psi_p = \text{atan2}\left(\frac{{y'}_p(\mu)}{{x'}_p(\mu)}\right), \tag{3.5}$$

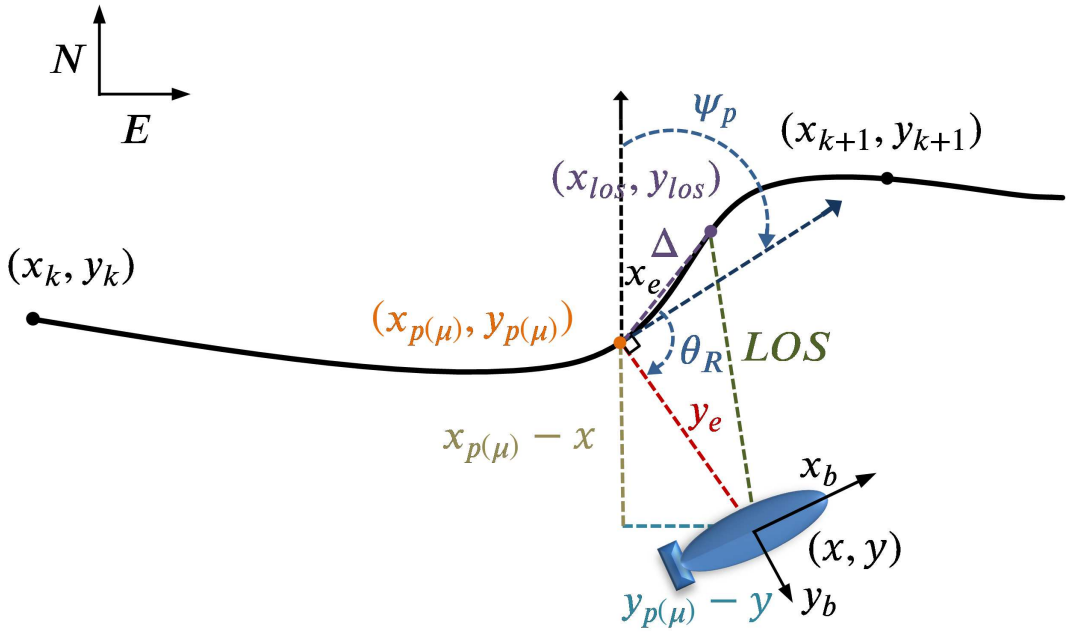

Figure 3.1: Geometry of a PF problem with *path heading* ψ_p and along-track and cross-track errors x_e and y_e. $p_{los} = (x_{los}, y_{los})$ is a LOS reference point on the path creating the LOS vector from the vehicle to it and $\triangle$ is the design gain known as the *lookahead distance*.

w.r.t the NED frame (T. Fossen & Pettersen, 2014), which is called as the *path-tangential angle* (T. I. Fossen et al., 2003; T. Fossen, 2011). This angle will be refered here as *path heading* in the horizontal plane, which is more intuitive. The variables $x'_p(\mu)$ and $y'_p(\mu)$ are defined as $y'_p(\mu) = \partial x_p/\partial\mu$ and $x'_p(\mu) = \partial y_p/\partial\mu$ (T. Fossen & Pettersen, 2014; T. Fossen & Lekkas, 2015). They can be intepretted here as deviations in p_x and p_y directions of the path reference frame defined by $\{P\} = \{p_x, p_y\}$. Thus, for a curved path, ψ_p varies according to (3.5). For a path consisting of straight lines between a set of successive waypoints (x_k, y_k) for $k = 1, 2, ..., N$, ψ_p is constant and given by (T. I. Fossen et al., 2003; T. Fossen, 2011):

$$\psi_p = \text{atan2}\left(\frac{y_k - y_{k-1}}{x_k - x_{k-1}}\right) = \text{atan2}\left(\frac{y_{k+1} - y_k}{x_{k+1} - x_k}\right) = constant. \tag{3.6}$$

The cross-track error y_e can be defined by the normal distance between the vehicle NED position (x, y) to the nearest point on the path $(x_p(\mu), y_p(\mu))$, i.e. the normal vector or straight line from the vehicle to the path in the horizontal plane. Thus, the cross-track

error is obtained by the following rotation (T. Fossen, 2011; T. Fossen & Pettersen, 2014):

$$\begin{bmatrix} x_e \\ y_e \end{bmatrix} = \boldsymbol{R}(\psi_p)^T \begin{bmatrix} x - x_p(\mu) \\ y - y_p(\mu) \end{bmatrix} = \begin{bmatrix} \cos(\psi_p) & -\sin(\psi_p) \\ \sin(\psi_p) & \cos(\psi_p) \end{bmatrix}^T \begin{bmatrix} x - x_p(\mu) \\ y - y_p(\mu) \end{bmatrix} \tag{3.7}$$

where x_e is called the *along-track error*, which is tangential to the path (T. Fossen, 2011). Expanding (3.7) gives:

$$x_e = \cos(\psi_p)\,(x - x_p(\mu)) + \sin(\psi_p)\,(y - y_p(\mu)) \tag{3.8}$$

$$y_e = -\sin(\psi_p)\,(x - x_p(\mu)) + \cos(\psi_p)\,(y - y_p(\mu)) \tag{3.9}$$

In PF, only the tracking of y_e is needed since $y_e = 0$ means that the vehicle is on the path. Setting $x_e = 0$ in (3.7) gives the following y-directional distance (T. Fossen & Pettersen, 2014; T. Fossen & Lekkas, 2015):

$$y - y_p(\mu) = -\frac{x - x_p(\mu)}{\tan \psi_p} \tag{3.10}$$

The propagation of μ is given by (T. Fossen, 2011):

$$\dot{\mu} = \frac{U}{\sqrt{{x'}_p(\mu)^2 + {y'}_p(\mu)^2}} > 0. \tag{3.11}$$

As shown by (Samson, 1992), there could be infinite solutions to (3.10) and hence for $y_e(\mu^*)$ if the path is a closed curve. Thus, the following guarantees a unique solution $y_e(\mu^*)$ of (3.9) (T. Fossen & Pettersen, 2014):

$$\mu^* = \arg\min_{\mu \geq 0} \left\{ \frac{U^2}{{x'}_p(\mu)^2 + {y'}_p(\mu)^2} \right\}. \tag{3.12}$$

which is subject to (3.10). This can be treated as a nonlinear optimization problem and solved numerically.

Revised Along-Track and Cross-Track Errors

The PF strategy depicted in the Fig 3.1 is more realistic and informative compared to the intial illustrations in (T. Fossen & Pettersen, 2014; T. Fossen & Lekkas, 2015). This is mainly manifested in its enabling of the formulation of the cross-track and along-track errors. When the North axis of NED is rotated to align with the path-heading, the co-ordinate transformations in (3.7) is not necessary to derive track errors. In this case, it can be seen from the revised Fig 3.1 that the cross-track error is given by the following Pythagoras relationship:

$$y_e = \sqrt{(y_p(\mu) - y)^2 + (x_p(\mu) - x)^2} \tag{3.13}$$

This method of rotating the North axis of NED to align with the path-heading is a common practice in stability analysis of the cross-track error (e.g. see (Nelson et al., 2005) and (Børhaug et al., 2008)). However, the coordinate transformation is not necessary since the rotation is completed by setting the path heading $\psi_p = 0$.

The along track error x_e can be similarly redefined by the distance from the projection of the vehicle from the path $(x_p(\mu), y_p(\mu))$ to a reference point of interest in the forward direction of the path. This reference point can be $\boldsymbol{p}_{los}$ in the case of LOS guidance. For straight-line PF, this along track error is equivalent to the lookahead distance $\triangle$ as can be seen in Fig 3.2. This is not the case for PF of curved paths from Fig 3.1, where x_e equals to the segment of the curve from $(x_p(\mu), y_p(\mu))$ to (x_{los}, y_{los}) by this new definition. In the maneuvering PF problem, the geometric task do not necessarily require the tracking of along track error, and $\boldsymbol{p}_{los}$ is mainly used as a reference point on the path for computing the desired heading, which will be discussed in the following section.

3.1.3 Guidance Laws

The guidance problem can be treated as a target tracking control objective as in (3.1), and guidance laws are required in satisfying the objectives of the geometric task that involves

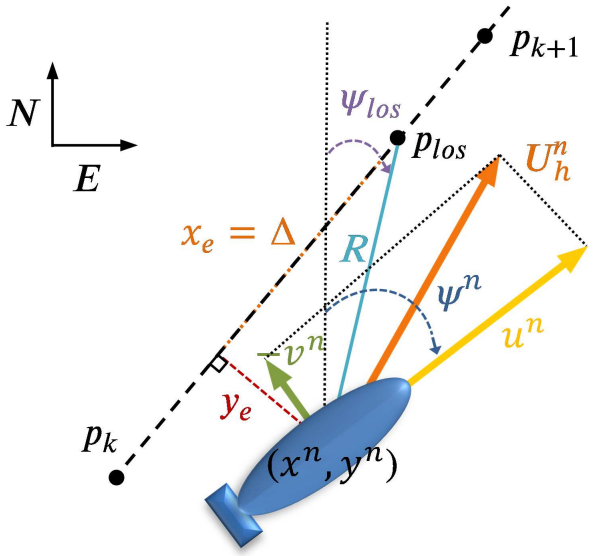

Figure 3.2: Straight-line path-following using waypoints in NED, where $U_h = \sqrt{u^2 + v^2}$ is the vehicle horizontal speed and it can be seen that the along-track error $x_e = \triangle$ in this case.

calculating the desired heading for the actual particle for approaching and following the path. The missile community perhaps is the oldest and first one studying and implementing guidance laws, and the marine community has been influenced by most of the common methods (A. Lekkas & Fossen, 2013). Common guidance laws for marine vehicles are the LOS, Pure-Pursuit (PP) and Constant Bearing (CBR) (T. I. Fossen et al., 2003; Breivik & Fossen, 2009; T. Fossen, 2011). The implementation of these guidance laws are discussed extensively for the case of AUVs in (Breivik & Fossen, 2009). Another common guidance law is the vector field (VF) guidance(Nelson et al., 2005; Caharija et al., 2015), which is also a popular guidance law in the aerospace community (Sujit, Saripalli, & Sousa, 2014) where it was first presented (Nelson et al., 2005). Guidance laws can also be designed using the linear quadratic regulator (LQR) control approach (Sujit et al., 2014), which allows to optimize the control effort if this is a priority.

The PP guidance is a two point guidance that mimics a predator chasing a prey, and often results in a tail-chase and is often employed in air-to-surface missiles (T. Fossen, 2011). The CBR guidance is also referred as *parallel navigation* and has been typically employed in air-to-air missiles (T. Fossen, 2011). Further discussions on these guidance

laws are presented in (T. Fossen, 2011), and the following discussions are limited to the two steering schemes of the LOS guidance, and VF guidance.

3.1.4 LOS Guidance Laws

The LOS guidance law is perhaps the most common guidance algotithm. In PF, LOS guidance corresponds to a PP strategy with moving target. It was first employed in LOS motion control of AUVs using the sliding mode for stablizing combined speed, steering and diving control by (Healey & Lienard, 1993). Subsequently, its was implemented on path following of straight-lines and curved paths in (T. I. Fossen et al., 2003) and (Breivik & Fossen, 2004), respectively. The LOS guidance law tradintionally refers the to proportional LOS guidance (3.2), which is then devided into following two steering schemes based on their calculation of the LOS angle (Breivik & Fossen, 2009; T. Fossen, 2011):

- Lookahead-based LOS (LLOS)
- Enclosure-based LOS (ELOS)

The LLOS scheme is the first to appear and is also referred as the traditional or conventional LOS guidance.

LLOS Guidance

In LLOS, the LOS angle ψ_{los} for desired heading is calculated as:

$$\psi_{los} = \psi_p + \tan^{-1}\left(\frac{-y_e}{\triangle}\right) = \psi_p + \tan^{-1}\left(-K_p y_e\right) \tag{3.14}$$

where $K_p = 1/\triangle > 0$ acts as a proportional gain. This is why the LLOS scheme represents a saturated proportional control law. The LOS guidance can also be seen in Fig 3.2. The lookahead distance can be designed as a time-varying parameter by using optimization (Pavlov, Nordahl, & Breivik, 2009), to improve its performance as in (A. Lekkas & Fossen, 2012).

The LLOS guidance corresponds to the *carrot chasing* guidance in aerospace community (Sujit et al., 2014), where it has been published in (Park, Deyst, & How, 2004).

ELOS Guidance

The ELOS scheme, on the other hand, calculates the LOS angle by drawing a circle centring the vehicle position which will intersect the path at two points. One of these points is chosen as reference point $\boldsymbol{p}_{los} = (x_{los}, y_{los})$ to compute the LOS angle for desired heading. In the waypoint following scenario where the path consists of straight lines, the ELOS guidance is given by (T. I. Fossen et al., 2003; T. Fossen, 2011):

$$(x_{los} - x)^2 + (y_{los} - y)^2 = R^2, \tag{3.15}$$

$$\frac{y_{los} - y_k}{x_{los} - x_k} = \frac{y_{k+1} - y_k}{x_{k+1} - x_k} = \tan \psi_p, \tag{3.16}$$

$$\psi_{los} = \psi_p + \text{atan2}\left(\frac{y_{los} - y}{x_{los} - x}\right) \tag{3.17}$$

where R is the tuning radius of the enclosing circle that will intersect the path to locate the reference point $\boldsymbol{p}_{los}$, and ψ_p becomes the path heading of the straight-line between the current and next waypoints $\boldsymbol{p}_k = (x_k, y_y)$ and $\boldsymbol{p}_{k+1} = (x_{k+1}, y_{k+1})$. Equations (3.15)-(3.16) represent a set of two equations with two unknowns. Note that it is highlighted in this thesis that (3.15) only holds for straight-line PF since it is a Pythagoras. The cosine law is used instead, thus, for a curved path.

It is critical for R to be greater than the cross-track error y_e so that the circle-path interception exist for locating $\boldsymbol{p}_{los}$. This can also be seen from Fig. 3.2. A large R can ensure that it always intercepts the path, a large R will result in heading angle that is less perpendicular to the path, and thus, results in longer path convergence time (Sujit et al., 2014). While a small R produces heading angles that are more perpendicular to the path and hence, quicker path convergence time, the interception will be lost when the vehicle deviates from the path and y_e becomes larger than R. This is also regarded as a drawback in microcontroller implementation of ELOS (Sujit et al., 2014).

In straight-line PF case, the relationship between $\triangle$, R and y_e is given by the following Pythagoras (T. Fossen, 2011):

$$R = \sqrt{{y_e}^2 + \triangle^2} \tag{3.18}$$

Note that this is not the case when the path is curved, i.e. when the distance between $(x_p(\mu), y_p(\mu))$ and p_{los} is not equal to $\triangle$. This can be seen from Fig 3.1 that the resulting triangle is not a right-angled one. In this case the relationship in (3.18) can be described using the *cosine rule* as:

$$R = \sqrt{{y_e}^2 + \triangle^2 - 2y_e\triangle\cos(\theta_R)}, \tag{3.19}$$

where θ_R is the angle opposite to LOS vector R. These show that the coordinate transformation in (3.7) is not necessary to define x_e and y_e if path coordinates are also in NED frame.

It should be noted that the ELOS guidance is the *nonlinear guidance law* in aerospace community (Park et al., 2004; Sujit et al., 2014), which was apparently published separately in the aerospace community by (Park et al., 2004) a year later than in the marine community by (T. I. Fossen et al., 2003). Its stability and performance analysis has also been carried out by the same authors in (Park, Deyst, & How, 2007).

It can be seen that both schemes of the LOS guidance laws can also represent a PP strategy where the vehicle ultimately chases the LOS reference point on the path.

3.1.5 VF Guidance

The idea of the VF guidance is to provide a negative potential towards the path, which will create the required heading directions for the vehicle to converge to the path. The desired heading is computed in VF guidance as (Nelson et al., 2005):

$$\psi_{vf} = \psi_p - \frac{2}{\pi}k_v\tan^{-1}(K_p y_e), \tag{3.20}$$

where $k_v \in (0, \pi/2]$ is a gain, also interpreted as the path approach angle. Its stability analysis has also been presented in (Nelson et al., 2005).

It can be highlighted here that this structure of the VF guidance law (3.20) is equivalent to the LLOS guidance (3.14) when $k_v = \pi/2$ since $K_p = -1/\triangle$.

3.1.6 Comparison

A comparison between the LOS, VF and LQR guidance laws in 2-D UAV path-following has been done in (Sujit et al., 2014) at the kinematic level including wind disturbances. It showed that the ELOS scheme performed superior to the LLOS scheme when the path-following also consisted of curved paths. This is because ELOS scheme provides a varying lookahead distance $\triangle$ compared to LLOS where this is traditionally fixed. However, it can be seen that the ELOS scheme requires solving a set two equations to compute the ψ_{los} angle, while this is computationally simpler in the LLOS scheme. Also, the LLOS guidance can be used for all types of paths, while the ELOS guidance requires a slightly different algorithm and a condition on the curvature of the path when following curved paths. This will be seen in Chapter 5.

The VF guidance (3.20) guidance has two tuning variables compared to LOS guidance where there is only one. It was shown in (Sujit et al., 2014) that the VF guidance has performed superior among all of these guidance laws, including a combined Pure-Pursuit LOS (PLOS) guidance. However, the VF guidance is known to exhibit chattering effect (Sujit et al., 2014; Caharija et al., 2015) and the VF guidance in (Sujit et al., 2014) has three tuning variables instead of two as in (3.20). Increased number of tuning variables can also be seen as a drawback (Sujit et al., 2014), since it can add to the complexity of the algorithm and can take longer tuning time in simulations.

3.2 LOS Guidance For PF Control

The LOS guidance, which referes to the LLOS scheme if not specified otehrwise, is the most common guidance law used in path-following control applications (Healey & Lienard, 1993; A. Lekkas & Fossen, 2013; Sujit et al., 2014). This is due to its nice path convergence properties and simplicity (Børhaug et al., 2008). It is often associated with the design of heading autopilots, where the two systems form a cascaded structure which is then analysed for its stability. One of the first such approaches is the results presented by Healey and Lienard (1993). The LOS path following problem has been since treated for straight-line case in (T. I. Fossen et al., 2003), and a curved-path case in (Breivik & Fossen, 2004) where the motion of a particle was considered.

Stabillity results of the guidance laws in PF consider their ability to stabilize the cross-track error in the inertial frame, where zero-cross track error means that the vechile is on the path. This is traditionally achieved in cascaded appraoches, which is the stabilization of the cross-track error throught stabilising the speed and heading errors. Such appraoches were first reported in (Pettersen & Lefeber, 2001) for the κ-exponential stability, which is defined by Lefeber (2000) as the combination of Global Asymptotic Stability (GAS) and Local Exponential Stability (LES), of the cross-track error for waypoint tracking control of ships using LOS guidance. The κ-exponential stability was extended to 3-D by Børhaug and Pettersen (2005) using a cascaded systems approach where the guidance system is connected with a sliding mode control. All of the aforementioned schemes refers to the traditional LLOS scheme with constant lookahead distance $\triangle$. It is observed that, in general, a small $\triangle$ will produce more perpendicular heading and thus, an aggressive steering and a faster path convergence, which may also result in unwanted oscillations. On the other hand, a larger $\triangle$ will provide smoother steering which can prevent oscillations, but may lead to slower path convergence (T. Fossen, 2011; A. Lekkas & Fossen, 2013). This led to later works of Breivik and Fossen (2005); Pavlov et al. (2009); Oh and Sun (2010); A. Lekkas and Fossen (2012) that combined and provided trade-offs between these behaviours and thus the discussions and possibilities of implementing a

time-varying lookahead distance. These works are based on different principles and techniques, but all show that a time-varying $\triangle$ can provide a faster path convergence and reduce oscillations around the path. It is thus worth noting here that the ELOS scheme inherently provides this time-varying lookahead distance by comparison to LLOS, and thus, can be contributed to the reason why it performs better than LLOS when the path-following involves curved paths. Regarding the stability results of the cross-track error, the semi-global exponential stability (SGES) of the proportional LOS guidance was shown by T. Fossen and Pettersen (2014), which is stronger stability result compared to κ-exponential stability.

The stability results aforementioned are limited to 2-D case of the LOS guidance. A. Lekkas and Fossen (2013) has presented the extension of the LOS guidance law to the vertical plane, where the *horizontal cross-track error* was formulated similar to the kinematic rotations of the cross-track and along-track errors in (3.8)-(3.9). A further discussion on vertical LOS guidance are presented in Chapter 6.

3.2.1 Integral LOS Guidance

Integral LOS (ILOS) guidance law designs have also gained popularity in the literature (Børhaug et al., 2008; Breivik & Fossen, 2009; Bibuli, Caharija, Pettersen, Bruzzone, & Zereik, 2014; Caharija et al., 2015). This is because the integral action represents a useful solution for underactuated vehicles that can only steer using attitude informaiton without having velocity information, enabling PF capabillities under the influnce of ocean currents (T. Fossen, 2011). The integral action on the cross-track error was initially introduced in (Breivik & Fossen, 2009) into the steering laws of the LOS guidance as:

$$\psi_{ilos} = \psi_p - \tan^{-1}\left(K_p y_e + K_i \int_0^t y_e d\tau\right) \tag{3.21}$$

where $K_i > 0$ is the integral gain. When applying integral action, care should be given to avoid wind-up and overshoot. This ILOS was also implemented in (T. Fossen & Lekkas,

2015) for the direct and indirect adaptive path-following controllers with the inclusion of sideslip angle in (3.12), thus making it a desired course angle. It was also implemented in (T. Fossen, Pettersen, & Galeazzi, 2015) path-following using Dubin's path where the sideslip angle has been treated as an unknown variable to be estimated adaptively for compensation of drift forces.

The ILOS guidance of Børhaug et al. (2008) is more popular and advanced compared to the basic integral approach in (3.21) (see e.g. (Caharija et al., 2012; Bibuli et al., 2014; Caharija et al., 2015)), where ILOS angle ψ_{ilos} for the desired course is given by:

$$\psi_{ilos} = \psi_p - \tan^{-1}(K_p y_e + K_i y_{int}) \tag{3.22}$$

$$\dot{y}_{int} = \frac{y_e \triangle}{\triangle^2 + (y_e + K_i y_{int})^2}, \tag{3.23}$$

where $K_i = \sigma/\triangle$ is the integral gain with $\sigma > 0$ being a design parameter. Note that as $y_e \to \infty$, $y_{int} \to 0$, which means that the integral action decreases when the cross-track error increases, hence reducing integral wind-up.

It has been shown in (A. Lekkas & Fossen, 2013) that the ILOS guidance pair (3.22)-(3.23) has performed much superior to the conventional ILOS guidance in (3.21). The comparison in (Caharija et al., 2015) is done between this ILOS guidance and the VF guidance of (Nelson et al., 2005), where the VF guidance performed slightly better but exhibited significant chattering. This ILOS guidance has been revisited and improved in (Caharija et al., 2012), where a stronger GAS and LES stability has also been proven.

3.3 UV Navigation and Localization

The navigation problem is more challenging for underwater platforms due mainly to the principle issues of attenuation of higher frequency signals and the unstructured nature of the undersea environment, which makes it difficult to achieve fast and accurate measurement data for state estimation. This in turn makes the localization problem also challenging. Above water, most autonomous systems rely on radio communications and global

positioning systems (GPS), whereas such signals propagate for very short distances underwater. Acoustic-based sensors perform better, but they still suffer from many shortcomings such as (Paull et al., 2014):

- Small bandwidth
- High latency due to the slow speed of sound (1500 m/s) compared to light
- Variable sound speed due to changing water temperature and salinity
- Unreliability due to frequent data loss in transmissions

For ships, it is comon to have a various number of position, velocity and attitude sensors on-board ships to construct the estimates. For example, the Inertial Measuremetn Unit (IMU) can be used to estimate the inertial displacement or position using information form its gyros and accelerometers. In shallow waters, Doppler Velocity Logs can be used to estimate the velocity relative to a nearby inertial terrain , where itworks by comparing the difference between its transmitting and receiving accoustic signals bounced back from the seabed. As to calculating the vehicle velocity relative to the fluid, Accoustic Doppler Current Profilers (ADCP), Pitometer logs and Paddle meters are also available. The ADCP's working principle is similar to the DVL, where it collects the echos returned to produce a profile of the sea current over a certain depth. The Pitometer can provide information about the fluid motion by comparing the difference between its static and dynamic presures, and the paddle meter estimates the flow speed by measuring the spin velocity of a paddle where the surrounding fluid is allowed to flow through. These are typical sensors on-board a ship as described in (Caharija et al., 2012). Common sensor technologies used for UVs are discussed in detail in (Paull et al., 2014), where e.g. the ADCP can be costly and huge to implement on some UVs. State estimations for localizations and navigations of UVs are also done using base-line approaches where the vehicle is able to transmit and/or receive signals from ships or known beacons embedded on the sea floor, and also using cooperative navigation techniques between multiple vehicles. These are also extensively discussed in (Paull et al., 2014).

3.3.1 State Estimation and Kalman Filter

State estimation is directly involved in solving the localization and positioning of AUVs, which will also encompass the popular technique of sensor fusion, where information from multiple sensors are fused to achieve estimations the states.

As mentioned earlier, KF is one of the most popular filtering approach for state estimation. It is is an efficient recursive filter in state estimation of linear or nonlinear dynamic systems from noisy measurements. The filter equations behave as a predictor in case of loss of measurements. When new measurements are available, the predictor is corrected and updated online to give minimum variance estimate. The feature is particularly useful, e.g. when satellite signals are lost since the vehicle motion can be predicted by the filter using only gyros and accelerometers.

Many variations of KF have been developed since it was introduced in the 1960s. KF algorithms extended to nonlinear systems is called an Extended Kalman Filter (EKF). Variations of KF algorithms and some other state estimation techniques common in marine applications are can be found in (Paull et al., 2014). KF algorithms are computationally demanding, difficult and time-consuming to tune the state estimator, a stochastic system constituting 15 states and 120 covariance equations. Despite widely used, they also suffer from sensitivity to bias and divergence in estimates, optimality of estimations relying on statistic distribution such as white noise and known mean or covariance. This has also provided an incentive for the development of nonlinear observers (T. Fossen, 2011). Other estimation techniques such as the particle filter and a brief comparison between them is given in (Paull et al., 2014).

3.4 Control Techniques

In the design of motion control systems a compromise between vehicle stability and manoeuvrability has to be made. A brief background on the application of some of these control techniques to marine vehicles can be found in (T. Fossen, 2011). The research on

control of underwater vehicles are not new topics in research, and popular classical approaches based on known system models have already been applied in both simulations and experiments for underwater vehicles in flight control (Lea, Allen, & Merry, 1999). Control techniques are mainly divided into model-based or model-free approaches. Due to availability of low-power on-board sensing and computational capabilities and nonlinearity and relative complexity UV system models, it is cheap and beneficial to have adaptive capabilities for controllers in general, lest the identified system models are not accurate. Adaptivity will also allow the controller to cope for changes in mass in modular designs, which has also become popular where an AUV has different sensor payloads for different missions, hence changes in mass and CG. However, adaptive controllers are not the easiest or necessarily the most robust controllers to design.

A review on comparison of control techniques for underwater flight vehicles are presented by (Lea et al., 1999), where the authors also carried out a comparison of three controllers with experimental results. Since dynamics of UVs are nonlinear, the report proposes that fuzzy logic and sliding mode controllers are left to be the preferred choice due to their robustness, which ere than compared to the classical linear controller using root locus methods on the mode linearize at $1.3m/s$ cruise speed. In terms of system model requirements, the classical linear controller was most simple to design but required a system model. The fuzzy logic controller was synthesized without a system model, but then required extensive tuning using simulation programs, which could also be tuned using the actual vehicle. The sliding mode controller (SMC) was the most complex to design and also stipulated a complete system model. In terms of performance, the classical linear controller could not produce a fast rise time w/o significant overshoots due to the nonlinearities in the system, where the other two could produce similarly fast rise times. However, the classical controller was also the most robust in terms of being least susceptible to changes in target speed due to the fact that it is less optimized. Of the other two, the SMC was clearly a winner in providing better performance, being more robust to speed changes and being less noisier in general.

It was concluded by Lea et al. (1999) that overall, there was no best controller and each controller had their advantages and disadvantages in performance and complexity. The SMC was most suited when an accurate system model was available even in simulation environments, which could then be readily synthesised and provide the best performance. The classical controller was deemed less involved to design compared to SMC, but had a slower response. If this can be tolerated from a designers perspective, then it would also present a reasonable solution. The fuzzy logic controller was the least worthy of consideration due to its response being less robust and nosier than the other two controllers, and the number of parameters to be tuned. Its advantage of requiring no system model could be reduced if the classical controller was also tuned via experimental testing. However, this didn't mean that fuzzy control of speed is unsuccessful, but that implementation of this particular control scheme did not produce the best result and could be improved (Lea et al., 1999).

The report (Lea et al., 1999) also supports a general intuition that it is not straight forward to compare control techniques since there are different schemes and ways to implement within each of the control techniques. It can be said that the choice of controller significantly depend on the dynamics of the system (e.g. nonlinearity) and design requirements (e.g. tolerance in response and performance degradation), and design and computational resources (e.g. complexity and availability of online tuing). Since UV do not have a wide range of cruising speeds (e.g. usually slow operating speeds $\leq 2m/s$ (T. Fossen, 2011)), the robustness and simplicity of the classical linear controllers can be extended to include models linearised only at a few operating speeds to be representative of the nonlinear model, which will make it additionally robust to speed changes and can provide faster response at a small additional cost of complexity. This is similar to the linear parameter varying approach can be said to all the approaches that use a bank of linearised models that are selected based on the operating speeds. This is relatively advantageous to system with a smaller range of operating conditions.

The challenges of TT and PF problems have also been addressed using the popular

Model Predictive Control (MPC) due to their explicit ability to handle input and state constraints. Examples of of MPC applications to PF problems include those of (Alessandretti, Aguiar, & Jones, 2013) for moving vehicles and (Yu, Li, Chen, & Allgöwer, 2015) for car-like robots. The MPC has advantages in providing optimal inputs, but its performance is centrally reliant on model accuracy. Since accurate modeling of UV systems is a non-trivial and not an easy process as mentioned earlier, MPCs could be attractive only when there are accurate models.

3.5 Integrated GNC

In more advanced designs, two or three of the GNC blocks were coupled and integrated into one block. Loose and tight coupling can be a trade-off between modularity and high performance. A loosely coupled system can be attractive from an industrial perspective, since it allows for software updates of a single block (T. Fossen, 2011). A discussion on integrated guidance and control is provided in this section.

3.5.1 Integrated Guidance and Control

The guidance and control systems are composed of two separate loops and are usually designed separately because it is simpler, and well-stablished techniques are available for the design of controllers(Park et al., 2004). This is based on the so-called *time-scale separation* principle, where the control system is designed to have a sufficiently large bandwidth compared to that of the guidance loop so that it can track the guidance commands. However, most of the practical underwater vehicle operations are at low speeds ($\leq 2m/s$ (T. Fossen, 2011) and $\pm\pi/2rad/s$ for yaw rate e.g.), the guidance commands have a much faster response and that the vehicle response will be slower than the guidance commands. The effects of nonlinearity and coupling between the DOFs are stronger in underwater than in air due to larger added mass and sometimes *fluid memory effect* in underwater vehicles ((T. Fossen, 2011)). Thus, the motion of UVs cannot be required to

be very agile in order to exactly follow the guidance commands. Therefore, the integrated guidance and control (IGC) approach may not be an ideal choice for UVs.

Other motivations on integrated guidance and control (IGC) arise from (Silvestre, Pascoal, & Kaminer, 2002):

a) guaranteeing the stability of the combined system, and

b) achieving zero steady-state error about trimming trajectories.

The trimming trajectories refer to helices parametrized by some operating points, such as vehicle linear speed, yaw rate and flight path angle (Silvestre et al., 2002). The IGC design of (Silvestre et al., 2002) was based on gain-scheduling control using trimming trajectories that resulted in accurate tracking.

Notable works also include the combined TT and PF scheme presented in (Encarnação & Pascoal, 2001) that focused on the effect of a weghting parameter between the TT and PF, where a greater emphasis was given to the path following than trajectory tracking so that the vehilce first to approaches to the path and then follows the desired trajectories. This additionally shows the flexibility of PF without temporal contraints over TT. However, IGC designs can also often result in systems where the stability analysis is difficult, too (Park et al., 2004).

3.6 Summary

This chapter has outlined a detailed introduction and review on GNC systems for PF control focusing on LOS guidance laws. The differences the TT and PF strategies have been highlighted, where the maneuvering problem of PF strategy has been selected as the PF control problem due to the flexibility of PF over TT. The 2-D general PF problem has been revised along with the revised formulations of along-track and cross-track errors. The popular guidance laws such as the LOS and VF guidance laws are introduced and discussed with some existing comparison between them. An existing review on UV flight

control techniques has also been presented. The localization and navigation problem for UVs are challenging and a trending research area since, unlike aerial vehicles, the underwater environment is not structured (e.g. vast oceans without any infrastructure) and hostile, and radio frequency signals are not available. Finally, the motivation and suitability of IGC techniques for UVs have been discussed.

Chapter 4

Advances in Relative Equations of Motion

This chapter will present some fundamental contributions on the relative equations and angles of motion. The revised relative states will lead to better representation of the system states, angles of attack in 3-D, the formula of *drift rate* for linear velocity estimation, and revised modeling and incorporation of environmental disturbances using an improved FLOW reference frame. The concept of *state relativity* is also presented. Newton's 3rd Law will also be elaborated using reference frames. Lyaponuv stability is integrated with Newton's 1st Law in formulating an analytic method for checking the stability of kinetic models at unforced conditions. This method is then used on arranging the hydrodynamic terms in vehicle kinetics to provide better analytic modeling regarding the signs of the added mass and damping terms in the equations of motions. The proofs of passivity and boundedness are also provided for the relative equations of motion that under the condition of neutral buoyancy.

4.1 On Relative Equations and Angles of Motion

4.1.1 Relative Equations of Motion with FLOW and CURRENT Frames

The relative equations of motion for UVs are given by the 6-DOF nonlinear model of (T. Fossen, 2011, 2012) from Chapter 2, which is:

$$\dot{\boldsymbol{\eta}}^n_{b/n} = \boldsymbol{J}(\boldsymbol{\Theta}^n_{b/n})\boldsymbol{\nu}_{b/f} + \boldsymbol{V}^n_{c/n}, \tag{4.1}$$

$$\boldsymbol{M}\dot{\boldsymbol{\nu}}_{b/f} + \boldsymbol{C}(\boldsymbol{\nu}_{b/f})\boldsymbol{\nu}_{b/f} + \boldsymbol{D}(\boldsymbol{\nu}_{b/f})\boldsymbol{\nu}_{b/f} + \boldsymbol{g}(\boldsymbol{\Theta}^n_{b/n}) = \boldsymbol{\tau}. \tag{4.2}$$

The three-index convention from (T. Fossen, 2011) is used here to represent the vectors which is beneficial in describing the relativity. This convention emphasises a distinction between *relative to* and *expressed in*, first noted by Encarnação and Pascoal (2000a). The index convention are read as $\boldsymbol{\eta}^n_{b/n} \triangleq [\dot{x}^n, \dot{y}^n, \dot{z}^n, \dot{\phi}^n, \dot{\theta}^n, \dot{\psi}^n]^T$ is the vehicle BODY position and Euler angles, relative to and epxressed in NED. Using these indexes, it follows that $\boldsymbol{\nu}^f_{b/f}$ is the vehicle BODY velocities and Euler rates relative to the fluid frame FLOW, $\boldsymbol{V}^n_{c/n}$ is the linear and angular velocities of ocean current, relative to and expressed in NED, $\boldsymbol{J}(\boldsymbol{\Theta}^n_{b/n})$ is the transformation matrix from NED to BODY with $\boldsymbol{\Theta}^n_{b/n} = [\phi^n, \theta^n, \psi^n]^T$ being the vehicle Euler angles, relative to and expressed in NED with right-hand convention, $\boldsymbol{g}(\boldsymbol{\Theta}^n_{b/n})$ is the vector of gravitational and restoring forces and moments relative to and expressed in NED, and the control input vector $\boldsymbol{\tau}$ consists of input and disturbance forces and moments. The difference is that the three-indexed notation is also extended to describe the Euler angles and rates in this thesis, compared to that in (T. Fossen, 2011).

The relationship between the vehicle velocity relative to the fluid was first published by ()Caccia00, which is subsequently given by (Børhaug et al., 2008; T. Fossen, 2011; Caharija et al., 2016) as:

$$\boldsymbol{\nu}_{b/f} = \boldsymbol{\nu}^b_{b/n} - \boldsymbol{\nu}^b_{c/n}, \tag{4.3}$$

where $\boldsymbol{\nu}^b_{b/n} \triangleq [u^n, v^n, w^n, q^n, p^n, r^n]^T$ is the vehicle BODY velocities and Euler rates relative to NED, expressed in BODY, and $\boldsymbol{\nu}^b_{c/n} \triangleq [u_c, v_c, w_c, q_c, p_c, r_c]^T$ is the ocean current ve-

locity and Euler rates relative to NED, expressed in BODY. It can now be seen that it is not clear in which reference frame $\boldsymbol{\nu}_{b/f}$ is expressed in. This requires further understanding of the FLOW reference frame and how it is defined. The effective volume of ambient fluid motion around the vehicle is described by the FLOW reference frame $\{f\} = \{x_f, y_f, z_f\}$ with a center of flow (CF) coinciding with the CO of BODY. The FLOW frame is defined by (T. Fossen, 2011, 2012) as being aligned with BODY, but in this paper, the FLOW frame will be defined as opposite to BODY, similar to that in (Ross, 2008). One of the reasons is that it is preferred from the perspective of Newton's 3rd Law. In this case, $\boldsymbol{\nu}_{b/f}$ can now be expressed in the FLOW frame, i.e. $\boldsymbol{\nu}_{b/f} = \boldsymbol{\nu}^f_{b/f} \triangleq [u^f, v^f, w^f, q^f, p^f, r^f]^T$, and the relationship of relativity (4.3) becomes:

$$\boldsymbol{\nu}^f_{b/f} = \boldsymbol{\nu}^b_{b/n} - \boldsymbol{\nu}^b_{c/n}, \tag{4.4}$$

When there is no current, $\boldsymbol{\nu}^b_{c/n} = 0$, and consequently, $\boldsymbol{\nu}^f_{b/f} = \boldsymbol{\nu}^b_{b/n}$. This means that, despite both $\boldsymbol{\nu}^f_{b/f}$ and $\boldsymbol{\nu}^b_{b/n}$ having the same sign, they are opposite to each other because $\boldsymbol{\nu}^f_{b/f}$ is expressed in FLOW and $\boldsymbol{\nu}^b_{b/n}$ is expressed in BODY, where FLOW and BODY are 180^o out of phase from each other. This is further illustrated through Figure 4.1 for 3 different motion scenarios in surge. Thus, the signs of the states depend on which reference frame they are being expressed in.

Using the updated $\boldsymbol{\nu}^f_{b/f}$, the relative equations of motion become more specific as:

$$\dot{\boldsymbol{\eta}}^n_{b/n} = \boldsymbol{J}(\boldsymbol{\Theta}^n_{b/n})\boldsymbol{\nu}^f_{b/f} + \boldsymbol{V}^n_{c/n} = \boldsymbol{J}(\boldsymbol{\Theta}^n_{b/n})\boldsymbol{\nu}^b_{b/n}, \tag{4.5}$$

$$\boldsymbol{M}\dot{\boldsymbol{\nu}}^f_{b/f} + \boldsymbol{C}(\boldsymbol{\nu}^f_{b/f})\boldsymbol{\nu}^f_{b/f} + \boldsymbol{D}(\boldsymbol{\nu}^f_{b/f})\boldsymbol{\nu}^f_{b/f} + \boldsymbol{g}(\boldsymbol{\Theta}^n_{b/n}) = \boldsymbol{\tau}. \tag{4.6}$$

The relationship of relativity can be expressed in NED to give:

$$\dot{\boldsymbol{\eta}}^n_{b/n} = \dot{\boldsymbol{\eta}}^n_{b/f} + \boldsymbol{V}^n_{c/n}, \tag{4.7}$$

where $\boldsymbol{\eta}^n_{b/f} \triangleq [\dot{x}^f, \dot{y}^f, \dot{z}^f, \dot{\phi}^f, \dot{\theta}^f, \dot{\psi}^f]^T$ is the vehicle velocities and Euler rates relative to

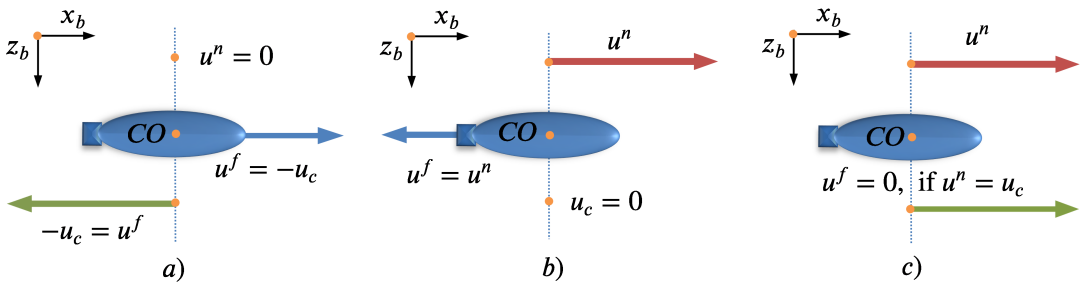

Figure 4.1: Relative velocities in surge DOF. a) Zero vehicle surge motion in NED $u^n = 0$, and an adverse current in surge. The vehicle is at still relative to NED, but is moving relative to FLOW at $u^f = -u_c$. b) Positive vehicle surge motion in NED $u^n \geq 0$, and zero surge CURRENT. Even though the CURRENT in surge is zero, the vehicle will still experience an adverse fluid motion in surge since it is moving against the fluid FLOW at $u^f = u^n \geq 0$. c) Positive vehicle surge motion in NED $u^n \geq 0$, and a positive CURRENT in surge. Even though the vehicle is moving relative to NED, it can be at still relative to the fluid FLOW, at $u^n = u_c$ if $u^f = 0$ in this case.

FLOW, but expressed in NED. $\dot{\boldsymbol{\eta}}^n_{b/f}$ is given by equating (4.7) and (4.5), or by transforming $\boldsymbol{\nu}^f_{b/f}$ to NED using $\boldsymbol{J}$. Hence:

$$\dot{\boldsymbol{\eta}}^n_{b/f} = \boldsymbol{J}(\boldsymbol{\Theta}^n_{b/n})\boldsymbol{\nu}^f_{b/f}. \tag{4.8}$$

Remark 4.1. The previous FLOW frame in (T. Fossen, 2012) is used to describe the ocean current. The ocean current here is decribed by both the improved FLOW and a CURRENT frame complete with its definition of the CURRENT Euler angles compared to previous works. This approach of representing liquids by their own reference frame is naturally also applicable to aerospace applications for modelling and incorporating 3-D wind. The FLOW frame in (T. Fossen, 2011) corresponded to the WIND frame in aerospace, while the CURRENT frame here can correspond to a WIND frame that can be similarly and completely defined to describe the relative motion of a volume of air relative to NED. The role of the updated FLOW frame remains the same in aerospace. The FLOW frame not only describes the fluid motion caused by the ocean current, but also describes the fluid motion in the absence of ocean current, i.e. the fluid motion caused due to the vehicle motion, not by the ocean current. Thus, the updated relationship of relativity (4.4) dictates that three separate reference frames, BODY, FLOW and CURRENT are

necessary for separate and complete modeling of the ocean current (or wind) to represent each state vectors. Since ocean currents and waves are both fluid motion, the CURRENT frame can also be used to describe the ocean wave through $\boldsymbol{\nu}^n_{c/n}$ and thus the CURRENT disturbance can also be referred as CURRENT and/or WAVE disturbances.

Remark 4.2. Note that $\boldsymbol{\nu}^b_{b/n}$ is also referred as absolute velocity in some works, e.g. in (T. Fossen, 2012). This does not contribute to understanding the problem in general since motion is always relative to a reference point/frame. This can also be seen from the relationship of relativity (4.3)-(4.4) that all the vectors here are relative to NED or FLOW.

4.1.2 Drift Rate

Estimates of the ocean current $\boldsymbol{\nu}^n_{c/n}$ or the vehicle FLOW velocity $\boldsymbol{\nu}^f_{b/f}$ are usually not available, and hence the relative and CURRENT velocities are not easily obtained. Since the relativity relationships have been made clear between the sates, these velocities can be obtained using a technique referred here as *drift rate*, which can describe the extend to the which vehicle is being drifted or rotated away by the velocity and angular rates of the CURRENT and/or WAVES. In this case, the drift rate matrix $\boldsymbol{R}_{drf}$ for motion in each DOF can be defined by the ratio between the the CURRENT and vehicle BODY velocities relative NED which is:

$$\boldsymbol{R}_{drf} = \left[\frac{u_c}{u^n}, \frac{v_c}{v^n}, \frac{w_c}{w^n}, \frac{p_c}{p^n}, \frac{q_c}{q^n}, \frac{r_c}{r^n}\right], \tag{4.9}$$

where

$$\boldsymbol{R}_{drf} \triangleq \left[R^u_{drf}, R^v_{drf}, R^w_{drf}, R^p_{drf}, R^q_{drf}, R^r_{drf}\right], \tag{4.10}$$

contains the constant drift rates for each corresponding DOF. The drift rate (4.9) can also be expressed alternatively using the relationship (4.10) as:

$$\boldsymbol{R}_{drf} = \left[\frac{u_c}{u^f + u_c}, \frac{v_c}{v^f + v_c}, \frac{w_c}{w^f + w_c}, \frac{p_c}{p^f + p_c}, \frac{q_c}{q^f + q_c}, \frac{r_c}{r^f + r_c}\right]. \tag{4.11}$$

if $\boldsymbol{\nu}^f_{b/f}$ is available instead of $\boldsymbol{\nu}^n_{c/n}$.

In order to help with understanding of the drift rate, the following two cases are explained. A drift rate of 1 can represent a case where a light object is moving relative to NED together in the direction and at the same speed of the current it is experiencing. A near zero drift rate can represent a case where a large ship is standing near still relative to NED despite experiencing some ocean current.

The drift rate is not an estimator in a sense of state estimation, but rather a lookup table and should only be used for non-zero inertial velocity $\boldsymbol{\nu}^n_{c/n}$ since (4.9) is undefined for zero $\boldsymbol{\nu}^n_{c/n}$. Hence, the approach is not global, but is very effective and simple as can be seen. It is a linear relationship between the relative $\boldsymbol{\nu}^n_{c/n}$ and $\boldsymbol{\nu}^b_{b/n}$. The drift rate can be identified off-line in experimental set-ups using pseudo-currents, or in on-board setups as long as the estimates of $\boldsymbol{\nu}^n_{c/n}$ and either $\boldsymbol{\nu}^b_{b/n}$ or $\boldsymbol{\nu}^f_{b/f}$ are obtainable. If the drift rates are available, then only one of $\boldsymbol{\nu}^f_{b/f}$, $\boldsymbol{\nu}^b_{b/n}$ or $\boldsymbol{\nu}^n_{c/n}$ is needed in (4.10) to obtain the rest of the velocities and achieve the relative kinetics (4.11). Alternatively, estimation of the CURRENT velocity $\boldsymbol{\nu}^n_{c/n}$ is also possible using (4.10) if the drift rate and either $\boldsymbol{\nu}^f_{b/f}$ or $\boldsymbol{\nu}^b_{b/n}$ are available. The drift rate can also be extended to aerospace systems by replacing the CURRENT frame with an equivalent WIND frame. The idea can also be extended to form a matrix of *drift acceleration* matrix by replacing the velocity with acceleration terms if this is desired. Thus, the drift rate can be a very simple and powerful estimation technique.

4.1.3 Angles of Motion

Vehicle, Particle Heading and Course Angle

First, the definition of the heading angle is revisited here in terms of relativity. The heading angle of the vehicle is conventionally the vehicle yaw angle relative to NED, i.e. the angle between x_b axis of BODY and x_n axis of NED, which is thus ψ^n as shown in Fig 4.2. This is only made explicit here emphasizing its relativity to NED.

There is another angle of motion that is desirable, which will be refered here as *particle heading*. This was first introduced by (Breivik & Fossen, 2005) as the direction of a particle motion in the horizontal plane. Similarly, the vehicle can be treated as a particle and this particle heading in N-E plane can now be explicitly expressed by:

$$\psi_{hp}^{n} \triangleq \text{atan2}\left(\frac{\dot{y}^{n}}{\dot{x}^{n}}\right) = \chi \triangleq \psi^{n} + \beta^{n}. \tag{4.12}$$

where χ is the conventional course angle given by (T. Fossen, 2011; A. Lekkas & Fossen, 2013; T. Fossen & Pettersen, 2014) and β^{n} is the sideslip angle relative to NED which will be defined shortly. Both are conventionally defined without the discussions or notations of relativity to NED in the superscript.

Thus, the particle heading ψ_{hp}^{n} and the course angle χ is the direction of vehicle horizontal speed vector U_{h}^{n} in NED that is given by:

$$U_{h}^{n} = \sqrt{u^{n2} + v^{n2}} = \sqrt{\dot{x}^{n2} + \dot{y}^{n2}}. \tag{4.13}$$

A desired horizontal particle heading can be defined to control the horizontal displacement of the vehicle in N-E rather than just its heading, which is given by:

$$\psi_{hdp}^{n} \triangleq \text{atan2}\left(\frac{\dot{y}_{d}^{n}}{\dot{x}_{d}^{n}}\right). \tag{4.14}$$

where $\dot{y}_{d}^{n}$ and $\dot{x}_{d}^{n}$ are the desired vehicle horizontal velocities relative to and expressed in NED to be designed.

Sideslip Angle

The sideslip is also revisited in terms of relativity. The sideslip is important in course control since that it will enable one to control the actual displacement of the vehicle other than just the heading. The sideslip angle can now be also be divided into two distinct components in terms of relativity to NED and FLOW frames. The conventional sideslip

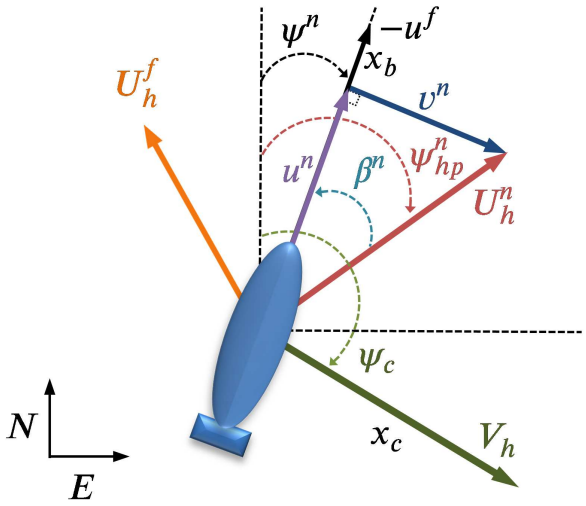

Figure 4.2: Heading, sideslip and particle heading and horizontal CURRENT $V_h = \sqrt{u_c^2 + v_c^2}$.

of a vehicle as in (2.38) is the one concerning the vehicle velocities relative to the fluid, which is:

$$\beta_r = \text{atan2}\left(\frac{v_r}{u_r}\right) = \sin^{-1}\left(\frac{v_r}{U_{rh}}\right). \tag{4.15}$$

where U_{hr} can be made explicit here to be the vehicle horizontal speed relative to FLOW given by:

$$U_{hr} = \sqrt{{u_r}^2 + {v_r}^2} = \sqrt{{\dot{x}_r}^2 + {\dot{y}_r}^2}. \tag{4.16}$$

where it is most likely that $u_r = u^f, v_r = v^f, \dot{x}_r = \dot{x}^f, \dot{x}^f = \dot{y}^f$ when using the new notations of relativity. Using the new notations, (4.15)-(4.16) become:

$$\beta_r = \beta^f = \text{atan2}\left(\frac{v^f}{u^f}\right) = \sin^{-1}\left(\frac{v^f}{U_h^f}\right), \tag{4.17}$$

$$U_{hr} = U_h^f = \sqrt{{u^f}^2 + {v^f}^2} = \sqrt{{\dot{x}^f}^2 + {\dot{y}^f}^2}. \tag{4.18}$$

where now β^f is the sideslip angle of the vehicle and U_h^f is its horizontal speed relative both relative to FLOW frame. Obviously, the benefit of using the new notations of relativity is that so we can identify the which reference frame the sideslip is relative to. Thus,

similarly, the other sidelsip angle relative to NED β^n is given by:

$$\beta^n = \text{atan2}\left(\frac{v^n}{u^n}\right) = \sin^{-1}\left(\frac{v^n}{U_h^n}\right), \tag{4.19}$$

$$U_h^n = \sqrt{u^{n2} + v^{n2}} = \sqrt{\dot{x}^{n2} + \dot{y}^{n2}}. \tag{4.20}$$

The sideslip relative to NED and is illustrated in Fig. 4.2 as the angle from U_h^n to x_b of BODY. Course control requires sideslip angle feedback and is further discussed in later Chapters.

Angle of attack

Angle of attack in marine applications are adopted from their aerospace counterparts (T. Fossen, 2011). The discussion on angle of attack is included here because its definition can also be made clear in terms of relativity, and that the angle of attack is also important in terms of modelling the lift force if the vehicel is treated as a low aspect-ratio wing from mathematical modeling perspective (e.g. as in (Blanke, 1981; Ross, 2008)). (The aspect-ratio is the ratio between the length over width of the vehicle.)

The angle of attack of the vehicle is generally relative to experienced ambient flow and is the angle between two vectors on the same plane. Considering a 2-D case first, when there is no fluid FLOW in vehicle sway direction y_b, i.e. when the vehicle BODY velocity in sway relative to FLOW $v^f = 0$, the 2-D angle of attack of the vehicle against the FLOW α_2^f is then given by:

$$\alpha_2^f = \text{atan2}\left(\frac{w^f}{u^f}\right) = \sin^{-1}\left(\frac{w^f}{U_{xz}^f}\right), \tag{4.21}$$

where U_{xz}^f is the speed of the vehicle relative to FLOW in surge-heave or N-D plane, i.e. in x_b-z_b or x_n-z_n plane, which is given by:

$$U_{xz}^f = \sqrt{u^{f2} + w^{f2}} = \sqrt{\dot{x}^{f2} + \dot{z}^{f2}}. \tag{4.22}$$

The 2-D angle of attack is illustrated in Fig. 4.3 on N-D plane. The angle of attack in vehicle sway-heave plane can also be derived in a similar manner for E-D.

When there is fluid flow in vehicle sway direction y_b, i.e. when $v^f \neq 0$, the angle of attack of the vehicle against the FLOW in 3-D has to include v^f. This means that the speed vector u^f becomes larger since it now has to include v^f in (4.18). This is because the vehicle can be treated as a wing and the definition of the angle of attack is the difference between the total speed vectors formed between the vehicle and the FLOW, and not just u^f. Thus, the angle of attack of the vehicle against the FLOW can now be derived as:

$$\alpha^f = \text{atan2}\left(\frac{w^f}{U^f_{xy}}\right) = \sin^{-1}\left(\frac{w^f}{U^f}\right). \tag{4.23}$$

where U^f_h and U^f are the horizontal and *total speed* of the vehicle relative to and expressed in FLOW given by:

$$U^f_h = \sqrt{u^{f2} + v^{f2}} = \sqrt{\dot{x}^{f2} + \dot{y}^{f2}}. \tag{4.24}$$

$$U^f = \sqrt{u^{f2} + v^{f2} + w^{f2}} = \sqrt{\dot{x}^{f2} + \dot{y}^{f2} + \dot{z}^{f2}}. \tag{4.25}$$

Notice that when $v^f = 0$, the 3-D angle of attack reduces the 2-D as in (4.20). The formulations of the speed vectors in the thesis are in accordance with SNAME adoptions (SNAME, 1950).

Remark 4.3. The expression for the vehicle angle of attack is similar to that in (T. Fossen, 2011) only in 2-D. The angle of attack in 3-D is only presented in this thesis. The angles of attack can be similarly extended to aircraft with CURRENT reference frame replaced with an equivalent WIND reference frame.

Using the opposite and coinciding relationship between FLOW and BODY, the angles of attack can also be represented using vehicle velocities relative to NED u^n, w^n, U^n_h, and U^n, where the signs of the angles of attack can just be reverted in (4.21) and (4.23) to achieve their NED equivalents. Notice that the angle of attack of the CURRENT in NED

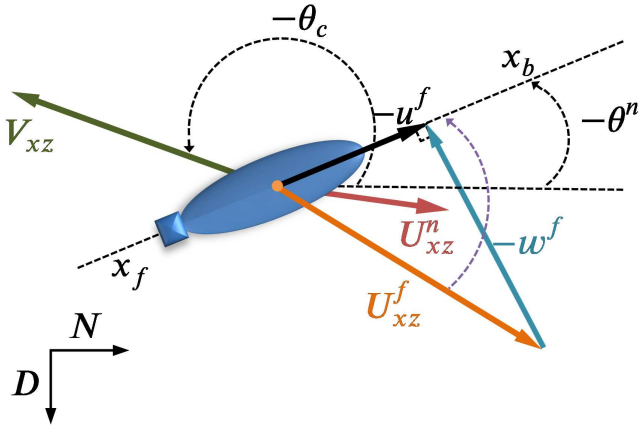

Figure 4.3: Angle of attack for $v^f = 0$ and the CURRENT $V_{xz} = \sqrt{u_c^2 + w_c^2} = \sqrt{V_x^2 + V_z^2}$ and its pitch angle θ_c in N-D plane. θ_c and θ^n are negated since they are rotated in counter-clockwise direction in the N-D plane here.

does not have to be explicitly defined here, since the angles of attack between BODY and FLOW already incorporate the CURRENT and/or WAVE velocities from the relativity relationship (4.4).

4.1.4 Lift

The lift force acting on the vehicle from the relative FLOW due to its motion is revisited here because of the 3-D model of the angle of attack. The lift discussed here is the induced vertical force on the vehicle duo to its linear motion in a flow. The theory of low aspect-ratio wing were applied to ships (e.g. (Blanke, 1981; Ross, 2008)), here a model for the lift force will be derived using the explicit models of the relative speed and the dimensionality of the angle of attack of the vehicle. The lift force considered here is the vertical force received by the vehicle from nonzero angles of attack against the FLOW, and not the action of lifting a body of water as in (Faltinsen, 2005). The conventional lift force acting on an UV is usually the 2-D angle of attack, which is also given by (Ross, 2008) as:

$$L_2^f = \frac{1}{2} U_{xz}^{f\,2} \rho A_p C_{l2}(\alpha_2^f, Re), \tag{4.26}$$

where A_p is an effective projected area with flat surface (e.g. the bottom surface area of the vehicle if it is treated like a short wing-body), C_{l2} is the non-dimensional lift coefficient as a function of the angle of attack and Reynolds number R_e in 2-D.

With the formulation of angle of attack in 3-D, the lift force can now also be extended to 3-D as:

$$L^f = \frac{1}{2} U^{f^2} \rho A_p C_l(\alpha^f, Re). \tag{4.27}$$

where $C_l(\alpha, Re)$ is the non-dimensional lift coefficient in 3-D.

The lift coefficients $C_l(\alpha_2^f, Re)$ and $C_l(\alpha^f, Re)$ are modelled as the following, which is similar to the approach in (Lewis, 1989; Ross, 2008):

$$C_{l2}(\alpha_2^f, Re) = C_{l2} \sin \alpha_2^f, \tag{4.28}$$

$$C_l(\alpha^f, Re) = C_l \sin \alpha^f, \tag{4.29}$$

where C_{l2} and C_l are proportional constants.

In (Lewis, 1989; Ross, 2008), sine of the sideslip angle β^n is used instead of $\sin \alpha_2^f$ and $\sin \alpha$ for the calculation of the coefficients (4.28)-(4.29). Blanke (1981) also used $\sin \alpha_{xz}$ for calculation of lift for small angles of attack. However, proportionality of $\sin \alpha_{xz}$ and $\sin \alpha$ to the lift forces are more realistic since a zero angle of attack means zero lift, no matter the values of other variables. Also, previous works do not differentiate between 2-D and 3-D cases as in here. The lift forces are thus different in the 2-D and 3-D cases since the total relative velocities involved are different, similar to the differences of the angle of attack in these two cases.

The shapes of UVs in general do not resemble a wing and thus the lift forces could be insignificant. If the shape of the vehicles are designed such that the lift forces are significant, they can now be incorporated into the relative modeling or relative equations of motion in a realistic and accurate manner, e.g. as vertical components added to the gravitation and restoring forces and moments proportional to the relative velocities U_{xz}^f and U^f.

4.2 Stability of Equations of Motion

An analytic method for more accurate modeling of the signs of the forces and moments is presented in this this section by integrating the stability theory and Newton's 1st Law in the stability analysis of the unforced system.

4.2.1 Instability of Decoupled Subsystem

The unforced stability is the stability of the origins of systems when all the inputs and external disturbances are removed (see e.g. (Khalil, 2002)), and such that only dissipative forces are present in the system. In this case, the origins of the systems representing relative equations of motion should be stable equilibrium points. This is explained by applying Newton's 1st Law that the body described by the equations of motion should stay at rest or at a uniform motion unless its state is changed by an external force.

The unforced stability analysis is first applied to the 1-DOF decoupled UV model that is common in the design of control systems (T. Fossen, 2011), which is obtained by the following assumptions:

Assumption 4.1 *The off-diagonal elements of the added mass matrix are small compared to their diagonal counterparts, and are null, such that* $\boldsymbol{M}_A$ *is diagonal.*

Assumption 4.2 *The off-diagonal elements of the hydrodynamic damping matrix are negligible at low operating speeds such that* $\boldsymbol{D}(\boldsymbol{\nu}^f_{b/f})$ *is diagonal.*

Assumptions 4.1 and 4.2 are reasonable assumptions and are common in most practical applications of UVs (e.g. (T. Fossen, 2011)), which leads to the following 1-DOF decoupled surge subsystem when $w^f = q^f = 0$:

$$(m - X_{\dot{u}})\dot{u}^f - (X_u + X_{|u|u}|u^f|)u^f = \tau_u + \zeta_x. \tag{4.30}$$

where ζ_x is the environmental disturbance in surge. This model is similar to the common model for decoupled surge dynamics (T. Fossen, 1994, 2002, 2011). Without inputs or

external disturbances (4.30) becomes:

$$\dot{u}^f = \frac{(X_u + X_{|u|u}|u^f|)u^f}{m - X_{\dot{u}}}. \tag{4.31}$$

Note that the control inputs are also the external forces that can change the state of the vehicle regarding Newton's 1st Law.

Proposition 4.1 *The origin $u^f = 0$ of the surge subsystem* (4.31) *is an unstable equilibrium point.*

Proof. The stability of the origin of the unforced surge subsystem (4.31) is analyzed using the positive definite and radially unbounded Lyapunov function candidate (LFC) $V(u^f) \triangleq (1/2){u^f}^2$ with its time-derivative given by:

$$\dot{V}(u^f) = \frac{(X_u + X_{|u|u}|u^f|){u^f}^2}{m - X_u} \geq 0. \tag{4.32}$$

LFC (4.32) shows that the origin $u^f = 0$ of the unforced surge subsystem (4.31) accelerates without bound even when there are no inputs or external disturbances present in the system, which is contrary to realistic behaviors of marine crafts that obviously require inputs or external disturbances to move. The condition for Lyapunov stability of the origin of (4.31) requires $\dot{V}(u^f)$ to be negative definite or semi-definite. Since the numerator of (4.32) is always positive, this condition requires the surge added mass $X_{\dot{u}}$ to be greater than m. However, the added mass is not as critical in modeling compared to the vehicle mass m, since the vehicle mass cannot be omitted in modeling, whereas the added mass can be omitted in rough approximations. Hence, it is not reasonable for the added mass to be more important than the vehicle mass and thus, to impose a requirement such that the energy of the entire system is bounded only if the added mass is greater than the vehicle mass. X_u is usually much smaller compared to m, and typically between 5% of m for normal elongated-body ship types (Faltinsen, 2005, p. 236). Thus, $X_{\dot{u}} < m$. Moreover, the LFC $V : D_b \to R_b$ is continuously differentiable on domain $D_b \subset R^n$ containing the origin $u^f = 0$ such that $V(0) = 0$. For an initial value u_o^f with an arbitrarily

small $\| u_o^f \|, V(u_o^f) > 0$. Let there be a ball B_{r1} with $r_1 > 0$ and a set U_b defined such that $B_{r1} = \{u^f \in R^n | \| u^f \| \leq r_1\}$ contains in D_b and $U_b = \{u^f \in B_{r1} | V(u^f) > 0\}$. Since $X_{\dot{u}} < m, \dot{V}(u^f) > 0$ in U_b. Then, according to Chetaev's instability theorem in (Khalil, 2002), the origin $u_r^f = 0$ is an unstable equilibrium point of (4.31). □

4.2.2 Difference in in Modeling the Signs of Forces and Moments

The instability of subsystems in the other degrees of freedom can also be proven similarly, as long as the forces and moments from the added mass and damping are passive by nature and thus, resisting the direction of motion. It is shown that if $X_{\dot{u}} < 0$, the origin is an unstable equilibrium point of the unforced surge subsystem. Furthermore, $X_{\dot{u}}$ cannot be equal to m which will create a singularity in (4.30). There is no solution to vehicle dynamics in (4.31) when $X_{\dot{u}} = m$, which means a zero total mass in the system and thus is not realistic. In fact, the added mass $X_{\dot{u}}$ in the denominator of (4.30) is making the total system mass $m - X_{\dot{u}}$ 'lighter' since it is being subtracted from m instead of being 'added' to it. This is contrary to the meaning of *added mass*, which should make the total system mass 'heavier' because it describes an increase in the resistive force of the mass. This is an apparent difference in approaches in literature regarding the modeling of signs of the added mass in the mass-inertia term.

Even if $X_{\dot{u}}$ is being added to m such that the system mass in the numerator of (4.30) becomes $m + X_{\dot{u}}$, it can still be shown that the origin of this new unforced surge subsystem system is still unbounded and is unstable, which will be due to the positive damping terms in the numerator of (4.30) which lead to an increasing energy in a new LFC. This now represents the second inconsistency in the literature regarding the modeling of sign of the damping terms. The correct modeling for the signs of the added mass and damping terms that will not result in an unstable origin of the unforced model can be derived by analyzing these two terms as forces acting on a free-body.

The added mass and linear and quadratic damping forces acting on the vehicle are illustrated with the free-body diagram in Fig 4.4. It considers a case where a positive

surge input force τ_x is acting on the vehicle and the added mass and damping forces resisting the motion in the opposite direction since they are *dissipative* forces. Using Newton's 2nd Law, the net force $\vec{F}$ acting on a body is represented by:

$$\sum \vec{F} = m\vec{a}, \tag{4.33}$$

where $\vec{a}$ is the acceleration of the body in the direction of $\vec{F}$. From Fig. 4.4, the net force acting on the surge DOF is,

$$\sum \vec{F} = \tau_x - X_{\dot{u}}\dot{u}^f - (X_u + X_{|u|u}|u^f|)u^f, \tag{4.34}$$

where the added mass and damping forces take negative signs because they are acting in the opposite direction of x_b and are also expressed in BODY as in Fig. 4.4. Equating the right-hand-sides of (4.33) and (4.34) and replacing $\vec{a}$ with $\dot{u}^f$ gives:

$$m\dot{u}^f = \tau_x - X_{\dot{u}}\dot{u}^f - (X_u + X_{|u|u}|u^f|)u^f, \tag{4.35}$$

Adding an environmental disturbance ζ_x and rearranging (4.35) gives:

$$(m + X_{\dot{u}})\dot{u}^f + (X_u + X_{|u|u}|u^f|)u^f = \tau_u + \zeta_x. \tag{4.36}$$

It can be seen now that the signs of the added mass and damping forces have become positive compared to (4.30). Without input forces or disturbances, (4.36) becomes:

$$\dot{u}^f = \frac{-(X_u + X_{|u|u}|u^f|)u^f}{m + X_{\dot{u}}}. \tag{4.37}$$

Proposition 4.2 *The origin $u^f = 0$ of the surge subsystem* (4.37) *is a globally exponentially stable (GES) equilibrium point.*

Proof. The LFC considered for the new unforced surge subsystem (4.37) $V(u^f) \triangleq$

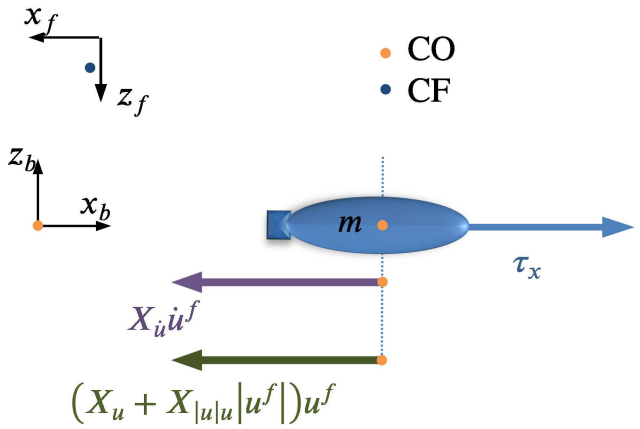

Figure 4.4: Free-body diagram showing forces acting in surge with a positive surge input force. The FLOW is opposite and parallel to the BODY frame with a chosen CF as shown.

$(1/2)u^{f\,2}$ with its time-derivative given by:

$$\dot{V}(u^f) = \frac{-(X_u + X_{|u|u}|u^f|)u^{f\,2}}{m + X_u} \geq 0. \tag{4.38}$$

Since $X_u, X_{|u|u} > 0$ from their positive definiteness from convention, $\dot{V}(u^f)$ is negative definite. Thus, the origin $u^f = 0$ of the unforced surge subsystem (4.37) is a GES equilibrium point. □

The surge subsystem (4.37) with a stable origin is also a common 1-DOF surge model in design of control systems (Caccia et al., 2000). The unforced stability analysis suggests that the added mass and hydrodynamic damping forces and moments matrices should be positive definite, by convention, and thus remain as addition to the rigid-body mass-inertia matrix term in the equations of motion, which are:

$$\boldsymbol{M} = \boldsymbol{M}_{rb} + \boldsymbol{M}_a, \tag{4.39}$$

$$\boldsymbol{M}\dot{\boldsymbol{\nu}}^f_{b/f} + \boldsymbol{C}(\boldsymbol{\nu}^f_{b/f})\boldsymbol{\nu}^f_{b/f} + \boldsymbol{D}(\boldsymbol{\nu}^f_{b/f})\boldsymbol{\nu}^f_{b/f} + \boldsymbol{g}(\boldsymbol{\Theta}^n_{b/n}) = \boldsymbol{\tau}_{act} + \boldsymbol{\tau}_{env}. \tag{4.40}$$

The total system mass is commonly given as a subtraction between the rigid-body and

added masses(T. Fossen, 1991, 1994, 2011):

$$\boldsymbol{M} = \boldsymbol{M}_{rb} - \boldsymbol{M}_a. \tag{4.41}$$

Notice now that the expression of $\boldsymbol{M}$ in (4.39) is the opposite of that in (4.41). Above analysis and formulations dictate that $\boldsymbol{M}$ in (4.39) is correct and that the elements of $\boldsymbol{M}_a$ and $\boldsymbol{D}(\boldsymbol{v}^f_{b/f})$ also have to be positive. The positivity of $\boldsymbol{M}_a$ can avoid singularity and making the system mass-inertia 'lighter', while the positivity of $\boldsymbol{D}(\boldsymbol{v}^f_{b/f})$ avoids instability of the origin as shown in the stability analysis.

The dissipative formulation of the added mass as an addition to the rigid-body mass as in (4.39) was first shown by Lamb (1895, p. 205), and was similarly described by Davidson and Schiff (1946) as an 'ascension to mass'. Notable works in the literature where the added mass is an addition to the system mass-inertia that avoid singularity are that of Cummins (1962), Son and Nomoto (1981), Yuh (1990), Caccia et al. (2000) and Faltinsen (2005, p. 174, pp. 394-395). On the other hand, the added mass was modelled as a subtraction in the system mass-inertia term (which would make the total systam mass 'lighter' and could lead to singularity) in (Abkowitz, 1964, p. 93; Humphreys & Watkinson, 1978, p. 11; Lewis, 1989, p. 193, p. 219; Sagatun & Fossen, 1991; T. Fossen, 1991, 1994, 2002, 2011; T. Fossen & Fjelstad, 1995; Ridao et al., 2004; Mark et al., 2006; Ross, 2008).

As for the sign of the damping terms, formulations of equations of motion where the linear or nonlinear damping terms are modelled positive and dissipative to the system inertia terms include models in (Norrbin, 1963; Abkowitz, 1964; Yuh, 1990; Caccia et al., 2000; Ridao et al., 2004; Avila et al., 2013). On the contrary, cases where either the linear or the quadratic damping terms are modeled as negative to the system inertia term, which could lead to unboundedness and thus instability of the origin as shown, include (T. Fossen, 1991, 1994, 2002, 2011; Sagatun & Fossen, 1991; T. Fossen & Fjelstad, 1995; Mark et al., 2006; Pepijin et al., 2007; Ross, 2008). These models will lead to instability

of the origin in unforced conditions.

There are difference ways to model the hydrodynamic dissipative forces and moments. However, unforced stability focuses on the signs of these forces and moments in the final equations of motion such that they do not produce an unstable origin without any input or external forces applied, and thus that they conform to Newton's 1st Law, which is a realistic expectation in the motion of bodies. Consequently, unforced stability analysis suggests the following general structure in for modeling the hydrodynamic dissipative forces and moments, which will always ensure the stability of the origin and non-singularity of the total system mass:

$$\dot{u}^f = \frac{-(X(u^f)u^f)}{m_{11}} \tag{4.42}$$

where $X(u^f)u^f$ represents the total damping/drag forces depending on the modeling approach and m_{11} is the mass and added-mass in surge. Both of these forces have to be positive no matter the type expressions used for the modeling such that their origins are not unstable and they avoid singularity in unforced condition and thus, conform with Newton's 1st Law and are more accurate models. Equation (4.42) can be similarly extended to other DOFs to formulate equivalent propositions.

Remark 4.4 While it has been analytically shown in this section that some popular model could lead to unstable and singular origins in the equations of motion, this problem could have been unknowingly avoided during implementation though, e.g., trial-and-error. This could especially be true for damping forces, because simulated or implemented models grow unbounded if these signs are not fixed. Therefore, results obtained through these models could still be true and the method here is concerned with a better approach to this modeling problem analytically.

4.3 Incorporation of Environmental Disturbances

Correct incorporation of environmental disturbances are crucial in obtaining models that interact with the environment, which are usually unstructured in marine applications and

hostile in both aerospace and marine applications. As shown earlier The analytic models of environmental disturbances for 3-D marine or aerospace systems are not complete. In addition to that, this section will provide a meaningful and more accurate incorporation of environmental disturbances in the equations of motion of UVs.

4.3.1 State Relativity

The following definition is defined first for describing the motion of particles or point masses before presenting the property of *state relativity*.

Definition 4.1 *(Motion State) The motion state of an origin is a state that can describe its position, orientation or any other time-derivatives of these two states.*

Time-derivatives of the position or orientation include, e.g. linear and angular velocities or accelerations, and the definition of motion state can be extended to describe any state that involves description of motion. The following property holds for all *motion states*.

Theorem 4.1 (State Relativity: Parallel Reference Frames) *For every motion state of an object relative to a subject reference frame and expressed in the object reference frame, there is an equal motion state of the subject relative to the object reference frame and expressed in the subject reference frame if these reference frames are parallel and opposite to each other.*

The motion state of the subject relative to the object reference frame and expressed in the subject reference frame is equal and opposite relative to the object reference frame and expressed in the subject reference frame if these reference frames are parallel and aligned with each other.

Proof. Assume that there are two vehicle in motion only relative to each other in two inertial parallel reference frames $A = [x_A, y_A, z_A]$ and $B = [x_B, y_B, z_B]$, resp., without a third reference frame. This is illustrated in Figures 4.5 and 4.6. Suppose that vehicle A has a velocity $u^A_{A/B}$ relative to B but expressed in A, then from the perspective of reference frame B, vehicle B has a velocity $u^B_{B/A}$ relative to A but expressed in B. This is true since

velocity $u^A_{A/B}$ is defined only relative to B and velocity $u^B_{B/A}$ is defined only relative to A and that there is no other reference frame. Without a third reference frame, it is not known whether A or B is actually moving, i.e. , either A is moving towards B or B is moving towards A. This is given mathematically as:

$$u^A_{A/B} = u^B_{B/A}, \tag{4.43}$$

where $u^A_{A/B}$ and $u^B_{B/A}$ are equal to each other from the perspectives of A and B, resp., since A and B are parallel and opposite to each other. This is shown in Figure 4.5.

If A and B are parallel and aligned with each other, then

$$u^A_{A/B} = -u^B_{B/A}, \tag{4.44}$$

where $u^A_{A/B}$ and $u^B_{B/A}$ are equal and opposite to each other from the perspectives of A and B, resp., since A and B are parallel and aligned to each other. This is shown in Figure 4.5.

This result can be directly extended to angular motion and is only true if both A and B have the same convention for rotation such as the right-hand-rotation as positive rotation in the reference frames. Hence, this concludes the proof. □

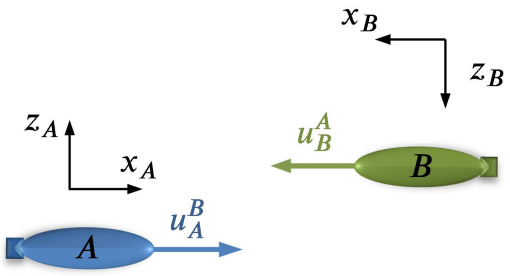

Figure 4.5: Motion of two vehicles relative to each other in surge, where inertial frames A and B are parallel and opposite to each other. Either A is moving forward observed from B, or B is moving forward observed from A.

Since motion of both vehicles only relative to each other is concerned, it cannot be known which one is actually moving without an external static reference frame/point independent from A and B.

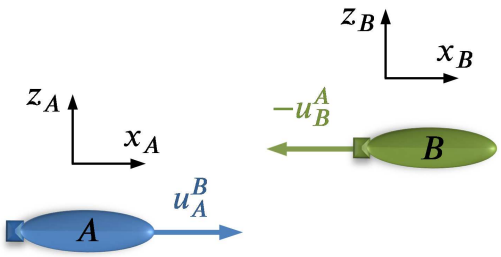

Figure 4.6: Motion of two vehicles relative to each other in surge, where inertial frames A and B are parallel and aligned to each other. Either A is moving forward observed from B, or B is moving backward observed from A.

Remark 4.5 State relativity is also applicable to cases where the origin and subject references frames are not parallel to each other. In such cases, the rotations between the two frames thus will not be 180 *deg*, but an existing phase difference between them. Rotations about the axes are also not effected as long as the same convention is used, e.g. the right-hand rotation convention.

4.3.2 Newton's 3rd Law and State Relativity

The concept of state relativity is based on further understanding of reference frames and this can be extended to describe Newton's 3rd Law more accurately using reference frames. Newton's 3rd Law of Motion is commonly known as:

Theorem 4.2 *For every action, there is an equal and opposite reaction.*

Theorem 4.2 can be rewritten using the conventions for reference frames in this thesis as follows.

Theorem 4.3 *For every action from a subject reference frame to an object reference frame, there is an equal reaction from the object reference frame to the subject reference frame if the two reference frames are parallel and aligned with each other. The reactions are equal and opposite if the reference frames are parallel but opposite to each other.*

Theorem 4.3 is similar to state relativity except that now force is concerned instead of motion state. However, there is no motion without force according to Newton's 2nd Law, and thus the directions of these entities are the same in the same reference frame.

Theorem 4.3 incorporates reference frames into Newton's 3rd Law, which makes it easier to apply it more accurately, and thus, can lead to more accurate physical modeling.

4.3.3 Incorporation of Environmental Disturbances

State relativity is combined with Newton's 3rd Law of motion to describe the hydrodynamic disturbances in the equations of motion of UVs using the relativity of the BODY and FLOW states to each other. The fluid FLOW is assumed to be in uniform motion with and around its center of flow (CF), which virtually coincides with CO of BODY. Then, the FLOW velocity and Euler rates relative to BODY but expressed in FLOW can be similarly defined as: The FLOW velocity and angular rates relative to and expressed in BODY can be defined as:

$$\boldsymbol{\nu}^b_{f/b} \triangleq [u^f_b, v^f_b, w^f_b, p^f_b, q^f_b, r^f_b]^T. \tag{4.45}$$

Since the FLOW frame is body-centered to vehicle CO, and is parallel and opposite to BODY frame. Then, from state relativity in Theorem 4.1, the following relationship exists between $\boldsymbol{\nu}^f_{b/f}$ and $\boldsymbol{\nu}^b_{f/b}$ and their respective time-derivatives:

$$\boldsymbol{\nu}^b_{f/b} = \boldsymbol{\nu}^f_{b/f}, \tag{4.46}$$

$$\dot{\boldsymbol{\nu}}^b_{f/b} = \dot{\boldsymbol{\nu}}^f_{b/f}. \tag{4.47}$$

Using (4.46)-(4.47), the modified vehicle kinetics in (4.40) can be rewritten in FLOW frame as:

$$\boldsymbol{M}\dot{\boldsymbol{\nu}}^b_{f/b} + \boldsymbol{C}(\boldsymbol{\nu}^b_{f/b})\boldsymbol{\nu}^b_{f/b} + \boldsymbol{D}(\boldsymbol{\nu}^b_{f/b})\boldsymbol{\nu}^b_{f/b} + \boldsymbol{g}(\boldsymbol{\eta}^n_{b/n}) = \boldsymbol{\tau}_{env}. \tag{4.48}$$

where $\boldsymbol{\tau}_{act} = 0$ since FLOW has no actuators. The hydrodynamic forces and moments from FLOW acting on BODY is caused by the active and reactive motion of FLOW relative to BODY. For fully submerged vehicles, $\boldsymbol{\tau}_{env}$ only consists of ocean CURRENT and WAVE disturbances which is now completely described by (4.48) since fluid FLOW

velocity and acceleration relative to BODY also incorporates CURRENT and/or WAVE velocity and acceleration through the relativity relationship (4.26) and its time-derivative. Thus, environmental disturbances from ocean CURRENT and WAVE $\boldsymbol{\tau}_{env} = \boldsymbol{\tau}_{current} + \boldsymbol{\tau}_{wave}$ can be modeled by FLOW disturbance forces and moments $\boldsymbol{\tau}_{flow}$ acting on BODY, which can now be obtained from (4.47):

$$\boldsymbol{\tau}_{flow} = \boldsymbol{\tau}_{env} = \boldsymbol{M}\dot{\boldsymbol{\nu}}^b_{f/b} + \boldsymbol{C}(\boldsymbol{\nu}^b_{f/b})\boldsymbol{\nu}^b_{f/b} + \boldsymbol{D}(\boldsymbol{\nu}^b_{f/b})\boldsymbol{\nu}^b_{f/b} + \boldsymbol{g}(\boldsymbol{\eta}^n_{b/n}). \tag{4.49}$$

The coefficients in system matrices $\boldsymbol{M}$ and $\boldsymbol{D}$ now can be interpreted as FLOW forces and moments coefficient matrices. The mass and added-mass of the FLOW are virtual in this case and are dissipative elements acting as reactive disturbances from FLOW to BODY, i.e. bigger the total mass, bigger the action and reaction forces or moments from BODY and FLOW during motion. The gravitational and restoring forces and moments $\boldsymbol{g}(\boldsymbol{\eta}^n_{b/n})$ consist of center of gravity vector, vehicle Euler angles $(\boldsymbol{\Theta}^n_{b/n})$ and buoyancy and weight forces and moments acting from the fluid to the vehicle. Thus, $\boldsymbol{g}$ is already a FLOW forces and moments and the three-index notation can be extended to describe forces and moments in this case to give $\boldsymbol{g} = \boldsymbol{g}^b_{f/b}$. This can be similarly read as the gravitational forces and moments of FLOW, acting on BODY, and expressed in BODY. The superscript similarly corresponds to which reference frame the vector is expressed in.

Now, all the elements in (4.49) are FLOW forces and moments acting on BODY from FLOW and this is the manifestation of Newton's 3rd Law such that in (4.49), for every action from FLOW to BODY, there is equal and opposite reaction from BODY to FLOW. Then, forces and moments acting on BODY from FLOW are equal and opposite to those acting on FLOW from BODY. Using (4.46)-(4.47), (4.49) can be rewritten as:

$$\boldsymbol{\tau}_{env} = \boldsymbol{M}\dot{\boldsymbol{\nu}}^f_{b/f} + \boldsymbol{C}(\boldsymbol{\nu}^f_{b/f})\boldsymbol{\nu}^f_{b/f} + \boldsymbol{D}(\boldsymbol{\nu}^f_{b/f})\boldsymbol{\nu}^f_{b/f} + \boldsymbol{g}(\boldsymbol{\eta}^n_{b/n}). \tag{4.50}$$

It can be seen that this environmental disturbance $\boldsymbol{\tau}_{env}$ in (4.50) is already present in the relative equations of motion (4.40). Hence, substituting $\boldsymbol{\tau}_{env}$ in (4.50) again into (4.40)

will result in canceling out of all the terms in (4.40) except for $\boldsymbol{\tau}_{act}$. Thus, the environmental disturbances $\boldsymbol{\tau}_{env}$ in (4.40) cannot be present in the relative equations of motion since the vehicle velocities and acceleration relative to the FLOW are already used to describe the hydrodynamic, hydrostatic and gravitational forces and moments. Therefore, removing $\boldsymbol{\tau}_{env}$ in (4.40) gives:

$$\boldsymbol{M}\dot{\boldsymbol{\nu}}^f_{b/f} + \boldsymbol{C}(\boldsymbol{\nu}^f_{b/f})\boldsymbol{\nu}^f_{b/f} + \boldsymbol{D}(\boldsymbol{\nu}^f_{b/f})\boldsymbol{\nu}^f_{b/f} + \boldsymbol{g}(\boldsymbol{\eta}^n_{b/n}) = \boldsymbol{\tau}_{act}. \tag{4.51}$$

which already incorporates environmental disturbances from CURRENT and/or WAVE forces and moments from the FLOW forces and moments acting on BODY.

This result shows that WAVE forces and moments are not required to be modeled redundantly using linear superposition into the relative equations of motion as in (T. Fossen, 2012), when the vehicle is not at rest.

Remark 4.6 It will be seen in Chapter 5 that when analyzing the stability of guidance laws, the common practice of linear superpositioning of a time-varying current disturbances onto the error system can be redundant if vehicle velocities and accelerations relative to FLOW are already used. In this case, any forces or moments terms superimposed additionally onto (4.51) are not caused by the fluid FLOW. For surface marine vehicles, additional non-fluid disturbance terms on (4.51) can be from the WIND component of environmental disturbances if they are modeled using a wind velocity and accelerations relative to the vehicle. For UVs, additional non-fluid disturbance terms will only mean that they either belong to changes in gravity, or that they are external rigid-body disturbances such as collisions.

4.4 Passivity and Boundedness

The passivity and boundedness are presented here under the assumption of hydrostatic neutrality. The proofs now can also incorporate CURRENT and/or WAVE disturbances due to the definition of the CURRENT reference frame, where conventionally only the

ocean current is considered as in (Breivick, 2003).

4.4.1 Passivity

The following corollary is used for the proof of passivity (Breivick, 2003).

Corollary 4.1 *Consider a system with input vector $u(t)$ and output vector $y(t)$. Suppose there exists a function $V(t) \geq 0$ that describes the total energy of the system, and a function $g(t)$ such that $\int_0^T g(t)dt \geq 0$ for all $T \geq 0$. If $\dot{V} \leq y^T(t)u(t) - g(t)$ for all $t \geq 0$ and all input runs, the system is said to be passive.*

Proposition 4.3 (Passivity) *The relative underwater-vehicle system including environmental disturbances in* (4.51) *is passive if it is neutrally buoyant such that $\boldsymbol{g}(\boldsymbol{\eta}^n_{b/n}) = 0$.*

Proof: The potential energy of the system (4.51) will be zero if it is neutrally buoyant and thus, the total energy of the vehicle can be described only by its kinetic energy, which is:

$$\boldsymbol{V}(t) = \frac{1}{2}\boldsymbol{\nu}^{f^T}_{b/f}\boldsymbol{\nu}^f_{b/f} \tag{4.52}$$

where $\boldsymbol{V}(t) > 0 \forall \boldsymbol{\nu}^f_{b/f} \neq 0$. Using (4.51) and setting $\boldsymbol{g}(\boldsymbol{\eta}^n_{b/n}) = 0$, time-derivative of $V(t)$ becomes:

$$\begin{aligned}
\boldsymbol{V}(t) &= \boldsymbol{\nu}^{f^T}_{b/f}\boldsymbol{M}\dot{\boldsymbol{\nu}}^f_{b/f} + \frac{1}{2}\boldsymbol{\nu}^{f^T}\dot{\boldsymbol{M}}\boldsymbol{\nu}^f_{b/f} \\
&= \boldsymbol{\nu}^{f^T}_{b/f}\left[\boldsymbol{\tau}_{act} - \boldsymbol{C}(\boldsymbol{\nu}^f_{b/f})\boldsymbol{\nu}^f_{b/f} - \boldsymbol{D}(\boldsymbol{\nu}^f_{b/f})\boldsymbol{\nu}^f_{b/f}\right] + \frac{1}{2}\boldsymbol{\nu}^{f^T}\dot{\boldsymbol{M}}\boldsymbol{\nu}^f_{b/f} \\
&= \frac{1}{2}\boldsymbol{\nu}^{f^T}_{b/f}\left[\dot{\boldsymbol{M}} - 2\boldsymbol{C}(\boldsymbol{\nu}^f_{b/f})\right]\boldsymbol{\nu}^f_{b/f} + \boldsymbol{\nu}^{f^T}_{b/f}\left[\boldsymbol{\tau}_{act} - \boldsymbol{D}(\boldsymbol{\nu}^f_{b/f})\boldsymbol{\nu}^f_{b/f}\right] \\
&= \boldsymbol{\nu}^{f^T}_{b/f}\boldsymbol{\tau}_{act} - \boldsymbol{D}(\boldsymbol{\nu}^f_{b/f})\boldsymbol{\nu}^f_{b/f}.
\end{aligned} \tag{4.53}$$

since $\dot{\boldsymbol{M}} - 2\boldsymbol{C}(\boldsymbol{\nu}^f_{b/f})$ is skew-symmetric (see e.g. Sciavicco & Siciliano, 2000). Comparing (4.53) with Corollary 4.1, it can be seen that $\boldsymbol{D}(\boldsymbol{\nu}^f_{b/f})\boldsymbol{\nu}^f_{b/f}$ represents the energy loss function $g(t)$ for the system, input $\boldsymbol{\tau}_{act}$ corresponds to $u(t)$ and the output vector $\boldsymbol{\nu}^f_{b/f}$ corresponds to $y(t)$. Hence, the relative underwater-vehicle system is passive. □

4.4.2 Boundedness

The boundedness of relative UV vehicles including CURRENT and/or WAVE disturbances is given as follows.

Proposition 4.4 (Boundedness) *The relative underwater-vehicle system including environmental disturbances in* (4.51) *subject to bounded input forces and moments* $\boldsymbol{\tau}_{act}$ *and CURRENT and/or WAVE states will have bounded relative states* $\boldsymbol{\nu}^f_{b/f}$ *and* $\boldsymbol{\nu}^b_{b/n}$ *if it is neutrally buoyant such that* $\boldsymbol{g}(\boldsymbol{\eta}^n_{b/n}) = 0$. *In other words,* $(\boldsymbol{\tau}_{act}, \boldsymbol{\nu}^b_{c/n}) \in L_\infty \Rightarrow (\boldsymbol{\nu}^f_{b/f}, \boldsymbol{\nu}^b_{b/n}) \in L_\infty$ *if* $\boldsymbol{g}(\boldsymbol{\eta}^n_{b/n}) = 0$.

Proof: If the vehicle is neutrally buoyant, from (4.53), it is shown that the energy of the system changes according to:

$$\begin{aligned} \boldsymbol{V}(t) &= \boldsymbol{\nu}^{f^T}_{b/f}\boldsymbol{\tau}_{act} - \boldsymbol{D}(\boldsymbol{\nu}^f_{b/f})\boldsymbol{\nu}^f_{b/f} \\ &= -\boldsymbol{\nu}^{f^T}_{b/f}\left[\boldsymbol{D}(\boldsymbol{\nu}^f_{b/f})\boldsymbol{\nu}^f_{b/f} - \boldsymbol{\tau}_{act}\right] \forall t \geq 0. \end{aligned} \tag{4.54}$$

Since $\boldsymbol{V}(t) > 0 \ \forall \boldsymbol{\nu}^f_{b/f} \neq 0$ and $\boldsymbol{\nu}^f_{b/f} = \boldsymbol{\nu}^b_{b/n} - \boldsymbol{\nu}^b_{c/n}$, it follows that $(\boldsymbol{\tau}_{act}, \boldsymbol{\nu}^b_{c/n}) \in L_\infty \Rightarrow (\boldsymbol{\nu}^f_{b/f}, \boldsymbol{\nu}^b_{b/n}) \in L_\infty$. □

It is realistic in marine vehicle applications that $(\boldsymbol{\tau}_{act}, \boldsymbol{\nu}_c) \in L_\infty$ and thus $(\boldsymbol{\nu}^f, \boldsymbol{\nu}^n) \in L_\infty$ by Proposition 4.4. This is a general result in 3-D for neutral buoyancy.

Remark 4.7 The neutrality assumption can be achieved by assuming that the vehicle weight W and buoyancy B are equal and the center of gravity (CG) and center of buoyancy (CB) are located at equal distances from CO such that the gravitational and restoring forces and moments matrix

$bmg(\boldsymbol{\eta}^n_{b/n})$ produces zero. This is a general assumption and specific cases for different structures of $\boldsymbol{g}(\boldsymbol{\eta}^n_{b/n})$ can be analyzed separately for different control problems. The proofs of passivity and boundedness can also be extended to space or air crafts.

4.5 Models of Irrotational Ocean CURRENT and/or WAVE

A complete and easy-to-follow model of the the irrotational ocean current and/or wave disturbances is presented in this section.

4.5.1 3-D Ocean Current and/or Wave

The ocean current is conventionally described by the old FLOW frame by T. Fossen (2012) using the current heading and a current angle of attack. While the definition of current heading in the inertial frame β_c is intuitive (?, ?), the definition of the current angle of attack α_c is not given. Plus, more justification could be provided for the principal transformation approach used in (T. Fossen, 2012). In this thesis, ocean current and/or wave are represented and modeled using the new CURRENT reference frame. The idea here is to treat the ocean current as a separate object by using its own reference frame. The CURRENT frame $\{c\} = \{x_c\}$ describing a volume of ocean current relative to NED with a chosen center of current (CC) and x_c as its direction of stream. The ocean current is not a rigid-body and thus cannot have its own roll-pitch-yaw angles, but its directions as those of the 3-D CURRENT intensity vector V_c in NED can now be defined by its Euler angles relative to and expressed in NED, which are denoted as $\boldsymbol{\Theta}^n_{c/n} \triangleq [\phi_c, \theta_c, \psi_c]^T$. The linear components of irrotational CURRENT in NED are defined by $\boldsymbol{V}^n_{cl/n} \triangleq [V_x, V_y, V_z]^T$, where the CURRENT intensity $V_c = \sqrt{{V_x}^2 + {V_y}^2 + {V_z}^2} = \sqrt{{u_c}^2 + {v_c}^2 + {w_c}^2}$ and is bounded. The CURRENT Euler angles can now be defined as $[\phi_c, \theta_c, \psi_c] \triangleq [atan2(V_z, V_y), atan2(V_z, V_x), atan2(V_y, V_x)]$. For constant CURRENT in NED, $\dot{\boldsymbol{V}}^n_{c/n} = 0$. With CURRENT Euler angles, $\boldsymbol{V}^n_{cl/n}$ can now be expressed in BODY from NED using the transpose of linear rotation matrix $\boldsymbol{R}(\boldsymbol{\Theta}^n_{c/n})$ as:

$$\boldsymbol{\nu}^b_{c/n} \triangleq [u_c, v_c, w_c]^T = \boldsymbol{R}(\boldsymbol{\Theta}^n_{c/n} - \boldsymbol{\Theta}^n_{b/n})^T \boldsymbol{V}^n_{cl/n}, \tag{4.55}$$

The rotation $\boldsymbol{\Theta}^n_{c/n} - \boldsymbol{\Theta}^n_{b/n}$ is logical because both $\boldsymbol{\Theta}^n_{c/n}$ and $\boldsymbol{\Theta}^n_{b/n}$ are expressed in the same NED frame. $\boldsymbol{\Theta}^n_{c/n} - \boldsymbol{\Theta}^n_{b/n}$ means that the angles used for decomposing $\boldsymbol{V}^n_{cl/n}$ into $\boldsymbol{\nu}^b_{b/n}$ are

the angular difference between them, and the transpose of transformation matrix $\boldsymbol{R}$ then rotates the linear CURRENT components in NED to BODY. This is also an easier-to-follow and more intuitive insight into coordinate transformations.

If angular component of $\boldsymbol{V}^n_{c/n}$ are not zero, this represents rotational ocean CURRENT and/or WAVE in NED. In this case, the 6-DOF transformation of CURRENT in NED to BODY is given by:

$$\boldsymbol{\nu}^b_{c/n} \triangleq [u_c, v_c, w_c, q_c, p_c, r_c]^T = \boldsymbol{J}(\boldsymbol{\Theta}^n_{c/n} - \boldsymbol{\Theta}^n_{b/n})^T \boldsymbol{V}^n_{c/n}. \tag{4.56}$$

Expanding (4.55) results in a 3-D CURRENT model that is more complete and different to that only given in (T. Fossen, 2012).

4.5.2 2-D Ocean Current and/or Wave

The 2-D irrotational CURRENT can be obtained from (4.55) when $\phi^n = \phi_c = \theta^n = \theta_c = 0$, which is:

$$u_c = V_x \cos(\psi_c - \psi^n) + V_y \sin(\psi_c - \psi^n) = V_h \cos(\psi_c - \psi^n), \tag{4.57}$$

$$v_c = V_x[c(\psi_c - \psi^n) - s(\psi_c - \psi^n)] + V_y[c(\psi_c - \psi^n) + s(\psi_c - \psi^n)] = V_h \sin(\psi_c - \psi^n), \tag{4.58}$$

where V_h is the horizontal intensity of the CURRENT given by:

$$V_h = \sqrt{u_c^2 + v_c^2} + \sqrt{V_x^2 + V_y^2}. \tag{4.59}$$

Note that this model of CURRENT is the same to that of (T. Fossen, 2012) only in 2-D, not in 3-D.

4.6 Summary

This Chapter has presented significant advances in relativity and expression of states of mobile systems and relative equations and angles of motion. It is established that signs of states ultimately depends on which reference frame they are expressed in. In particular in relative equations of motion, it is shown which reference frame the vehicle velocity relative to FLOW is expressed in, which leads to better formulation and understanding of the relationship of relativity. This was also achieved by improved modeling of the FLOW frame and creation of the CURRENT frame to describe the ocean CURRENT and/or WAVE velocities.

The angle of attack has been broken down into 2-D and 3-D representations for more accurate calculations of lift forces.

An analytic method derived by integration of Lyapunov stability and Newton's 1st Law has been devised to logically improve dynamic modeling of equations of motion by checking the stability of their origins in unforced conditions.

The concept of state relativity has been presented to describe the relativity of motion between two reference frames that are relative to each other. This has been applied together with Newton's 3rd Law to incorporate the CURRENT and/or WAVE disturbances in the relative equations of motion through the updated FLOW reference frame. This has mathematically shown that CURRENT and/or WAVE disturbances already exist in the relative equations of motion if vehicle velocities and accelerations relative to FLOW are used.

Newton's 3rd Law of Motion has been further explained using reference frames.

Proofs of passivity and boundedness of the relative equations of motion in 3-D including CURRENT and/or WAVE disturbances has been presented under the assumption of hydrostatic neutrality.

Finally, a more intuitive and complete model of irrotational ocean CURRENT and/or WAVE have been derived which includes definitions of CURRENT Euler angles in NED.

Chapter 5

2-D LOS Course Control with Speed Allocation

The LOS guidance has nice properties as mentioned earlier and is a widely-used technique for PF control of mobile systems (T. Fossen & Pettersen, 2014). The LOS course control for PF presented here focuses on the ELOS scheme in 2-D using the relative models developed in previous chapters for both the equations of motion and environmental disturbances. First, the the switching mechanism for ELOS guidance and the stability and linear analysis of horizontal LOS guidance laws in their ability to minimize the cross-track error are presented. Then, PF for cross-track course control in the horizontal plane using the modified ELOS guidance have been presented using both a nonlinear PID and SMC for fully and underactuated cases of sway DOF. Thanks to the relative models of the states, the *speed allocation* problem has been presented, which will also leads to control of the new relative velocity at the BODY level, and corresponding error states for stability analysis. Simulation results show the existence of relative state vectors for PF an AUV for waypoints consisting of straight-lines. A comparison between three popular guidance laws including the resulting new ELOS guidance are also provided at the end.

5.1 The Switching ELOS Guidance

As mentioned earlier, a fixed lookahead-distance $\triangle$ is not an optimal solution to path-following that a small $\triangle$ will achieve faster path convergence but may produce overshoot and oscillations, while a large $\triangle$ can eliminate these problems but results in slower path convergence. The trade-off that has been sought in the literature is provided naturally with the ELOS scheme, where it inherently employs a time-varying lookahead distance $\triangle$ which provides a perpendicular heading near the edge of the radius R and thus a faster path convergence, while changing the heading towards a path-parallel direction as the vehicle comes closer to the path, eliminating the overshoot and oscillation. This presents an inherent advantage of the ELOS scheme is that it provides a varying lookahead-distance $\triangle$, which is probably the reason why it performs better when the path-following involves curved paths (Sujit et al., 2014). However, the enclosing radius R of the ELOS scheme guidance is required to be larger than the cross-track error y_e to ensure solutions to the guidance law. If not, other guidance laws are required to guide the vehicle towards the path. This also presented an implementation issue of the ELOS scheme (Sujit et al., 2014). In waypoint-following scenarios, $R \geq R_k$, where R_k is radius of the circle of acceptance at k^th way-point. There were two past propositions to address this issue, and a switching mechanism has been designed and employed in this section.

5.1.1 Linearly and Exponentially Varying R

The ELOS scheme of the LOS guidance is rewritten here from Chapter 3 by replacing x, y with their expressions in terms of relativity x^n, y^n, which is:

$$(x_{los} - x^n)^2 + (y_{los} - y^n)^2 = R^2, \tag{5.1}$$

$$\frac{y_{los} - y_k}{x_{los} - x_k} = \frac{y_{k+1} - y_k}{x_{k+1} - x_k} = \tan \psi_p, \tag{5.2}$$

$$\psi_{los} = \psi_p + \text{atan2}\left(\frac{y_{los} - y^n}{x_{los} - x^n}\right) \tag{5.3}$$

The ELOS guidance is redrawn in Fig 5.1 with now using the notations of relativity.

The radius R is tuned accordingly as n times the ship length L_{pp} in practice. There were two propositions in the literature regarding the tuning of R to address this issue. Moreira et al. (2007) proposed to increase R linearly with y_e, while Khaled and Chalhoub (2013) proposed to increase it exponentially with y_e. The linear varying R is given by (Moreira et al., 2007):

$$(x_{los} - x^n)^2 + (y_{los} - y^n)^2 = R^2 = (L_{pp} + |y_e|), \tag{5.4}$$

The exponentially varying R is given by (Khaled & Chalhoub, 2013) as:

$$R = y_e + \sqrt{2} R'_{min} e^{-y_e x'_B} \tag{5.5}$$

$$R'_{min} = 2^{-0.5} R_{min} e^{2^{-0.5} b R_{min}} \tag{5.6}$$

$$x'_B = d^{-1} \left[lambertw(R'_{min} e^{-0.5\sqrt{2} d y_e}) + 0.5\sqrt{2} d y_e \right] \tag{5.7}$$

where the Lambert-W function is inverse of $f(x) = xe^x$, $R_{min} = nL_{pp}$, and d is the rate of decay for the exponential term.

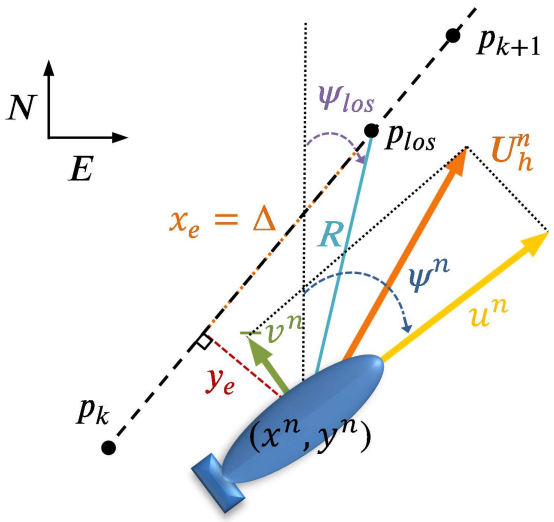

Figure 5.1: Geometry of LOS guidance for straight path.

The equations for exponentially varying scheme lead to $R \approx |y_e|$ for large $|y_e|$, creating

a circle tangent to the desired path. This results in a perpendicular path approaching angle for ψ_d, which is a natural strategy to pursue the shortest path between the current vehicle position and desired path. The exponential term dominated the value of R for small values of $|y_e|$, which ensured that R is increased at a lower rate compared to the linearly varying scheme ($R = R_{min} + |y_e|$). This can keep the value of R small at lower values of $|y_e|$, which, as mentioned earlier, provides a steeper angle for ψ_d that can significantly improve the path convergence rate of the vehicle Khaled and Chalhoub (2013). The exponentially varying scheme achieved a faster path convergence, but it can be seen that this is a rather complex solution.

5.1.2 The Switching Scheme for R

A simple and effective scheme is proposed for the ELOS guidance to tune R conditionally, where is given by:

$$R = \begin{cases} R_{min}, & \text{if } |y_e| \leq R_{min} \\ a|y_e|, & \text{if } |y_e| > R_{min} \end{cases} \tag{5.8}$$

where $a \geq 1$ is a tuning parameter which determines the path approaching strategy outside R_{min}, which also determines the norlmality of R to the path outside R_{min}. As can be seen, R is a function of y_e only when $|y_e| > R_{min}$, preventing y_e from entering the guidance law, which preserves the properties of ELOS inside R_{min}. This is not the case for both linearly or exponentially varying schemes where R is always a function of y_e. Equation (5.8) also guarantees the circle-path interceptions always exist since $a \geq 1$ gives $R \geq |y_e|$. Hence, The following two cases further explain (5.8).

Case 1: ($|y_e| < R_{min}$). The guidance is exactly as ELOS.

Case 2: ($|y_e| \geq R_{min}$). If $a = 1$, $R = |y_e|$. This implies that ψ_d is perpendicular to the path, corresponding to a shortest-path strategy. This is always guaranteed for ψ_d if $1 \leq a \approx 1$, with gives an enclosing circle tangent to the path.

The resulting ELOS guidance is referred as swithcing ELOS (SELOS).

Tuning R_{min}

R_{min} is chosen in a similar way as nL_{pp} and in general, smaller R_{min} is preferred which project shorter $\triangle$ and thus faster path convergence time. Particularly, the lower bound for R_{min} is not limited or affected by y_e as opposed the linearly or exponentially varying schemes. The ELOS guidance corresponds to the LLOS guidance by a time-varying $\triangle$ as shown earlier in (3.19):

$$R = \sqrt{{y_e}^2 + \triangle^2 - 2y_e\triangle\cos(\theta_R)}, \tag{5.9}$$

If $\triangle$ is too small, it corresponds to a large proportional action which results in an aggressive steering (T. Fossen, 2011), and this also applies to ELOS guidance. Nevertheless, the notion of aggressive steering described by (T. Fossen, 2011) is more applicable when both $\triangle$ and $|y_e|$ are small, which represents a case where the vehicle is very close to the path but the desired heading is still near perpendicular to it. In this case, if the aggressive steering required is not provided by the actuators, the vehicle may fly across the path without being able to turn towards an adequate $\triangle$ ahead if it is traveling at a sufficient forward speed. This can result in an oscillating behavior. On the other hand, if $\triangle$ is small but $|y_e|$ is large, the vehicle is far away from the path and a perpendicular desired heading is projected, which may not imply an aggressive steering but a shortest-path strategy. Therefore, a small $\triangle$ is desired when the vehicle is far away from the path to achieve the shortest-path strategy, and a larger $\triangle$ is desired when the vehicle is close to the path to avoid an aggressive steering. This is an intrinsic path following strategy provided by ELOS guidance: provision of a varying $\triangle$, which is achieved by both the exponentially varying and the switching-based schemes. As mentioned earlier, the steering required may become aggressive if the actuators cannot provide the required steering. Thus, the minimum allowable radius for R_{min} depends on vehicle actuators and can be a lower-saturated function of actuator constraints.

Outside R_{min}, the perpendicularity of the desired heading to the path can be changed

by adjusting a. The switching will not produce large jumps when it switches from R_{min} to $a|e_{yz}|$ if $a \approx 1$ since the vehicle heading is already perpendicular to path when it is about to leave the radius R_{min}. Thus, the switching action is only a change from a perpendicular heading to a near perpendicular heading due to $a \approx 1$. It is required to keep $a \approx 1$ if shortest-path strategy is desired outside R_{min}.

The Continuous SELOS

The switching action in (5.8) can be replaced with a continuous function to make it a continuous switch. This is achieved using a sigmoid function, which is:

$$R = R_{min} + \frac{1}{2}\left[\frac{(a|y_e| - R_{min})(|y_e| - R_{min})}{c + \big||y_e| - R_{min}\big|}\right], \tag{5.10}$$

where $1/c > 0$ is the slope of the sigmoid function at the origin. For $a \approx 1$ and $c \approx 0$, Eq. (5.10) becomes:

$$R = \begin{cases} R_{min}, & \text{if } |y_e| \leq R_{min} \\ a|y_e|, & \text{if } |y_e| > R_{min} \end{cases} \tag{5.11}$$

5.1.3 Comparison between Linearly Varying, Exponentially Varying, and Continuous SELOS

The evolution of R over $|y_e|$ is compared between the linearly varying, exponentially varying and switching schemes in (5.10). This is shown in Fig 5.2, where it shows how ψ_{los} is produced over the range of $|y_e|$. The gains are set as $R_{min} = 3, a = 1, d = 0.05$ and $c = 0.01$. It shows that SELOS reaches the $R = |y_e|$ slope representing the shortest-path as soon as $|y_e| > R_min$, while the exponentially varying scheme reaches it very slowly, producing less steep ψ_{los} and hence, slower path convergence. The linearly varying scheme does not reach the line $R = |y_e|$, and hence does not provide a shortest-path strategy (or ψ_{los} normal to the path).

It should be noted that higher values for d an improve the convergence rate of the

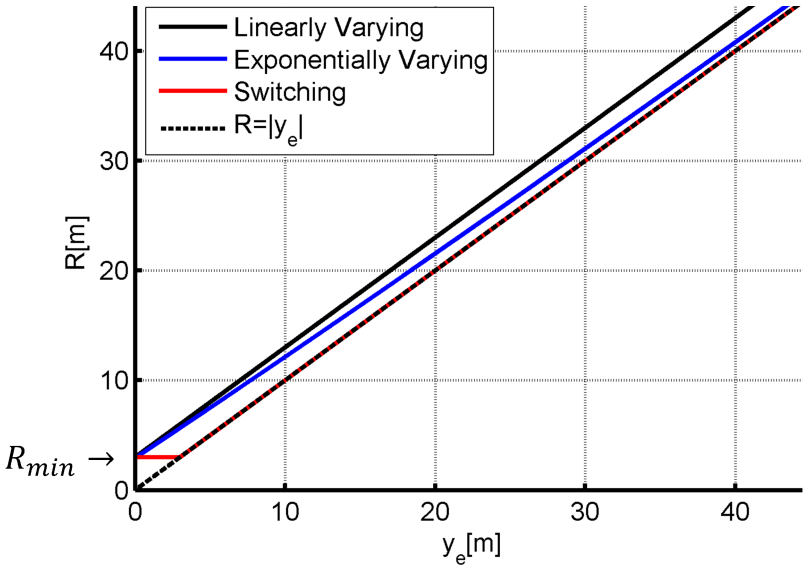

Figure 5.2: Evolution of R over $|y_e|$

exponentially varying scheme to the slope $R = |y_e|$, but this results in an initial R below R_{min}, which does not give a solution to the ELOS guidance equations. Therefore, the maximum value of d could only be set to 0.05, and thus the exponentially varying scheme is not an effective solution as well.

Thus, the SELOS scheme represents the following advantages over the other two past schemes:

- Simple and effective solution for the guidance for all values of y_e,
- Provision of perpendicular ψ_{los} to the path for heading as the shortest-path strategy as soon as $y_e > R_{min}$,
- Preserves the natural behavior of ELOS scheme within R_{min}, and
- Allows the tuning of R_{min} to be as small as possible for quicker path convergence without the risk of having no solution to the guidance when the cross-track error (or *off-track error* in 3-D) is larger than R_{min}.

5.2 Cross-Track Error Dynamics and Stability of LOS Guidance Laws

The ability of the LLOS and ELOS guidance laws with course control in stabilizing the cross-track error are given separately in this section because they can achieve different stability results. As mentioned earlier, the stability results of guidance laws are non-trivial and can be time-consuming due their analytic complexity. These results are also shown here to allow an analytic comparison between guidance laws.

5.2.1 Cross-Track Error Dynamics

Before deriving the cross-track error, the velocity errors are defined first. The horizontal 3-DOF kinematics for surge, sway and yaw are extracted from the explicit 6-DOF explicit relative kinematics (4.25), which is:

$$\dot{x}^n = u^n \cos\psi^n - v^n \sin\psi^n, \tag{5.12}$$

$$\dot{y}^n = u^n \sin\psi^n + v^n \cos\psi^n, \tag{5.13}$$

$$\dot{\psi}^n = r^n. \tag{5.14}$$

when $w^n = \phi^n = \theta^n = 0$. The relationship of relativity from previous Chapter is given by:

$$\boldsymbol{\nu}^f_{b/f} = \boldsymbol{\nu}^b_{b/n} - \boldsymbol{\nu}^b_{c/n}. \tag{5.15}$$

It can be seen that there are two relative velocity vectors at the BODY level that are to be controlled, $\boldsymbol{\nu}^b_{b/n}$ and $\boldsymbol{\nu}^f_{b/f}$. The natural choice is to control the BODY velocity relative to NED, $\boldsymbol{\nu}^b_{b/n}$, and not to FLOW. The errors states in surge, sway and yaw that are relative

to NED and expressed in BODY are defined as:

$$\tilde{u} = u_d^n - u^n, \tag{5.16}$$

$$\tilde{v} = v_d^n - v^n, \tag{5.17}$$

$$\tilde{\psi} = \psi_d - \psi^n, \tag{5.18}$$

where u_d^n and v_d^n are the desired BODY velocities relative to NED to be designed that requires a speed allocation technique, which is presented later in this Chapter. The dynamic task of the maneuvering problem now requires these errors in speed to converge to zero, while the geometric task will require the cross-track error y_e to converge to zero so that the vehicle is on the path.

In course control as referred in this thesis, the desired heading incorporates sideslip angle β^n in the desired heading angle that is given by the guidance law. In this case, the desired heading for SELOS course control is given by (A. Lekkas & Fossen, 2013; T. Fossen & Pettersen, 2014):

$$\psi_d = \psi_{los} - \beta^n, \tag{5.19}$$

where ψ_{los} is given by the chosen LOS guidance laws.

The cross-track error dynamics $\dot{y}_e$ is commonly given by placing the center of NED on the vehicle projection point x_p, y_p, z_p on the path and aligning North as the direction of the path so that $\dot{y}$ becomes $\dot{y}_e$ and that the path Euler angles relative to and expressed in NED $\phi_p = \theta_p = \psi_p = 0$. In this case, the cross-track error dynamics $\dot{y}_e$ can be described by replacing $\dot{y}^n$ in kinematics (5.13) with $\dot{y}_e$ and using the new expressions for error from (5.16)-(5.18), which is:

$$\dot{y}_e = u^n \sin\psi_d - v^n \cos\psi_d, \tag{5.20}$$

when $\tilde{u} = \tilde{v} = \tilde{\psi} = 0$. This can be written in phase-amplitude form as:

$$\begin{aligned} \dot{y}_e &= \sqrt{u^{n2} + v^{n2}} \sin\left[\psi_d + \tan^{-1}\left(\frac{v^n}{u^n}\right)\right] \\ &= \sqrt{u^{n2} + v^{n2}} \sin\left[\psi_{los} - \beta^n + \tan^{-1}\left(\frac{v^n}{u^n}\right)\right], \end{aligned} \tag{5.21}$$

using (5.19). This is also rewritten by defining the desired horizontal speed in NED $U_h^n = \sqrt{u^{n2} + v^{n2}}$, which is:

$$\dot{y}_e = U_h^n \sin\left[\psi_d + \tan^{-1}\left(\frac{v^n}{u^n}\right)\right] = U_h^n \sin\left[\psi_{los} - \beta^n + \tan^{-1}\left(\frac{v^n}{u^n}\right)\right]. \tag{5.22}$$

5.2.2 Stability of Horizontal LLOS Guidance Law at Constant Lookahead Distance

The LOS angle of LLOS guidance is given by:

$$\psi_{los} = \tan^{-1}\left(\frac{-y_e}{\triangle}\right) \tag{5.23}$$

where the path heading $\psi_p = 0$ when it is aligned with North axis of NED. The sideslip angle in NED is given by:

$$\beta^n = \text{atan2}\left(\frac{v^n}{u^n}\right) = \sin^{-1}\left(\frac{v^n}{U_h^n}\right). \tag{5.24}$$

Now substituting ψ_{los} and β^n in (5.23)-(5.24) into (5.22) yields the cross-track error for LLOS guidance law as:

$$\dot{y}_e = U_h^n \sin\left[\tan^{-1}\left(\frac{-y_e}{\triangle}\right)\right] = -\frac{U_h^n}{\sqrt{\triangle^2 + {y_e}^2}} y_e. \tag{5.25}$$

where the trigonometric identity $\sin(\tan^{-1}(x)) = x/\sqrt{1+x^2}$ is used.

Theorem 5.1 *(Horizontal LLOS Guidance Law with Constant Lookahead Distance) The horizontal LLOS guidance law* (5.23) *with sideslip* (5.24) *renders the origin* $y_e = 0$ *of*

the cross-track error dynamics (5.25) *SGES if* U_h^n *and* $\triangle$ *satisfy* $0 < U_{hmin}^n < U_h^n < U_{hmax}^n$ *and* $0 < \triangle_{min} < \triangle < \triangle_{max}$ *are constant, and the desired heading angle* ψ_d *is perfectly tracked such that* $\tilde{\psi} = 0$.

Proof. The proof is given by (T. Fossen & Pettersen, 2014, Theorem 1). The definition of USGES in the proof is obtained from (Loria & Panteley, 2004, Definition 2.7). □

Theorem 5.1 implies that the cross-track error $y_e \to 0$ exponentially as $t \to 0$. This satisfies the geometric task such that the vehicle is on the path.

Remark 5.1 Note that one of the distinctions in this thesis in stability analysis also include the fact that the cross-track error dynamics for guidance laws have different formulas for straight and curved paths, except for LLOS guidance. The stability result of the LLOS guidance also holds for curved paths since the same guidance law is used for all types of path. In addition, the fact that the vehicle speed U_h^n and tuning parameters such as the lookahead distance have to be constant to provide the cross-track error dynamics (5.25) is made clear in this thesis, since non-constant speed and tuning parameters will produce different cross-track error dynamics.

Remark 5.2 GES for this class of guidance laws are not achievable due to the structural properties of (5.25) since the sinusoidal function produces saturation, which results in system gain in (5.25) to decrease with the increasing y_e. Thus, the global exponential convergence cannot be provided uniformly (T. Fossen & Pettersen, 2014). SGES offers stronger robustness properties compared to global κ-exponential stability (T. Fossen & Pettersen, 2014), the proof of which is provided in (A. Lekkas & Fossen, 2013). Aside from being slightly stronger than the global $\varkappa$-exponential stability (UGAS + ULES) as first shown by (Pettersen & Lefeber, 2001) and then in (A. Lekkas & Fossen, 2013), SGES is important in terms of robustness against perturbations, which are analyzed by (Pettersen, 2017).

Remark 5.3 Note that even in non-course control, i.e. w/o sideslip angle in ψ_d, the cross-track error dynamics will remain the same if they are derived using the common steps as in Section 5.2.1. So the stability results in the literature without sideslip are also

valid.

Remark 5.4 It is common to incorporate underactuated dynamics of sway v^n in the stability analysis as in (Wigg et al., 2016; Caharija et al., 2016). However, when total speed U_h^n is considered in the stability analysis, this is not necessary since underactuation does not change the condition of U_h^n in the stability analysis.

5.2.3 Stability of Horizontal ELOS Guidance with Constant R

The stability of ELOS guidance law is provided in this section, where it is are also treated separately for straight and curved paths.

ELOS Guidance: Straight Path

In straight-line path-following as shown in Fig. 5.1, the relationship between R, y_e and $\triangle$ is a Pythagoras, and the LOS vector R is also given by (5.9):

$$LOS = R = \sqrt{{y_e}^2 + \triangle^2 - 2y_e\triangle\cos\theta_R} = \sqrt{{y_e}^2 + \triangle^2}, \tag{5.26}$$

when $\theta_R = \pm\pi/2$ when the segment of the path between p_{los} and $(x_p(\mu), y_p(\mu))$ is straight, i.e. when the along-track error x_e is a straight line. Substituting (5.26) into (5.25) gives the cross-track error dynamics for ELOS in straight-line PF as:

$$\dot{y}_e = -\frac{U_h^n}{R} y_e. \tag{5.27}$$

Theorem 5.2 *(Horizontal ELOS Guidance Law for Straight Path and Constant LOS Vector) The horizontal ELOS guidance law given by* (5.3) *with sideslip* (5.24) *renders the origin* $y_e = 0$ *of the cross-track error dynamics* (5.27) *LES if* U_h *and* R *are constants and satisfy* $0 < U_h^n$ *and* $0 < y_e \leq R$*, and that* ψ_d *is tracked such that* $\tilde{\psi} = 0$.

Proof. The cross-track dynamics (5.27) is not time-varying since it does not explicitly depend on time and can be completely described by its states as in the general form $\dot{x} = f(x(t))$ for autonomous systems in (Khalil, 2002), and not in the form $\dot{x} = f(t,x)$ for

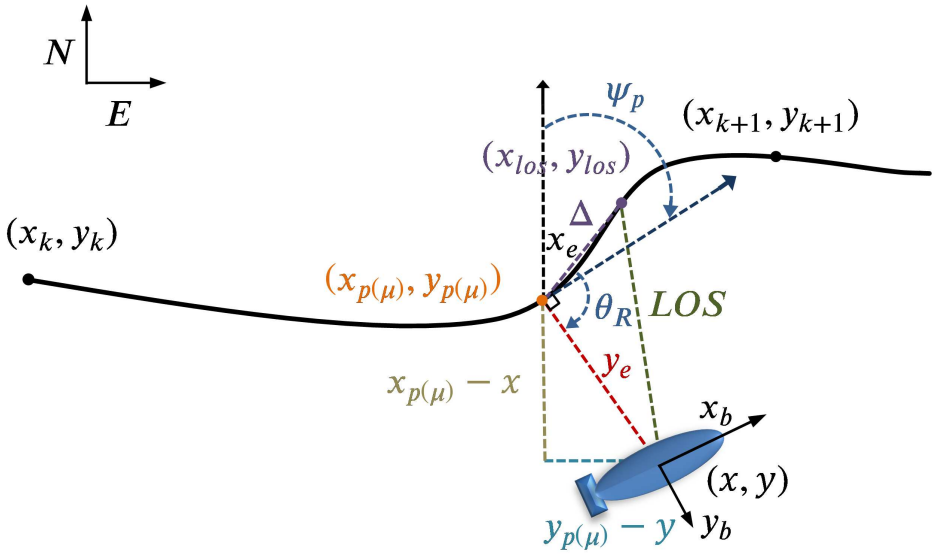

Figure 5.3: Geometry of a PF problem with *path-tangential angle* γ_p and the cross-track error y_e. $p_{los} = (x_{los}, y_{los})$ is the LOS reference point on the path creating the LOS vector from the vehicle to it and $\triangle$ the user-defined *lookahead distance*.

the definition of non-autonomous systems. Note that this is true only when U_h^n is constant such that the system dynamics is the same for all $0 < t < T$, where T could be infinity. See e.g. the mass-spring system in (Khalil, 2002) is autonomous, which is a common analogy to the dynamics of mobile robots. Thus, marine vehicle systems in this thesis are autonomous systems. Stability of the cross-track error dynamics (5.27) is analyzed using the time-derivative of LFC $V_{y_e} \triangleq (1/2)y_e^2$, which is:

$$\dot{V}_{y_e} = -\frac{U_h^n}{R} y_e^2 \leq -k_3 y_e^2 \leq 0. \tag{5.28}$$

on the ball $B_r = \{y_e \in \mathbb{R} | y_e \leq R\}$ with $0 < k_3 < U_h^n/R$. Since $U_h^n, R > 0$ are constant, and $\dot{V}_{y_e}$ is negative definite, the origin $y_e = 0$ of Eq. (5.27) is LES. The stability of ELOS guidance law cannot be global since $y_e \leq R$ is required for real solutions. □

ELOS Guidance: Curved Path

SGES for the cross-track error dynamics (5.27) of ELOS can be shown when the path is curved. This is because the expression of R as in (5.26) is not a right-angled triangle, and which will produce a different dynamics for (5.27). This can be seen from the difference

between $\triangle$ and x_e, i.e. $\triangle \neq x_e$ as reshown in Fig 5.3, which is a copy of Fig 3.1. When following a curved-path, $\theta_R \neq \pm\pi/2$ in (5.26), and thus R is given by:

$$R^2 = {y_e}^2 + \triangle^2 - 2y_e\triangle\cos\theta_R. \tag{5.29}$$

Substituting (5.29) into (5.25) gives the cross-track error dynamics for ELOS in curved path as:

$$\dot{y}_e = -\frac{U_h^n}{\sqrt{R^2 + 2y_e\triangle\cos\theta_R}}y_e. \tag{5.30}$$

Since the path is not a straight-line, R will not be constant and the condition $R \geq y_e$ for existence of circle-path interception for ELOS is not required. New condition for R can be imposed based on the geometry of the path.

Theorem 5.3 *(Horizontal ELOS Guidance Law for Curved Path) The horizontal ELOS guidance law given by* (5.3) *with sideslip* (5.24) *renders the origin* $y_e = 0$ *of the cross-track error dynamics* (5.30) *SGES if* $U_h^n, \triangle$ *are constant and along with R satisfy* $0 < U_{hmin}^n \leq U_h^n$ *and* $0 < R \leq R_{max}$, $\triangle > 0$, *and that* ψ_d *is perfectly tracked such that* $\tilde{\psi} = 0$.

Proof. The proof is similar to the approach in ((T. Fossen & Pettersen, 2014; Pettersen, 2017)), albeit the system is autonomous here. Stability of the system (5.30) is analyzed using the time-derivative of LFC $V_{y_e} \triangleq (1/2)y_e^2$, which is:

$$\dot{V}_{y_e} = -\frac{U_h^n}{\sqrt{R^2 + 2y_e\triangle\cos\theta_R}}y_e^2 \leq -2b(r_e)V_{y_e} \leq 0. \tag{5.31}$$

for each $r_e > 0$, all $|y_e(t)| < r_e$, and $b(r_e)$ given by:

$$b(r_e) \triangleq \frac{U_{hmin}^n}{\sqrt{R_{max}^2 + 2r_e\triangle\cos\theta_R}}, \tag{5.32}$$

First part of (5.31) means $|y_e(t)| \leq y_{e_0}$ for all $t \geq 0$. By invoking the the comparison lemma (Khalil, 2002, Lemma 3.4), the second part of (5.31) implies $y_e(t) \leq e^{-2b(r_e)}y_{e_0}$, for all $t \geq 0$. Thus, (5.31) implies that $y_e(t) \leq e^{-b(r_e)}y_{e_0}$ for $\forall t > 0$ and $y_{e_0} = y_e(0)$. Therefore, the origin $y_e = 0$ is a SGES equilibrium point of (5.30) (Loria & Panteley,

2004, Definition 2.7). □

Note that for curved paths, the ELOS guidance requires that the curvature of the path to be less than that of the enclosing circle with radius R so that there are only two maximum sets of intersection points p_{los}, and the point that is in forward direction of the path is chosen. This is because there could be more than two solutions for the guidance law when the curvature of the path is equal to or less than that of the enclosing circle. This condition on path curvature is similar to the one presented for general PF problem where the solution to the cross-track error has to be unique.

5.2.4 Stability of Horizontal SELOS Guidance Law

The stability analysis of ELOS guidance presented above stands for the SELOS guidance only when $|y_e| < R_{min}$ so that R is constant during path-following. When $y_e > R$, the SELOS is activated, and in this case, R is not a constant and thus the dynamics of the cross-track error is different. Thus, the stability analysis of the SELOS guidance is also shown here for straight and curved paths.

Straight Path

The ELOS guidance in (5.1)-(5.3) can be rewritten as SELOS guidance by equating (5.1) and (5.10), which is:

$$R^2 = (x_{los} - x^n)^2 + (y_{los} - y^n)^2 \tag{5.33}$$

$$\frac{y_{los} - y_k}{x_{los} - x_k} = \frac{y_{k+1} - y_k}{x_{k+1} - x_k} = \tan \psi_p, \tag{5.34}$$

$$\psi_{los} = \tan \psi_p + \text{atan2}\left(\frac{y_{los} - y^n}{x_{los} - x^n}\right) \tag{5.35}$$

$$R = R_{min} + \frac{1}{2}\left[\frac{(ay_e - R_{min})(y_e - R_{min})}{c + |y_e - R_{min}|}\right], \tag{5.36}$$

When $c \approx 0$ and $a \approx 1$, R in (5.36) becomes:

$$R \approx y_e. \tag{5.37}$$

In straight-line path-following, $R = \sqrt{y_e{}^2 + \triangle^2} \approx y_e$. Substituting this into the cross-track error dynamics (5.27) gives the cross-track error for SELOS straight-line PF as:

$$\dot{y}_e = -\frac{U_h^n}{y_e} y_e = -U_h^n. \tag{5.38}$$

Theorem 5.4 *(Horizontal SELOS guidance law for straight-path) The horizontal SELOS guidance law and the sideslip given by* (5.33)-(5.36) *and* (5.24) *renders the origin* $y_e = 0$ *of the cross-track error dynamics* (5.38) *SGES if* U_h^n *and* c *satisfy* $0 < U_{hmin}^n < U_h$ *and* $0 < c \leq c_{max}$*, and* ψ_d *is tracked such that* $\tilde{\psi} = 0$.

Proof. The proof is similar to that of the previous theorem, and stability of the system (5.38) is analyzed using the time-derivative of LFC $V_{y_e} \triangleq (1/2)y_e^2$, which is:

$$\dot{V}_{y_e} = -\frac{U_h^n y_e^2}{\sqrt{c^2 + y_e^2}} \leq -2b(r_e)V_{y_e} \leq 0. \tag{5.39}$$

for each $r_e > 0$, all $|y_e(t)| < r_e$, and $b(r_e)$ given by:

$$b(r_e) \triangleq \frac{U_{hmin}^n}{\sqrt{c_{max}^2 + r_e^2}}, \tag{5.40}$$

First part of (5.39) means $|y_e(t)| \leq y_{e_0}$ for all $t \geq 0$. By invoking the the comparison lemma (Khalil, 2002, Lemma 3.4), the second part of (5.39) implies $y_e(t) \leq e^{-2b(r_e)} y_{e_0}$, for all $t \geq 0$. Thus, (5.39) implies that $y_e(t) \leq e^{-b(r_e)} y_{e_0}$ for $\forall t > 0$ and $y_{e_0} = y_e(0)$. Therefore, the origin $y_e = 0$ is a SGES equilibrium point of (5.38) (Loria & Panteley, 2004, Definition 2.7). □

Curved Path

The dynamics of the cross-track error for SELOS is can be obtained by substituting R in (5.41) into (5.30), which is given by:

$$\dot{y}_e = -\frac{U_h^n}{\sqrt{y_e^2 + 2y_e\triangle\cos\theta_R}}y_e = -\frac{U_h^n}{\sqrt{R^2 + 2y_e\triangle\cos\theta_R}}y_e. \tag{5.41}$$

when $c \approx 0$ and $a \approx 1$, and since $R \approx y_e$ in SELOS.

Theorem 5.5 *(Horizontal SELOS guidance law for curved path) The horizontal SELOS guidance law with sideslip given by* (5.37)-(5.40) *and* (5.23) *renders the origin* $y_e = 0$ *of cross-track error dynamics* (5.41) *SGES if* U_h^n *and* R *satisfy* $0 < U_h^n, 0 < R_{min} < y_e < R \leq R_{max}$, *and* ψ_d *is tracked such that* $\tilde{\psi} = 0$.

Proof. The proof is similar to that of Theorem 5.3 and, thus, is given in Appendix B.

5.3 Linear Analysis of LOS Guidance Laws

One of the conventional methods to analyse the performance of the guidance laws is by assessing its sensitity against disturbances, which is done by linearizing them at an equillibrium and injecting disturbacnes on the linearized system. A similar anlaysis for VF and ILOS guidance laws has been reported in Caharija et al. (2015) for small time-varying ocean current disturbances. For ELOS guidance, this was done in (Park et al., 2007) but only for a small desired heading angles. The linear analysis is carried out for LLOS and ELOS guidance laws in this section since the improved relative equations of motion can better incorporate such disturbance as well. The input/output 2nd-order linear transfer function of the ELOS guidance law was also obtained to assess its linear dynamics in lateral motion with constant LOS rate.

5.3.1 LLOS Guidance Law at Equilibrium with Constant Lookahead Distance

The cross-track error dynamics for LLOS course control is given by (5.25) as:

$$\dot{y}_e = U_h^n \sin\left[\tan^{-1}\left(\frac{-y_e}{\triangle}\right)\right] = U_h^n \sin\psi_{los}. \tag{5.42}$$

At the equilibrium $y_e = 0$, and thus the vehicle is very close to the path. In this case, $\sin\psi_{los} \approx \psi_{los}$ when ψ_p is zero. Then the above becomes:

$$\dot{y}_e = U_h^n \psi_{los}. \tag{5.43}$$

Taking the partial derivative of this for constant $\triangle$ and time-varying U_h^n yields:

$$\ddot{y}_e = \dot{U}_h^n \psi_{los} - U_h^n \frac{\dot{y}_e \triangle}{\triangle^2 + y_e^2}. \tag{5.44}$$

It can be seen that this second-order dynamics of LLOS is highly nonlinear. Linearising this at $y_e = 0$ keeping rest of the variables as constants yields:

$$\ddot{y}_e = \dot{U}_h^n \psi_{los} - U_h^n \frac{\dot{y}_e}{\triangle}. \tag{5.45}$$

For small y_e, $\psi_{los} \approx y_e$. In this case, (5.45) becomes:

$$\ddot{y}_e = \dot{U}_h^n y_e - U_h^n \frac{\dot{y}_e}{\triangle}. \tag{5.46}$$

When the North axis is aligned with Path x-axis, $y_e = y_{los} - y^n$ as shown in Fig 5.4. In this case, (5.44) is rewritten as:

$$\ddot{y}_{los} - \ddot{y}^n = \dot{U}_h^n (y_{los} - y^n) - (U_h^n / \triangle)(\dot{y}_{los} - \dot{y}^n). \tag{5.47}$$

When following a straight-line, the constant lateral input y_{los} resembles a step response of a linear system as in Fig 5.4 such that the vertical reference y_{los} is constant, and thus, $\dot{y}_{los} = \ddot{y}_{los} = 0$. Therefore, (5.47) becomes:

$$\dddot{y}^n - (U_h^n/\triangle)\ddot{y}^n + \dot{U}_h^n \dot{y}^n = \dot{U}_h^n y_{los}. \tag{5.48}$$

Taking the Laplace transform of both sides gives the input/output transfer function as:

$$\frac{y^n(s)}{y_{los}(s)} = \frac{\dot{U}_h^n}{s^2 - (U_h^n/\triangle)s + \dot{U}_h^n}. \tag{5.49}$$

The negative sign in front of $\frac{U_h^n}{\triangle}$ can be reverted to positive since it is dependent on which reference frame the y_e and the velocity vectors are expressed in as made clear in previous Chapter. This system is always stable when the vehicle speed U_h^n is converging towards the path. Thus,

$$\frac{y^n(s)}{y_{los}(s)} = \frac{\dot{U}_h^n}{s^2 + (U_h^n/\triangle)s + \dot{U}_h^n} = \frac{\omega_n^2}{s^2 + 2\zeta\omega_n s + \omega_n^2}. \tag{5.50}$$

which represents a second-order low-pass linear system with natural frequency $\omega_n = \sqrt{\dot{U}_h^n}$ and damping ratio $\zeta = U_h^n/(2R\sqrt{\dot{U}_h^n})$. Fig 5.4 also shows that the vehicle particle heading is eventually aligned with LOS angle for general path convergence.

The relativity relationship can be extended to the total speeds of the vehicle to show that:

$$U_h^n = U_h^f + V_h \tag{5.51}$$

It can now be seen that the ocean CURRENT disturbance already exist in the system (5.50) through V_h in (5.51), and thus it is not required to inject and superimpose any flow-dependent disturbances in (5.50) as was done in (Caharija et al., 2015). Since V_h can also represent CURRENT and/or WAVE intensity due to the FLOW frame, and and the rela-

tionship of relativity, additional disturbances superimposed to (5.50) can only represent external non-flow disturbances such as rigid-body collision.

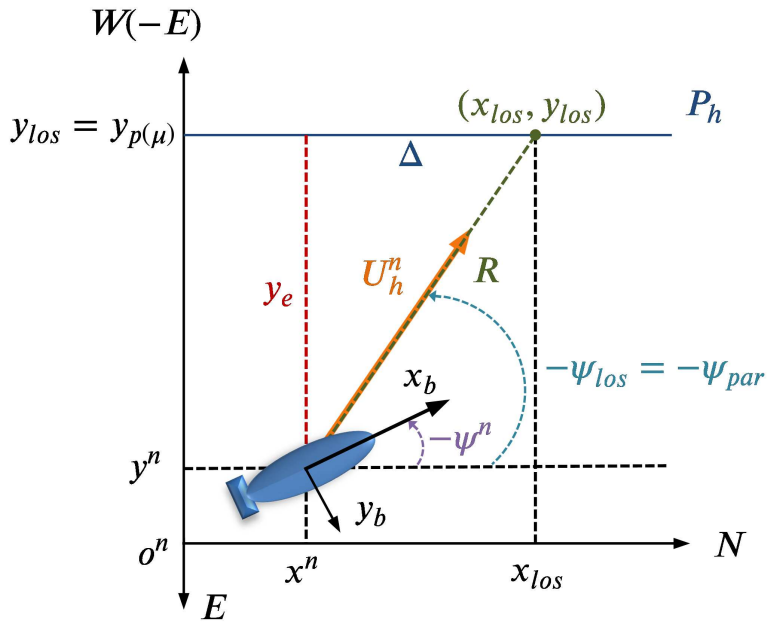

Figure 5.4: Geometry of LOS guidance with $\psi_p = 0$, and W=West=-East (E).

5.3.2 ELOS Guidance at Equilibrium

The ELOS guidance can also be linearised at the equilibrium, but without the small desired angle or small cross-track error assumptions as assumed in (Park et al., 2007) and as in the previous section for the case of LLOS guidance, respectively. The linear analysis is also be separated into straight and curved paths cases.

Linearized ELOS: Straight Path with Constant LOS Rate

Substituting the ELOS angle (5.35) with $\gamma_p = 0$ into (5.42) gives the cross-track error dynamics for ELOS guidance as:

$$\dot{y}_e = U_h^n \sin\left\{\tan^{-1}\left(\frac{y_{los} - y^n}{x_{los} - x^n}\right)\right\} \tag{5.52}$$

$$\dot{y}_e = U_h^n \frac{y_{los} - y^n}{\sqrt{(x_{los} - x^n)^2 + (y_{los} - y^n)^2}} = \frac{U_h^n (y_{los} - y^n)}{R}, \tag{5.53}$$

by using R in (5.33). Taking the partial derivative of (5.53) with constant R and time-varying U_h^n gives the second-order dynamics as:

$$\ddot{y}_e = \frac{\dot{U}_h^n(y_{los} - y^n) + U_h^n(\dot{y}_{los} - \dot{y}^n)}{R}. \tag{5.54}$$

Substituting $y_e = y_{los} - y^n$ and $\dot{y}_{los} = \ddot{y}_{los} = 0$ into (5.54) for a straight-line PF gives:

$$-\ddot{y}^n = \frac{\dot{U}_h^n(y_{los} - y^n) - U_h^n(\dot{y}^n)}{R}. \tag{5.55}$$

$$-\ddot{y}^n R + U_h^n \dot{y}^n + \dot{U}_h^n y^n = \dot{U}_h^n y_{los}. \tag{5.56}$$

Taking the Laplace transform and rearranging the above gives the input/output transfer function as:

$$\frac{y^n(s)}{y_{los}(s)} = \frac{\dot{U}_h^n}{-Rs^2 + U_h^n s + \dot{U}_h^n} = \frac{-\dot{U}_h^n/R}{s^2 - (U_h^n/R)s - \dot{U}_h^n/R}. \tag{5.57}$$

Since we know that the vehicle will only converge to the path when the velocity is opposite to the axes of the P-frame, the system (5.57) is stable and the sign of U_h^n depends on which reference frame it is being expressed in and is similarly reverted to give:

$$\frac{y^n(s)}{y_{los}(s)} = \frac{\dot{U}_h^n/R}{s^2 + (U_h^n/R)s + \dot{U}_h^n/R} = \frac{\omega_n^2}{s^2 + 2\zeta\omega_n s + \omega_n^2}. \tag{5.58}$$

which represents a second-order low-pass linear system with natural frequency $\omega_n = \sqrt{\dot{U}_h^n/R}$ and damping ratio $\zeta = U_h^n/(2R\sqrt{\dot{U}_h^n/R})$.

It can be seen that the natural frequency of ELOS depends on the tuning variable R, while this is not the case for the linearized LLOS guidance in (5.50). Both linearized systems are of second order damped system that they also incorporate ocean CURRENT and/or WAVE disturbances compared to existing results. However, the linear LLOS guidance is linearized at $y_e \approx 0$, while the linear ELOS guidance is representative at all $y_e < R$. This means that the LLOS guidance is more nonlinear due to varying R than ELOS guid-

ance, while R is constant in ELOS.

As an example, the traditional step response of the system now can be visualized for given simulation values for the three variables. In this case, they are set as: $\dot{U}_h^n = 1m/s^2, U_h^n = 1.4$ and $R = 1$ and the magnitude of the step input is set as $y_e = 1$ to achieve the desirable damping ratio 0.7. These values give the following transfer function:

$$\frac{y^n(s)}{y_{los}(s)} = \frac{1}{s^2 + 0.7s + 1}. \tag{5.59}$$

The step response of $y_e = 1$ is shown in Fig. 5.5. It can be seen that there is a slight overshoot of about 33% and the settling time is around $10s$.

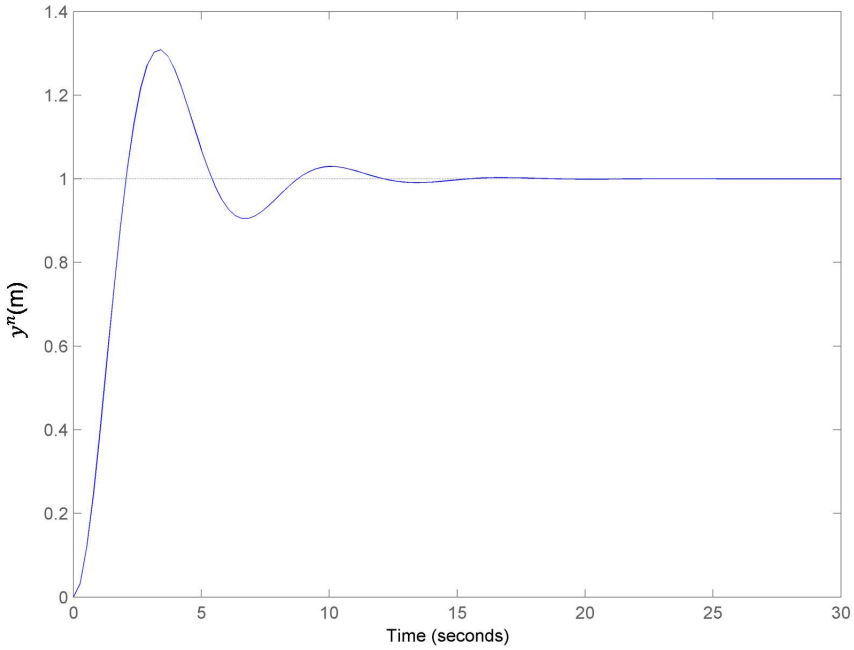

Figure 5.5: Step Response of ELOS for straight-line and at constant LOS rate

Linearized ELOS: Curved Path

When following a curved path, not only that R becomes time-varying, the LOS target position as input y_{los} becomes time-varying such that $\dot{y}_{los}$ and $\ddot{y}_{los}$ are nonzero in (5.54).

Taking the partial derivative of (5.53) with time-varying R and U_h^n and y_{los} gives:

$$\ddot{y}_e = \frac{RU_h^n(\dot{y}_{los} - \dot{y}^n) - \dot{R}U_h^n(y_{los} - y^n) - R\dot{U}_h^n(y_{los} - y^n)}{R^2}. \tag{5.60}$$

Substituting $y_e = y_{los} - y^n$ into this gives:

$$\ddot{y}^n - (U_h^n/R)\dot{y}^n - (\dot{U}_h^n/R)y^n = \ddot{y}_{los} - (U_h^n/R)\dot{y}_{los} - (\dot{U}_h^n R - U_h^n\dot{R})y_{los}/R. \tag{5.61}$$

Taking the Laplace transform of this and rearranging gives the input/output transfer function of ELOS for curved path as:

$$\frac{y^n(s)}{y_{los}(s)} = \frac{s^2 - (U_h^n/R)s - (\dot{U}_h^n R - U_h^n\dot{R})/R}{s^2 - (U_h^n/R)s - (\dot{U}_h^n/R)}. \tag{5.62}$$

Reverting the signs of the vectors for the same reasons as in previous cases gives:

$$\frac{y^n(s)}{y_{los}(s)} = \frac{s^2 + (U_h^n/R)s + (\dot{U}_h^n R + U_h^n\dot{R})/R}{s^2 + (U_h^n/R)s + (\dot{U}_h^n/R)}. \tag{5.63}$$

Unlike in the case of LLOS and the straight-path ELOS, this is not an all-pole second-order spring-damper system.

Remark 5.5 As for the linear analysis of SELOS guidance, it is only activated when $y_e > R$ and since R is usually tuned to around an equal length of the vehicle, the SELOS is only activated when the vehicle is not at the equilibrium. SELOS guidance always switches to ELOS when it is close to the path, i.e. when the vehicle is around $y_e = 0$, and thus, its linear analysis around $y_e = 0$ is the same as those of the ELOS guidance.

5.4 SELOS Course Control with Speed Allocation of Underactuated UVs

The course control problem is solved using the revised relative equations of motion and the SELOS guidance scheme with speed allocation for the sway underactuated UVs. The PF control problem considers UVs subject to ocean CURRENT and/or WAVE disturbances and measurement noises for straight-line. The sway-unactuated case is considered first since most of the existing AUVs are torpedo-shaped and thus underactuated since this provides energy efficiency and robustness through general design simplicity (Caharija et al., 2012). A SMC is designed first for surge and yaw DOFs mainly due to nonlinearities of the vehicle dynamics and the robustness of SMC against model uncertainties. The common PID control is then applied directly to the nonlinear systems to allow a comparison with the SMC.

5.4.1 System Model

The horizontal 3-DOF system model is reduced from the revised 6-DOF relative kinematics and relationship of relativity in (4.5) and (4.4), and the relative equations of motion (4.51) by setting the states $w^n = p^n = q^n = \phi^n = \theta^n = 0$, which is:

$$\dot{\boldsymbol{\eta}}^n_{b/n} = \boldsymbol{J}(\boldsymbol{\Theta}^n_{b/n})\boldsymbol{\nu}^b_{b/n}, \tag{5.64}$$

$$\boldsymbol{\nu}^f_{b/f} = \boldsymbol{\nu}^b_{b/n} - \boldsymbol{\nu}^b_{c/n}, \tag{5.65}$$

$$\boldsymbol{M}\dot{\boldsymbol{\nu}}^f_{b/f} + \boldsymbol{C}(\boldsymbol{\nu}^f_{b/f})\boldsymbol{\nu}^f_{b/f} + \boldsymbol{D}(\boldsymbol{\nu}^f_{b/f})\boldsymbol{\nu}^f_{b/f} + \boldsymbol{g}(\boldsymbol{\eta}^n_{b/n}) = \boldsymbol{B}\boldsymbol{f}. \tag{5.66}$$

where $\dot{\boldsymbol{\eta}}^n_{b/n} = [\dot{x}^n, \dot{y}^n, \dot{\psi}^n]$, $\boldsymbol{\nu}^b_{b/n} = [u^n, v^n, r^n]$, $\boldsymbol{\nu}^f_{b/f} = [u^f, v^f, r^f]$, and $\dot{\boldsymbol{\nu}}^f_{b/f} = [\dot{u}^f, \dot{v}^f, \dot{r}^f]$. The 2-D ocean CURRENT is irrotational and constant in NED, and hence, $\dot{V}_h = V_r = r_c = 0$ and from (4.57)-(4.58):

$$\boldsymbol{\nu}^n_{c/n} = [u_c, v_c, r_c]^T = [V_h \cos(\psi_c - \psi^n), V_h \sin(\psi_c - \psi^n), 0]. \tag{5.67}$$

The dynamics of the CURRENT expressed in BODY is obtained by time-differentiating (5.67) as:

$$\dot{\boldsymbol{\nu}}^n_{c/n} = [\dot{u}_c, \dot{v}_c, \dot{r}_c]^T = [-r^n v_c, r^n u_c, 0]^T \tag{5.68}$$

The vector $\boldsymbol{g}(\boldsymbol{\eta}^n_{b/n}) = 0$ and the control input vector $\boldsymbol{M}^{-1}\boldsymbol{B}\boldsymbol{f} = [\tau_u, 0, \tau_\psi]$ consists of the surge force and yaw moment, where $\boldsymbol{B} \in \mathbb{R}^3 \times 2$ is the actuator configuration matrix and $\boldsymbol{f} \in \mathbb{R}^2$ is the control input vector. This structure of the control input vector is obtained by assuming that CO of BODY is positioned in the pivot point such that yaw moment has no effect on sway motion (Fredriksen & Pettersen, 2006). The system in (5.66) is underactuated since the dimension of $\boldsymbol{f}$ is less than that of the system. Expanding (5.64) gives the relative kinematics as:

$$\dot{x}^n = u^n \cos\psi^n - v^n \sin\psi^n, \tag{5.69}$$

$$\dot{y}^n = u^n \sin\psi^n + v^n \cos\psi^n, \tag{5.70}$$

$$\dot{\psi}^n = r^n. \tag{5.71}$$

The system matrices take the following structure:

$$\boldsymbol{M} \triangleq \begin{bmatrix} m_{11} & 0 & 0 \\ 0 & m_{22} & m_{23} \\ 0 & m_{23} & m_{33} \end{bmatrix} = \begin{bmatrix} m + X_{\dot{u}} & 0 & 0 \\ 0 & m + Y_{\dot{v}} & mx_g \\ 0 & mx_g & I_z + N_{\dot{r}} \end{bmatrix}, \tag{5.72}$$

$$\boldsymbol{C}(\boldsymbol{\nu}^f) \triangleq \begin{bmatrix} 0 & 0 & c_{13}(r^f, v^f) \\ 0 & 0 & c_{23}(u^f) \\ -c_{13}(r^f, v^f) & -c_{23}(u^f) & 0 \end{bmatrix}, \tag{5.73}$$

$$\boldsymbol{D}(\boldsymbol{\nu}^f) \triangleq diag\{d_{11}, d_{22}, d_{33}\} = diag\{X_u + X_{|u|u}|u^f|, Y_v + Y_{|v|v}|v^f|, N_r + N_{|r|r}|r^f|\}. \tag{5.74}$$

The structure of the system matrices in (5.72) and (5.73) are obtained by assuming that the vehicle is symmetric in port-starboard, and that the BODY frame is located along the centre-line of the vehicle (T. Fossen, 2011), in which case it is common that $y_g \approx 0$. The

system dynamics relative to FLOW is obtained by expanding (5.66):

$$\dot{u}^f = -\frac{1}{m_{11}}(c_{13}r^f + d_{11}u^f - \tau_u), \tag{5.75}$$

$$\dot{v}^f = -\frac{1}{m_{22}}(m_{23}\dot{r}^f + c_{23}r^f + d_{22}v^f), \tag{5.76}$$

$$\dot{r}^f = -\frac{1}{m_{33}}(m_{23}\dot{v}^f + d_{33}r^f - c_{13}u^f - c_{23}v^f - \tau_\psi). \tag{5.77}$$

Note that $r^n = r^f$ since $r_c = 0$ in (5.65) for irrotational CURRENT in NED.

5.4.2 Speed Allocation and Control Objective

The path-following problem is solved as a manoeuvring problem (Breivik & Fossen, 2005) that consists of a geometric and a dynamic task are solved. In 2-D case, the control objectives that will drive the vehicle towards the path include controlling the vehicle heading ψ^n and horizontal speed U_h^n in NED towards the desired course angle ψ_d and desired horizontal speed $U_{hd}^n > 0$ relative to NED along the path. This is a course control problem that includes the sideslip because the vehicle is subject to constant and irrotational CURRENT and/or WAVE disturbances.

Speed Allocation

The desired horizontal speed $U_{hd}^n > 0$ relative to NED is required to be allocated to the desired BODY speeds u_d^n and v_d^n relative to NED, which is the general approach to the design of u_d^n. There is no general or explicit structure or solution to this problem in the literature, and this will be referred as the speed allocation problem in this thesis. More generally this can also describe the problem of transforming speeds between reference frames. For instance, Børhaug et al. (2008) designs u_d^n using $U_{hd}^n > 0$ as:

$$u_d^n = U_d^n \cos\psi_{los}, \tag{5.78}$$

As in the more common approach taken by (T. Fossen, 2011), the vehicle sway velocity is $v^n \approx 0$ in most applications, and thus $u^n \approx U^n$ that also results in simplified vehicle kinematics as in(A. Lekkas & Fossen, 2012). This then also results in the design $u_d^n = U_{hd}^n$.

The formulation of the general and unique structure of the speed allocation problem is inspired by improved representation of the relativity relationship (5.65), which is now be given by:

$$U_d^n \triangleq \sqrt{u_d^{n2} + v_d^{n2} + w_d^{n2}}, \tag{5.79}$$

$$U_{hd}^n \triangleq \sqrt{u_d^{n2} + v_d^{n2}}, \tag{5.80}$$

$$u_d^n \triangleq u_d^f + u_c, \tag{5.81}$$

$$v_d^n \triangleq v_d^f + v_c, \tag{5.82}$$

$$w_d^n \triangleq w_d^f + w_c, \tag{5.83}$$

where U_d^n is the desired user-specified total speed, $\boldsymbol{\nu}_{db/n}^b = [u_d^n, v_d^n, w_d^n]^T$ and $\boldsymbol{\nu}_{db/f}^f = [u_d^f, v_d^f, w_d^f]^T$ are the desired BODY velocities in surge, sway and heave relative to NED and FLOW frames, respectively. Equations (5.79)-(5.83) represent the structure for the speed allocation problem: allocation of desired inertial speed into desired BODY speeds. In general, it can represent the logical method for speed allocation between such reference frames and not just between the NED and BODY.

In the sway-unactuated case in this section, v_d^f can be set to zero in (5.86) to give:

$$v_d^n = v_c, \tag{5.84}$$

which gives the solution to u_d^f from (5.80) as:

$$u_d^n = \sqrt{{U_{hd}^n}^2 - v_d^{n2}} = \sqrt{{U_{hd}^n}^2 - {v_c}^2}, \tag{5.85}$$

and U_{hd}^n is user-assigned.

Remark 5.6 It should noted that whether there is actuation or not in sway, v_d^f has be

set to zero to solve for u_d^n using (5.82) and (5.84). This is because the setting a nonzero value for v_d^f will create an undesired lateral motion in sway. This is because the vehicle heading is measured from the direction of u^n in x_b-axis, and not from v_d^n in sway direction, and that a nonzero v_d^f implies that the vehicle has to move in sway relative to the FLOW at all cases even when the vehicle is on the path and that there is no CURRENT in sway to counteract with nonzero v_d^f. This is not the same in surge because the vehicle desired to stay on the path with a non-zero surge velocity. The sideways drift is taken into account by the sideslip that uses v_d^n, and not v_d^f. If the vehicle heading is calculated from the direction of sway v^f, then v_d^f can now be nonzero and u_d^f will be set to zero to solve for v_d^n in (5.81)-(5.82). In this case, the vehicle will follow the path sideways, which is not a common practice. Therefore, v_d^f has to be zero when the heading is the direction of surge.

Control Objective

The geometric task of the maneuvering problem in 2-D requires the vehicle to be on the path, which means that the cross-track error $e_{yz} \to 0$. Then, the control objectives for sway-unactuated 2-D PF in NED are formulated as:

$$\lim_{t\to\infty} u^n(t) = u_d^n(t), \tag{5.86}$$

$$\lim_{t\to\infty} \psi^n(t) = \psi_d(t), \tag{5.87}$$

$$\lim_{t\to\infty} y_e(t) = 0. \tag{5.88}$$

where ψ_d is the horizontal desired heading for course control as given by:

$$\psi_d = \psi_{los} - \beta^n. \tag{5.89}$$

and ψ_{los} is given by the SELOS guidance (5.1)-(5.3) and (5.10).

Notice that for successful path-following under CURRENT and/or WAVE disturbances, (5.85) now requires that $U_{hd}^n \geq v_c^n$ to avoid imaginary solutions for u_d^n.

The control objective for the cross-track error (5.88) are satisfied by the stability properties of horizontal LOS guidance laws.

5.4.3 SMC

Yaw Control

The yaw error and its dynamics are defined and given as $\tilde{\psi} \triangleq \psi_d - \psi^n$ and $s \triangleq \dot{\tilde{\psi}} + \lambda \tilde{\psi}$, where $\lambda_r > 0$ is controller bandwidth. Taking the time-derivative of $\tilde{\psi}$ and s, and using kinematics (5.71) and yaw dynamics (5.77) gives:

$$\dot{\tilde{\psi}} = \dot{\psi}_d - r^f, \tag{5.90}$$

$$\begin{aligned} \dot{s} = \ddot{\tilde{\psi}} + \lambda_r \dot{\tilde{\psi}} &= \ddot{\psi}_d - \dot{r}^f \\ &= \ddot{\psi}_d + \frac{1}{m_{33}}(m_{23}\dot{v}^f + d_{33}r^f - c_{13}u^f - c_{23}v^f - \tau_\psi) + \lambda(\dot{\psi}_d - r^f). \end{aligned} \tag{5.91}$$

The feedback-linearizing sliding controller for yaw is given by:

$$\tau_\psi = c_{13}u^f + c_{23}v^f - d_{33}r^f - m_{23}\dot{v}^f + m_{33}\left[\ddot{\psi}_d + \lambda_r(\dot{\psi}_d - r^f) + k_\psi \tilde{\psi} + k_d s\right], \tag{5.92}$$

where $k_\psi, k_d > 0$ are constant gains. The time-derivative of radially unbounded and positive definite LFC $V_\psi = (1/2)\tilde{\psi}^2 + (1/2)s^2$ is used for stability analysis of error dynamics (5.90)-(5.91), which is:

$$\dot{V}_\psi = \dot{\tilde{\psi}}\tilde{\psi} + \dot{s}s = -\lambda_r \tilde{\psi}^2 - k_d s^2 \leq 0. \tag{5.93}$$

Since $\dot{V}_\psi$ is negative definite thus, the equilibrium $(\psi, s) = (0,0)$ is GES, and hence $(\tilde{\psi}, s) \to (0,0)$ exponentially as $t \to \infty$. This satisfies the control objective (5.87). Exponential convergence of $(\tilde{\psi}, s) \to (0,0)$ also implies exponential convergence of $r^n \Rightarrow \psi_d$ since $s - \lambda_r \tilde{\psi} = \psi_d - r^n$.

In order to prevent large ψ_d being fed into the controller, e.g. during waypoint switch-

ing, the following integration is used to generate small increments of ψ_d:

$$\psi_{dr} = \psi^n + \dot{\psi}_d T_s = \psi^n - k_r T_s \tilde{\psi}, \tag{5.94}$$

where T_s is the integrator sampling time, and $\tilde{\psi} \to 0$ also implies $\psi^n \to \psi_d$ in (5.96). Reference signals for $\dot{\psi}_d, \ddot{\psi}_d$ are obtained by:

$$\dot{\psi}_d = k_r(\psi_d - \psi^n) = k_r \tilde{\psi}, \tag{5.95}$$

$$\ddot{\psi}_d = k_a(\dot{\psi}_d - \dot{\psi}^n) = k_a \dot{\tilde{\psi}}, \tag{5.96}$$

where k_r, k_a are gains.

Surge Control

The error in surge is defined as $\tilde{u} \triangleq u_d^n - u^n$. Using the time-derivative of relative velocity relationship in BODY in (5.65), and CURRENT and surge dynamics (5.68) and (5.75), the surge error dynamics becomes:

$$\dot{\tilde{u}} = \dot{u}_d^n - \dot{u}^n = \dot{u}_d^n - (\dot{u}^f + \dot{u}_c) = \dot{u}_d^n + \frac{1}{m_{11}}(c_{13} r^f + d_{11} u^f - \tau_u) + r^f v_c. \tag{5.97}$$

The feedback-linearizing proportional control law for surge is given by:

$$\tau_u = c_{13} r^f + d_{11} u^f + m_{11}(\dot{u}_d^n + k_u \tilde{u} + r^f v_c), \tag{5.98}$$

since $r^n = r^f$ for CURRENT irrotational in NED and $k_u > 0$ is proportional gain. The desired surge acceleration $\dot{u}_d^n$ is given by $\dot{u}_d^n = k_1 \tilde{u}$, where $k_1 > 0$ is a gain.

Stability of the closed-loop system (5.97) is analyzed using the time-derivative of the LFC $V_u \triangleq (1/2)\dot{\tilde{u}}^2$, which is:

$$\dot{V}_u = -k_u \tilde{u}^2 \leq 0. \tag{5.99}$$

$\dot{V}_u$ is negative definite and hence, the origin $\tilde{u} = 0$ of (5.97) is GES. Thus, $\tilde{u}(t) \to 0$ as

$t \to \infty$. This achieves control objective (5.86). Note that under current disturbance, v_c and either r^n or r^f are required in for feedback control.

5.4.4 Nonlinear PID Control

The classical PID control law is easy to design and can serve as a benchmark to assess the performance of the SELOS guidance without more advanced control techniques such as the SMC.

Yaw Control

The control objectives and errors definitions are the same for each DOF as in Section 5.2, where:

$$\tilde{\psi} = \psi_d - \psi^n, \tag{5.100}$$

$$\dot{\tilde{\psi}} = \dot{\psi}_d - r^n = k_r \tilde{\psi} - r^f, \tag{5.101}$$

using the reference signal (5.95). The error dynamics of the yaw rate is given by time-differentiating (5.101) and using the reference signals (5.95)-(5.96), yaw kinematics and dynamics (5.71) and (5.77) gives:

$$\ddot{\tilde{\psi}} = k_r \dot{\tilde{\psi}} - \dot{r}^f = k_r k_a \dot{\tilde{\psi}} + \frac{1}{m_{33}}(d_{33} r^f - c_{13} u^f - c_{23} v^f - \tau_\psi) + m_{23} \dot{v}^f, \tag{5.102}$$

The PID controller is given by:

$$\tau_\psi = k_{p\psi} \tilde{\psi} + k_{d\psi} \dot{\tilde{\psi}} + k_{i\psi} \int \tilde{\psi} dt, \tag{5.103}$$

where $k_{p\psi}, k_{d\psi}, k_{i\psi} > 0$ are the proportional, derivative and integral gains respectively. Substituting (5.103) into (5.102) gives the closed-loop dynamics as:

$$\ddot{\tilde{\psi}} = k_r k_a \dot{\tilde{\psi}} + \frac{1}{m_{33}}(d_{33} r^f - c_{13} u^f - c_{23} v^f - k_{p\psi}\tilde{\psi} - k_{d\psi}\dot{\tilde{\psi}} - k_{i\psi}\int \tilde{\psi} dt) + m_{23}\dot{v}^f, \tag{5.104}$$

The time-derivative of radially unbounded, positive definite LFC $V_\psi = (1/2)\tilde{\psi}^2 + (1/2)\dot{\tilde{\psi}}^2$ for (5.101) and (5.102) is given by and simplified to:

$$\begin{aligned}\dot{V}_\psi = \dot{\tilde{\psi}}\tilde{\psi} + \ddot{\tilde{\psi}}\dot{\tilde{\psi}} = \dot{\tilde{\psi}}\tilde{\psi} + k_r k_a \dot{\tilde{\psi}}^2 + \frac{\dot{\tilde{\psi}}}{m_{33}}\Big(d_{33} r^f - c_{13} u^f - c_{23} v^f - k_{p\psi}\tilde{\psi}\dot{\tilde{\psi}} - k_d d\psi\dot{\tilde{\psi}}^2 \\ -k_{i\psi}\int \tilde{\psi} dt\,\dot{\tilde{\psi}}\Big) + m_{23}\dot{v}^f\end{aligned} \tag{5.105}$$

Substituting (5.101) into some of the terms and rearranging yields:

$$\begin{aligned}\dot{V}_\psi = k_r\left(1 - \frac{k_{p\psi}}{m_{33}}\right)\tilde{\psi}^2 + \left(k_r k_a - \frac{k_{d\psi}}{m_{33}}\right)\dot{\tilde{\psi}}^2 - \frac{k_r}{m_{33}}\left(k_{i\psi}\int \tilde{\psi} dt + c_{13} u^f\right) - \frac{d_{33}}{m_{33}} {r^f}^2 \\ + \frac{r^f}{m_{33}}\left(k_{p\psi} + k_{i\psi}\int \tilde{\psi} dt + k_r d_{33}\right) + \frac{r^f}{m_{33}}\left(c_{13} u^f + c_{23} v^f\right)\end{aligned} \tag{5.106}$$

It can be seen that $\dot{V}_\psi$ is negative semi-definite when $\frac{k_{p\psi}}{m_{33}} > 1, \frac{k_{d\psi}}{m_{33}} > k_r k_a$, and the following inequality is satisfied:

$$\begin{aligned}-k_r\left(1 - \frac{k_{p\psi}}{m_{33}}\right)\tilde{\psi}^2 - \left(k_r k_a - \frac{k_{d\psi}}{m_{33}}\right)\dot{\tilde{\psi}}^2 + \frac{k_r}{m_{33}}\left(k_{i\psi}\int \tilde{\psi} dt + c_{13} u^f\right) + \frac{d_{33}}{m_{33}} {r^f}^2 \\ > \frac{r^f}{m_{33}}\left(k_{p\psi} + k_{i\psi}\int \tilde{\psi} dt + k_r d_{33}\right) + \frac{r^f}{m_{33}}\left(c_{13} u^f + c_{23} v^f\right)\end{aligned} \tag{5.107}$$

If $\dot{V}_\psi$ is negative semi-definite, then the equilibrium points $(\tilde{\psi}, \dot{\tilde{\psi}}) = (0,0)$ of the closed-loop systems (5.100)-(5.101) are globally stable (GS). This satisfies the control objective (5.87).

Surge Control

The surge error and its dynamics are similarly given by:

$$\tilde{u} = u_d^n - u^n, \tag{5.108}$$

$$\dot{\tilde{u}} = \dot{u}_d^n - \dot{u}^n = \dot{u}_d^n - (\dot{u}^f + \dot{u}_c) = \dot{u}_d^n + \frac{1}{m_{11}}\left(c_{13}r^f + d_{11}u^f - \tau_u\right) + r^f v_c. \tag{5.109}$$

And $\dot{u}_d^n$ is designed by $\dot{u}_d^n = k_1\tilde{u}$, where $k_1 > 0$ is a gain. The PID controller for surge is similarly given by:

$$\tau_u = k_{pu}\tilde{u} + k_{du}\dot{\tilde{u}} + k_{iu}\int \tilde{u}dt, \tag{5.110}$$

where $k_{pu}, k_{du}, k_{iu} > 0$ are the proportional, derivative and integral gains respectively. Substituting (5.110) into (5.109) gives the closed-loop error dynamics as:

$$\begin{aligned}\dot{\tilde{u}} &= k_1\tilde{u} + \frac{1}{m_{11}}\left(c_{13}r^f + d_{11}u^f - k_{pu}\tilde{u} - k_{du}\dot{\tilde{u}} - k_{iu}\int \tilde{u}dt\right) + r^f v_c. \\ &= \frac{m_{11}}{m_{11}+k_{du}}\left[\left(k_1 - \frac{k_{pu}}{m_{11}}\right)\tilde{u} + r^f v_c\right] + \frac{1}{m_{11}+k_{du}}\left(c_{13}r^f + d_{11}u^f - k_{iu}\int \tilde{u}dt\right).\end{aligned} \tag{5.111}$$

The time-derivative of a LFC $V_u = (1/2)\tilde{u}^2$ for analyzing the dynamics (5.111) is given by and simplified to:

$$\begin{aligned}\dot{V}_u = \dot{\tilde{u}}\tilde{u} &= \frac{m_{11}}{m_{11}+k_{du}}\left[\left(k_1 - \frac{k_{pu}}{m_{11}}\right)\tilde{u} + r^f v_c\right]\tilde{u} + \frac{\tilde{u}}{m_{11}+k_{du}}\left(c_{13}r^f + d_{11}u^f - k_{iu}\int \tilde{u}dt\right) \\ &= \frac{k_1 m_{11} - k_{pu}}{m_{11}+k_{du}}\tilde{u}^2 + \frac{\tilde{u}}{m_{11}+k_{du}}(m_{11}r^f v_c + c_{13}r^f + d_{11}u^f) - \frac{k_{iu}\int \tilde{u}dt}{m_{11}+k_{du}}.\end{aligned} \tag{5.112}$$

Now it can be seen that $\dot{V}_u$ is negative definite when $k_{pu} > k_1 m_{11}$ and the following inequality is satisfied:

$$-\frac{k_1 m_{11} - k_{pu}}{m_{11}+k_{du}}\tilde{u}^2 + \frac{k_{iu}\int \tilde{u}dt}{m_{11}+k_{du}}\tilde{u} > \frac{\tilde{u}}{m_{11}+k_{du}}(m_{11}r^f v_c + c_{13}r^f + d_{11}u^f) \tag{5.113}$$

Thus, if $\dot{V}_u$ is negative definite, the equilibrium $\tilde{u} = 0$ of the surge closed-loop system (5.111) is GAS. This satisfies the control objective (5.86).

Remark 5.7 State feedback controllers are are not easy to implement since they require knowledge or estimations of the state. One reason for using feedback controllers is to achieve GES or at least asymptotic stability (AS), which obviously provides better performance and robustness at the kinetic level. The yaw error dynamics in both SMC and PID cases show that feedback terms are necessary to achieve at least AS. If feedback terms are not available, only GS can be achieved directly using any of the PID-type controllers with high gains. Without AS, integral action is necessary to achieve zero steady-state error for $\tilde{\psi}$, which in turn requires anti-windup. The stability results of surge and yaw error dynamics do not affect the stability the guidance laws at the kinematic level, but it can reduce the performance and robustness at the kinetic level, which thus can affect the cross-tracking performance. Thus, robust kinetic controllers can provide better comparison for the analysis of course control and speed allocation.

5.4.5 Underactuated Sway Error Dynamics

It is important to analyze the behavior of the unactatued sway since there is no control input in sway, especially under environmental disturbances so that it is at least bounded. The error in sway under CURRENT disturbance is defined similarly and expressed using the speed allocation in (5.84) and relative velocity relationship (5.65) as:

$$\tilde{v} \triangleq v_d^n - v^n = v_c - v^n = -v^f. \tag{5.114}$$

Using CURRENT and sway dynamics (5.68) and (5.76), the sway error dynamics is given by:

$$\dot{\tilde{v}} = -\dot{v}^f = \frac{1}{m_{22}}(m_{23}\dot{r}^f + c_{23}r^f + d_{22}v^f). \tag{5.115}$$

This equation represents a general 3-DOF coupled underactuated sway error dynamics at BODY level relative to NED in the presence of CURRENT disturbance. It can be seen

that sway will drift in the direction of net force resulting in (5.115), without any actuation in sway. It is shown in previous Chapter that $(\boldsymbol{\nu}^f_{b/f}, \boldsymbol{\nu}^b_{b/n})$ are bounded for bounded $(\boldsymbol{\tau}_{act}, \boldsymbol{\nu}^b_{c/n})$ under neutral buoyancy. Thus, the relative underactuated sway dynamics will remain bounded for bounded $(\boldsymbol{\tau}_{act}, \boldsymbol{\nu}^b_{c/n})$.

The drift in sway is minimized with actuation in surge and yaw when sideslip is taken into account in course control since the sideslip also describes the amount of v by definition and the vehicle is required to steer accordingly to counteract the drift in sway using surge. This empathizes the importance of incorporating slip angles in heading control and thus, of course control, especially when there are CURRENT disturbance and sway is underactuated, which cause bigger drift.

Remark 5.8 Note that the stability results of surge and sway error dynamics does not affect the stability result of the track-error dynamics. However, the surge and sway velocities have an impact on cross-tracking performance, and also course control performance through the definition of sideslip.

5.4.6 Simulation

The PF performance of the SELOS guidance for course control using the SMC and nonlinear PID controllers designed is studied using the model of 3-DOF Girona-500 AUV with the new relative vehicle dynamics and CURRENT disturbance in MatLab. The Girona-500 is a multi-purpose re-configurable AUV with three torpedo-shaped hull design that is mainly used for research, where the bottom hull can be replaced with robotic arms or other payloads for different missions. The vehicle can be actuated fully in 4-DOF with passively-stabilized roll and pitch. Model parameters of the vehicle are extracted from (Karras et al., 2013), which are also provided in Appendix 1. The initial NED position, vehicle heading and relative velocities were set to $\boldsymbol{\eta}^n_{b/n} = [4,5,0]$ and $\boldsymbol{\nu}^b_{b/n} = \boldsymbol{\nu}^f_{b/f} = [0,0,0]$, and the maximum desired horizontal relative velocity is $U^n_{hd} = 1m/s$. The PF problem consists of straight-lines connecting the waypoints given by: $wpx = [5,22,22,8,\ 17.5]$, $wpy = [10,14,21,26,32]$. The PF task is carried out with

and w/o horizontal CURRENT disturbances and/or position and heading zero average random uncertainties of $\pm 5cm$ in x^n, y^n and $\pm 3^o$ in ψ^n. The guidance system gains are set as: $R_{min} = 0.9, a = 1.01, c = 0.001, k_r = k_a = k_1 = 1, T_s = 0.05$. As mentioned earlier, R_{min} is usually about the length of the vehicle and can only be tuned using trail and error for the specific vehicle dynamics. Acceleration gains k_1, k_a, k_r are usually small and tuned by trial and error. To achieve a more realistic representation, the control input saturate at $\pm 450N$ in surge and heave, and $\pm 250Nm$ in yaw, and that there is a rate limit for maximum yaw rate at $57.3deg/s(1rad/s)$.

The vehicle dynamics $\dot{\boldsymbol{\nu}}^f_{b/f}$ are obtained by through the model parameters and the speed vector $\boldsymbol{\nu}^f_{b/f}$ obtained by differentiating $\dot{\boldsymbol{\nu}}^f_{b/f}$ in the simulation. Then, for a know CURRENT speed V_x and V_y, $\boldsymbol{\nu}^b_{b/n}$ is obtained using the relationship of relativity in (5.65) using the BODY equivalents of V_x and V_y. The kinematics values are then integrated and collected at every sampling time to produce the simulation results. The accuracy of these data are default by the program which is sufficiently high.

SMC

The SMC is simulated first and the controller gains are set as: $\lambda = 1, k_\psi = 11, k_d = 55, k_u = 55, k_1 = 1$. The controller gains are not very high since the nonliniearities are canceled out by the feedback terms and are only tuned using trial and error. Fig. 5.6 show that the vehicle can follow the path accurately under significant CURRENT disturbances of $V_h = 1.5m/s$ (i.e. 150% of $U^n_{hd} = 1m/s$). Fig. 5.7 show that the vehicle can also follow the path closely when there are both significant CURRENT and/or WAVE disturbances and position and heading uncertainty. It can be seen that the vehicle correctly sways in the direction of the CURRENT disturbance. The 150% disturbance rejection is high compared those in publications for PF of vehicles subject to wind or CURRENT and/or WAVE disturbances. For example, in (Sujit et al., 2014), the maximum wind velocity during constant altitude aerial vehicle PF was $7.5m/s$ which was around 50% of the vehicle total speed of $15m/s$, while the ocean current intensity in (Caharija et al., 2012) for PF

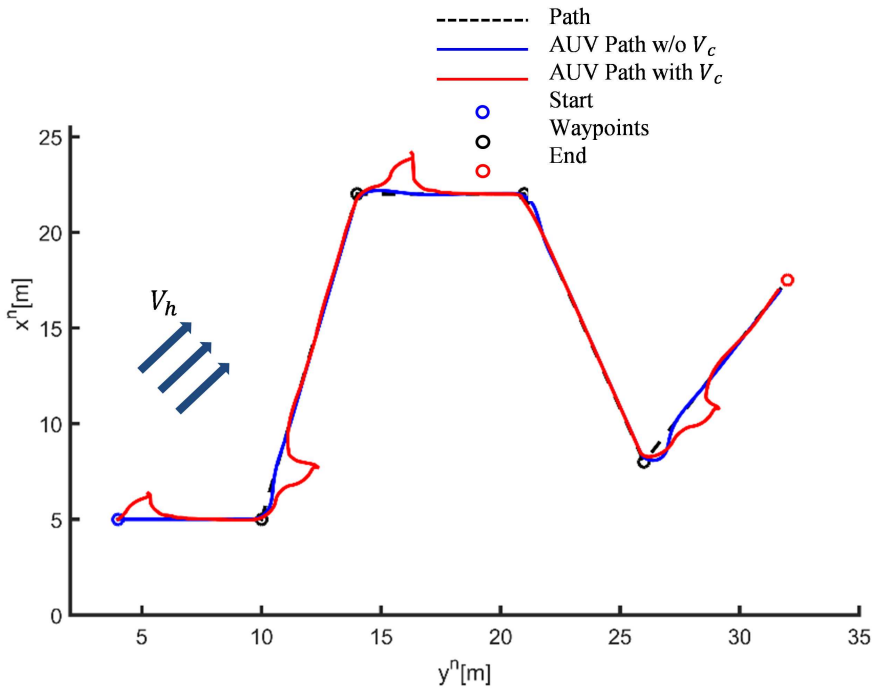

Figure 5.6: Performance of SELOS sliding course control with and w/o CURRENT disturbance of $V_h = 1.5m/s$ at $\psi_c = 45^o$.

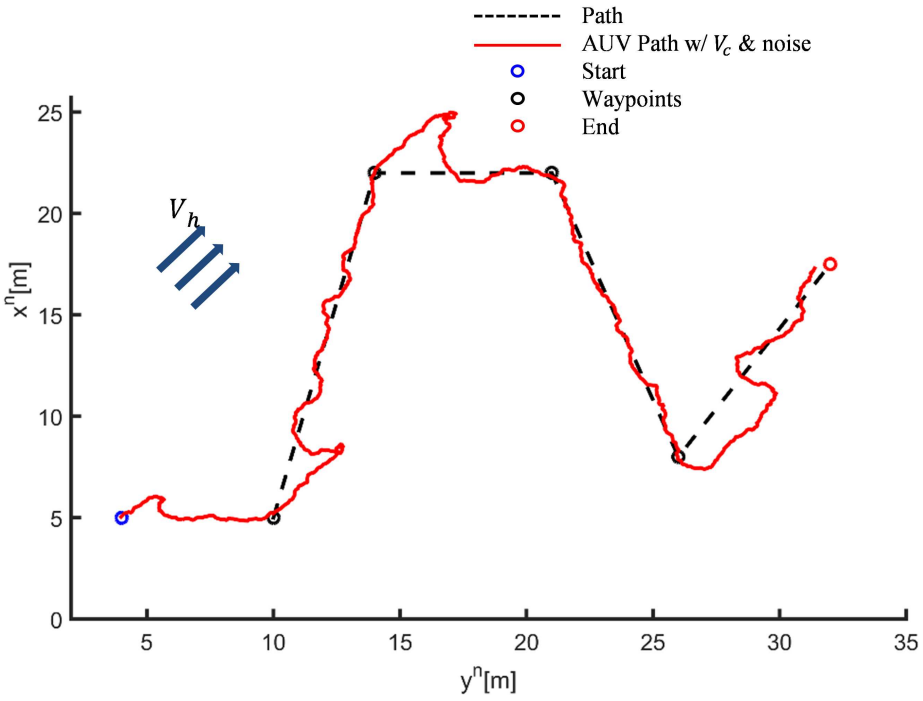

Figure 5.7: Performance of SELOS sliding course control with CURRENT disturbance of $V_c = 1m/s$ at $\psi_c = 45^o$, and position and heading zero-average random uncertainties of $\pm 5cm$ and $\pm 3^o$ in x^n, y^n and ψ^n, resp..

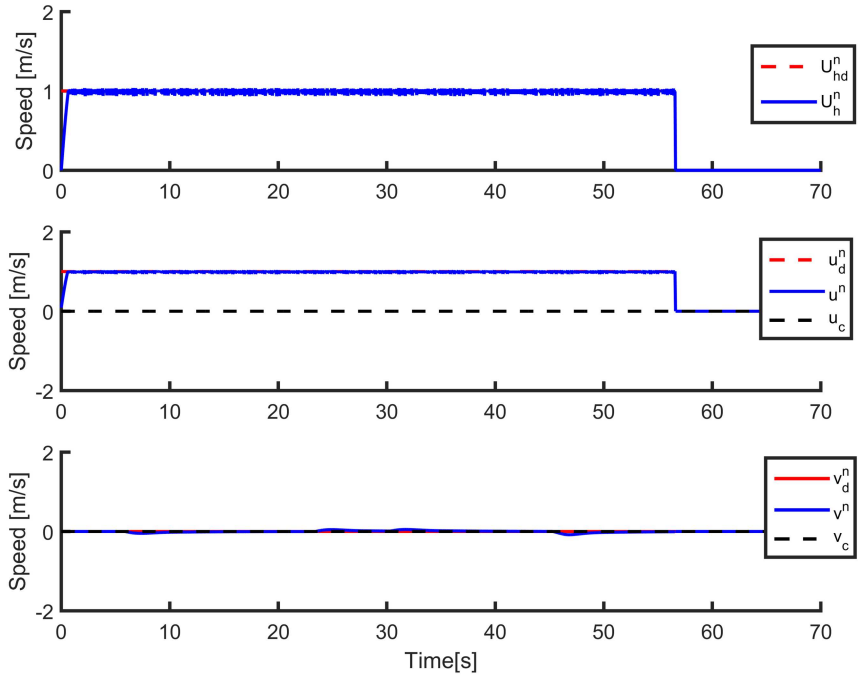

Figure 5.8: Velocity tracking profile of SELOS sliding course control

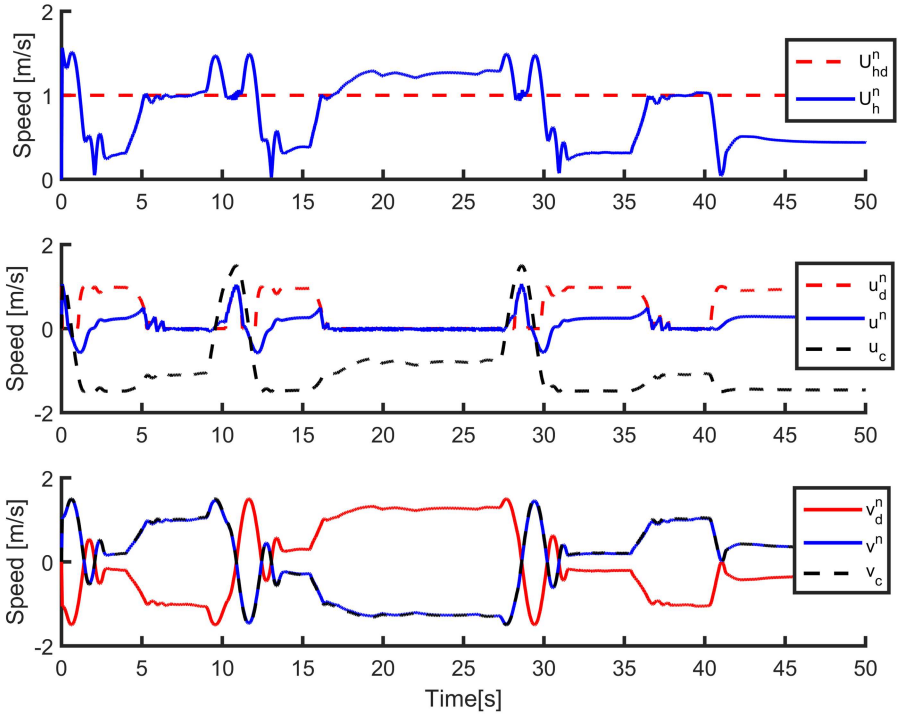

Figure 5.9: Velocity tracking profile of SELOS sliding course control with CURRENT disturbance of $V_h = 1.5m/s$ at $\psi_c = 45^o$.

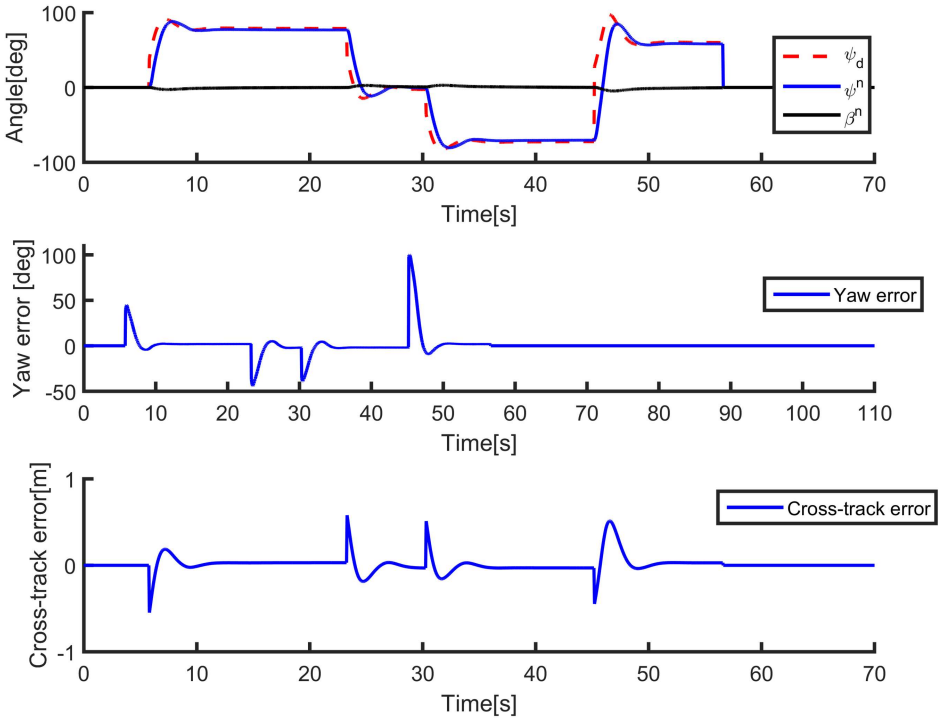

Figure 5.10: Course angle and cross-track error tracking profile of SELOS sliding course control

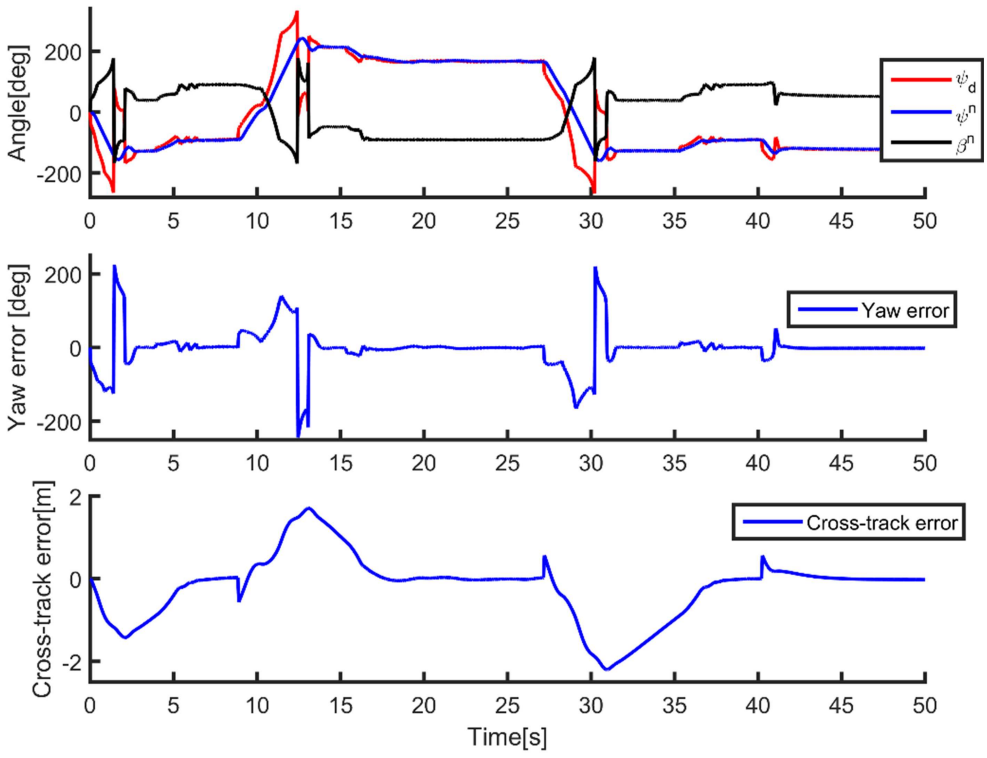

Figure 5.11: Course angle and cross-track error tracking profile of SELOS sliding course control with CURRENT disturbance of $V_h = 1.5m/s$ at $\psi_c = 45^o$.

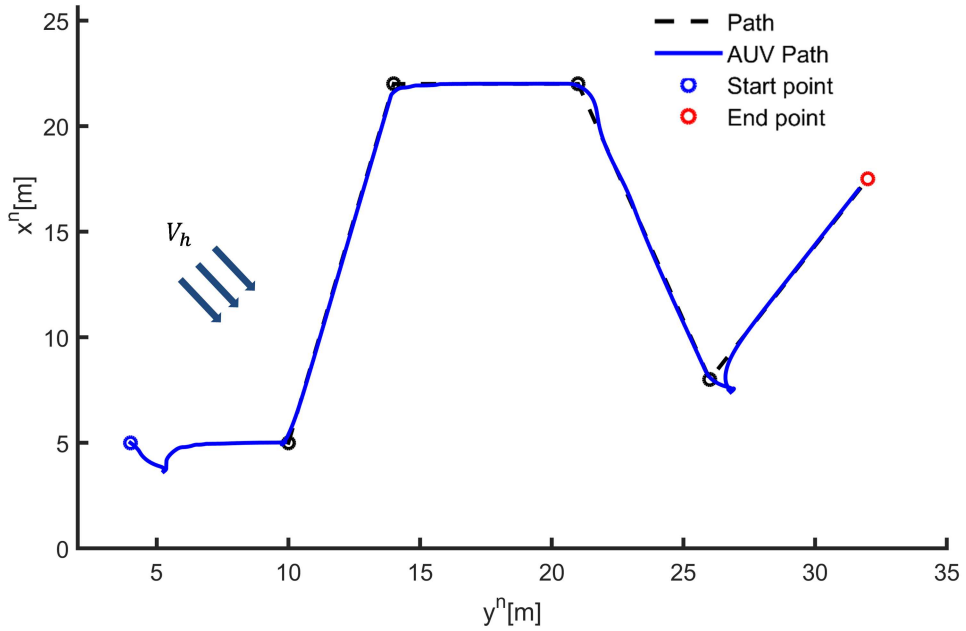

Figure 5.12: Performance of SELOS sliding course control with a CURRENT disturbance of $V_h = 1.5m/s$ at $\psi_c = 135^o$.

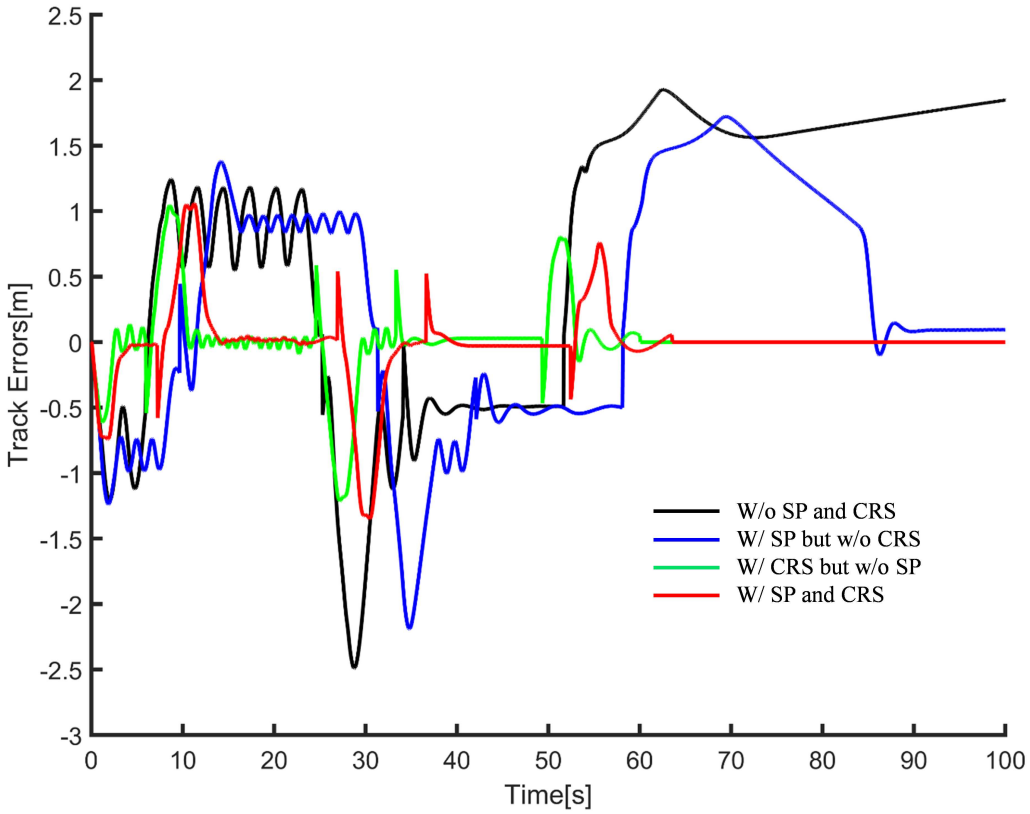

Figure 5.13: Cross-track error w/ and w/o speed allocation and/or course control with CURRENT disturbance of $V_h = 1.1m/s$ at $\psi_c = 45^o$ (CRS=Course control).

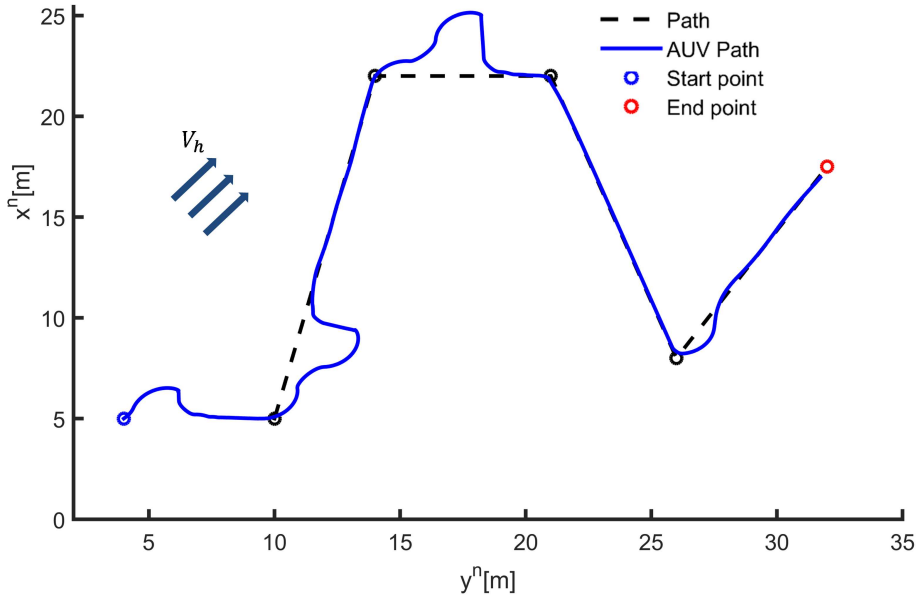

Figure 5.14: SELOS PF performance with course control and speed allocation with CURRENT disturbance of $V_h = 1.1m/s$ at $\psi_c = 45^o$ and maximum desired yaw rate of $r_d^n = 0.5rad/s$.

of surface marine vessels was $\sqrt{2}m/s$ which was around 28% of the desired relative U_{hd}^n of $5m/s$. In a more recent simulation done for marine vehicles by Caharija et al. (2016), $U_{hd}^n = 1.2m/s$ while maximum CURRENT intensity $V_h = 0.2m/s$, which only provides around 17% of disturbance rejection. This means that the disturbance rejection achieved by SELOS course control with speed allocation is at least 3-4 times better than existing publications. The ability to reject disturbances from CURRENT and/or WAVE forces and moments can be attributed to course control, speed allocation, and more accurate modeling of the relative system dynamics. PF performance with and w/o course control and/or speed allocation is also shortly and shown in Figure 5.12. From tuning perspective, robustness against disturbance is dependent the desired speed, actuator saturation and in turn the turning limit for Euler rates achieved by such saturation. Note that however, saturation and the limits on Euler rates are not discussed in (Caharija et al., 2012; Sujit et al., 2014; Caharija et al., 2016). In an ideal case without saturation or other limits, the revised relative equations of motion (4.51) mathematically shows that any amount of CURRENT and/or WAVE disturbances can be rejected by sufficient amount of actuation input $\boldsymbol{\tau}_{act}$.

Note that the vehicle starts at a position away from the first waypoint, and this distance

between the starting position and the first waypoint is constructed as a zero waypoint in the program and the vehicle is thus guided accordingly. This is similar in all simulations throughout the thesis.

Figures 5.8-5.9 show the velocity tracking profile with and w/o CURRENT disturbances, where in 5.9 it can be noticed that the when there is a strong CURRENT disturbance, the vehicle travels the path faster due to an increase in U_h^n. This is because since there is no actuation in sway, the vehicle cannot directly counteract the sway component of the CURRENT v_c since $v_d^f = 0$ in the speed allocation (5.82). It can be seen in Figure 5.9 that v_d^n is small as usually assumed in the literature and sways along wing v_c since there is no actuation in sway to counteract v_c. When v_c is greater than U_{hd}^n in (**??**), $u_d^n = 0$ to keep the total speed U_h^n within its maximum value of $1m/s$ since the vehicle sways along with v_c and setting a value for $u_d^n > 0$ for $v_c > U_{hd}^n$ will result in U_h^n bigger than $U_h^n = 1m/s$. This is an important for comparison between disturbance rejection since higher U_h^n can result in stronger disturbance rejection. Figures 5.10-(5.11) show the tracking profile of the desired heading in course control and cross-track error, where the cross-track errors are also kept minimal under disturbances and measurements uncertainties. The fluctuation in sideslip angle is due to the sign changes in u^n and v^n, and the rate of ψ^n lags slightly behind ψ_d since there is a maximum rate on $r_d^n = \dot{\psi}_d$ of $1rad/s$ in the program. Raising this limit along with available level of actuation can increase the amount of disturbance rejection. Figure 5.12 shows that vehicle can also follow the path accurately when only the direction of the CURRENT is changed to $\psi_c = 135^o$.

The PF performance of the vehicle w/ and w/o course control (CRC) and/or speed allocation (SA) are shown in Figure 5.13. The the desired heading angle w/o sideslip is given by $\psi_d = psi_{los}$ and the desired surge speed w/o speed allocation is commonly given as $u_d = U_{hd}$. The desired heading and speed are well tracked by the controllers and thus only cross-track errors are shown here. It can be seen that the PF performance is worst when there is no speed allocation and course control (path-following is slow and the vehicle cannot converge to the last waypoint), and is the best when there are both

speed allocation and course control. See that the main advantage of speed allocation here is reduction in oscillation in both cases. However, it can allow the design of desired sway velocity and thus can have more significant benefits if there is actuation in sway. In addition, just course control alone can hugely reduce the cross-track error hugely. Thus, course control is a very effective and simple disturbance rejection method.

The limit on desired maximum yaw rate can be a bit agile for most vehicles, and thus, r_d^n is reduced to $0.5 rad/s$ to see its effect on disturbance rejection. The PF performance in this case is shown in Figure 5.14 where it results in larger total cross-track error compared to that in Figure 5.6 with maximum r_d^n of $1 rad/s$.

Nonlinear PID

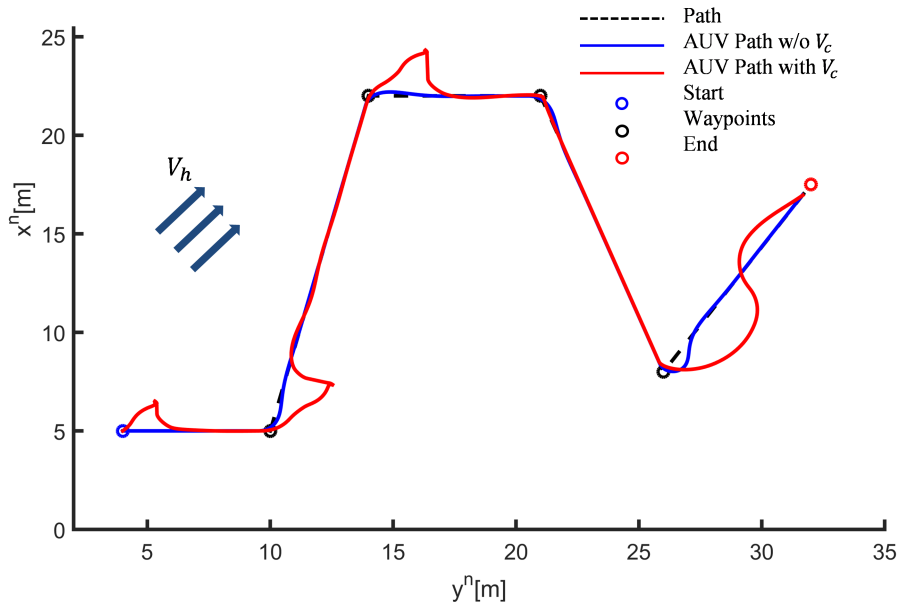

Figure 5.15: Performance of SELOS PID course control with and w/o CURRENT disturbance of $V_h = 1.5 m/s$ and $\psi_c = 45^o$.

The PID controller gains are set as: $k_{pu} = k_{p\psi} = 1000, k_{du} = 300, k_{d\psi} = 10, k_{iu} = k_{i\psi}$. These gains are tuned using trial-and-error and should be high in order to cancel out all the nonlinear forces and moments since there is no feed-back terms compared to the SCM controllers. Fig. 5.15 show that the vehicle can also follow the path closely under significant CURRENT disturbances of $V_h = 1.5 m/s$ (i.e. 150% of $U_{hd}^n = 1 m/s$).

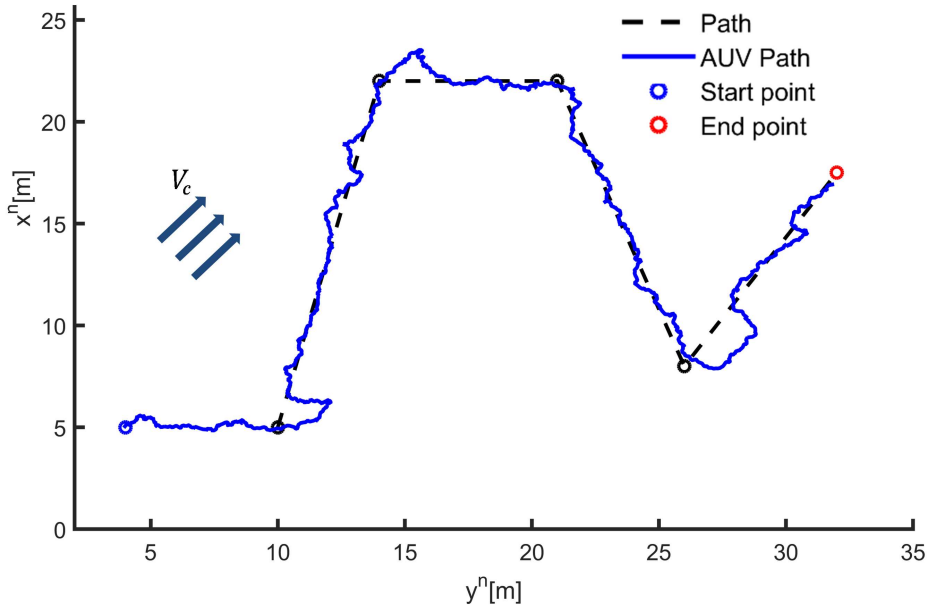

Figure 5.16: Performance of SELOS PID course control with CURRENT disturbance of $V_c = 1m/s$ and $\psi_c = 45^o$, and and position and heading zero average random uncertainties of $\pm 5cm$ and $\pm 3^o$ in x^n, y^n and ψ^n respectively.

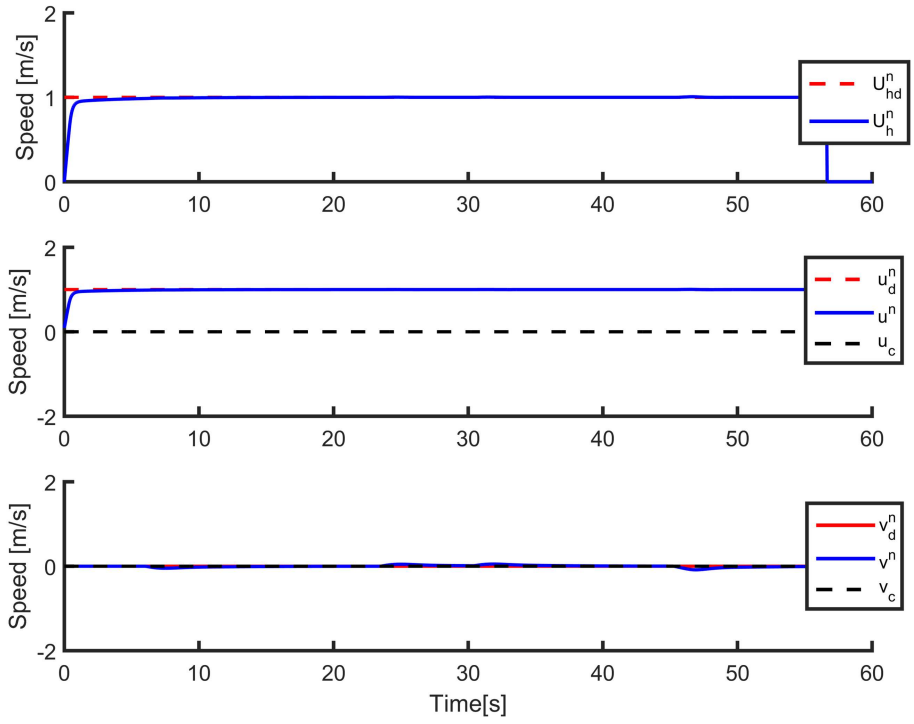

Figure 5.17: Velocity tracking profile of SELOS PID course control

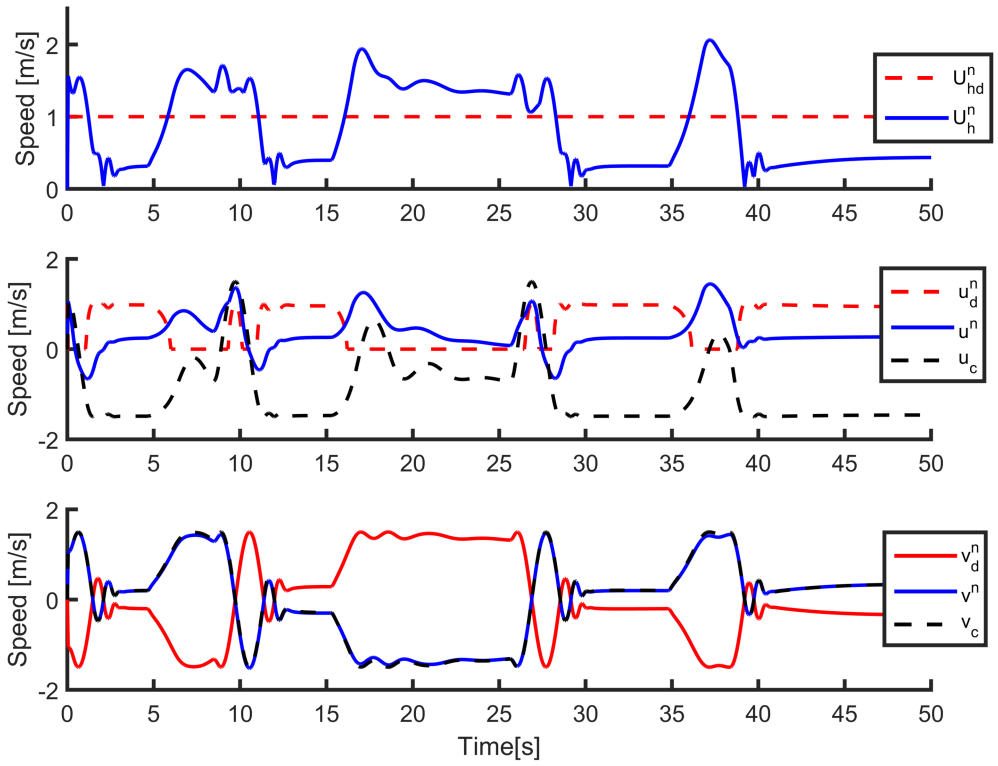

Figure 5.18: Velocity tracking profile of SELOS PID course control with CURRENT disturbance of $V_h = 1.5m/s$ at $\psi_c = 45^o$.

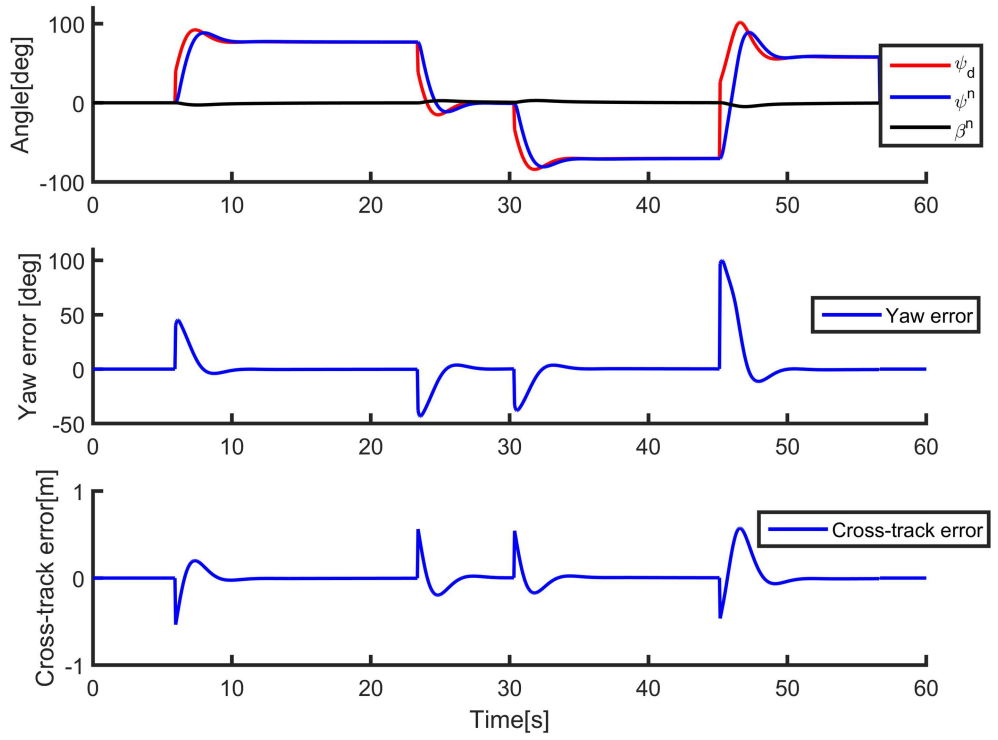

Figure 5.19: Course angle and cross-track error tracking profile of SELOS PID course control

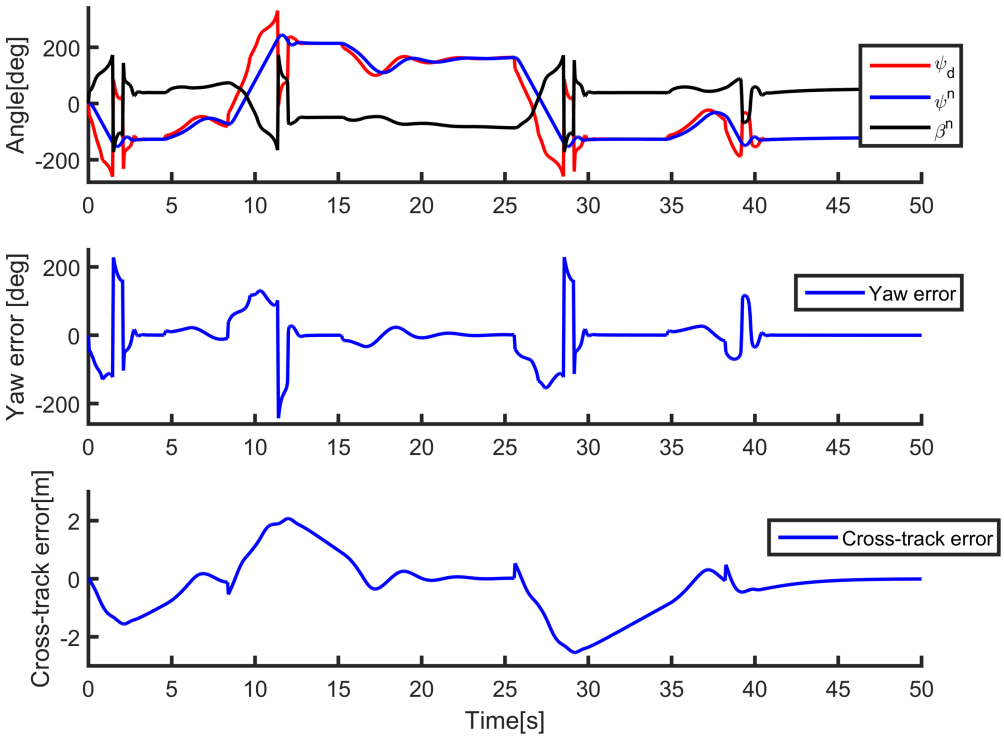

Figure 5.20: Course angle and cross-track error tracking profile of SELOS PID course control with CURRENT disturbance of $V_h = 1.5m/s$ at $\psi_c = 45^o$.

Figures 5.16-5.20 also describe similar tracking profiles to those of the SMC with slight differences which are further discussed in the following section.

Nonlinear PID Vs. SMC

It can be seen that both the linear PID and SMC controllers can deal with at least CURRENT disturbances of $V_h = 1.5m/s$ for same actuator saturation. The SMC controller is known to exhibit chattering effect caused if λ is high, which is small in this case. However, the feedback SMC provides better disturbance rejection in total, which is more visible at the last section of the path between Figure 5.6 and **??**. This is mostly due to the feedback terms in SMC exactly canceling out the nonlinear terms in the error dynamics (since $\lambda = 1$ is small), which is why it can provide the stronger GES in both yaw and surge while the PID can only provide GS and GAS in yaw and surge, resp.. However, note that these feedback terms are not easily and accurately obtainable in practice, and that the surge feedback control exhibits small fluctuations as seen in Figure **??**, although

w/o CURRENT disturbance. This fluctuation does not exist in PID control, but can be reduced by designing a smooth acceleration reference for surge as it is done for yaw. The non-linearities in system model are canceled out in the nonlinear state feedback of SMC and thus the closed-loop dynamics are less sensitive to controller gains but to model parameters which consist of the feedback terms. On the other hand, the linear PID does not linearize the system and thus all the nonlinearities are overcome by larger controller gains, which can make the closed-loop dynamics more dependent on and sensitive to these gains. If an identified model is available, then a nonlinear controller that can cancel out the nonlinearities provides a more robust alternative to control of a highly nonlinear system.

5.5 Comparison between LLOS, SELOS and VF Guidance Laws

The comparison for UAV path-following in (Sujit et al., 2014) also includes three popular guidance laws: LLOS (i.e. carrot-chasing) guidance, ELOS (i.e. nonlinear) guidance, and VF guidance. The comparison is done with wind disturbances and at the kinematic level and thus also applies to UVs. However, the desired heading does not include the wind velocities and thus there is no sideslip taken into account in the design, which makes it a non-course control problem. As shown earlier, this has significant degradation in the disturbance rejection ability of the guidance laws. Therefore, this section provides a comparison between these three guidance laws with SELOS instead of ELOS with course control and speed allocation for PF of underactuated UVs.

The performances of the guidance laws are evaluated using Pareto efficiency for multiple of tuning parameters in areas of interest for each guidance to select optimal tuning parameters that result in low total cross-track error and total control effort. The total cross-track error CT and total control effort U from are calculated by the following sum-

mations:

$$CT = \sum y_e, \tag{5.116}$$

$$U = \sum (\tau_u + \tau_\psi) \tag{5.117}$$

Note that in (5.116) only the surge and yaw control effort are considered since sway is unactuated.

Simulations were carried out using the model of Girona-500 AUV in waypoint following scenarios w/ and w/o ocean CURRENT and/or WAVE disturbance of $V_c = 0.6m/s$ from Northeast direction $\psi_c = \pi/4$. The SMC controller from previous section is used during PF. The initial conditions and desired states are set as $\boldsymbol{\eta}^n_{b/n} = [4,5,-3]^T, \boldsymbol{\nu}^f_{b/f} = \boldsymbol{\nu}^b_{b/n} = [0,0,0]^T, U^n_{hd} = 1m/s$. The gains for the controller are as: $R_k = 0.8, \lambda = 120, k_d = 25, k_r = k_a = k_\psi = k_1 = 1, k_u = 25$. The waypoints used are: $wpx = 10,14,21,26,32$,$wpy = 5,22,22,8,17.5$. The control inputs saturate at $\pm 450N$ and $\pm 450Nm$, and the maximum desired yaw rate $\dot{\psi}_d = 1rad/s$.

5.5.1 LLOS Guidance

The desired heading angle for LLOS course control is given by inserting (5.23) as ψ_{los} into (5.89) when $\psi_p = 0$, which is:

$$\psi_d = \psi_{los} - \beta^n = tan^{-1}\left(\frac{-y_e}{\triangle}\right) - \beta^n. \tag{5.118}$$

The PF performance of the guidance law is shown in Fig 5.21-5.22. It shows that the vehicle is able to follow the path accurately with and w/o a strong CURRENT disturbance. The Pareto efficiency is shown in Figures 5.23-5.24 for both cases. Figure 5.22 shows that LLOS can also handle a large CURRENT disturbance of $V_h = 1.5$ similar to SELOS guidance, which means that the significant disturbance rejection achieved in SELOS is not just specific to SELOS guidance law.

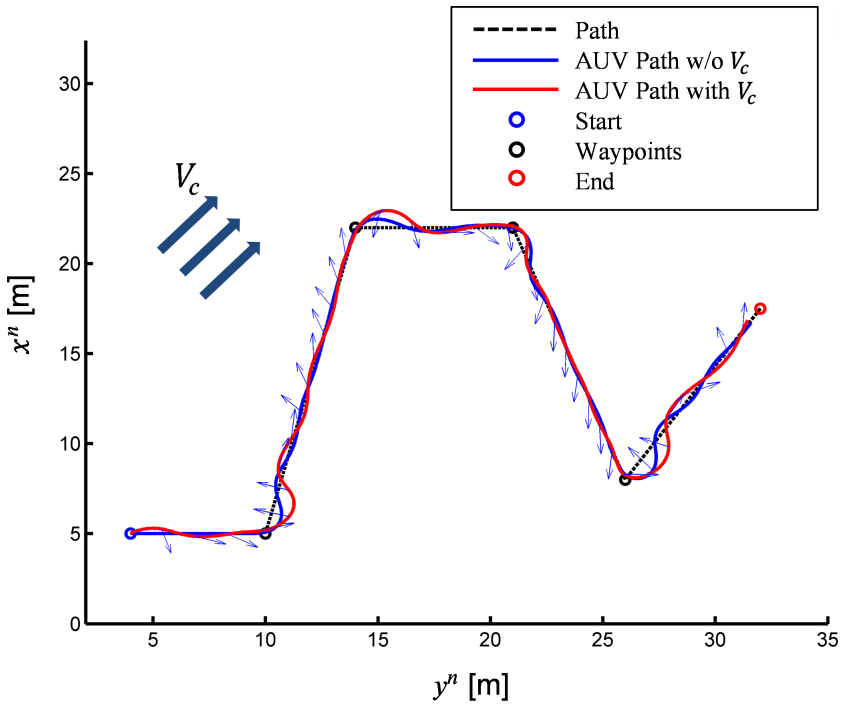

Figure 5.21: Performance of LLOS course control at $\triangle = 0.4$ with and w/o CURRENT disturbance of $V_h = 0.6m/s$ at $\psi_c = pi/4$.

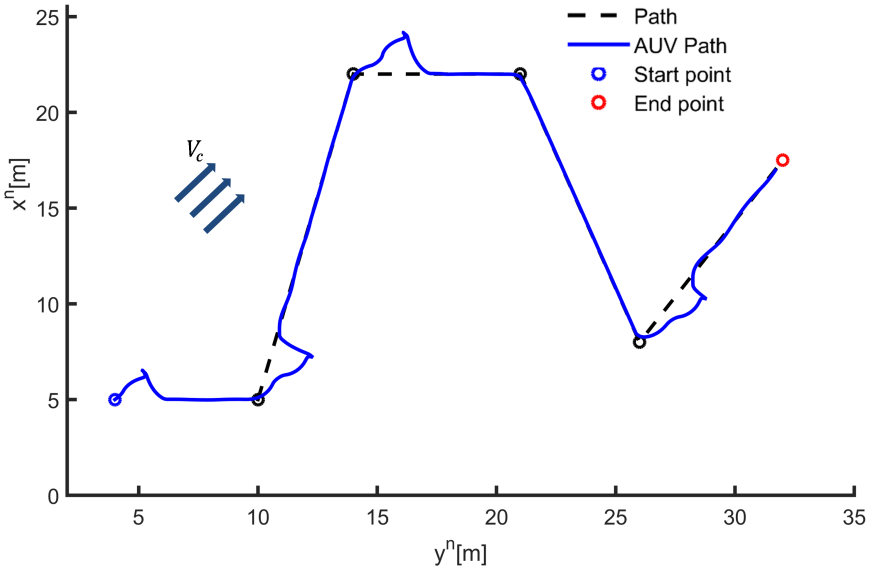

Figure 5.22: Performance of LLOS course control at $\triangle = 0.4$ with CURRENT disturbance of $V_h = 1.5m/s$ at $\psi_c = pi/4$.

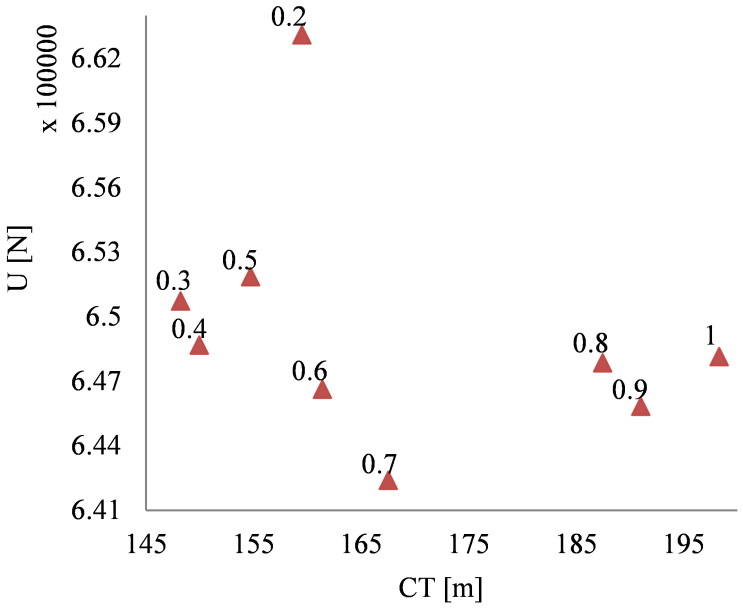

Figure 5.23: Pareto efficiency of LLOS course control without CURRENT disturbance.

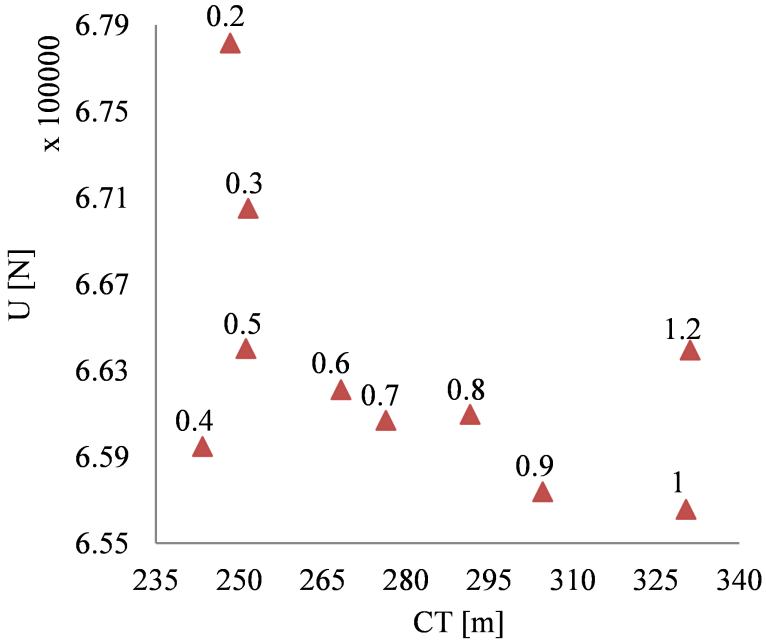

Figure 5.24: Pareto efficiency of LLOS course control with CURRENT disturbances of $V_h = 0.6m/s$ and $\psi_c = pi/4$.

5.5.2 SELOS Guidance

The SELOS guidance with course control is given by (5.89) with (5.1)-(5.3) and (5.10), which is:

$$\psi_d = \psi_{los} - \beta^n = tan^{-1}\left(\frac{y_{los} - y^n}{x_{los} - x^n}\right) - \beta^n. \tag{5.119}$$

The SELOS guidance gains are set as: $R_{min} = 0.9, a = 1.001, c = 0.001$. The PF performance and Pareto efficiency with and w/o CURRENT disturbance are shown in Fig 5.25-5.27.

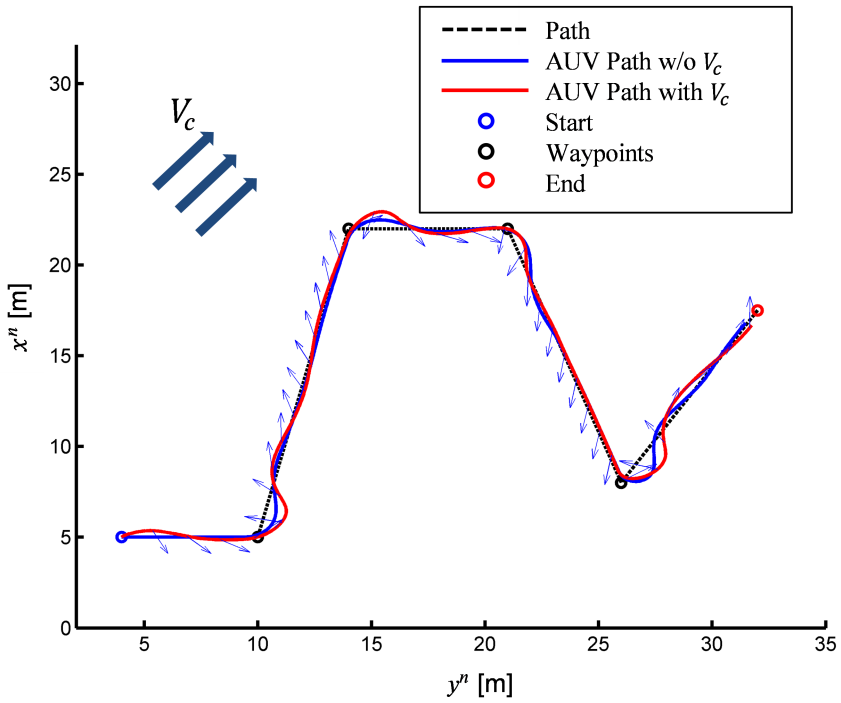

Figure 5.25: Performance of SELOS course control at $R_{min} = 0.9$ with CURRENT disturbances of $V_h = 0.6m/s$ at $\psi_c = pi/4$.

5.5.3 VF Guidance

The desired heading angle with course control for VF guidance is given by replacing ψ_{los} with ψ_{vf} in (3.20) when $\gamma_p = 0$, which is:

$$\psi_d = \psi_{vf} - \beta^n = -\frac{2}{\pi} k_v \tan^{-1}(K_p y_e) - \beta^n. \tag{5.120}$$

The performance and Pareto efficiency of VF guidance in course control are illustrated in Figures 5.28-5.31, which also show that the guidance can closely follow the path under significant CURRENT disturbance of $V_h = 1.5m/s$ similarly to LLOS and SELOS.

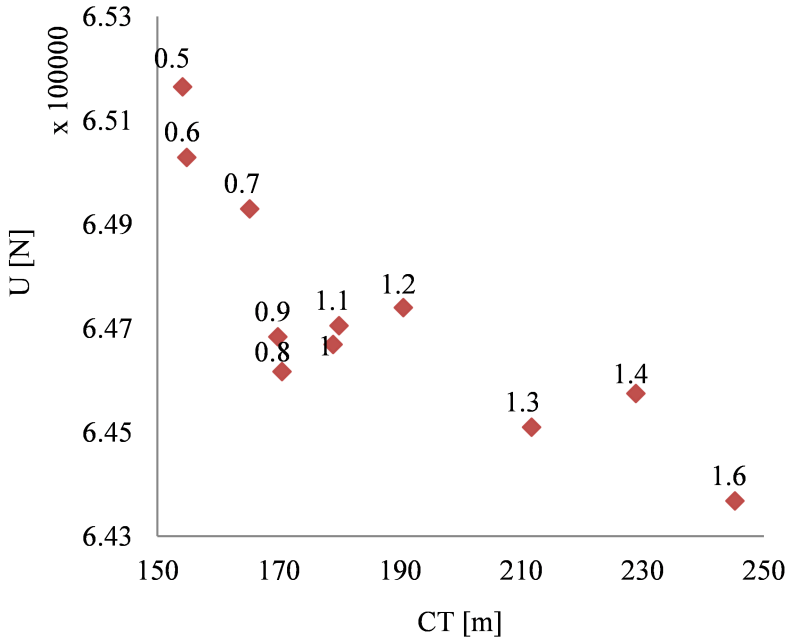

Figure 5.26: Pareto efficiency of SELOS course control without CURRENT disturbance.

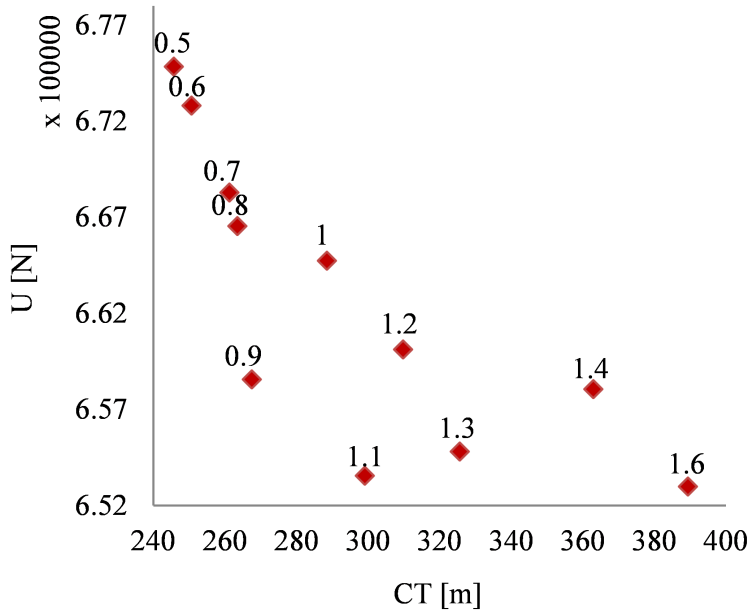

Figure 5.27: Pareto efficiency of SELOS course control with CURRENT disturbances of $V_h = 0.6m/s$ at $\psi_c = pi/4$.

5.5.4 Comparison

The sample sum of the cross-track error and control effort are shown in Table 5.1 for the best tuning values of the guidance laws chosen from their Pareto efficiency plots. The

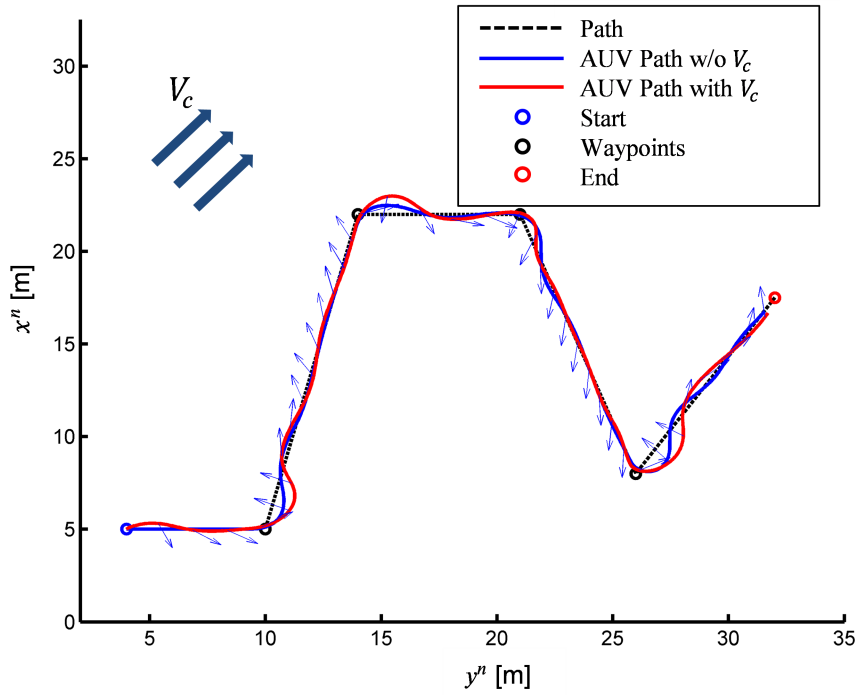

Figure 5.28: Performance of VF course control at $k_v = 1.8$ and $K_p = 1.4$ with and w/o a CURRENT disturbances of $V_h = 0.6m/s$ at $\psi_c = pi/4$.

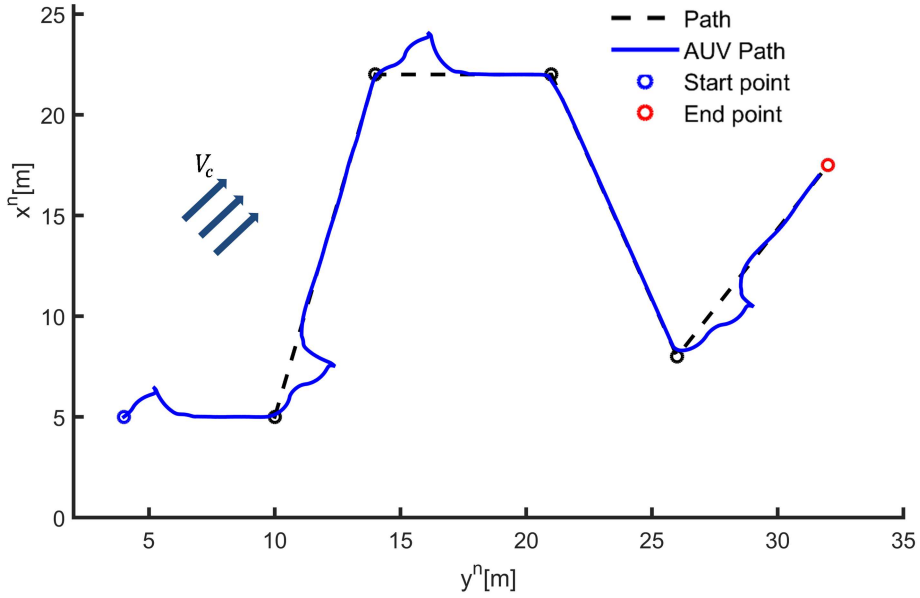

Figure 5.29: Performance of VF course control at $k_v = 1.8$ and $K_p = 1.4$ with CURRENT disturbances of $V_h = 1.5m/s$ at $\psi_c = pi/4$.

advantages and disadvantages of the guidance laws are grouped in Table 5.2, and it is clear that there is no simultaneous winner in both performance indexes.

All of the guidance laws provide similar robustness against CURRENT disturbances,

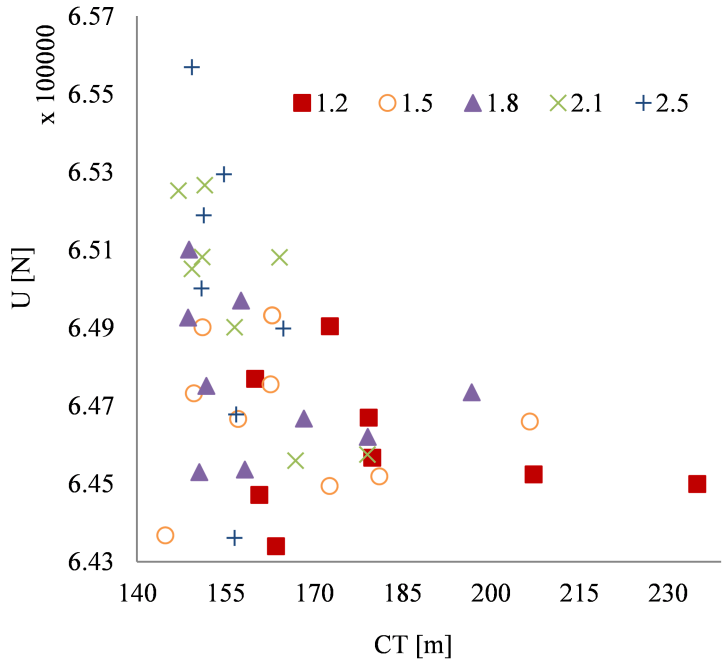

Figure 5.30: Pareto efficiency of VF course control without CURRENT disturbance.

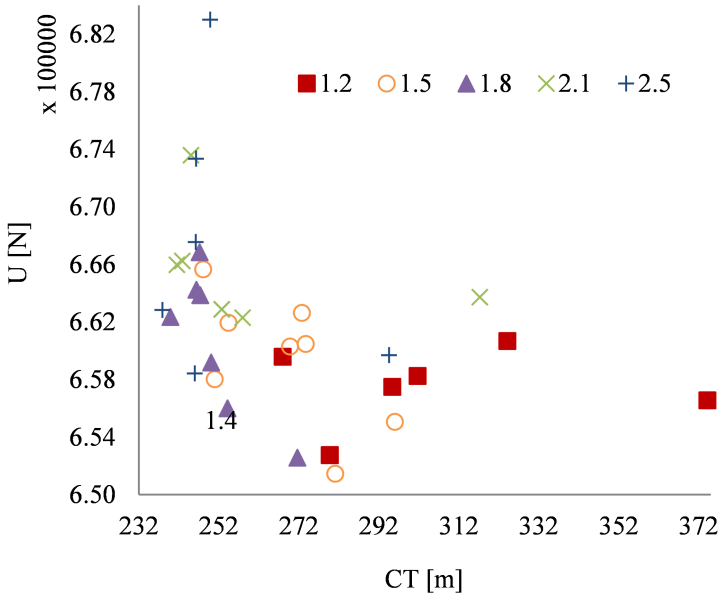

Figure 5.31: Pareto efficiency of VF course control with CURRENT disturbances of $V_h = 0.6m/s$ at $\psi_c = pi/4$.

Guidance law	Tuning values	Cross-track error (CT[m])	Control effort (U[N])
SELOS	$R_{min} = 0.9$	169.9	646840
SELOS ($V_c = 0.6\ m/s$)		267.5	658570
LLOS	$\Delta = 0.4$	149.9	648680
LLOS ($V_c = 0.6\ m/s$)		243.4	659490
VF	$k_v = 1.8$ $k_f = 1.4$	158.3	645360
VF ($V_c = 0.6\ m/s$)		254.2	656020

Table 5.1: The cross-track error and control effort produced for each guidance under the best tuning values.

Guidance law	Tuning values	Advantages	Disadvantages
SELOS	$R_{min} = 0.9$	Less control effort than LLOS; Better at following curved paths (Sujit et. al., 2014)	Highest cross-track error
LLOS	$\Delta = 0.4$	Lowest cross-track error; simplest design	Highest control effort
VF	$k_v = 1.8$ $k_f = 1.4$	Lowest control effort; less cross-track error than SELOS	Two tuning parameters; chattering effect (Sujit et. al., 2014; Caharija et. al., 2015)

Table 5.2: Summary of the performance of each guidance laws in course control with constant CURRENT disturbance of $V_h = 0.6m/s$ and $\psi_c = \pi/2$.

constrary to what is reported in (Sujit et al., 2014). The LLOS guidance law is a relatively simple design and provides the lowest cross-track error. However, it can only provide a low cross-track error when $\triangle$ is tuned small, and a global small constant $\triangle$ can result in overshoot and oscillations. In addition, note that the cross-track error for all three guidance laws do not differ remarkably. Thus, other than slightly being simple and good at providing low cross-track error, the LLOS guidance law is the worst choice in terms of control effort and thus energy efficiency.

The VF guidance provides medium cross-track error and lowest control effort, requires two tuning parameters, and is known to exhibit chattering effect. As shown in Chapter 3, the VF guidance law is structurally similar to the LLOS guidance law when $k_v = \pi/2$. There are two tuning parameters for VF guidance where there is no intuitive way to tune them other than trial-and-error based approaches. Thus, VF guidance is only a good choice if energy efficiency is of utmost concern and that the tuning effort and chattering effects are not of concern.

The SELOS guidance provides medium control effort and there is only on tuning variable. In this case, the SELOS is the best choice when energy efficiency are of top priorities and the path involves curved paths and some cross-track errors are tolerable.

Therefore, selecting a best guidance law highly depends on the nature of the task. The comparison here provides a good idea on how to select the best guidance law for a chosen application.

5.6 SELOS Course Control of Fully-Actuated UVs

The fully-actuated UV PF case with actuation in sway DOF obviously provides better performance against disturbances due to the available control input to counteract the CURRENT in sway. The PF performance and robustness of SELOS course control with speed allocation in this case under CURRENT and/or WAVE disturbances are studied using the revised relative dynamics.

5.6.1 System Model

In the fully actuated case the relative system model is obtained by updating the sway dynamics by inserting a sway input force τ_v into the yaw kinetics (5.76):

$$\dot{v}^f = -\frac{1}{m_{22}}(-m_{23}\dot{r}^f + c_{23}r^f + d_{22}v^f - \tau_v). \tag{5.121}$$

5.6.2 Speed Allocation and Control Objective

Speed Allocation

The speed allocation similarly allows the design of both v_d^n and v_d^f, but v_d^n isof main interest in PF applications. An intuitive design for v_d^n in sway actuated case and under CURRENT and/or WAVE disturbance is to let it equal to the opposite of v_c so that it can counteract the effect of drift caused by v_c, i.e. $v_d^n = -v_c$. However, the vehicle could not follow the path under CURRENT disturbance using this design and a feedback sway controller. This is because the yaw controller competes with the sway controller in course control through the feedback of sideslip in the desired heading, which is a function of sway. After a few successful trial and error, a design of $v_d^n = k_{sa}v_c$ with k_{sa} between 0.2 and 0.8 produced significant disturbance rejection for the given CURRENT disturbance. Therefore, in this case, v_d^n is designed as:

$$v_d^n = .3v_c. \tag{5.122}$$

There could be an optimal value for different designs, system parameters and different direction of the CURRENTNote that when v_d^n is designed the same as the underactuated case (5.84), which corresponds to $k_{sa} = 1$, the disturbance rejection quality was similar despite having an actuation and a controller in sway.

The solution for u_d^n sways the same as in the underactuated case.

Control Objective

The additional control objective for sway in this case is added to the existing ones in (5.90)-(5.92) for tracking v_d^n, which is:

$$\lim_{t\to\infty} v^n(t) = v_d^n(t), \tag{5.123}$$

5.6.3 Sway Controller

The error in sway under CURRENT disturbance is defined similarly and expressed using speed allocation in (5.82) where $v_d^f \neq 0$ in this case due to (5.122), and relative velocity relationship (5.15) as:

$$\tilde{v} \triangleq v_d^n - v^n = 0.3v_c - v^n = -v^f - 0.7v_c. \tag{5.124}$$

Using CURRENT dynamics (5.68) and the new sway dynamics (5.121), the sway error dynamics is given by:

$$\dot{\tilde{v}} = -\dot{v}^f - 0.7\dot{v}_c = \frac{1}{m_{22}}(m_{23}\dot{r}^f + c_{23}r^f + d_{22}v^f - \tau_v) - 0.7r^n u_c. \tag{5.125}$$

The feedback controller for sway is then given by:

$$\tau_v = c_{23}r^n + d_{22}v^f + m_{23}\dot{r}^n + m_{22}(k_v\tilde{v} - 0.7r^n u_c), \tag{5.126}$$

since $r^n = r^f$ for CURRENT irrotational in NED and $k_v > 0$ is proportional gain. The desired horizontal acceleration $\dot{U}_{hd}^n$ can simply be designed by $\dot{U}_{hd}^n = k_U\tilde{U}$, where $k_U > 0$ is derivative gain and $\tilde{U} = U_{hd}^n - U_h^n$. Again, the feedback controller requires relative velocities and CURRENT and/or WAVE velocities. Stability of the closed-loop system (5.125) is analysed using the time-derivative of the LFC $V_v \triangleq (1/2)\tilde{v}^2$, which is:

$$\dot{V}_v = -k_v\tilde{v}^2 \leq 0. \tag{5.127}$$

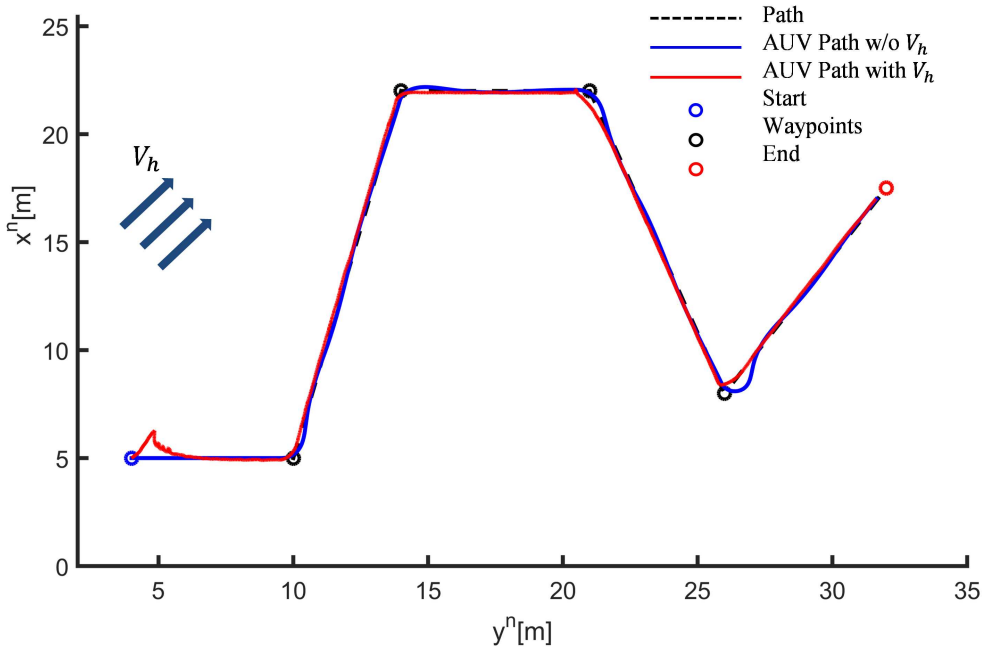

Figure 5.32: Performance of SELOS sliding course control with and w/o CURRENT disturbance of $V_h = 1.5m/s$ at $\psi_c = 45^o$.

$\dot{V}_v$ is negative definite and hence, the origin $\tilde{v} = 0$ of (5.125) is GES. Thus, $\tilde{v}(t) \to 0$ as $t \to \infty$. This achieves control objective (5.123).

5.6.4 Simulation

The PF performance of course control for the fully-actuated UV is studied using the model of 3-DOF Girona-500 AUV with the new relative vehicle dynamics and CURRENT disturbance. The initial NED position, vehicle heading and relative velocities were set to $\boldsymbol{\eta}^n_{b/n} = [4,5,0]$ and $\boldsymbol{\nu}^b_{b/n} = \boldsymbol{\nu}^f_{b/f} = [0,0,0]$, and the maximum desired horizontal relative velocity is $U^n_{hd} = 1m/s$. The PF problem consists of straight-lines connecting waypoints given by: $wpx = [5,22,22,8,\ 17.5]$, $wpy = [10,14,21,26,32]$. The PF tasks are also carried out with and w/o horizontal CURRENT disturbances and position and heading zero average random noises, which remain the same. The SELOS guidance SMC gains, actuator limits and maximum desired yaw rate remain the same as in the underactuated case, and the additional gain for sway controller is $k_v = 55$. The guidance system gains are set as: $R_{min} = 0.9, a = 1.01, c = 0.001, k_r = k_a = k_1 = 1, T_s = 0.05$.

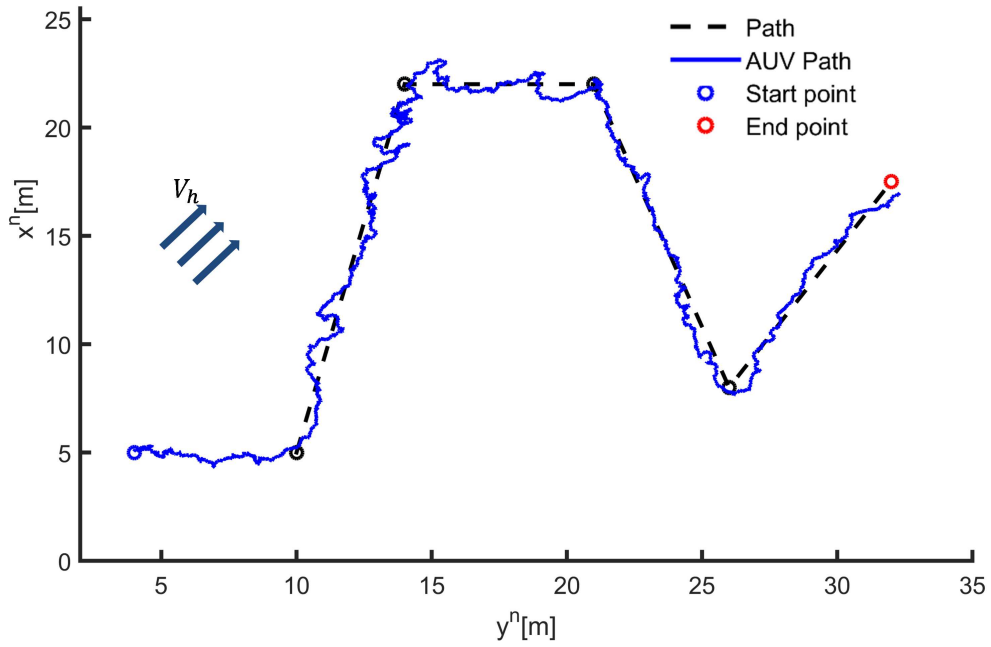

Figure 5.33: Performance of SELOS sliding course control with CURRENT disturbance of $V_h = 1.5m/s$ at $\psi_c = 45^o$, and position and heading zero average random noise of $\pm 5cm$ and $\pm 3^o$ in x^n, y^n and ψ^n resp..

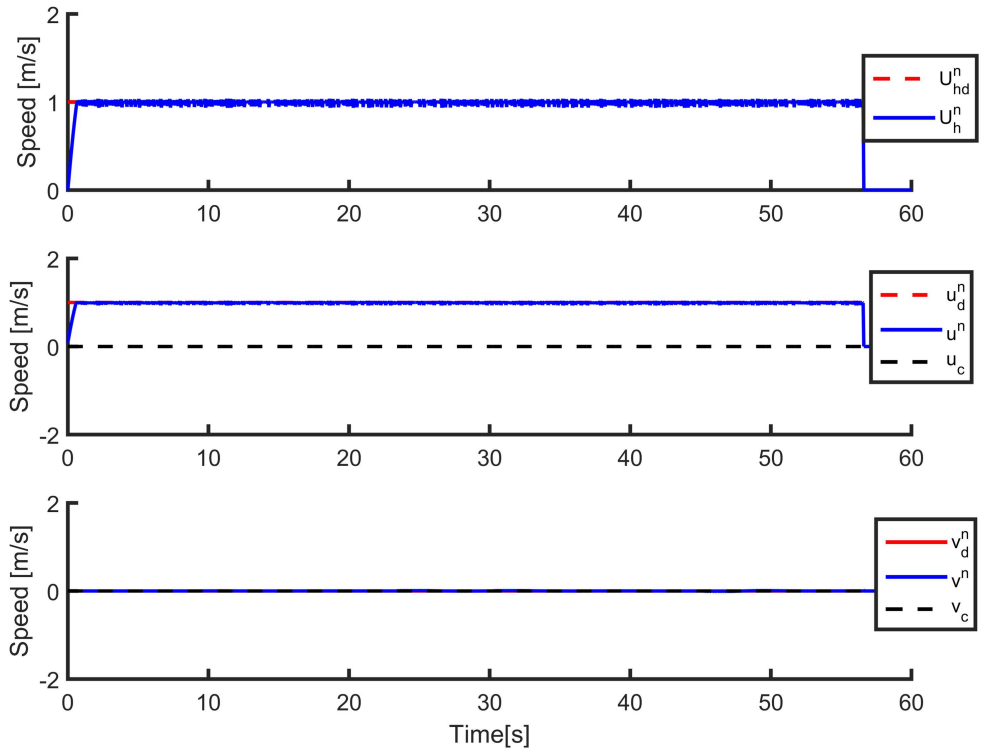

Figure 5.34: Velocity tracking profile of SELOS sliding course control

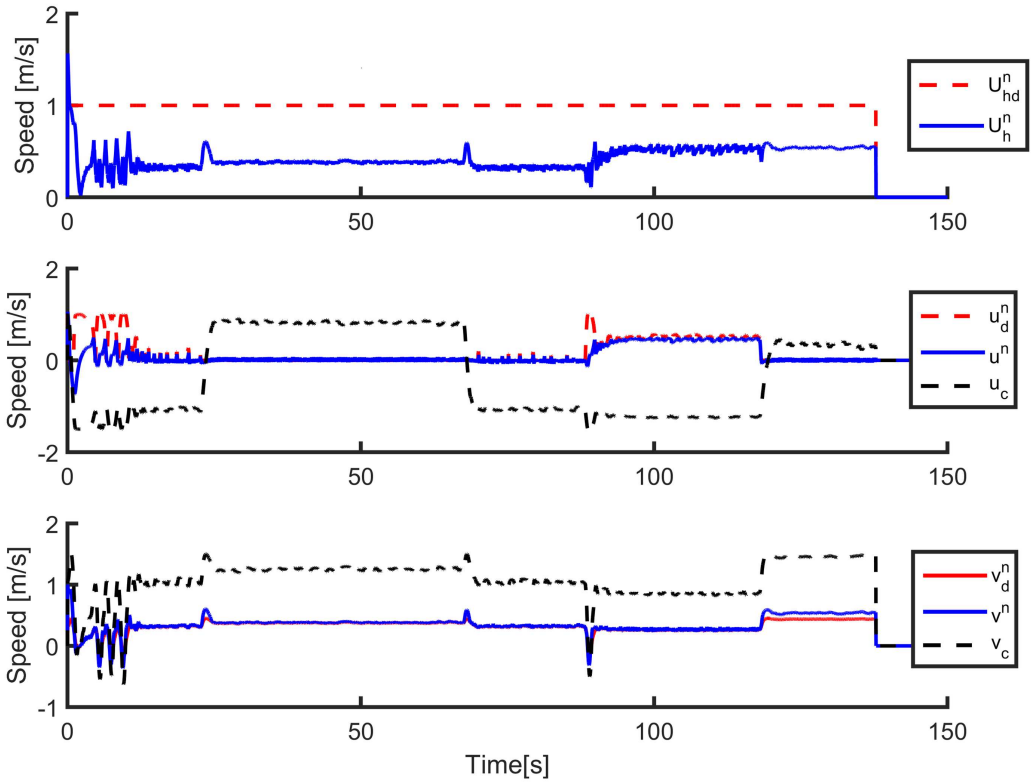

Figure 5.35: Velocity tracking profile of SELOS sliding course control with CURRENT disturbance of $V_h = 1.5m/s$ at $\psi_c = 45^o$.

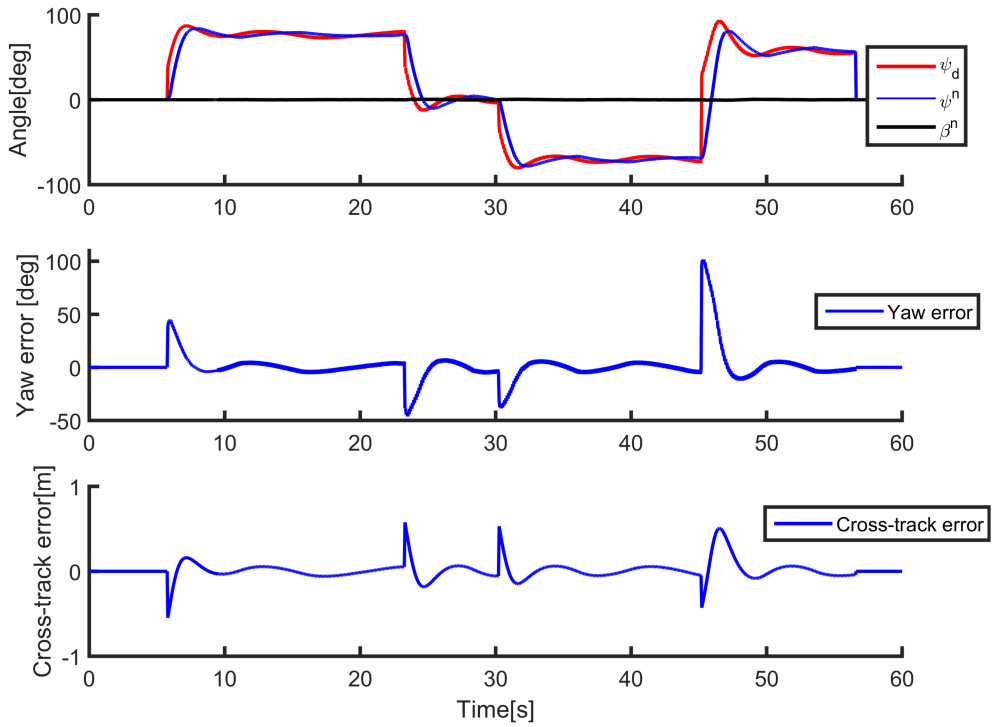

Figure 5.36: Course angle and cross-track error tracking profile of SELOS sliding course control

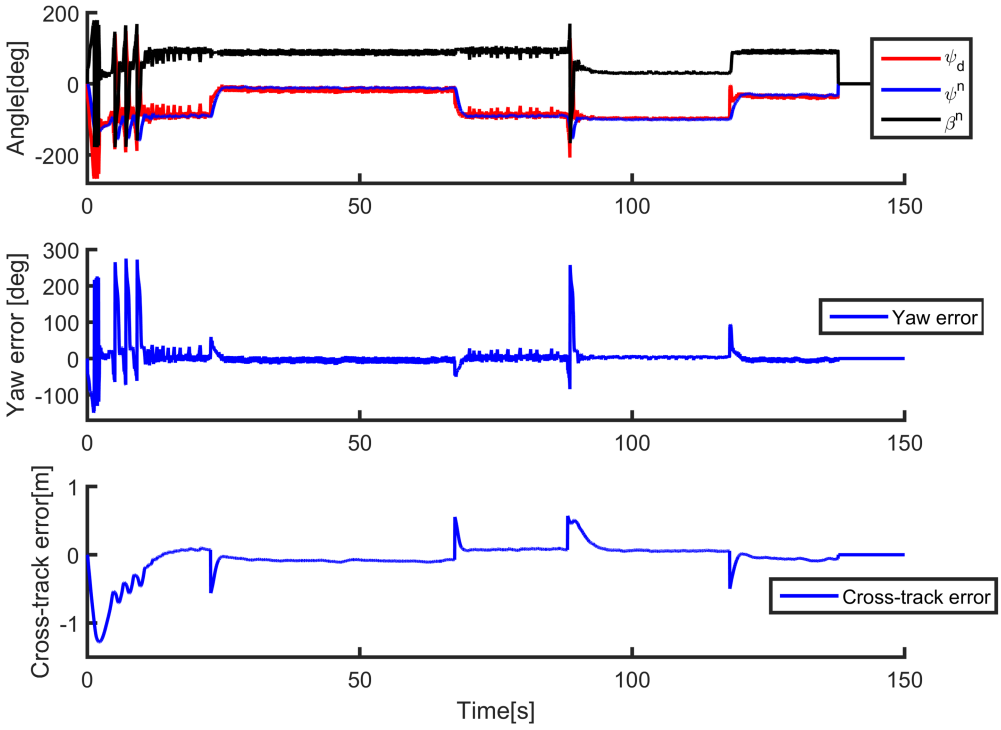

Figure 5.37: Course angle and cross-track error tracking profile of SELOS sliding course control with CURRENT disturbance of $V_h = 1.5m/s$ at $\psi_c = 45^o$.

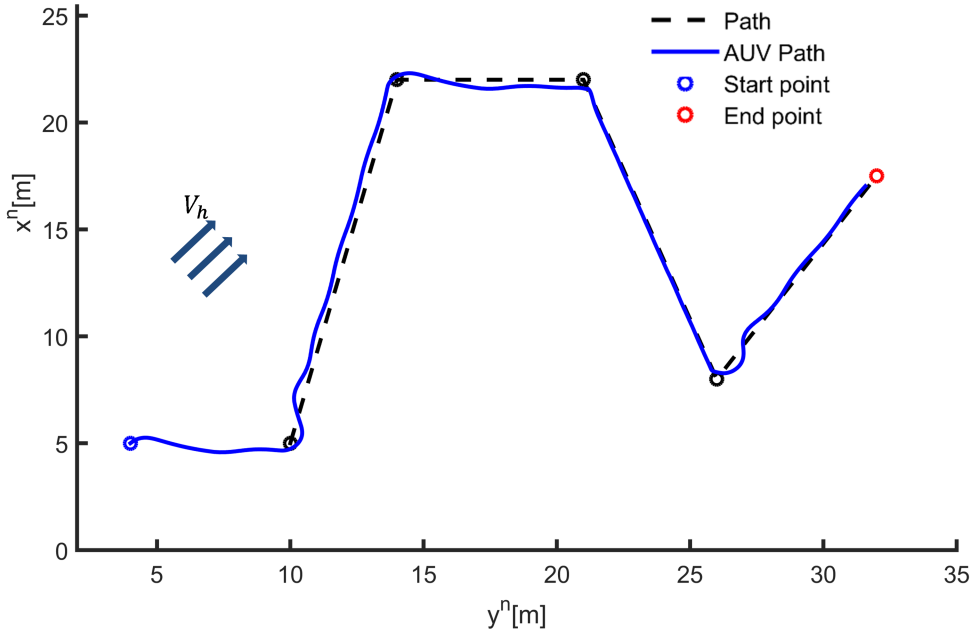

Figure 5.38: Performance of SELOS sliding control with CURRENT disturbance of $V_h = 1.0m/s$ at $\psi_c = 45^o$ and w/o course control.

It can be seen from Figures 5.32-5.33 that the vehicle can follow the path accurately w/ and w/o CURRENT and/or WAVE disturbances of $V_c = 1.5m/s = 150\%U^n_{hd}$. As expected, the vehicle can handle disturbance better with large reduction in cross-track error during turning compared to the underactuated case. Figures 5.34-5.37 show the velocity, heading and cross-track error tracking profiles, where it can be seen that the desired total speed U^n_d is not fully tracked. This is because $k_{sa} < 1$ in (5.122), which produces less u^n_d through the speed allocation. k_{sa} is such designed such to minimize the cross-track error w/o consideration its effect on tracking of U^n_d. Thus, this represents a case for the competition between the dynamics and geometric tasks as discussed in Chapter 3, where clearly a trade-off must be made between the two for limited actuation. This is also a manifestation of performance loss over robustness. The vehicle also took much longer to complete the path. The tracking profile of the heading angle is similar to that of the underactuated case.

During the design of speed allocation for v^n_d that a direct counteracting design of $v^n_d = -v_c$ against v_c could not result in disturbance rejection due to a competition between yaw and sway control action in course control. Thus, this design of $v^n_d = -v_c$ has been tested without course control and its PF performance is shown in 5.38, where it can be seen that this design can also handle a CURRENT disturbance of $V_h = 1m/s$ w/o course control. This is also a better disturbance rejection compared to the underacatuaed case w/o course control as shown in the comparison of Figure 5.13 for cross-track errors. However, course control still allows much better disturbance rejection in both cases.

5.7 Summary

The LOS course control for PF of UVs subject to environmental disturbances has been presented in this chapter with linear and nonlinear stability analysis. An effective and simple tuning strategy for the ELOS guidance have been presented, which is also simpler than previous such modifications proposed. Nonlinear stability analysis has been separated for straight and curved-paths due to time-variance of the LOS vector R. These stability results

include LES and SGES of ELOS guidance laws for straight and cuved paths, resp., SGES of SELOS guidance law. Using the improved understanding of the relative velocities, it was shown in the linear analysis that the all fluid-dependent disturbances (CURRENT and/or WAVE) already exist in the cross-track error dynamics.

The nonlinear control systems designed for kinetics simulations are SMC and nonlinear PID, where both has shown similar level of disturbance rejection. The SMC provided stronger GES but some chattering and requires full-state feedback, while the PID guaranteed GAS and requires anti-windup. The PF course control employs the unique formulation and solution of the speed allocation problem, which additionally contributed to reduction in oscillations. The PF has been carried out for both fully and sway-underactuated cases where it has been shown that course control has significant impact on disturbance rejection, while in full actuation the speed allocation also offers significant disturbance rejection.

A comparison between SELOS, LLOS and VF guidance laws has been provided, and their advantages and disadvantages has been discussed to point out their suitability to different PF tasks.

Chapter 6

3-D LOS Course Control with Speed Allocation

This chapter presents the extension of the LOS course control and stability analysis to 3D PF scenarios in 4 and 5-DOFs. The vertical course control problem has been formulated with a new definition of the vertical-slip with detailed illustrations of the 3-D PF problem. In the more common 4-DOF scenario with passively stabilized roll and pitch DOFs, a planar speed assignment method has been developed to track the LOS vector in 3-D. In the 5-DOF case, a yaw and pitch diving scenario with surge is considered, which represents the case of most of the torpedo-shaped UVs without direct heave control. Using the new models of CURRENT in 3-D, simulation results also show the guidance systems can follow the path under significant CURRENT and/or WAVE disturbances and position and heading measurement noises.

6.1 3-D LOS Guidance with Course Control

The LOS guidance laws and course control can be extended to 3-D, but its formulation is not trivial as will be seen in this section. Before formulating the vertical LOS guidance laws in this thesis, the 3-D lookahead distance $\triangle$ and LOS vector R have to be decom-

posed into three components each in relative to NED frame. Thus, $\triangle$ and R satisfy:

$$\triangle^2 = \triangle_x^2 + \triangle_y^2 + \triangle_z^2, \tag{6.1}$$

$$R^2 = R_x^2 + R_y^2 + R_z^2. \tag{6.2}$$

where $\triangle_x^2, \triangle_y^2, \triangle_z^2$ and R_x^2, R_y^2, R_z^2 are the projections of $\triangle$ and R onto the North, East and Down axes of the NED frame, respectively. In general, they are given by using their Euler angles in NED as:

$$\triangle_x = \triangle \cos\psi_p, \quad \triangle_y = \triangle \cos\phi_p, \quad \triangle_z = \triangle \cos\theta_p, \tag{6.3}$$

$$R_x = x_{los} - x^n, \quad R_y = y_{los} - y^n, \quad R_z = z_{los} - z^n. \tag{6.4}$$

where ϕ_p and θ_p are the path roll path pitch angles and defined for the general case as:

$$\phi_p = \text{atan2}\left(\frac{z'_p(\mu)}{y'_p(\mu)}\right), \tag{6.5}$$

$$\theta_p = \text{atan2}\left(\frac{z'_p(\mu)}{x'_p(\mu)}\right). \tag{6.6}$$

Note that only the path yaw or heading and path pitch angles θ_p exist in the literature, which are referred as the path-tangential and vertical path-tangential angles in (T. Fossen, 2011).

The geometry of 3-D LOS guidance for straight-line PF is depicted in Fig 6.1. The figure also illustrates the off-track error e_{yz} which is the normal distance from the vehicle to the path and can be generally defined as:

$$e_{yz} = \sqrt{(x^n - x_p(\mu))^2 + (y^n - y_p(\mu))^2 + (z^n - z_p(\mu))^2} = \sqrt{e_x^2 + e_y^2 + e_z^2}. \tag{6.7}$$

where $P_p(\mu) = (x_p(\mu), y_p(\mu), z_p(\mu))$ is the intersection of this normal line and the path which is assumed unique. It can also be seen from Fig 6.1 that the off-track error e_{yz} is

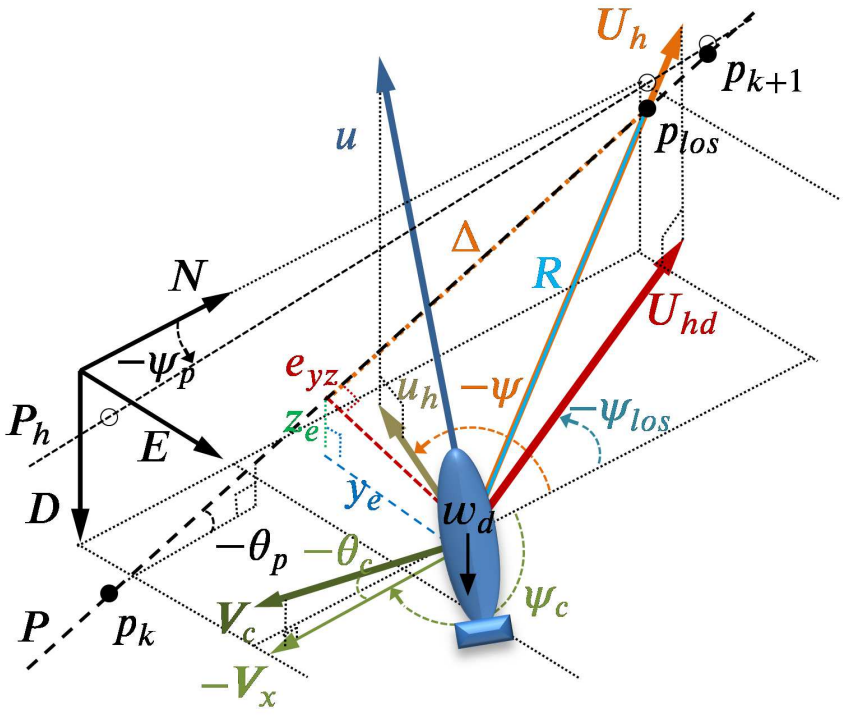

Figure 6.1: Geometry of 3-D ELOS guidance, where $u_h^n = u^n \cos\theta^n$ is the horizontal projection of u^n on N-E plane, P_h is the horizontal projection of the path P on N-E. The angle ψ^n took negative sign because it is temporarily rotated in anti-clockwise direction from North in this case.

the hypotenuse of the Pythagoras formed between y_e, z_e and e_{yz} and is also given by:

$$e_{yz} = \sqrt{{y_e}^2 + {z_e}^2}. \tag{6.8}$$

where z_e is the vertical-track error similarly defined by:

$$z_e = \sqrt{(x^n - x_p(\mu))^2 + (z^n - z_p(\mu))^2} = \sqrt{e_x^2 + e_z^2}, \tag{6.9}$$

as can be seen from Figure 6.2. The definition of z_e is similar to that first presented in (Børhaug & Pettersen, 2005). Note as discussed in the revised cross-track and along-track error in Chapter 3, the coordinate transformation as in (A. Lekkas & Fossen, 2013) which will result in a different z_e is not necessary for its formulation since the center of NED is already placed on $P_p(\mu) = (x_p(\mu), y_p(\mu), z_p(\mu))$, where consequently, $\phi_p = \theta_p = \psi_p = 0$.

Vertical LLOS Guidance Law

The vertical LOS guidance can now be devised to produce a desired vertical LOS angle θ_{los} if pitch DOF is actuated and controlled in the vertical plane. The general vertical LOS angle was initially presented by (Børhaug & Pettersen, 2005) as:

$$\theta_{los} = \tan^{-1}\left(\frac{z_e}{\triangle}\right), \tag{6.10}$$

A. Lekkas and Fossen (2013) also propose a different vertical LOS guidance where the $\triangle$ is separated into the vertical and horizontal components, which is given by:

$$\theta_d = \theta_{los} = \theta_p + \alpha + \tan^{-1}\left(\frac{z_e}{\triangle_v}\right), \tag{6.11}$$

where α was referred as an angle of attack of the vehicle, where it is not stated whether it is relative to NED or FLOW, and $\triangle_v$ is the vertical look-ahead distance which is only denoted and not defined.

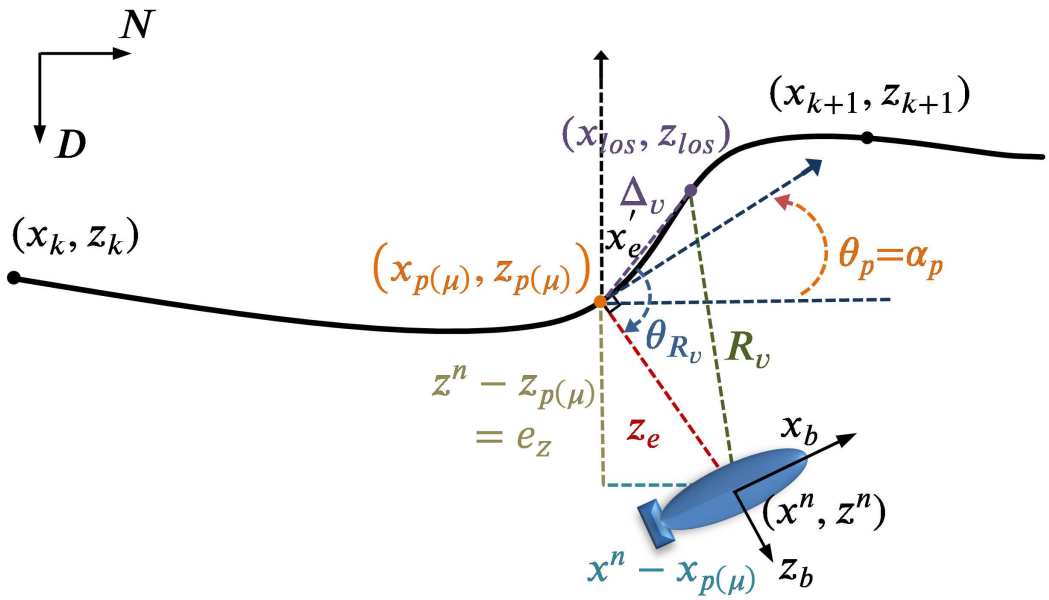

Figure 6.2: Geometry of vertical LOS guidance for PF of curved path.

The the vertical LOS guidance law in this thesis is different to these past approaches and has been formulated according to a more detailed illustration in the N-D plane for

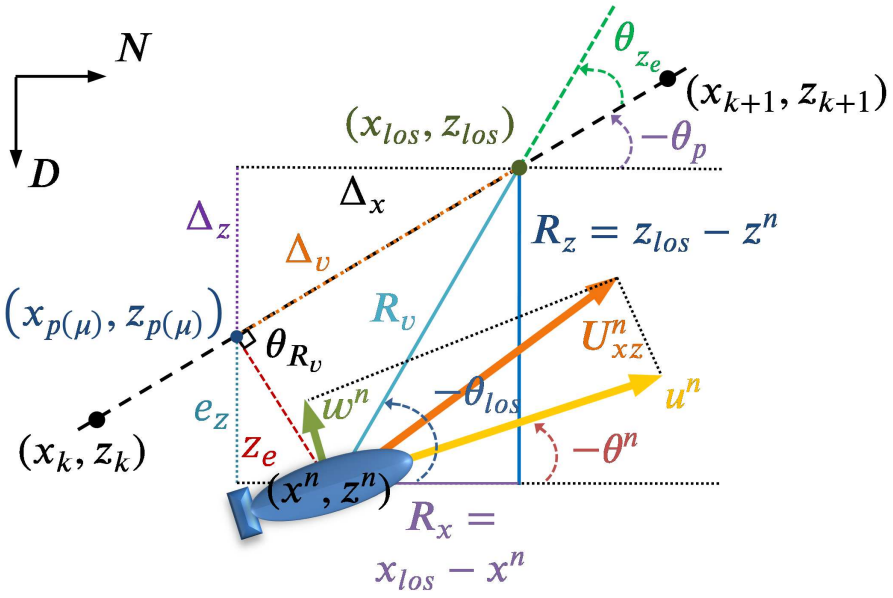

Figure 6.3: Geometry of vertical LOS guidance for PF of straight path.

curved and straight line PF cases in Figures 6.2 and 6.3. From Fig 6.2, the vertical LOS angle for straight-line PF is then given by:

$$\theta_{los} = \text{atan2}\left(\frac{z_{los} - z^n}{x_{los} - x^n}\right) = \theta_p - \theta_{z_e} = \theta_p - \tan^{-1}\left(\frac{z_e}{\triangle_v}\right). \tag{6.12}$$

where $\triangle_v$ referred as the *look-above distance*. $\triangle_v$ and R_v are given by:

$$\triangle_v^2 = \triangle_x^2 + \triangle_z^2, \tag{6.13}$$

$$R_v^2 = R_x^2 + R_z^2. \tag{6.14}$$

It can be seen that the look-ahead distances in (6.3) are also given by:

$$\triangle_x = x_{los} - x_p(\mu), \quad \triangle_y = y_{los} - y_p(\mu), \quad \triangle_z = z_{los} - x_z(\mu), \tag{6.15}$$

Vertical ELOS Guidance Law

In case of ELOS guidance, the conventional ELOS guidance creates an enclosing circle around the vehicle in 2-D (T. I. Fossen et al., 2003). In 3-D, it can similarly create an

enclosing sphere with the LOS vector R centered at vehicle NED position and use one of the sphere-path interceptions as the reference point $p_{los} = (x_{los}, y_{los}, z_{los})$ to calculate ψ_{los} for horizontal heading. The equation for the enclosing sphere is given by:

$$(x_{los} - x^n)^2 + (y_{los} - y^n)^2 + (z_{los} - z^n)^2 = R^2, \tag{6.16}$$

$$\frac{y_{los} - y_k}{x_{los} - x_k} = \frac{y_{k+1} - y_k}{x_{k+1} - x_k} = \tan\psi_p, \tag{6.17}$$

$$\frac{z_{los} - z_k}{x_{los} - x_k} = \frac{z_{k+1} - z_k}{x_{k+1} - x_k} = \tan\theta_p, \tag{6.18}$$

and the vertical ELOS angle is given by (6.12).

Horizontal LOS Guidance in 3-D

The horizontal LOS guidance law will take different notations in 3-D since the look-ahead distance is also decomposed into 3 components. In this case, the horizontal LOS guidance law is expressed in 3-D as:

$$\psi_{los} = \text{atan2}\left(\frac{y_{los} - y^n}{x_{los} - x^n}\right) = \psi_p - \tan^{-1}\left(\frac{y_e}{\triangle_h}\right) \tag{6.19}$$

where only $\triangle_h = \sqrt{\triangle_x + \triangle_y}$ as the horizontal lookahead distance is replaced with $\triangle$ of the 2-D case in previous chapter.

For horizontal ELOS guidance in 3-D, the horizontal LOS angle is also given by (6.19)

3-D SELOS Guidance Law

The switching mechanism of the SELOS scheme is also extended to 3-D from 2-D and is achieved similarly using a sigmoid function that acts as a continuous switch, where R is now given by:

$$R = R_{min} + \frac{1}{2}\left[\frac{(ae_{yz} - R_{min})(e_{yz} - R_{min})}{c + |e_{yz} - R_{min}|}\right], \tag{6.20}$$

For $a \approx 1$ and $c \approx 0$, this becomes:

$$R = \begin{cases} R_{min}, & \text{if } e_{yz} \leq R_{min} \\ ae_{yz}, & \text{if } e_{yz} > R_{min} \end{cases} \tag{6.21}$$

The condition $R \geq e_{yz}$ provided by the SELOS scheme in (6.21) also ensures $R \geq z_e$. As in the 2-D case, the guidance law achieved using (6.20) behaves exactly as the traditional ELOS guidance when $e_{yz} \leq R_{min}$, and when $e_{yz} > R_{min}$, R becomes nearly normal to the path providing a perpendicular ψ_{los} and θ_{los} for $a \approx 1$. This is naturally desired as the vehicle is far away from the path, and thus providing a shortest-path strategy for path-approaching when the vehicle is outside R_{min}. The vertical and horizontal components of the SELOS can also be formulated using the corresponding vectors in the vertical and horizontal planes.

3-D Course Control

In 4-DOF course control with pitch and roll passively stabilized, the vertical LOS guidance is not necessary to make the vehicle follow the path. In this case, a different mechanism is required to make the vehicle follow the LOS vector simultaneously in both planes, which is presented later in this chapter. Thus, the 3-D course control in 4-DOF is realized with course control only in the horizontal plane, i.e. only ψ_d with β^n is tracked in terms of attitude control.

In 5-DOF, both yaw and pitch angles are activated and controlled towards the horizontal and vertical courses angle in yaw and pitch ψ_d and θ_d, resp., to track the LOS reference point. The desired horizontal heading angle is similarly to that in the 2-D case, but formulated using the notations and horizontal LOS angle in 3-D as in (6.19):

$$\psi_d = \psi_{los} - \beta^n = \text{atan2}\left(\frac{y_{los} - y^n}{x_{los} - x^n}\right) - \beta^n = \psi_p - \tan^{-1}\left(\frac{y_e}{\triangle_h}\right) - \text{atan2}\left(\frac{v^n}{u^n}\right). \tag{6.22}$$

The desired pitch angle for vertical course control θ_d is now similarly formulated

by incorporates the new *vertical-slip* β_z^n in NED which is similarly adopted from the horizontal plane to the vertical plane for compensating the vertical drift. This is now given by:

$$\theta_d = \theta_{los} - \beta_z^n = \text{atan2}\left(\frac{z_{los} - z^n}{x_{los} - x^n}\right) - \beta_z^n = \theta_p + \tan^{-1}\left(\frac{-z_e}{\triangle_v}\right) - \beta_z^n, \tag{6.23}$$

where β_z^n is given by:

$$\beta_z^n = \text{atan2}\left(\frac{w^n}{u^n}\right) = \sin^{-1}\left(\frac{w^n}{U_h^n}\right), \tag{6.24}$$

Note that the vertical-slip is only defined in this thesis. A vertical-slip for roll DOF can also be formulated to complete the 3-D course control problem. However, the 3-D course control in this thesis focuses on yaw and pitch DOFs, and that it is achieved by tracking the desired yaw and pitch angles with sideslip and vertial-slip.

6.2 Track Error Dynamics and Stability of 3-D LOS Guidance Laws

The off-track error formulated can be a part of the geometric task of the maneuvering problem to be minimized to achieve the PF objective. Time-differentiating (6.9) gives the dynamics of the off-track error:

$$\dot{e}_{yz} = \frac{\dot{y}_e y_e + \dot{z}_e z_e}{4\sqrt{{y_e}^2 + {z_e}^2}}. \tag{6.25}$$

which is a combination of the cross-track and vertical-track error dynamics. Thus, stability of the vertical LOS guidance laws for stabilizing the vertical track-error dynamics are presented in this section.

6.2.1 4-DOF Vertical-Track Error Dynamics

Stability of Vertical-Track Error w/o Guidance Laws

The vertical-track error dynamics can be studied independently w/o vertical guidance laws. The vertical-track error can also be similarly described by the kinematics in D-position of the NED frame when the center of NED is coincided with the path-projection point $P_p(\mu) = (x_p(\mu), y_p(\mu), z_p(\mu))$. First, the 4-DOF relative kinematics is extracted from (4.5) and expanded as:

$$\dot{x}^n = u^n \cos\psi^n - v^n \sin\psi^n, \tag{6.26}$$

$$\dot{y}^n = u^n \sin\psi^n + v^n \cos\psi^n, \tag{6.27}$$

$$\dot{z}^n = w^n, \tag{6.28}$$

$$\dot{\psi}^n = r^n. \tag{6.29}$$

Then, the dynamics in path-z direction is given by replacing $\dot{z}^n$ with $\dot{z}_e$, which is:

$$\dot{z}_e = w^n. \tag{6.30}$$

Note that similarly to the reasoning behind direction of convergence towards a reference frame, the vehicle is only convergent to the path when it is moving opposite to the direction of the path axes. In this case, the vehicle is on the path projection point $P_p(\mu) = (x_p(\mu), y_p(\mu), z_p(\mu))$ which is the center of NED, and thus the vehicle has to move against the directions of NED to converge towards this point. Therefore, when the sign of w^n is reverted in (6.30), it becomes:

$$\dot{z}_e = -w^n. \tag{6.31}$$

Theorem 6.1 *(Vertical-Track Error in 4-DOF w/o Vertical Guidance Laws) The origin* $z_e = 0$ *of the vertical-track error dynamics* (6.31) *is GAS.*

Proof. The time-derivative of the LFC considered for (6.31) $V_z = (1/2){z_e}^2$ is given by:

$$\dot{V}_z = \dot{z}_e z_e = -w^n z_e. \tag{6.32}$$

Since $\dot{V}_z$ is negative definite, the origin $z_e = 0$ of (6.31) is GAS. □

Thus, the stability of the vertical-track error does not require any guidance laws in the 4-DOF case.

6.2.2 5-DOF Vertical-Track Error Dynamics

In 5-DOF with passively-stabilized roll, the vertical-track error dynamics is obtained similarly by setting $\phi^n = 0$ in the relative kinematics. SGES tability results of vertical LLOS guidance law has been analyzed in (Wigg et al., 2016), although it is in the form of integral LLOS and for straight line PF. The stability results of LOS guidance laws for 5-DOF track-error dynamics in this section include SGES of vertical ELOS and SELOS guidance laws for straight and curved paths.

Stability of Vertical ELOS Guidance with Constant R: Straight Path

The 5-DOF relative kinematics with pitch is given by:

$$\dot{x}^n = u^n \cos\psi^n \cos\theta^n - v^n \sin\psi^n + {}^n w \cos\psi^n \sin\theta^n, \tag{6.33}$$

$$\dot{y}^n = u^n \sin\psi^n \cos\theta^n + v^n \cos\psi^n + w^n \sin\psi^n \sin\theta^n, \tag{6.34}$$

$$\dot{z}^n = -u^n \sin\theta^n + w^n \cos\theta^n, \tag{6.35}$$

$$\dot{\theta}^n = q^n, \tag{6.36}$$

$$\dot{\psi}^n = r^n / \cos\theta^n. \tag{6.37}$$

The vertical-track error dynamics $\dot{z}_e$ in 5-DOF is similarly given by the vehicle z-kinematics in (6.35) for similar choice of the origin and direction of NED on $P_p(\mu) = (x_p(\mu), y_p(\mu), z_p(\mu))$

of the path. Thus, replacing $\dot{z}_e$ with $\dot{z}$ and using the error expression $\tilde{\theta} = \theta_d - \theta^n$ gives:

$$\dot{z}^n = -u^n \sin(\theta_d - \tilde{\theta}) + w^n \cos(\theta_d - \tilde{\theta}). \tag{6.38}$$

When θ_d is tracked such that $\tilde{\theta} = 0$, this becomes:

$$\dot{z}_e = -u^n \sin\theta_d + w\cos\theta_d = \sqrt{u^{n2} + w^{n2}} \sin\left[\theta_d + \tan^{-1}\left(\frac{w^n}{u^n}\right)\right]. \tag{6.39}$$

in phase-amplitude form, where w^n is reverted as $-w^n$ for the same reason as in Theorem 6.1. Substituting θ_d from (6.23) into (6.39) and using the identity $\sin(\tan^{-1}(x)) = x/\sqrt{1+x^2}$ gives:

$$\dot{z}_e = \sqrt{u^{n2} + w^{n2}} \left(\frac{-z_e}{\sqrt{\triangle_v^2 + {z_e}^2}}\right) = -\frac{U_v^n z_e}{R_v}. \tag{6.40}$$

for straight-path when $R_v = \sqrt{\triangle_v^2 + {z_e}^2}$ and $U_v^n = \sqrt{u^{n2} + w^{n2}}$.

Theorem 6.2 *(Vertical ELOS Guidance Law for Straight-Path) The vertical ELOS guidance law with the vertical-slip given by* (6.23) *renders the origin* $y_e = 0$ *of the vertical-track error dynamics* (6.40) *LES if* U_v^n *and* R_v *satisfy* $0 < U_v^n$ *and* $0 < z_e \leq R_v$*, and that* θ_d *is tracked such that* $\tilde{\theta} = 0$.

Proof. The proof is similar to the horizontal case and is given in the Appendix B.

Stability of Vertical ELOS Guidance with Constant R: Curved Path

When following a curved-path, the relationship between R, e_{yz} and $\triangle$ is not a Pythagoras but a triangle and thus, R is given by using the cosine rule as:

$$R_v^2 = z_e^2 + \triangle_v^2 - 2z_e\triangle_v \cos\theta_{R_v}, \tag{6.41}$$

using the cosine law where θ_R. Substituting (6.41) into the vertical-track error dynamics of LLOS in (6.40) gives the vertical-track error dynamics of vertical ELOS for curved

path as:

$$\dot{z}_e = -\frac{U_v^n z_e^2}{\sqrt{R_v^2 + 2z_e \triangle_v \cos\theta_{R_v}}}. \tag{6.42}$$

Theorem 6.3 *(Vertical ELOS Guidance Law for Curved-Path) The vertical ELOS guidance law with the vertical-slip given by* (6.23) *renders the origin* $y_e = 0$ *of the vertical-track error dynamics* (6.42) *SGES if* U_v^n *and* R_v *satisfy* $0 < U_{vmin}^n \leq U_v^n$ *and* $0 < z_e \leq R_v \leq R_{vmax}$*, and that* θ_d *is tracked such that* $\tilde{\theta} = 0$.

Proof. The proof is similar to previous approaches and is given in Appendix B.

Stability of Vertical SELOS Guidance: Straight Path

In the vertical plane, R_v for SELOS scheme can also be given by:

$$R_v^2 = (x_{los} - x^n)^2 + (z_{los} - z^n)^2 \tag{6.43}$$

$$R_v = R_{vmin} + \frac{1}{2}\left[\frac{(az_e - R_{vmin})(z_e - R_{vmin})}{c + |z_e - R_{vmin}|}\right], \tag{6.44}$$

For $z_e > R_{vmin}$, $c \approx 0$ and $a \approx 1$:

$$R_v \approx z_e. \tag{6.45}$$

In straight-line path-following, $R_v = \sqrt{{z_e}^2 + {\triangle_v}^2} \approx z_e$. Substituting this into the cross-track error dynamics (6.40) gives the cross-track error of vertical SELOS for straight-line PF as:

$$\dot{z}_e = -\frac{U_v^n}{z_e} z_e = -U_v^n. \tag{6.46}$$

Theorem 6.4 *(Vertical SELOS Guidance Law for Straight-Path) The vertical SELOS guidance law with sideslip given by* (6.18)*,* (6.23) *and* (6.43)-(6.44) *renders the origin* $z_e = 0$ *of the cross-track error dynamics* (6.46) *SGES if* U_v^n*,* $z_e > R_{vmin}$ *and* c *satisfy* $0 < U_{vmin}^n < U_v^n$*,* $z_e > R_{vmin}$ *and* $0 < c \leq c_{max}$*, and* θ_d *is tracked such that* $\tilde{\theta} = 0$.

Proof. The proof is similar to previous approaches and is given in Appendix B.

Stability of Vertical SELOS Guidance: Curved Path

The dynamics of the vertical-track error for SELOS is can be obtained by substituting R_v in (6.45) into (6.42), which is given by:

$$\dot{z}_e = -\frac{U_v^n}{\sqrt{z_e^2 + 2z_e\triangle\cos\theta_{R_v}}}z_e = -\frac{U_v^n}{\sqrt{R_v^2 + 2z_e\triangle\cos\theta_{R_v}}}z_e. \tag{6.47}$$

when $c \approx 0$ and $a \approx 1$, and since $R_v \approx z_e$ in SELOS.

Theorem 5.5 *(Vertical SELOS guidance law for curved path) The vertical SELOS guidance law with sideslip given by* (6.18)*,* (6.23) *and* (6.43)-(6.44) *renders the origin* $z_e = 0$ *of vertical-track error dynamics* (6.47) *SGES if* U_v^n *and* R_v *satisfy* $0 < U_v^n, 0 < R_{vmin} < z_e < R_v \leq R_{vmax}$*, and* θ_d *is tracked such that* $\tilde{\theta} = 0$.

Proof. The proof is similar to previous approaches and, thus, is given in Appendix B.

6.3 4-DOF SELOS Course Control

Most underwater vehicles are controlled in 4-DOF with passively-stabilized pitch and roll DOFs, and the 4-DOF model, thus, represents a wide class of UVs. Both fully actuated and sway underactuated cases of 4-DOF PF cases are considered in this section.

6.3.1 Underactuated UVs

System Model

With passively-stabilized roll and pitch DOFs, the 4-DOF relative system model is extracted from the 6-DOF relative kinematics, the relationship of relativity (4.4)-(4.5), and

the relative kinetics (4.51) as:

$$\dot{\boldsymbol{\eta}}^n_{b/n} = \boldsymbol{J}(\boldsymbol{\Theta}^n_{b/n})\boldsymbol{\nu}^b_{b/n}, \tag{6.48}$$

$$\boldsymbol{\nu}^f_{b/f} = \boldsymbol{\nu}^b_{b/n} - \boldsymbol{\nu}^b_{c/n}, \tag{6.49}$$

$$\boldsymbol{M}\dot{\boldsymbol{\nu}}^f_{b/f} + \boldsymbol{C}(\boldsymbol{\nu}^f_{b/f})\boldsymbol{\nu}^f_{b/f} + \boldsymbol{D}(\boldsymbol{\nu}^f_{b/f})\boldsymbol{\nu}^f_{b/f} + \boldsymbol{g}(\boldsymbol{\Theta}^n_{b/n}) = \boldsymbol{\tau}_{act}. \tag{6.50}$$

where $\boldsymbol{\eta}^n_{b/n} \triangleq [x^n, y^n, z^n, \psi^n]^T$ is the vehicle position and heading relative to and expressed in NED, $\dot{\boldsymbol{\eta}}^n_{b/n} = [\dot{x}^n, \dot{y}^n, \dot{z}^n, \dot{\psi}^n]^T$ is the vehicle velocities and yaw rate relative to and expressed in NED, $\boldsymbol{\nu}^b_{b/n} \triangleq [u^n, v^n, w^n, r^n]^T$ is the vehicle velocities in surge, sway, heave, and yaw rate relative to NED and expressed in BODY, $\boldsymbol{\nu}^f_{b/f} \triangleq [u^f, v^f, w^f, r^f]^T$ is the vehicle velocities in surge, sway, heave, and yaw rate relative to FLOW frame and expressed in BODY, and $\boldsymbol{\nu}^n_{c/n} \triangleq [u_c, v_c, w_c, 0]^T$ is CURRENT velocities and yaw rate relative to NED and expressed in BODY. The control input vector $\boldsymbol{M}^{-1}\boldsymbol{B}\boldsymbol{f} = [\tau_u, 0, \tau_w, \tau_\psi]^T$ consists of surge, heave forces and yaw moment. This structure of the control input vector is obtained by assuming that $\{b\}$ of BODY is positioned in the pivot point such that yaw moment has no effect on sway motion Fredriksen and Pettersen (2006). The system in (6.60) is underactuated in sway since the dimension of $\boldsymbol{f}$ is less than that of the system. Expanding (6.48) gives the 4-DOF relative kinematics as:

$$\dot{x}^n = u^n \cos\psi^n - v^n \sin\psi^n, \tag{6.51}$$

$$\dot{y}^n = u^n \sin\psi^n + v^n \cos\psi^n, \tag{6.52}$$

$$\dot{z}^n = w^n, \tag{6.53}$$

$$\dot{\psi}^n = r^n. \tag{6.54}$$

The 4-DOF CURRENT is irrotational and constant (or slowly varying) such that the CURRENT yaw rate $V_\psi = r_c = 0$ and $\dot{\boldsymbol{V}}_c = 0$. The 4-DOF CURRENT expressed in BODY

can be reduced from 6-DOF in (4.56) by setting $\phi^n = \theta^n = 0$, which is:

$$\boldsymbol{\nu}^b_{c/n} \triangleq [u_c, v_c, w_c, r_c]^T = \boldsymbol{J}(\boldsymbol{\Theta}^n_{c/n} - \boldsymbol{\Theta}^n_{b/n})^T \boldsymbol{V}^n_{c/n}, \tag{6.55}$$

The linear part of this expands to:

$$u_c = V_x c(\psi_c - \psi^n)c\theta_c + V_y s(\psi_c - \psi^n)c\theta_c - V_z s\theta_c, \tag{6.56}$$

$$\begin{aligned} v_c = {} & V_x[c(\psi_c - \psi^n)s\theta_c s\phi_c - s(\psi_c - \psi^n)c\phi_c] \\ & + V_y[c(\psi_c - \psi^n)c\phi_c + s(\psi_c - \psi^n)s\theta_c s\phi_c] + V_z c\theta_c s\phi_c, \end{aligned} \tag{6.57}$$

$$\begin{aligned} w_c = {} & V_x[s(\psi_c - \psi^n)s\phi_c + c(\psi_c - \psi^n)c\phi_c s\theta_c] \\ & + V_y[s(\psi_c - \psi^n)s\theta_c c\phi_c - c(\psi_c - \psi^n)s\phi_c] + V_z c\theta_c c\phi_c. \end{aligned} \tag{6.58}$$

The dynamics of the CURRENT can be obtained by time-differentiating (6.56)-(6.58):

$$\dot{u}_c = r^n[V_x s(\psi_c - \psi^n)c\theta_c - V_y c(\psi_c - \psi^n)c\theta_c], \tag{6.59}$$

$$\begin{aligned} \dot{v}_c = {} & -r^n V_x[s(\psi_c - \psi^n)s\theta_c s\phi_c + c(\psi_c - \psi^n)c\phi_c] \\ & + r^n V_y[c(\psi_c - \psi^n)s\theta_c s\phi_c - s(\psi_c - \psi^n)c\phi_c], \end{aligned} \tag{6.60}$$

$$\begin{aligned} \dot{w}_c = {} & r^n V_x[c(\psi_c - \psi^n)s\phi_c - s(\psi_c - \psi^n)c\phi_c s\theta_c] \\ & - r^n V_y[s(\psi_c - \psi^n)s\phi_c - c(\psi_c - \psi^n)s\theta_c c\phi_c], \end{aligned} \tag{6.61}$$

since $\dot{V}_c = 0$ and the CURRENT Euler rates $\dot{\boldsymbol{\Theta}}^n_{c/n} = \mathbf{0}$ for irrotational CURRENT in NED.

The system matrices are given by the following:

$$\boldsymbol{M} \triangleq \begin{bmatrix} m_{11} & 0 & 0 & 0 \\ 0 & m_{22} & 0 & m_{24} \\ 0 & 0 & m_{33} & 0 \\ 0 & m_{24} & 0 & m_{44} \end{bmatrix} = \begin{bmatrix} m + X_{\dot{u}} & 0 & 0 & 0 \\ 0 & m + Y_{\dot{v}} & 0 & mx_g \\ 0 & 0 & m + Z_{\dot{w}} & 0 \\ 0 & mx_g & 0 & I_z + N_{\dot{r}} \end{bmatrix}, \tag{6.62}$$

$$\boldsymbol{C}(\boldsymbol{\nu}^f) \triangleq \begin{bmatrix} 0 & 0 & 0 & c_{14}(v^f, r^f) \\ 0 & 0 & 0 & c_{24}(u^f) \\ 0 & 0 & 0 & 0 \\ -c_{14}(v^f, r^f) & -c_{24}(u^f) & 0 & 0 \end{bmatrix}, \tag{6.63}$$

$$\begin{aligned} \boldsymbol{D}(\boldsymbol{\nu}^f) &\triangleq \{d_{11}(u^f), d_{22}(v^f), d_{33}(w^f), d_{44}(r^f)\} \\ &= diag\{X_u + X_{|u|u}|u^f|, Y_v + Y_{|v|v}|v^f|, Z_w + Z_{|w|w}|w^f|, N_r + N_{|r|r}|r^f|\}. \end{aligned} \tag{6.64}$$

The structure of the system matrices in (6.62)-(6.63) are obtained by assuming that the vehicle is symmetric in port-starboard, and that the BODY frame is located along the centre-line of the vehicle (T. Fossen, 2011), in which case it is common that $y_g \approx 0$. The system dynamics relative to FLOW is obtained by expanding relative kinetics (6.50) as:

$$\dot{u}^f = -\frac{1}{m_{11}}(c_{14}r^f + d_{11}u^f - \tau_u), \tag{6.65}$$

$$\dot{v}^f = -\frac{1}{m_{22}}(-m_{24}\dot{r}^f + c_{24}r^f + d_{22}v^f), \tag{6.66}$$

$$\dot{w}^f = -\frac{1}{m_{33}}(d_{33}u^f - \tau_w), \tag{6.67}$$

$$\dot{r}^f = -\frac{1}{m_{44}}(-m_{24}\dot{v}^f + d_{44}r^f - c_{14}u^f - c_{24}v^f - \tau_\psi). \tag{6.68}$$

Note that $r^n = r^f$ since the CURRENT is irrotational in NED and that the yaw component of CURRENT $V_\psi = 0$.

Control Objective and Speed Allocation

The control objectives are similar to that formulated in the 2-D case which also have to include heave DOF and the off-track error. The control objectives for solving the

maneuvering problem in 4-DOF sway underactuated case are given by:

$$\lim_{t\to\infty} u^n(t) = u_d^n(t), \tag{6.69}$$

$$\lim_{t\to\infty} w^n(t) = w_d^n(t), \tag{6.70}$$

$$\lim_{t\to\infty} \psi^n(t) = \psi_d(t), \tag{6.71}$$

$$\lim_{t\to\infty} y_e(t) = 0. \tag{6.72}$$

$$\lim_{t\to\infty} z_e(t) = 0. \tag{6.73}$$

Desired speeds u_d^n and w_d^n are solved by the speed allocation problem presented in chapter 5:

$$U_d^n \triangleq \sqrt{u_d^{n2} + v_d^{n2} + w_d^{n2}}, \tag{6.74}$$

$$U_{hd}^n \triangleq \sqrt{u_d^{n2} + v_d^{n2}}, \tag{6.75}$$

$$u_d^n \triangleq u_d^f + u_c, \tag{6.76}$$

$$v_d^n \triangleq v_d^f + v_c, \tag{6.77}$$

$$w_d^n \triangleq w_d^f + w_c, \tag{6.78}$$

where U_d^n and U_{hd}^n are pre-assigned to solve for w_d^n and u_d^n, or w_d^n can also be pre-assigned and only the solution for u_d^n is required. $v_d^f = 0$ in (6.77) and u_d^n is given by substituting (6.78) into (6.75):

$$u_d^n = \sqrt{{U_{hd}^n}^2 - v_d^{n2}} = \sqrt{{U_{hd}^n}^2 - {v_c}^2}, \tag{6.79}$$

Planar Speed Assignment

Existing literature on 3-D PF primarily focus on 3, 5 or 6-DOF cases, e.g. (Caharija et al., 2012, 2016; ?, ?), and there are very limited publications on 4-DOF vehicle dynamics. In 4-DOF PF with passively-stabilized vehicle roll and pitch DOFs, the dynamic task has to be divided into horizontal and vertical components to produce the respective speeds for

U_d^n and w_d^n such that the vehicle aims to track the LOS reference point p_{los} simultaneously in both planes. This competition between the horizontal and vertical planes hasn't been sufficiently addressed in guidance-based strategies, to the best knowledge of the authors (A. Lekkas & Fossen, 2013; Caharija et al., 2016). The usual approach is to solve either the horizontal or the vertical task first, which is obviously not energy efficient and is a limited design approach. This problem can classified and is conveniently referred here as *planar speed assignment* problem between the planes.

The speed assignment in this work is achieved by a trajectory generating system that will assign suitable values for U_d^n and w_d^n using the LOS look-above angle θ_{R_z} corresponding to the amount of look-above distance R_z, which is given by:

$$\theta_{R_z} = \text{atan2}\left((z_{los} - z^n), \sqrt{(x_{los} - x^n)^2 + (y_{los} - y^n)^2}\right) = \text{atan2}\left(R_z, R_h\right). \tag{6.80}$$

The desired speed trajectories U_d^n and w_d^n are then given by:

$$U_{hd}^n = \begin{cases} U_{hdmax}^n, & \text{if } \dfrac{|R_z|}{|w^n|} < \dfrac{R_h}{U_h^n} \\ |w_{dmax}^n \tan\theta_{R_z}|, & \text{if } \dfrac{|R_z|}{|w^n|} \geq \dfrac{R_h}{U_h^n} \end{cases} \tag{6.81}$$

$$w_d^n = -\text{sgn}(e_z) \begin{cases} w_{dmax}^n, & \text{if } \dfrac{|R_z|}{|w^n|} < \dfrac{R_h}{U_h^n} \\ \left|U_{hdmax}^n / \tan\theta_{R_z}\right|, & \text{if } \dfrac{|R_z|}{|w^n|} \geq \dfrac{R_h}{U_h^n} \end{cases} \tag{6.82}$$

where $U_{hdmax}^n, w_{dmax}^n > 0$ are the preassigned maximum operating speeds in horizontal and vertical planes of NED, and $\text{sgn}(e_z)$ helps determine the direction of w_d^n which is reversed since the directions of vertical axes of NED frame and the z-axis in software are opposite to each other. The idea behind the speed assignment scheme in Eq. (6.80)-(6.82) is that it compares the expected times of arrival of the vehicle to p_{los} in both planes using the current speeds U_h^n and w^n, and assigns correct values for U_{hd}^n and w_d^n so that he vehicle is commanded to arrive at the reference p_{los} simultaneously in both planes. This

is also equivalent to commanding the vehicle to follow the 3-D LOS vector R in 4-DOF. This is a simple and effective method for desired speed trajectory generation in this 4-DOF case, and another speed allocation system will be required if there are additional DOFs. Therefore, in general, such a speed assignment is a minimal necessity whenever the vehicle aims track a 3-D path closely in both planes, and more advanced designs can be built on this strategy.

The final value for w_d^n will fluctuate between $\pm w_{dmax}^n$ during depth keeping, which is not good for actuators and may result in fluctuation at constant depth. This is similarly avoided at the simplest case by designing w_d^n as increments of the error in heave to added to the current heave speed w^n, which is: $w_d^n = w^n + k_5\tilde{w}$, where k_5 is a gain.

Heave Control

The convergence of the cross-track error is achieved through the same yaw controller as in 2-D and vertical-track error is minimized by a heave controller in 4-DOF. The uncontrolled relative sway dynamics remain the same as in Section 5.2.4 in 4-DOF since the heave dynamics is not coupled with sway when both roll and pitch are decoupled. Note that the underactuated sway error dynamics only remains the same when $v_d^f = 0$ in the speed allocation that is used to derive its error dynamics. In this case, the additional controller required is for the heave DOF to satisfy the control objective (6.70).

The error in heave is defined as $\tilde{w} \triangleq w_d^n - w^n$. Using the CURRENT and heave dynamics in (6.61) and (6.67), the heave error dynamics is given by:

$$\dot{\tilde{w}} = \dot{w}_d^n - \dot{w}^n = \dot{w}_d^n - (\dot{w}^f + \dot{w}_c) = \dot{w}_d^n + \frac{1}{m_{33}}(d_{33}w^f - \tau_w)$$
$$- r^n V_x[s(\psi_c - \psi^n)c\phi_c s\theta_c - c(\psi_c - \psi^n)s\phi_c] + r^n V_y[s(\psi_c - \psi^n)s\phi_c - c(\psi_c - \psi^n)s\theta_c c\phi_c]. \tag{6.83}$$

The feedback-linearizing controller for heave is given by:

$$\begin{aligned}\tau_w = d_{33}w^f + m_{33}\{\dot{w}_d^n + k_w\tilde{w} - r^n V_x[c(\psi_c-\psi^n)c\phi_c s\theta_c - (\psi_c-\psi^n)s\phi_c] \\ -r^n V_y[s(\psi_c-\psi^n)s\phi_c - c(\psi_c-\psi^n)s\theta_c c\phi_c]\},\end{aligned} \tag{6.84}$$

where $k_w > 0$ is proportional gain. The desired surge acceleration $\dot{w}_d^n$ is obtained by: $\dot{w}_d^n = k_2\tilde{w}$, and $k_2 \geq 0$ is gain. Stability of the closed-loop heave system (6.83) is analyzed using the time-derivative of LFC $V_w \triangleq (1/2)\tilde{w}^2$, which is:

$$\dot{V}_w = -k_w\tilde{w}^2 \leq 0. \tag{6.85}$$

$\dot{V}_w$ is negative definite and V_w is positive definite, the origin $\tilde{w} = 0$ of (6.83) is GES. Thus, $\tilde{w}(t) \to 0$ as $t \to \infty$. This achieves control objective (6.70).

Simulation: 4-DOF Underactuation

The straight-line 4-DOF PF performance of 4-DOF Girona-500 AUV has been simulated. The 3-D path consists of straight-lines between waypoints given in NED coordinates by: $wpx = [5,18,25,35,40], wpy = [10,23,25,35,35], wpz = [-15,-15,-6,-6,-15]$. The initial NED position, vehicle heading and relative velocities are set to $\boldsymbol{\eta}_{b/n}^n = [4,1,-1,0]$ and $\boldsymbol{\nu}_{b/n}^b = \boldsymbol{\nu}_{b/f}^f = [0,0,0,0]$, and the maximum desired relative velocities $U_{hdmax}^n = 1m/s$ and $w_{dmax}^n = 0.5m/s$, which gives a total maximum speed of $U_{dmax}^n = 1.12m/s$ in 3-D. The CURRENT velocities are $V_x = V_y = 1.3m/s$, and $V_z = 0.3m/s$, which give its direction in NED as $\phi_c = \theta_c = 18.4^o$ and $\psi_c = 45^o$, which are constant in NED. The guidance and control system gains are set as follows: $R_{min} = 1, a = 1.01, c = 0.001, k_r = k_a = 1, k_\psi = 10, k_d = 55, T_s = 0.05, k_u = k_w = 55, k_1 = k_2 = 1, k_5 = 0.2, \lambda = 1$. Acceleration gains k_1, k_2 are usually small and other controller gains are not very high since the nonliniearities are canceled out by the feedback terms. Similar to the 2-D case, the control input saturate at $\pm 450N$ in surge and heave, and $\pm 250Nm$ in yaw, and there is a limit in yaw rate of $\dot{\psi}_{dmax} = r_{dmax} = 57.3^o/s$.

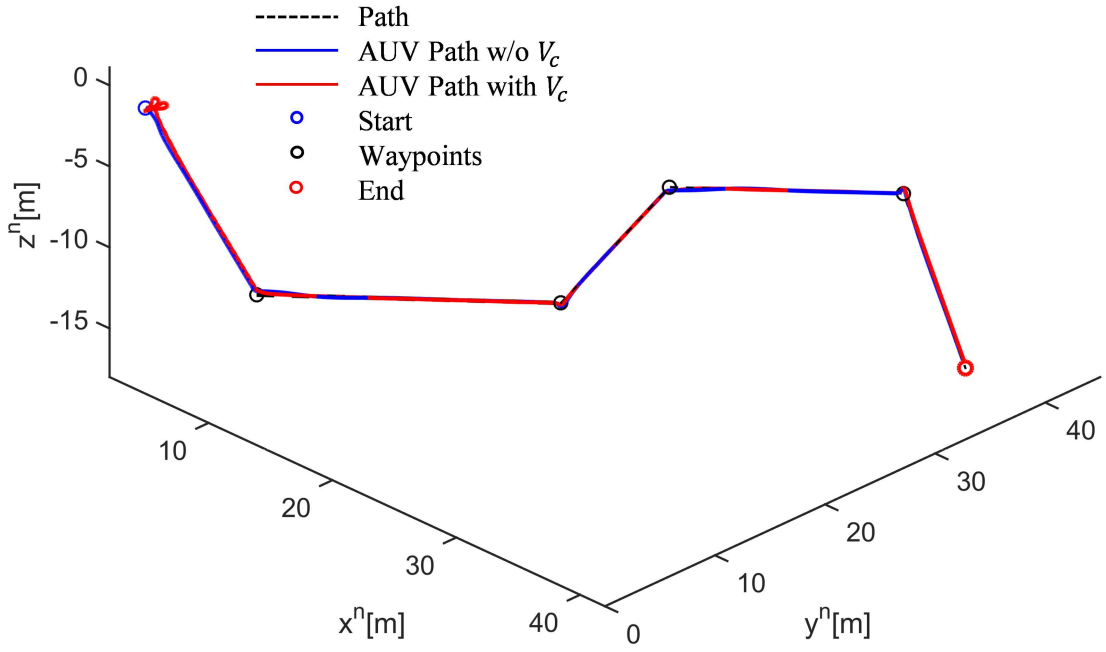

Figure 6.4: Performance of SELOS course control w/ and w/o CURRENT disturbance of $V_x = V_y = 1.3m/s$, and $V_z = 0.3m/s$.

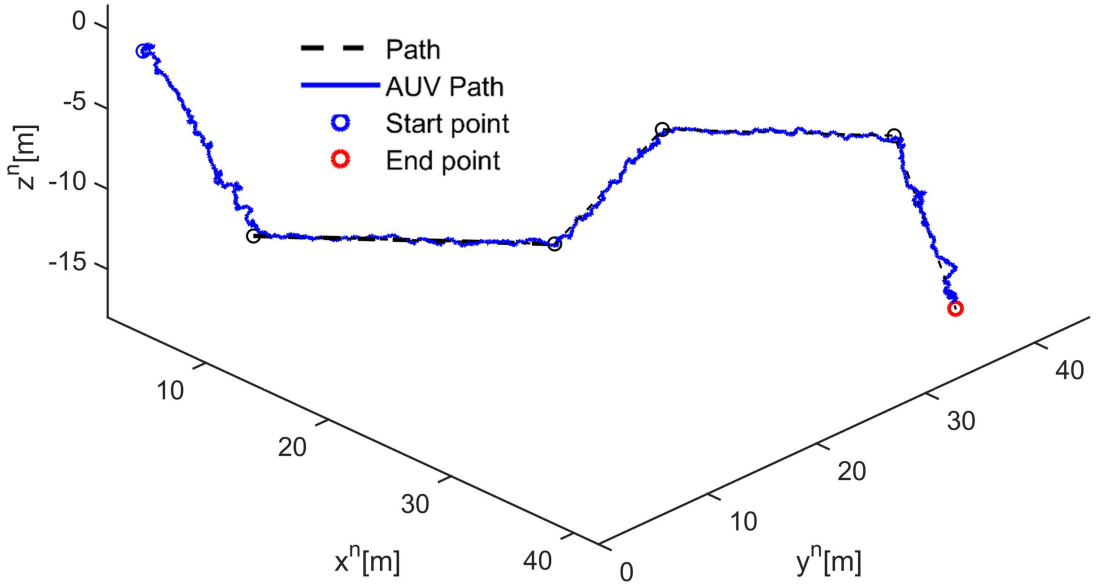

Figure 6.5: Performance of SELOS course control with CURRENT disturbance of $V_x = V_y = 1.3m/s$, and $V_z = 0.3m/s$, and position and heading zero average random uncertainties of $\pm 4cm$ and $\pm 3^o$ in x^n, y^n, z^n and ψ^n, resp..

Figures 6.4-6.5 show that the SELOS course control can make the vehicle accurately track the path with significant CURRENT disturbances and/or measurement noises, with less accuracy in the latter case. The total desired velocity in 3-D would be $U_d^n =$

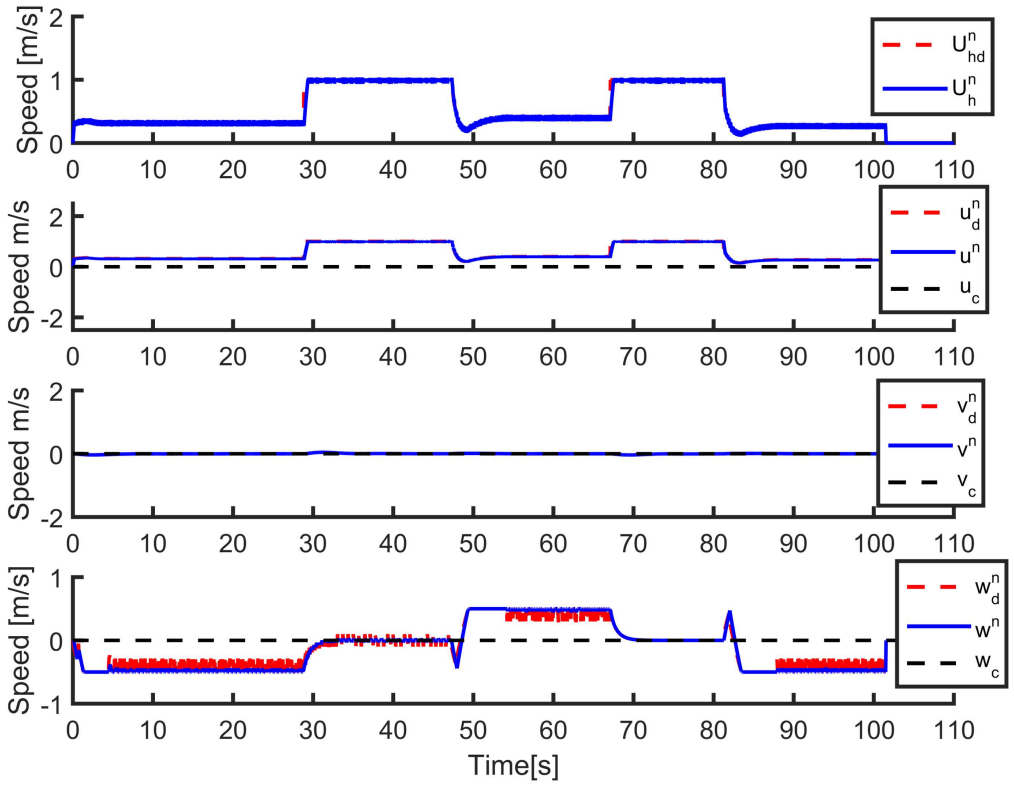

Figure 6.6: Velocity tracking profile of SELOS sliding course control.

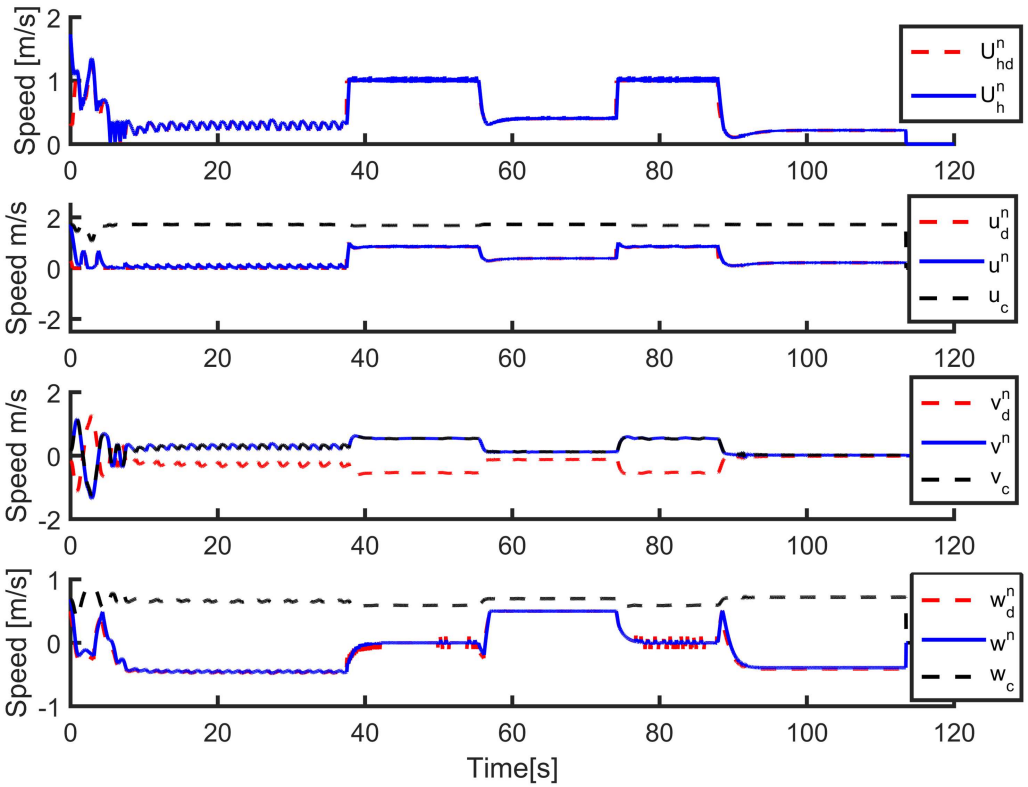

Figure 6.7: Velocity tracking profile of SELOS sliding course control with CURRENT disturbance of $V_x = V_y = 1.3m/s$, and $V_z = 0.3m/s$.

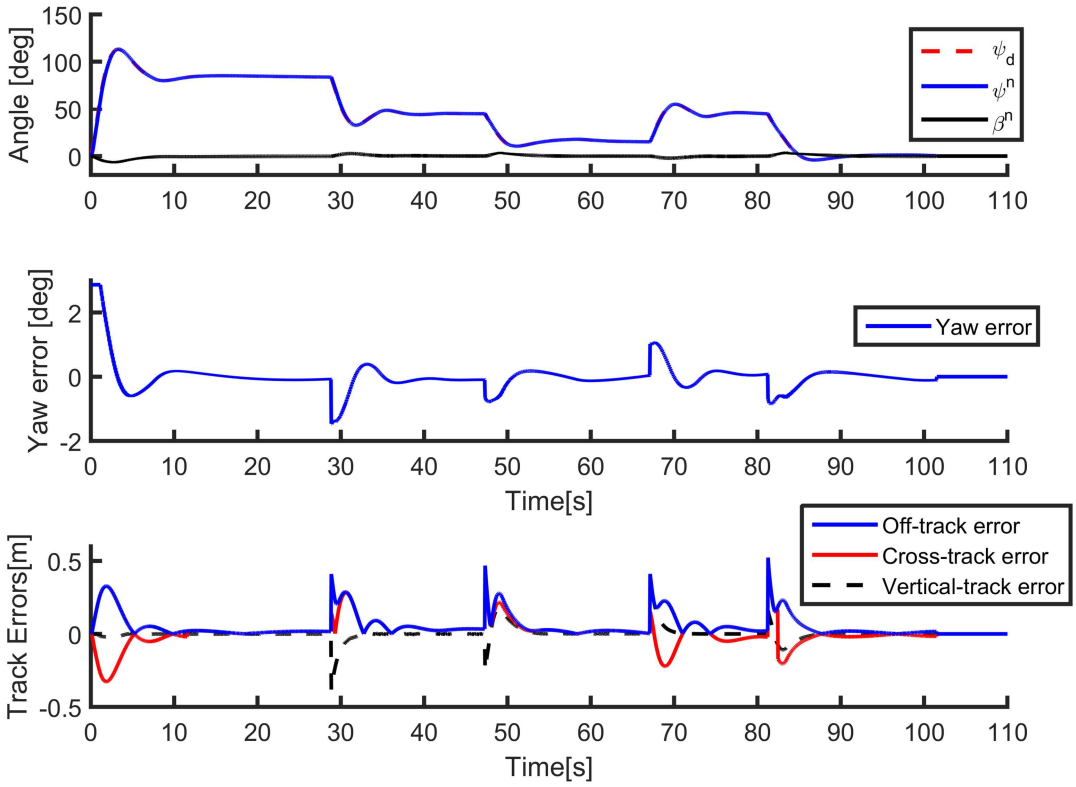

Figure 6.8: Heading angle and track-error tracking profile of SELOS sliding course control.

$\sqrt{{U^n_{hdmax}}^2 + {w^n_{dmax}}^2} = U^n_d = 1.12m/s.$, which puts the strength of the CURRENT intensity at 167%, i.e. $V_c = 1.67U^n_d$. It can be seen from Figure 6.4 that the vehicle struggles to converge to the path in the beginning. This is because the vehicle starting velocity is zero and hence, it cannot counteract the CURRENT as much as it can after it has gained some velocity.

Figures 6.6-6.9 show the velocity, heading angle, and track-error tracking profiles w/ and w/o CURRENT disturbances. These are similar to the ones in 2-D case and show that the track-errors are kept at minimal, and that the higher frequency desired signals are not necessary tracked at all times, which is due to the actuation saturation and also the limit on turning rate that is set at $57.3deg/s(1rad/s)$ for yaw rate.

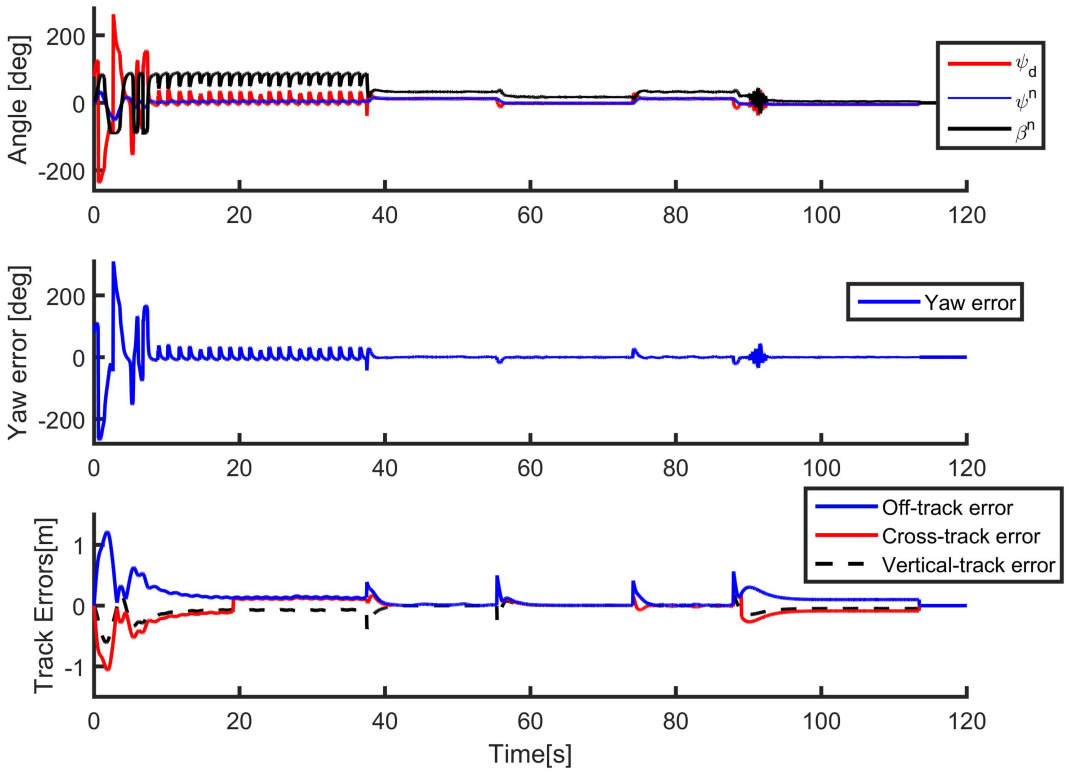

Figure 6.9: Heading angle and track-error tracking profile of SELOS sliding course control with CURRENT disturbance of $V_x = V_y = 1.3m/s$, and $V_z = 0.3m/s$.

6.3.2 Fully-Actuated UVs

In fully-actuated 4-DOF case, the sway error dynamics change when the speed allocation includes CURRENT sway dynamics, which is now different as given by (6.60).

Sway Control

The error dynamics in sway is updated from (5.124)-(5.124) by setting $k_{sa} = 0.4$ by trial and error and using the 3-D CURRENT dynamics in sway (6.60), which is:

$$\begin{aligned}\dot{\tilde{v}} = & -\dot{v}^f - 0.6\dot{v}_c = \frac{1}{m_{22}}(m_{24}\dot{r}^f + c_{24}r^f + d_{22}v^f - \tau_v) \\ & + 0.6r^n V_x[s(\psi_c - \psi^n)s\theta_c s\phi_c + c(\psi_c - \psi^n)c\phi_c] \\ & - 0.6r^n V_y[c(\psi_c - \psi^n)s\theta_c s\phi_c - s(\psi_c - \psi^n)c\phi_c].\end{aligned} \tag{6.86}$$

The feedback controller for sway is then given by:

$$\tau_v = c_{24}r^n + d_{22}v^f + m_{24}\dot{r}^n + m_{22}\Big(k_v\tilde{v} + 0.6r^nV_x[s(\psi_c-\psi^n)s\theta_c s\phi_c + c(\psi_c-\psi^n)c\phi_c] - 0.6r^nV_y[c(\psi_c-\psi^n)s\theta_c s\phi_c - s(\psi_c-\psi^n)c\phi_c]\Big). \tag{6.87}$$

Simulation: 4-DOF Full Actuation

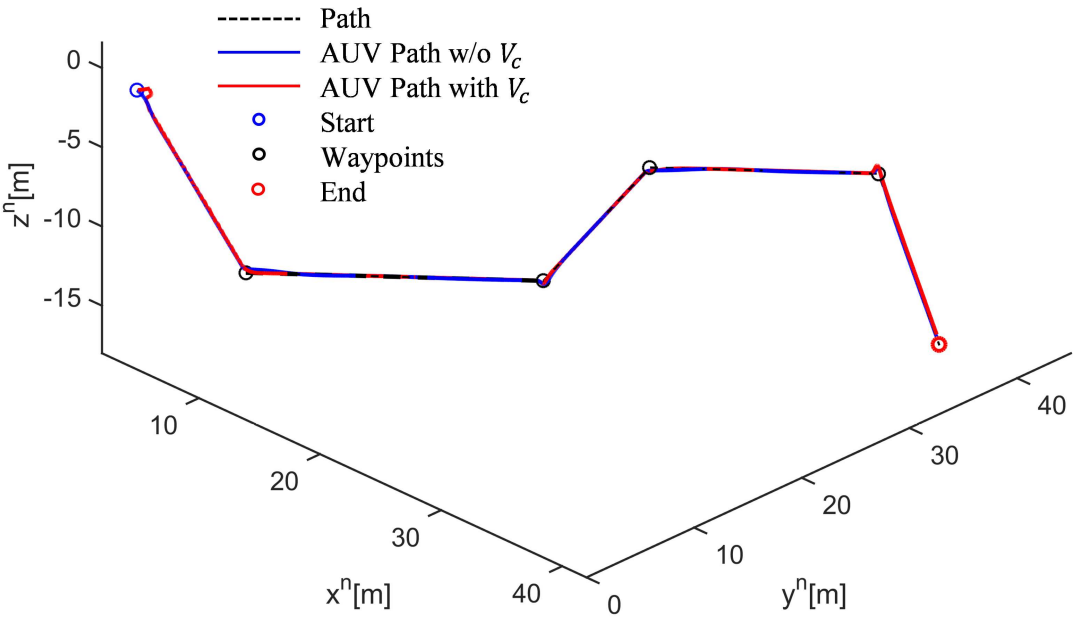

Figure 6.10: Performance of SELOS course control w/ and w/o CURRENT disturbance of $V_x = V_y = 1.3m/s$, and $V_z = 0.3m/s$.

The controllers with SELOS guidance law are applied to the 4-DOF model of Girona-AUV for the straight-line course control problem. The waypoints are given by: $wpx = [5,20,25,35,40], wpy = [10,25,25,35,35], wpz = [-15,-15,-6,-6,-15]$. The initial NED position, vehicle heading and relative velocities were set to $\boldsymbol{\eta}^n_{b/n} = [4,1,-1,0]$ and $\boldsymbol{\nu}^b_{b/n} = \boldsymbol{\nu}^f_{b/f} = [0,0,0,0]$, and the maximum desired relative velocities are $U^n_{hdmax} = 1m/s$ and $w^n_{dmax} = 0.5m/s$. The CURRENT velocities are $V_x = V_y = 1.3m/s$, which give its NED direction at $\phi_c = \theta_c = 18.4^o$ and $\psi_c = 45^o$. The guidance and control system gains are similarly set as follows: $R_{min} = 1, a = 1.01, c = 0.001, k_r = k_a = 1, \lambda = 1, k_\psi = k_s =$

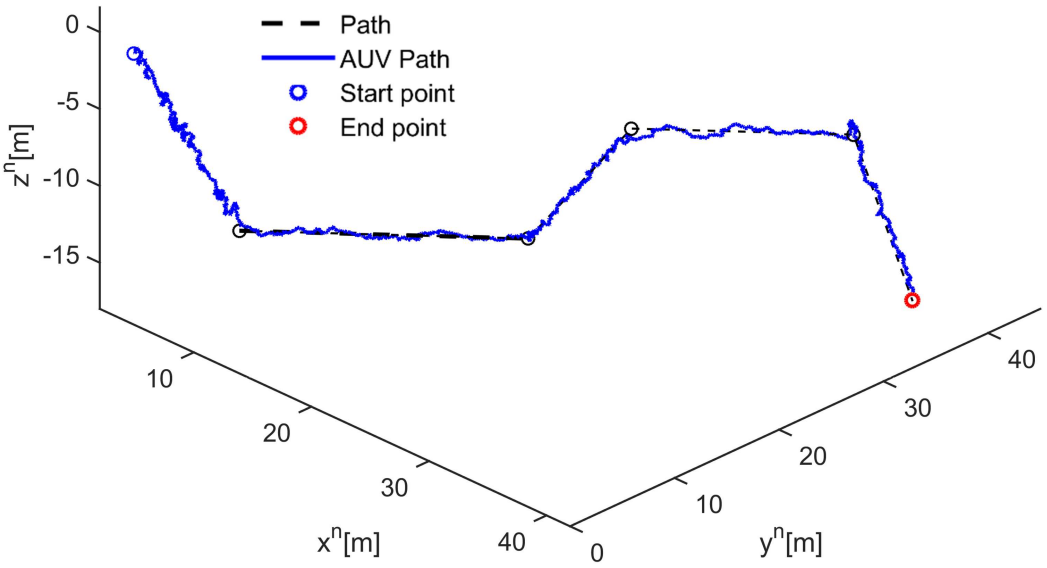

Figure 6.11: Performance of SELOS course control with CURRENT disturbance of $V_x = V_y = 0.6m/s$, and $V_z = 0.3m/s$, and position and heading zero-mean random noise of $\pm 4cm$ and $\pm 3^o$ in x^n, y^n, z^n and ψ^n resp..

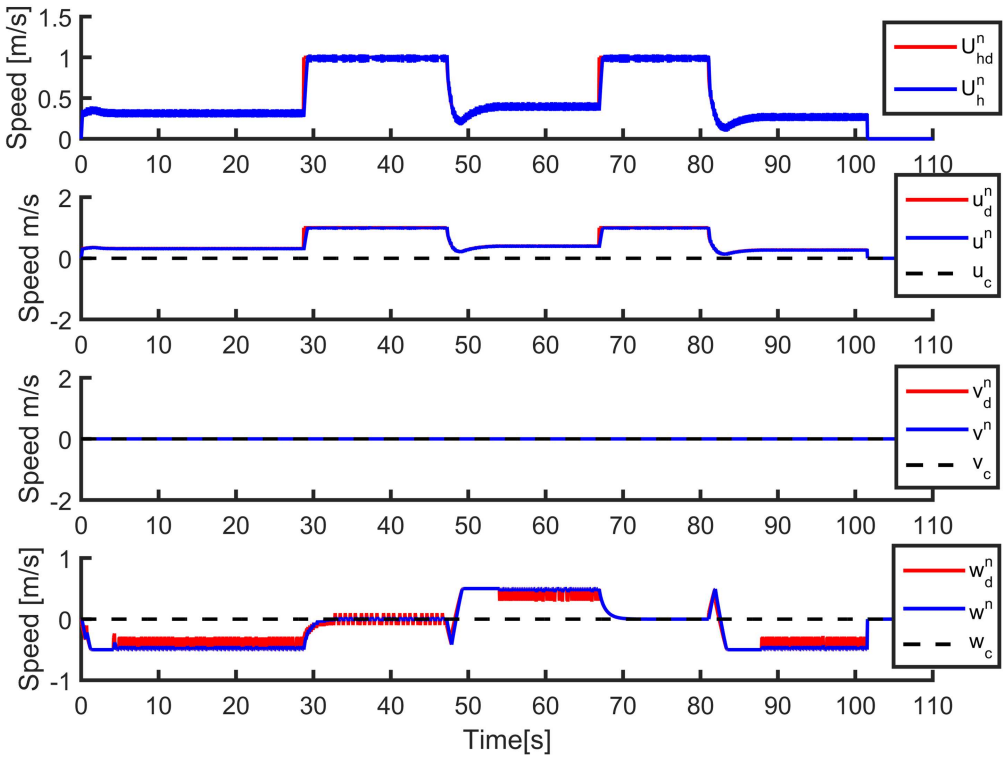

Figure 6.12: Velocity tracking profile of SELOS sliding course control.

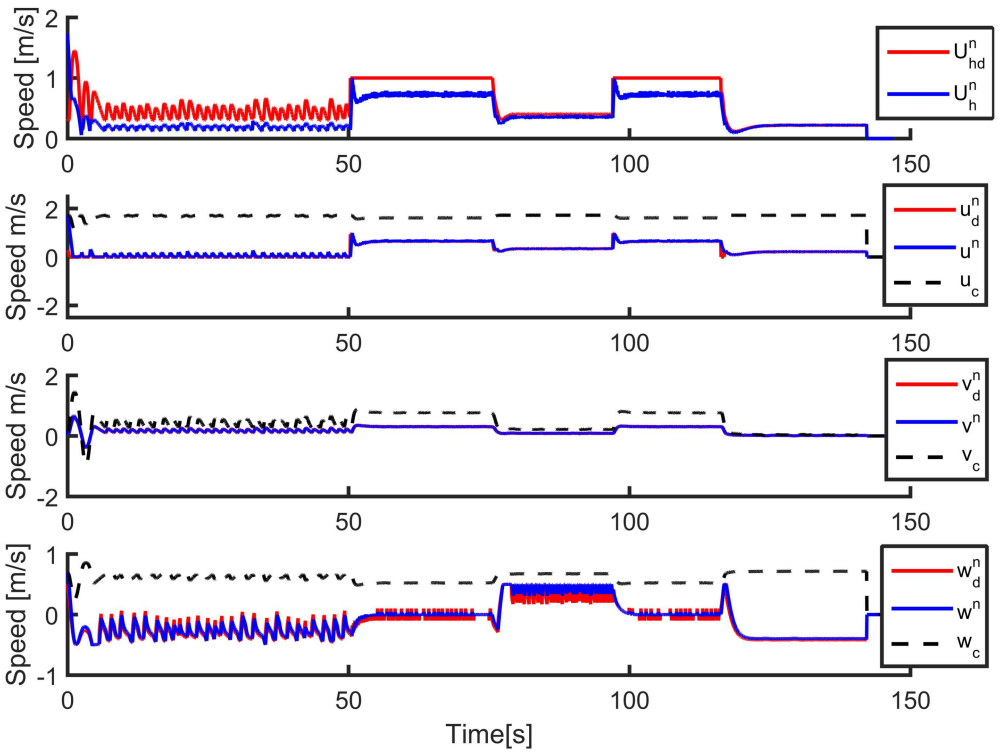

Figure 6.13: Velocity tracking profile of SELOS sliding course control with CURRENT disturbance of $V_x = V_y = 1.3m/s$, and $V_z = 0.3m/s$.

$10, k_d = 55, T_s = 0.05, k_u = k_w = 55, k_v = 25, k_1 = k_2 = 1, ,.$ Control inputs saturate at $\pm 450N$ in surge, sway and heave, and $\pm 250Nm$ in yaw. The rate limit for maximum yaw rate at $57.3deg/s(1rad/s)$.

Figures 6.10-6.11 show that the SELOS course control can make the vehicle accurately track the path with and w/o significant CURRENT, with less accuracy in the case of present disturbances and measurement noises. Figures 6.12-6.15 show the velocity, heading angle, and track-error tracking profiles w/ and w/o CURRENT disturbances. These responses are similar to the underactuated case, other than better cross-tracking due to actuation in sway and the specific speed allocation. Similar to the 2-D case, the total velocity is not fully tracked due to the competition between the dynamic and geometric tasks for the given amount of actuation.

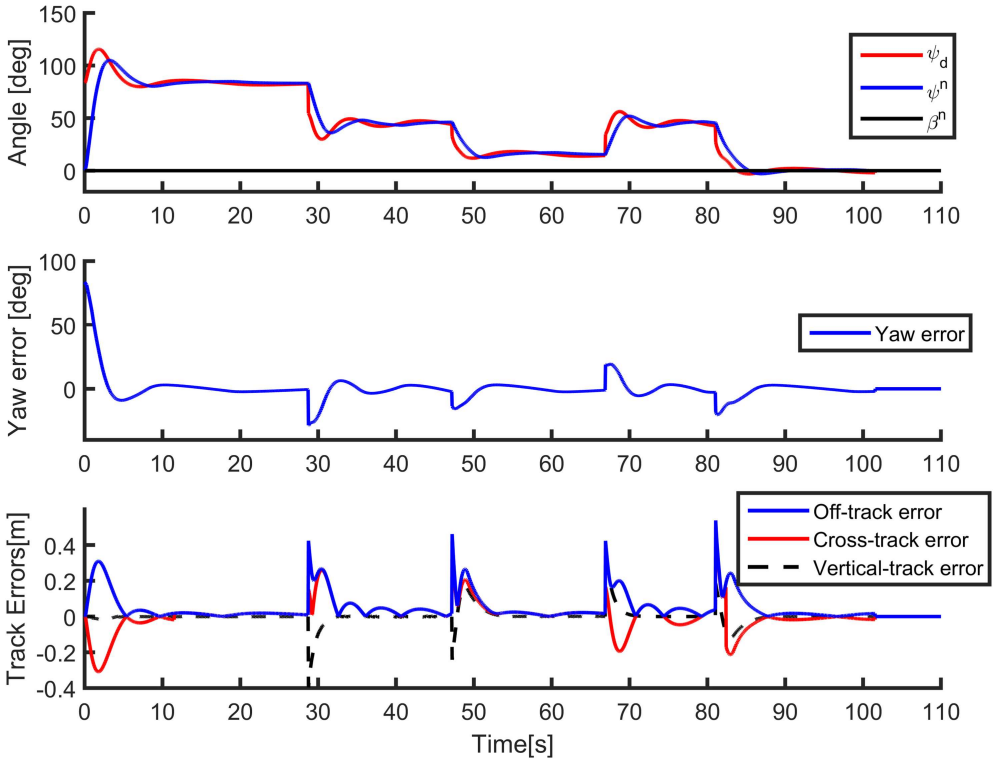

Figure 6.14: Course angle and track-errors tracking profile of SELOS sliding course control.

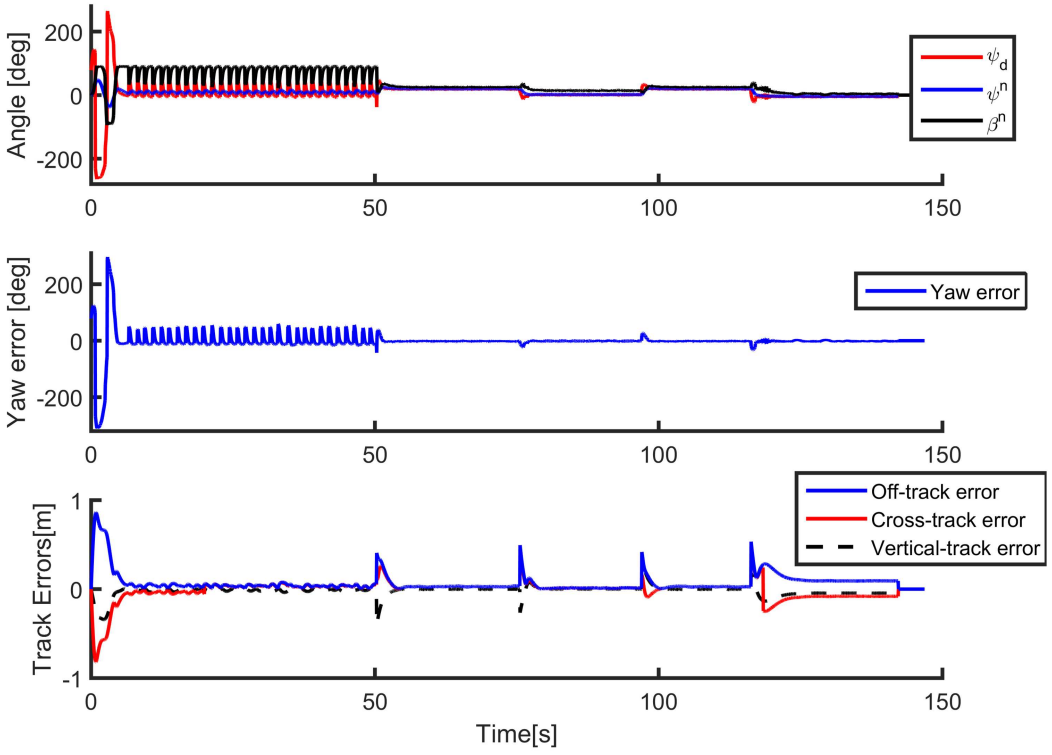

Figure 6.15: Course angle and track-error error tracking profile of SELOS sliding course control with CURRENT disturbance of $V_x = V_y = 1.3m/s$, and $V_z = 0.3m/s$.

6.4 5-DOF SELOS Course Control

The 5-DOF model considers the active control of pitch DOF while only roll is passively stabilized, which will require vertical guidance laws for minimizing the pitch error, and consequently, the vertical-track error. The heave DOF is also not actuated, which makes the 5-DOF underactuated model able to represent a wide range of torpedo-shaped UVs that have horizontal and vertical rudders that are manipulated to control the pitch and yaw angels, and a main propeller for surge.

6.4.1 Sway and Heave Underactuated UVs

System Model

The 5-DOF relative system model is extracted from the 6-DOF relative kinematics, relationship of relativity (4.4)-(4.5), and the relative kinetics (4.51) as:

$$\dot{\boldsymbol{\eta}}^n_{b/n} = \boldsymbol{R}(\boldsymbol{\Theta}^n_{b/n})\boldsymbol{\nu}^b_{b/n}, \tag{6.88}$$

$$\boldsymbol{\nu}^f_{b/f} = \boldsymbol{\nu}^b_{b/n} - \boldsymbol{\nu}^b_{c/n}, \tag{6.89}$$

$$\boldsymbol{M}\dot{\boldsymbol{\nu}}^f_{b/f} + \boldsymbol{C}(\boldsymbol{\nu}^f_{b/f})\boldsymbol{\nu}^f_{b/f} + \boldsymbol{D}(\boldsymbol{\nu}^f_{b/f})\boldsymbol{\nu}^f_{b/f} + \boldsymbol{g}(\boldsymbol{\Theta}^n_{b/n}) = \boldsymbol{\tau}_{act}. \tag{6.90}$$

where $\boldsymbol{\eta}^n_{b/n} \triangleq [x^n, y^n, z^n, \theta^n, \psi^n]^T$ is the vehicle position, heading and pitch agngles relative to and expressed in NED, $\dot{\boldsymbol{\eta}}^n_{b/n} = [\dot{x}^n, \dot{y}^n, \dot{z}^n, \dot{\theta}^n, \dot{\psi}^n]^T$ is the vehicle velocities, and pitch and yaw rates relative to and expressed in NED, $\boldsymbol{\nu}^b_{b/n} \triangleq [u^n, v^n, w^n, q^n, r^n]^T$ is the vehicle BODY velocities in surge, sway, heave, and yaw rate relative to NED, $\boldsymbol{\nu}^f_{b/f} \triangleq [u^f, v^f, w^f, q^r, r^f]^T$ is the vehicle BODY velocities in surge, sway, heave, and pitch and yaw rates relative to the fluid FLOW frame, and $\boldsymbol{\nu}^b_{c/n} \triangleq [u_c, v_c, w_c, 0, 0]^T$ is CURRENT velocities and yaw rate relative to NED and expressed in BODY. The control input vector $\boldsymbol{M}^{-1}\boldsymbol{B}\boldsymbol{f} = [\tau_u, 0, \tau_w, \tau_\theta, \tau_\psi]^T$ consists of surge, heave forces, and pitch and yaw moments. This structure of the control input vector is obtained by assuming that $\{b\}$ of BODY is positioned in the pivot point such that yaw moment has no effect on sway motion Fredriksen

and Pettersen (2006). The system in (6.90) is underactuated in sway since the dimension of $\boldsymbol{f}$ is less than that of the system. Expanding (6.88) gives the 5-DOF relative kinematics as:

$$\dot{x}^n = u^n \cos\psi^n \cos\theta^n - v^n \sin\psi^n + w^n \cos\psi^n \sin\theta^n, \tag{6.91}$$

$$\dot{y}^n = u^n \sin\psi^n \cos\theta^n + v^n \cos\psi^n + w^n \sin\psi^n \sin\theta^n, \tag{6.92}$$

$$\dot{z}^n = -u^n \sin\theta^n + w^n \cos\theta^n, \tag{6.93}$$

$$\dot{\theta}^n = q^n, \tag{6.94}$$

$$\dot{\psi}^n = r^n / \cos\theta^n. \tag{6.95}$$

The 5-DOF CURRENT is irrotational and constant (or slowly varying) such that the CURRENT yaw and pitch rates $V_\psi = V_\theta = q_c = r_c = 0$ and $\dot{\boldsymbol{V}}_c = 0$. The 5-DOF CURRENT expressed in BODY is obtained by reducing (4.56) with $\phi^n = 0$ as:

$$\boldsymbol{\nu}^b_{c/n} \triangleq [u_c, v_c, w_c, q_c, r_c,]^T = \boldsymbol{J}(\boldsymbol{\Theta}^n_{c/n} - \boldsymbol{\Theta}^n_{b/n})^T \boldsymbol{V}^n_{c/n}, \tag{6.96}$$

The linear part of this expands to:

$$u_c = V_x c(\psi_c - \psi^n)c(\theta_c - \theta^n) + V_y s(\psi_c - \psi^n)c(\theta_c - \theta^n) - V_z s(\theta_c - \theta^n), \tag{6.97}$$

$$\begin{aligned} v_c = {} & V_x[c(\psi_c - \psi^n)s(\theta_c - \theta^n)s\phi_c - s(\psi_c - \psi^n)c\phi_c] \\ & + V_y[c(\psi_c - \psi^n)c\phi_c + s(\psi_c - \psi^n)s(\theta_c - \theta^n)s\phi_c] + V_z c(\theta_c - \theta^n)s\phi_c, \end{aligned} \tag{6.98}$$

$$\begin{aligned} w_c = {} & V_x[s(\psi_c - \psi^n)s\phi_c + c(\psi_c - \psi^n)c\phi_c s(\theta_c - \theta^n)] \\ & + V_y[s(\psi_c - \psi^n)s(\theta_c - \theta^n)c\phi_c - c(\psi_c - \psi^n)s\phi_c] + V_z c(\theta_c - \theta^n)c\phi_c. \end{aligned} \tag{6.99}$$

The dynamics of the CURRENT is obtained by time-differentiating (6.97)-(6.99):

$$\begin{aligned}\dot{u}_c = {} & V_x r^n [s(\psi_c - \psi^n)c(\theta_c - \theta^n) - q^n c(\psi_c - \psi^n)c(\theta_c - \theta^n)] \\ & + V_y r^n [c(\psi_c - \psi^n)c(\theta_c - \theta^n) - q^n s(\psi_c - \psi^n)c(\theta_c - \theta^n)],\end{aligned} \tag{6.100}$$

$$\begin{aligned}\dot{v}_c = {} & -V_x[r^n s(\psi_c - \psi^n)s(\theta_c - \theta^n)s\phi_c - q^n c(\psi_c - \psi^n)c(\theta_c - \theta^n)s\phi_c - r^n c(\psi_c - \psi^n)c\phi_c] \\ & + V_y[r^n c(\psi_c - \psi^n)s(\theta_c - \theta^n)s\phi_c + q^n s(\psi_c - \psi^n)c(\theta_c - \theta^n)s\phi_c - r^n s(\psi_c - \psi^n)c\phi_c] \\ & + V_z q^n s(\theta_c - \theta^n)s\phi_c,\end{aligned} \tag{6.101}$$

$$\begin{aligned}\dot{w}_c = {} & V_x[r^n s(\psi_c - \psi^n)c\phi_c s(\theta_c - \theta^n) - q^n s(\psi_c - \psi^n)c\phi_c c(\theta_c - \theta^n) + r^n c(\psi_c - \psi^n)s\phi_c] \\ & + V_y[r^n s(\psi_c - \psi^n)s\phi_c - r^n c(\psi_c - \psi^n)s(\theta_c - \theta^n)c\phi_c - q^n s(\psi_c - \psi^n)c(\theta_c - \theta^n)c\phi_c] \\ & + V_z q^n s(\theta_c - \theta^n)c\phi_c,\end{aligned} \tag{6.102}$$

since $\dot{V}_c = 0$ and the CURRENT Euler rates $\dot{\boldsymbol{\Theta}}^n_{c/n} = \mathbf{0}$ for irrotational CURRENT in NED.

The system matrices are given by the following:

$$\boldsymbol{M} \triangleq \begin{bmatrix} m_{11} & 0 & 0 & m_{14} & 0 \\ 0 & m_{22} & 0 & 0 & m_{25} \\ 0 & 0 & m_{33} & -m_{34} & 0 \\ m_{14} & 0 & -m_{34} & m_{44} & 0 \\ 0 & m_{25} & 0 & 0 & m_{55} \end{bmatrix} = \begin{bmatrix} m + X_{\dot{u}} & 0 & 0 & mz_g & 0 \\ 0 & m + Y_{\dot{v}} & 0 & 0 & mx_g \\ 0 & 0 & m + Z_{\dot{w}} & -mx_g & 0 \\ mz_g & 0 & -mx_g & I_y + M_{\dot{q}} & 0 \\ 0 & mx_g & 0 & 0 & I_z + N_{\dot{r}} \end{bmatrix}, \tag{6.103}$$

$$\boldsymbol{C}(\boldsymbol{\nu}^f) \triangleq \begin{bmatrix} 0 & 0 & 0 & c_{14} & c_{15} \\ 0 & 0 & 0 & c_{24} & c_{25} \\ 0 & 0 & 0 & c_{34} & c_{35} \\ -c_{14} & -c_{24} & -c_{34} & 0 & c_{45} \\ -c_{15} & -c_{25} & -c_{35} & -c_{45} & 0 \end{bmatrix}, \tag{6.104}$$

$$\boldsymbol{D}(\boldsymbol{\nu}^f) \triangleq \{d_{11}(u^f), d_{22}(v^f), d_{33}(w^f), d_{44}(q^f), d_{55}(r^f)\}$$
$$= diag\{X_u + X_{|u|u}|u^f|, Y_v + Y_{|v|v}|v^f|, Z_w + Z_{|w|w}|w^f|, M_q + M_{|q|q}|q^f|, N_r + N_{|r|r}|r^f|\}. \tag{6.105}$$

The structure of the system matrices in (6.103) and (6.104) are obtained by assuming that the vehicle is symmetric in port-starboard, and that the BODY frame is located along the centre-line of the vehicle (T. Fossen, 2011), in which case it is common that $y_g \approx 0$. The system dynamics relative to FLOW is obtained by expanding the relative kinetics (6.90) as:

$$\dot{u}^f = -\frac{1}{m_{11}}(m_{14}\dot{q}^f + c_{14}q^f + c_{15}r^f + d_{11}u^f - \tau_u), \tag{6.106}$$
$$\dot{v}^f = -\frac{1}{m_{22}}(m_{25}\dot{r}^f + c_{24}q^f + c_{25}r^f + d_{22}v^f), \tag{6.107}$$
$$\dot{w}^f = -\frac{1}{m_{33}}(-m_{34}\dot{q}^f + c_{34}q^f + c_{35}r^f + d_{33}u^f - \tau_w), \tag{6.108}$$
$$\dot{q}^f = -\frac{1}{m_{44}}(m_{14}\dot{u}^f - m_{34}\dot{w}^f - c_{14}u^f - c_{24}v^f - c_{34}q^f + c_{45}r^f + d_{44}q^f - \tau_\theta), \tag{6.109}$$
$$\dot{r}^f = -\frac{1}{m_{55}}(m_{25}\dot{v}^f - c_{15}u^f - c_{25}v^f - c_{35}w^f - c_{45}q^f + d_{55}r^f - \tau_\psi). \tag{6.110}$$

Note similarly that $r^n = r^f$ and $q^n = q^f$ since the CURRENT is irrotational in NED and that the yaw component of CURRENT $V_\psi = V_\theta = 0$.

Control Objective and Speed Allocation

The control objectives are similar to that formulated in the 4-DOF sway underactuated case, which will now include additional θ^n for tracking θ_d, which is:

$$\lim_{t\to\infty} \theta^n(t) = \theta_d(t), \tag{6.111}$$

The linear speed allocation in 3-D is given by:

$$U_d^n \triangleq \sqrt{u_d^{n2} + v_d^{n2} + w_d^{n2}}, \tag{6.112}$$

$$U_{hd}^n \triangleq \sqrt{u_d^{n2} + v_d^{n2}}, \tag{6.113}$$

$$u_d^n \triangleq u_d^f + u_c, \tag{6.114}$$

$$v_d^n \triangleq v_d^f + v_c, \tag{6.115}$$

$$w_d^n \triangleq w_d^f + w_c, \tag{6.116}$$

which remains the the as in all of the sway underactuated cases with $v_d^f = 0$. For heave underactuation, similarly, $w_d^f = 0$ to expressed the heave error dynamics.

Pitch Control

In the 4-DOF case w/o roll and pitch DOFs, heave control was necessary to achieve vertical motion towards the path. However, in 5-DOF with pitch control, the 3-D vehicle position can be controlled by only controlling the surge, pich and yaw DOFs. The sliding surge and yaw controllers in 2-D can be modified to include the feedback terms from the new surge and yaw dynamics in (6.106) and (6.110) to achieve the same stability properties and the respective control objectives. The additional controller in pitch will be required to achieve control objective (6.110). The yaw error and its dynamics are defined and given as $\tilde{\theta} \triangleq \theta_d - \theta^n$ and $s \triangleq \dot{\tilde{\theta}} + \lambda_q \tilde{\theta}$, where $\lambda_q > 0$ is controller bandwidth. Taking the time-derivative of $\tilde{\theta}$ and s, and using kinematics (6.97) and pitch dynamics (6.108) gives:

$$\dot{\tilde{\theta}} = \dot{\theta}_d - q^f, \tag{6.117}$$

$$\begin{aligned} \dot{s} &= \ddot{\tilde{\theta}} + \lambda_q \dot{\tilde{\theta}} = \ddot{\theta}_d - \dot{q}^f + \lambda_q(\dot{\theta}_d - q^f) \\ &= \ddot{\theta}_d + \frac{1}{m_{44}}(m_{14}\dot{u}^f - m_{34}\dot{w}^f - c_{14}u^f - c_{24}v^f - c_{34}q^f + c_{45}r^f + d_{44}q^f - \tau_\theta) \\ &+ \lambda_q(\dot{\theta}_d - q^f). \end{aligned} \tag{6.118}$$

The feedback-linearizing SMC is used for pitch is chosen as:

$$\begin{aligned}\tau_\theta = {} & m_{14}\dot{u}^f - m_{34}\dot{w}^f - c_{14}u^f - c_{24}v^f - c_{34}q^f + c_{45}r^f + d_{44}q^f \\ & + m_{44}\left[\ddot{\theta}_d + \lambda_q(\dot{\theta}_d - q^f) + k_\theta\tilde{\theta} + k_q s\right],\end{aligned} \tag{6.119}$$

where $k_\theta, k_q > 0$ are gains. The time-derivative of radially unbounded and positive definite LFC $V_\theta = (1/2)\tilde{\theta}^2 + (1/2)s^2$ is used for stability analysis of error dynamics (6.117)-(6.118), which is:

$$\dot{V}_\theta = \dot{\tilde{\theta}}\tilde{\theta} + \dot{s}s = -\lambda_q\tilde{\theta}^2 - k_q s^2 \leq 0. \tag{6.120}$$

Since $\dot{V}_\theta$ is negative definite thus, the equilibrium $(\theta, s) = (0,0)$ is UGES, and hence $(\tilde{\theta}, s) \to (0,0)$ exponentially as $t \to \infty$. This satisfies the control objective (6.111). Exponential convergence of $(\tilde{\theta}, s) \to (0,0)$ also implies exponential convergence of $q^n \Rightarrow \dot{\theta}_d$ since $s - \lambda\tilde{\theta} = \dot{\theta}_d - q^n$.

Reference signals for $\dot{\theta}_d, \ddot{\theta}_d$ are similarly designed as:

$$\dot{\theta}_d = k_3(\theta_d - \theta^n) = k_3\tilde{\theta}, \tag{6.121}$$

$$\ddot{\theta}_d = k_4(\dot{\theta}_d - \dot{\theta}^n) = k_4\dot{\tilde{\theta}}, \tag{6.122}$$

where k_3, k_4 are gains.

In order to prevent large θ_d being fed into the controller, e.g. during waypoint switching, the following integration is used to generate small increments of θ_d:

$$\theta_d = \theta^n + \dot{\theta}_d T_s = \theta^n - k_3 T_s\tilde{\theta}, \tag{6.123}$$

where $\tilde{\theta} \to 0$ also implies $\theta^n \to \theta_d$.

Underactuated Sway Error Dynamics

The relative underactuated error in sway under CURRENT disturbance is defined similarly and expressed using speed allocation with $v_d^f = 0$, which is given by using the relative

velocity relationship (6.89) as:

$$\tilde{v} \triangleq v_d^n - v^n = v_c - v^n = -v^f. \tag{6.124}$$

Using the sway dynamics (6.107), the sway error dynamics is given by:

$$\dot{\tilde{v}} = -\dot{v}^f = \frac{1}{m_{22}}(m_{25}\dot{r}^f + c_{24}q^f + c_{25}r^f + d_{22}v^f). \tag{6.125}$$

The sway error dynamics will remain bounded for bounded CURRENT disturbances and control input since it is shown in boundedness proof in Section 4.4.

Underactuated Heave Error Dynamics

With $w_d^f = 0$ in the speed allocation (6.116), the heave error is given by using the relative velocity relationship (6.89) as:

$$\tilde{w} \triangleq w_d^n - w^n = w_c - w^n = -w^f. \tag{6.126}$$

Using the heave dynamics (6.108), the heave error dynamics is given by:

$$\dot{\tilde{w}} = -\dot{w}^f = \frac{1}{m_{33}}(-m_{34}\dot{q}^f + c_{34}q^f + c_{35}r^f + d_{33}u^f), \tag{6.127}$$

with $\tau_w = 0$. The heave error dynamics will also remain bounded for bounded CURRENT disturbances and control input since it is shown in boundedness proof in Section 4.4.

Simulation: 5-DOF Underactuation

The controllers with SELOS guidance law are applied to a reduced 5-DOF model of the ODIN spherical UV in MatLab for the straight-line course control problem. The ODIN UV has been a test bed for numerous control implementations and its 6-DOF model parameters are given in Appendix A2. It is a spherical UV with tether, which is ignored.

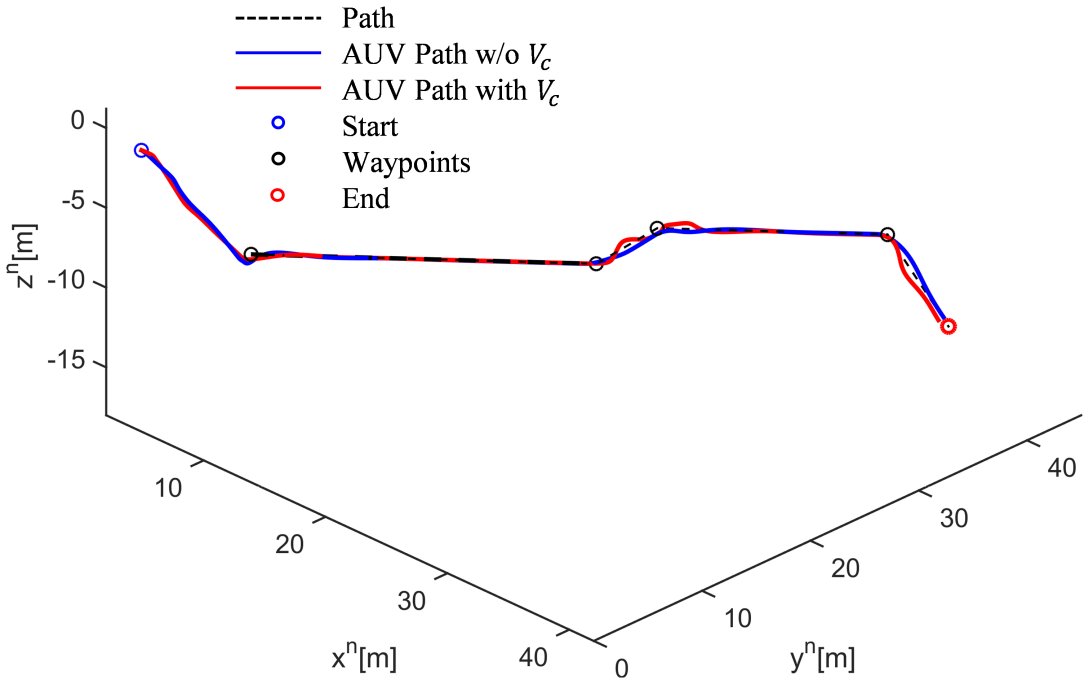

Figure 6.16: Performance of SELOS course control w/ and w/o CURRENT disturbance of $V_x = V_y = 0.6m/s$, and $V_z = 0.1m/s$.

The waypoints are given by: $wpx = [5,20,25,35,40], wpy = [10,25,25,35,35], wpz = [-10,-10,-6,-6,-10]$. The initial NED position, vehicle heading and relative velocities were set to $\boldsymbol{\eta}^n_{b/n} = [4,1,-1,0,0]$ and $\boldsymbol{\nu}^b_{b/n} = \boldsymbol{\nu}^f_{b/f} = [0,0,0,0,0]$, and the maximum desired relative velocities are $U^n_{hd} = 1m/s$ and $w^n_d = 0m/s$. The CURRENT intensity, heading and pitch angles are $V_x = V_y = 0.6m/s$, and $V_z = 0.1m/s$. The guidance and control system gains are set as follows: $R_{min} = 1, a = 1.01, c = 0.001, k_r = k_a = k_1 = k_2 = k_3 = k_4 = \lambda_r = \lambda_q = k_\psi = 1, k_u = k_d = k_q = 25, T_s = 0.05,$. The control input aslo saturate at $\pm 450N$ in surge, and $\pm 350Nm$ in yaw and pitch, and that also the same reason, there is a rate limit for maximum pitch and yaw rates and for their desired pitch and yaw course angles at $57.3deg/s(1rad/s)$.

Figures 6.16-6.17 show that the SELOS horizontal and vertical course control can make the vehicle accurately to track the path under significant CURRENT and measurement noises w/o sway or heave actuation, with less accuracy in the measurement-noise case. The total desired velocity in 3-D $U^n_{hd} = 1m/s$ giving a strength of the CURRENT intensity at 85% of U^n_{hd} since $V_c = 0.85U^n_d$, which is significant considering underactua-

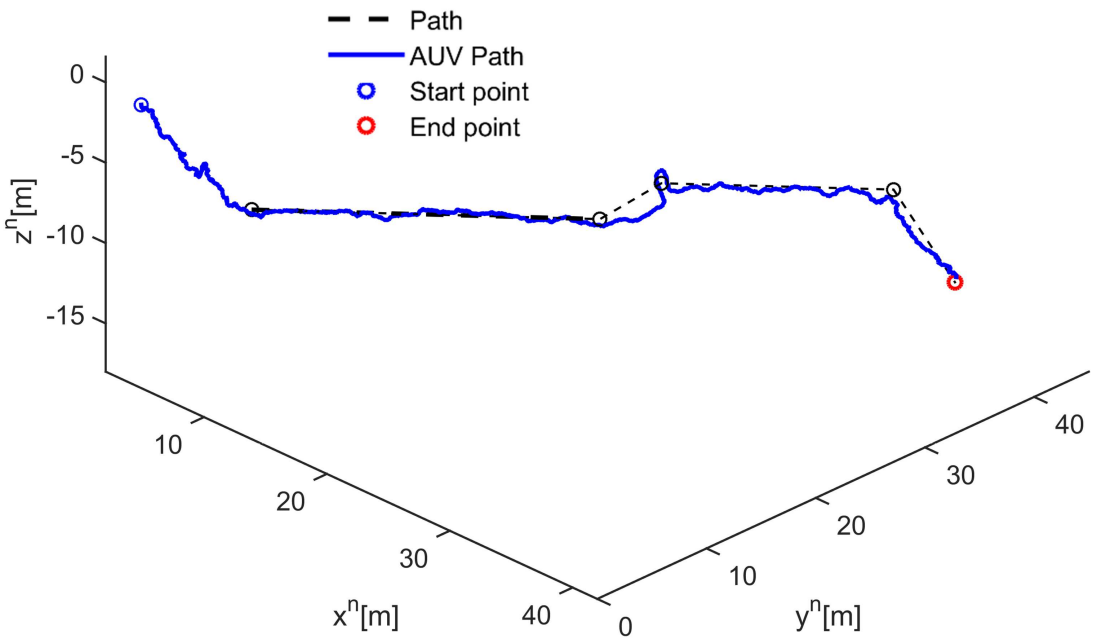

Figure 6.17: Performance of SELOS course control with CURRENT disturbance of $V_x = V_y = 0.6m/s$, and $V_z = 0.1m/s$, and position and heading zero average random uncertainties of $\pm 3cm$ and $\pm 3^o$ in x^n, y^n, z^n and ψ^n, resp..

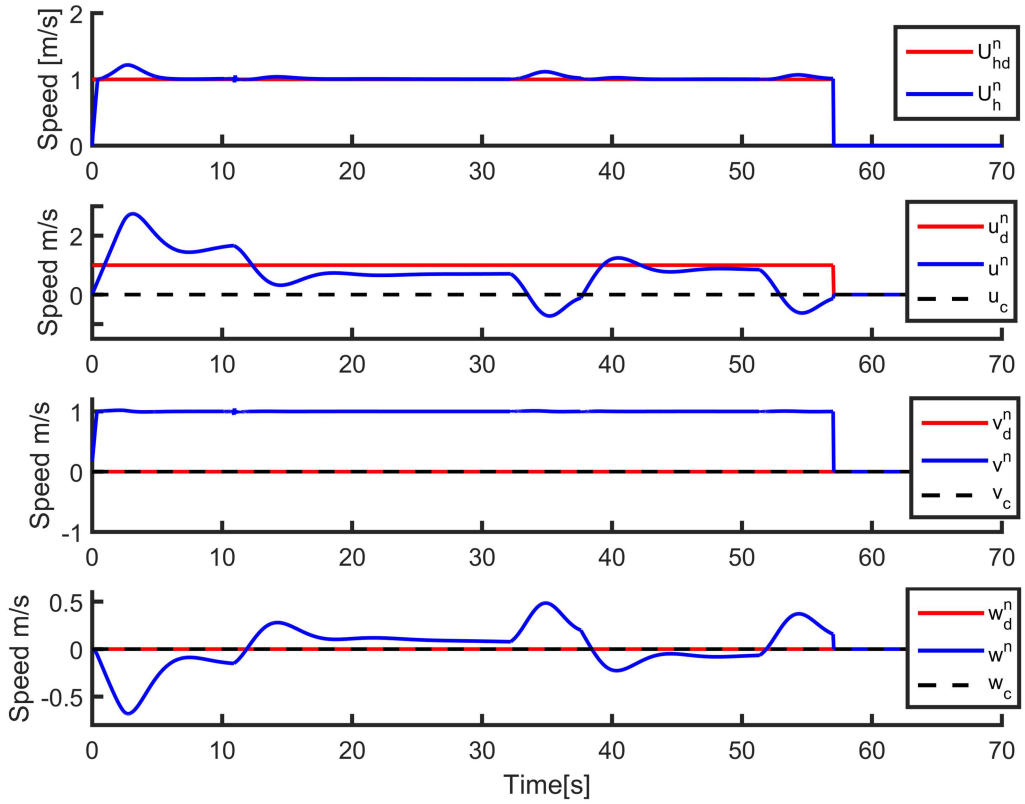

Figure 6.18: Velocity tracking profile of SELOS sliding course control.

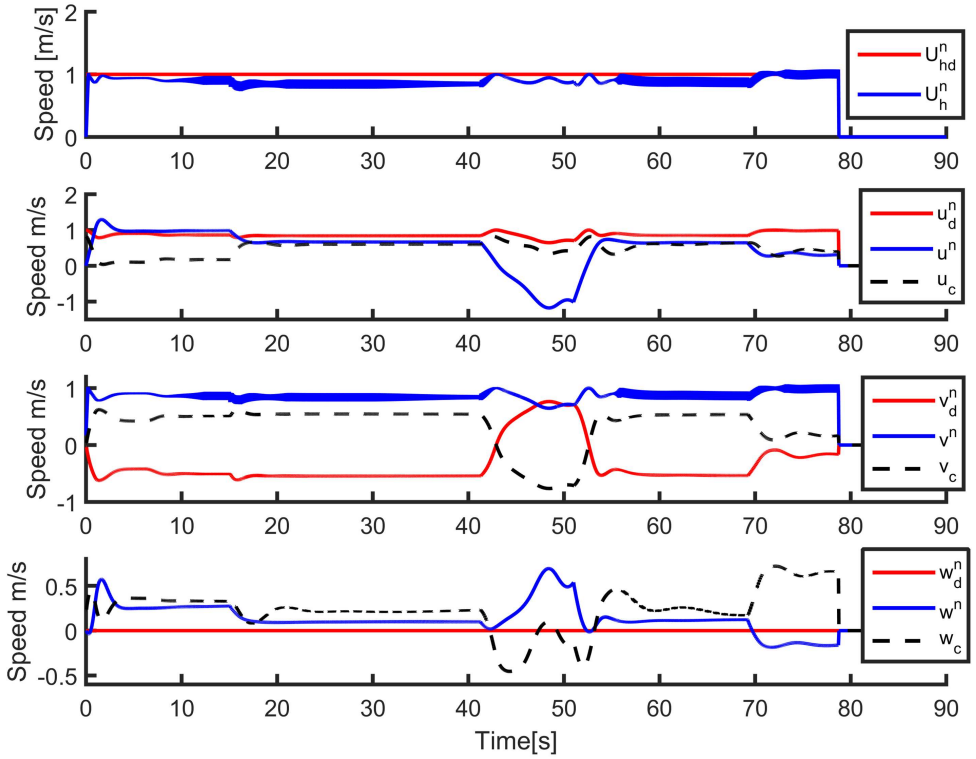

Figure 6.19: Velocity tracking profile of SELOS sliding course control with CURRENT disturbance of $V_x = V_y = 0.6m/s$, and $V_z = 0.1m/s$.

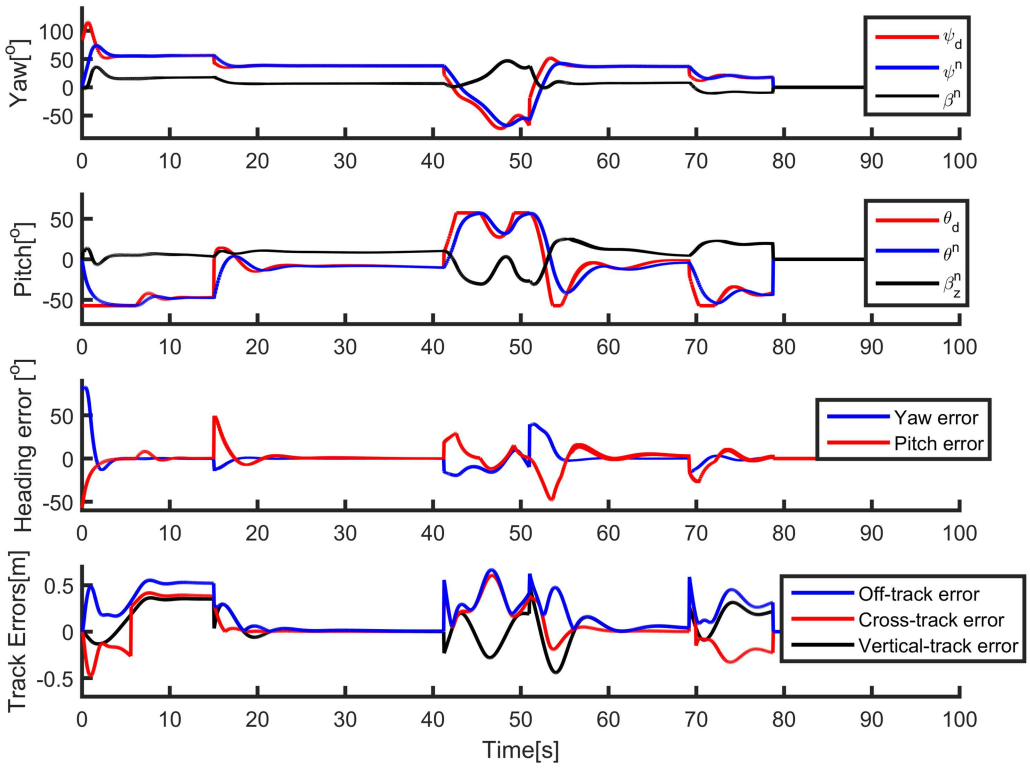

Figure 6.20: Heading angle and track-error tracking profile of SELOS sliding course control.

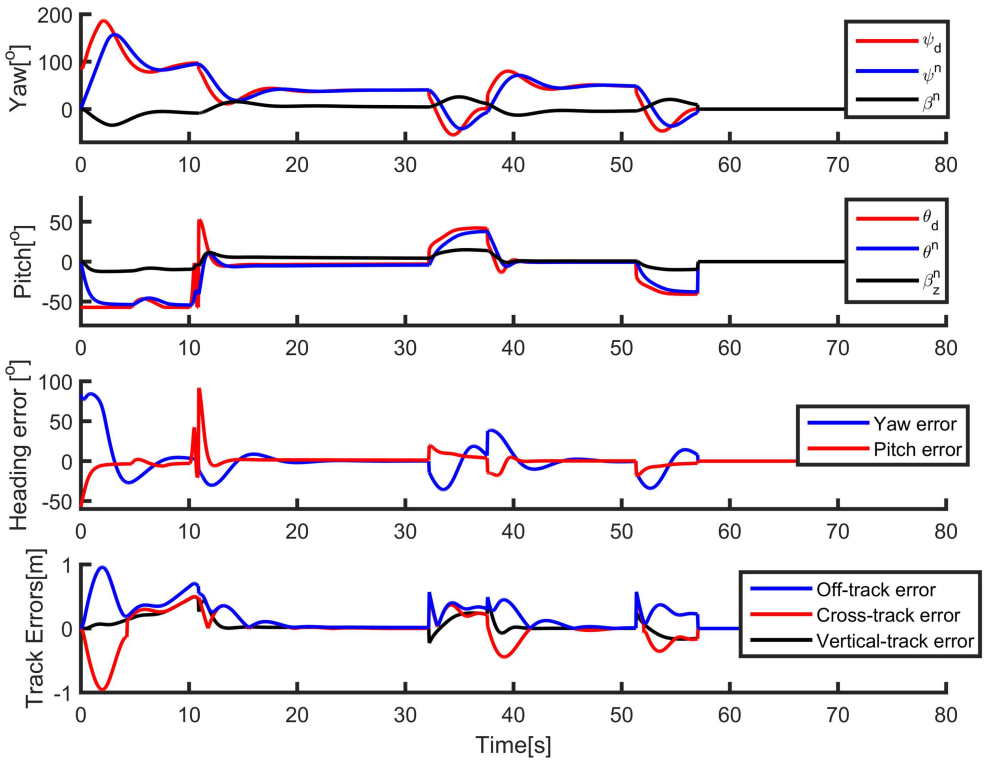

Figure 6.21: Heading angle and track-error tracking profile of SELOS sliding course control with CURRENT disturbance of $V_x = V_y = 0.6m/s$, and $V_z = 0.1m/s$.

tion in sway and heave. It can be seen from Figure 6.16 that there is a reasonable level deviation from the path during diving and ascending compared to the 4-DOF case with heave control. This is due to the coupling forces from pitch w/o any counteraction by heave, which can be reduced with heave actuation. W/o heave actuation, the vertical CURRENT is also reduced to $V_z = 0.1m/s$ from 0.3 m/s simulated in 4-DOF. The vertical waypoints are also made less steep w/o heave actuation and due to limits on maximum desired and actual pitch angle at 1 rad. Therefore, the disturbance rejection can be improved by increasing these, actuator limits and actual yaw and pitch rates allowed. The maximum pitch angle can reach less or greater than $\pm 90^o$ with full actuation with the given actuation saturation and CURRENT disturbances.

Figures 6.18-6.21 show the velocity, heading angle, and track-error tracking profiles, where Figure 6.18 shows that the surge velocity is not as closely tracked as the total velocity despite having no CURRENT disturbance. This is also due to coupling forces

in surge and that the speed allocation prioritizes the tracking of desired total speed U_{hd}^n rather than u_d^n. In addition, the drift in surge is inherently larger than any other DOFs due to a smaller drag coefficient in surge for hydro-dynamical efficiency. Furthermore, the drift in sway can also be reduced by allowing negative values for reverse motion in the desired surge speed. This will require reverse rotating propellers, which most propellers are capable of.

6.4.2 Fully-Actuated UVs

Control Objective and Speed Allocation

The sway dynamics in 5-DOF is different due to k_{sa} not being equal to -1 as in the sway underactuated cases. With $v_d^f = 0$, the speed allocation gives:

$$v_d^n = k_{sa} v_c. \tag{6.128}$$

where k_{sa} will be determined later by trial and error. Substituting this into surge speed allocation (6.84) gives the solution for u_d^n as:

$$u_d^n = \sqrt{{U_{hd}^n}^2 - {v_d^n}^2} = \sqrt{{U_{hd}^n}^2 - (k_{sa} v_c)^2}. \tag{6.129}$$

The additional control objectives for fully-actuated 5-DOF maneuvering problem are:

$$\lim_{t\to\infty} v^n(t) = v_d^n(t), \tag{6.130}$$

$$\lim_{t\to\infty} w^n(t) = w_d^n(t), \tag{6.131}$$

Control System

The additional sway and heave controllers are also feedback controllers where, in addition to the 5-DOF underactuated sway and heave dynamics in the previous section, the controllers can include the 5-DOF CURRENT dynamics in sway and heave to provide

GES of the new sway and heave error dynamics based on the speed allocation in (6.128). The design of the controllers are similar to the 4-DOF case, and hence omitted here.

Planar Speed Assignment

The planar speed assignment technique developed in 4-DOF has to be modified to include the vertical speed contribution from surge for non-zero pitch angle. The 3-D LOS vector is now being also tracked by surge due to non-zero pitch, in which case only the comparison terms will include the speed component $u_n sin(\theta^n)$. Thus, the new speed assignment for 5-DOF is obtained by modifying (6.81)-(6.82) as:

$$U_{hd}^n = \begin{cases} U_{hdmax}^n, & \text{if } \dfrac{|R_z|}{|w^n + u^n \sin(\theta^n)|} < \dfrac{R_h}{U_h^n} \\ |w_{dmax}^n \tan\theta_{R_z}|, & \text{if } \dfrac{|R_z|}{|w^n \cos(\theta^n) + u^n \sin(\theta^n)|} \geq \dfrac{R_h}{U_h^n} \end{cases} \tag{6.132}$$

$$w_d^n = -\text{sgn}(e_z) \begin{cases} w_{dmax}^n, & \text{if } \dfrac{|R_z|}{|w^n + u^n \sin(\theta^n)|} < \dfrac{R_h}{U_h^n} \\ \left| U_{hdmax}^n / \tan\theta_{R_z} \right|, & \text{if } \dfrac{|R_z|}{|w^n \cos(\theta^n) + u^n \sin(\theta^n)|} \geq \dfrac{R_h}{U_h^n} \end{cases} \tag{6.133}$$

where only w^n becomes $w^n \cos(\theta^n) + u^n \sin(\theta^n)$. This is because the vertical LOS vector is tracked in the kinematics and thus, the vertical speed should correspond to the kinematic vertical speed. A smoother reference signal for U_{hd}^n is also designed as $U_{hd}^n = U_h^n + k_U(U_{hd}^n - U_h^n)$ to reduce the fluctuation in the reference signal.

Simulation: 5-DOF Full Actuation

The controllers with SELOS course control are applied to a reduced 5-DOF model of the ODIN spherical UV for the straight-line PF. The waypoints are given by: $wpx = [5, 20, 25, 35, 40], wpy = [10, 25, 25, 35, 35], wpz = [-10, -10, -6, -6, -10]$. The initial NED position, vehicle heading and relative velocities were set to $\boldsymbol{\eta}_{b/n}^n = [4, 1, -1, 0, 0]$ and $\boldsymbol{\nu}_{b/n}^b = \boldsymbol{\nu}_{b/f}^f = [0, 0, 0, 0, 0]$, and the maximum desired relative velocities are $U_{hdmax}^n =$

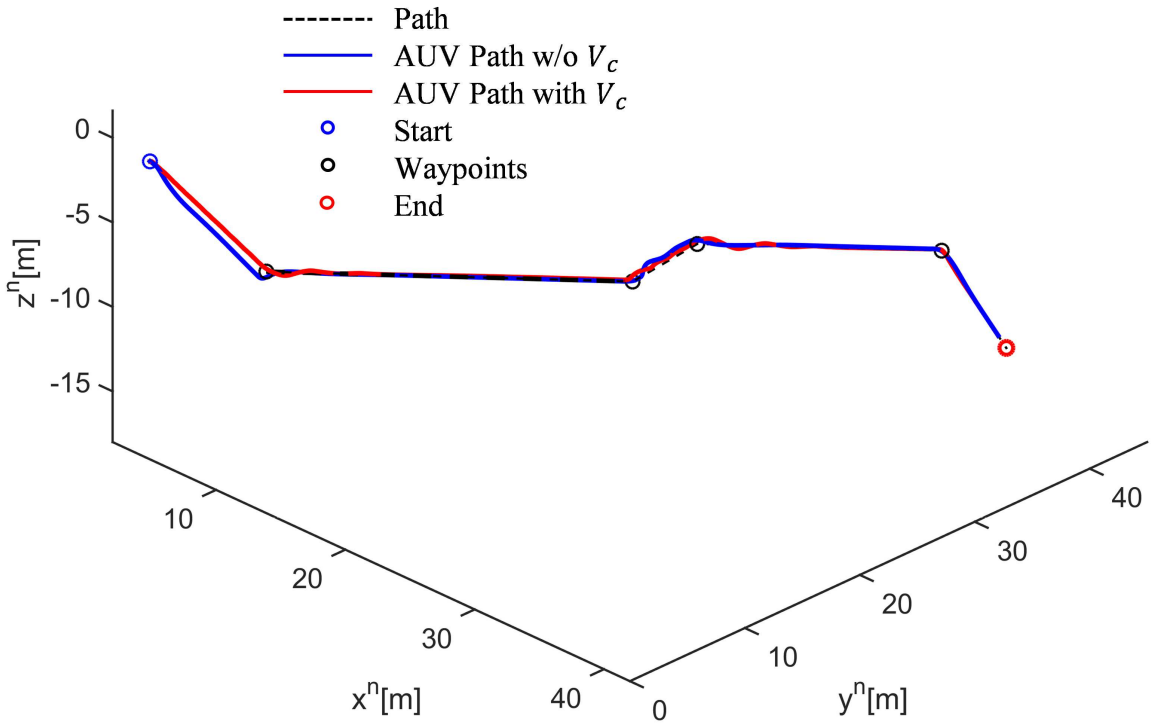

Figure 6.22: Performance of SELOS course control w/ and w/o CURRENT disturbance of $V_x = V_y = 0.8m/s$, and $V_z = 0.2m/s$.

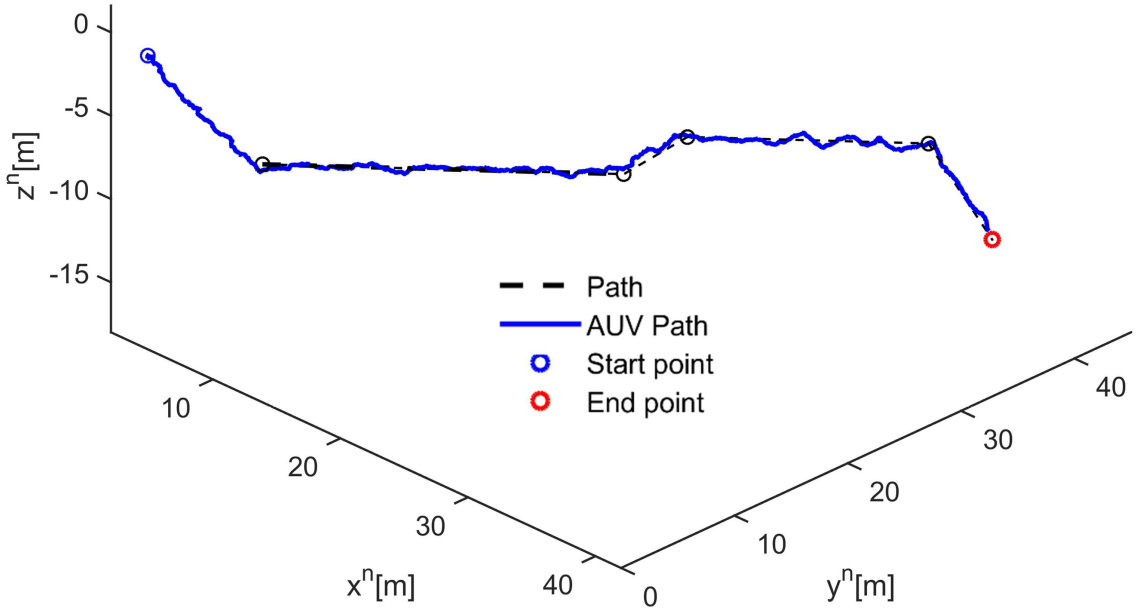

Figure 6.23: Performance of SELOS course control w/ and w/o CURRENT disturbance of $V_x = V_y = 0.4m/s$, and $V_z = 0.1m/s$, and position and heading zero average random uncertainties of $\pm 3cm$ and $\pm 3^o$ in x^n, y^n, z^n and θ^n, ψ^n, resp..

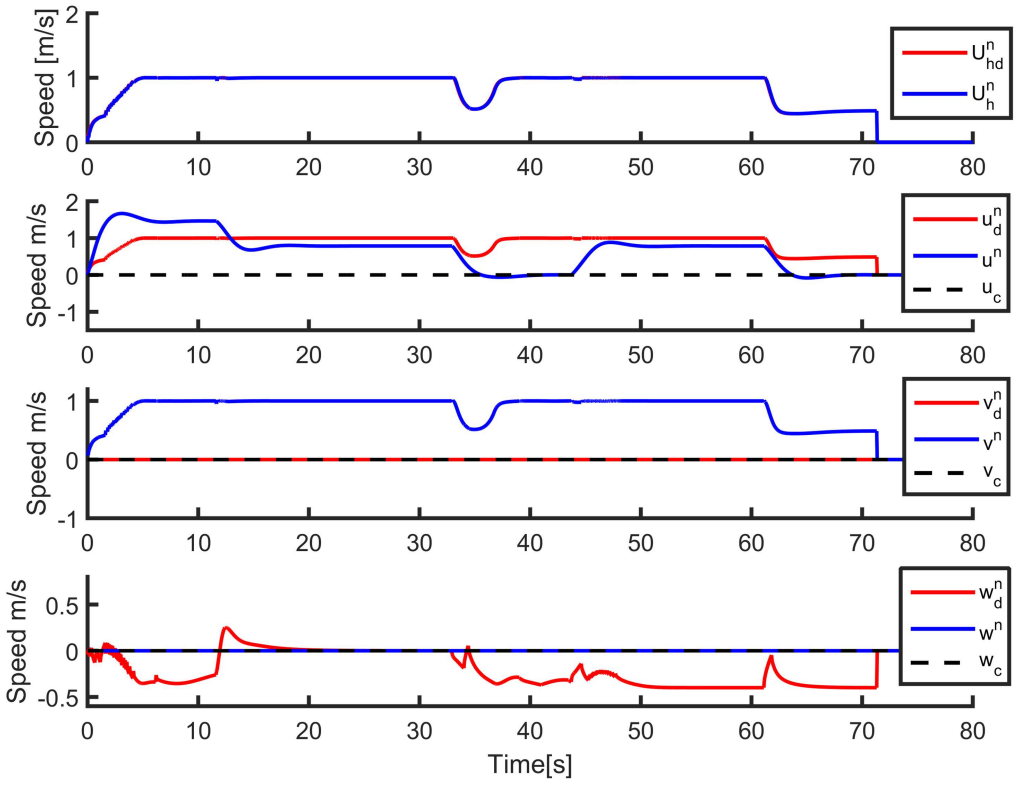

Figure 6.24: Velocity tracking profile of SELOS sliding course control.

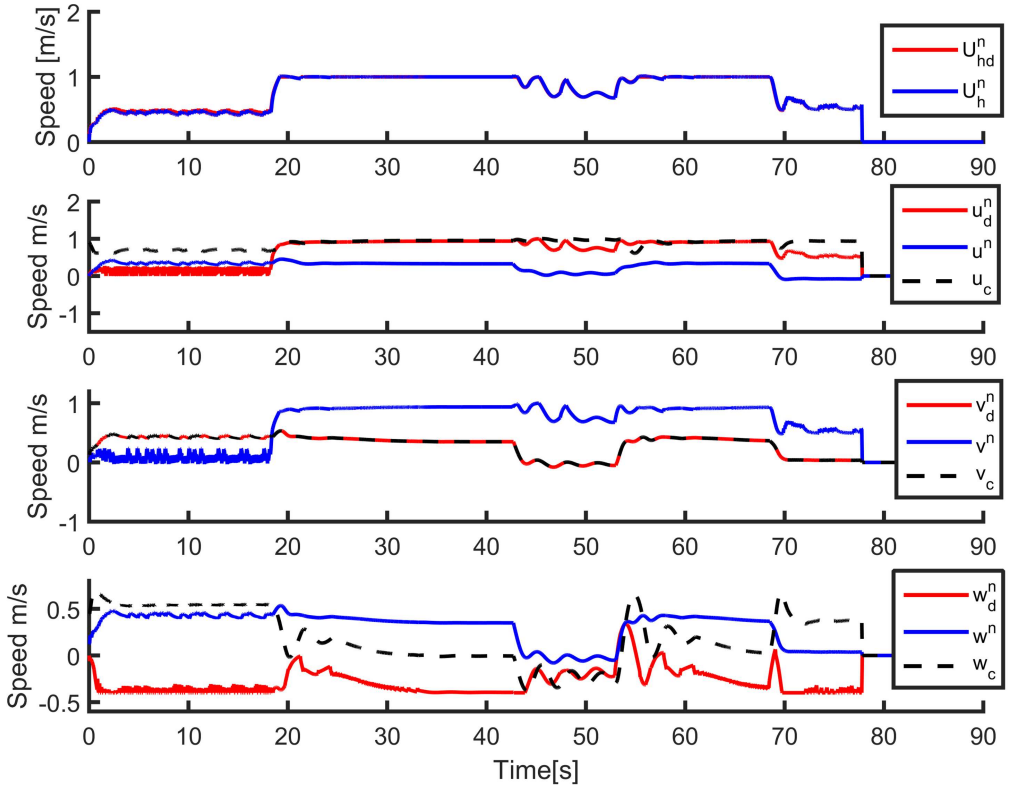

Figure 6.25: Velocity tracking profile of SELOS sliding course control with CURRENT disturbance of $V_x = V_y = 0.8m/s$, and $V_z = 0.2m/s$.

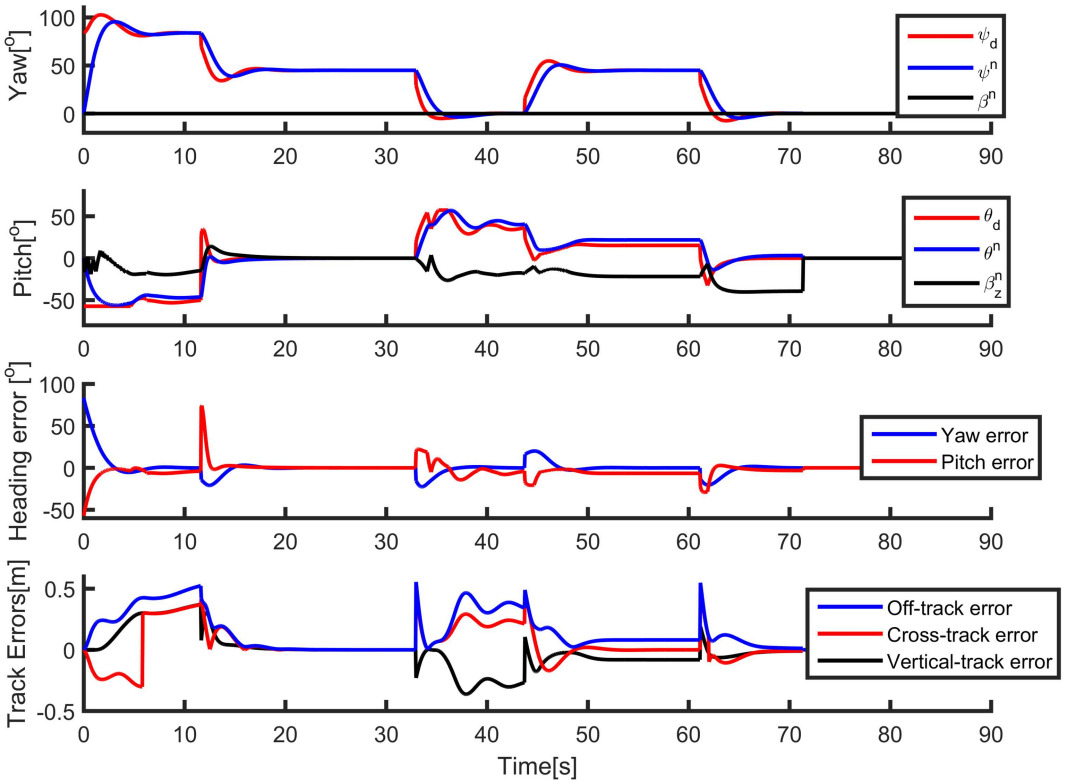

Figure 6.26: Heading angles and track-error tracking profile of SELOS sliding course control.

$1m/s$ and $w^n_{dmax} = 0.5m/s$. The CURRENT intensity, heading and pitch angles are $V_c = 2m/s$, $\phi_c = 0$, $\psi_c = 45^o$ and $\theta_c = 20^o$. The guidance and control system gains are set as follows: $R_{min} = 1, a = 1.01, c = 0.001, k_r = k_a = k_1 = k_2 = k_3 = k_4 = \lambda_r = \lambda_q = k_\psi = k_s = 1, k_d = k_w = k_q = k_u = k_v = 25, T_s = 0.05$, $k_5 = 0.2, k_U = 0.1$. The control inputs saturate at $\pm 450N$ in surge, sway and heave, and $\pm 250Nm$ in yaw and pitch. The rate limits for maximum desired and actual pitch and yaw rates and pitch and yaw angles are at $57.3deg/s(1rad/s)$ and $57.3deg$, resp..

Figures 6.22-6.23 show that the SELOS horizontal and vertical course control can make the vehicle accurately track the path w/ and w/o significant CURRENT disturbances and measurement noises, with less accuracy in the case of measurement noises. The maximum desired speed in 3-D is $U^n_d = 1.18m/s$ which gives a strength of the CURRENT intensity at 97% of U^n_d since $V_c = 0.97U^n_d$. They also show that the vehicle can indeed handle more intense disturbance and in a better way compared to the 5-DOF underac-

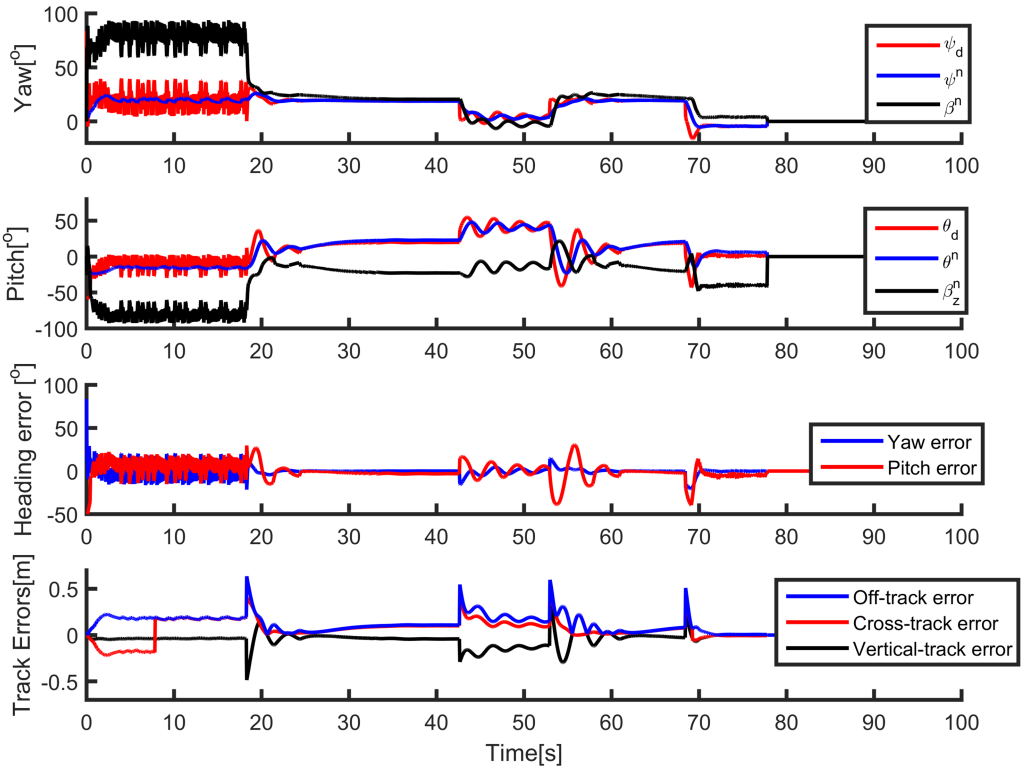

Figure 6.27: Heading angles and track-error error tracking profile of SELOS sliding course control with CURRENT disturbance of $V_x = V_y = 0.8m/s$, and $V_z = 0.2m/s$.

tuated case w/o sway and heave actuation, as can be expected. Similarly, the level of disturbance rejection can be increased by increasing the actuator saturation, limits and rate limits in corresponding DOFs.

Figures 6.24-6.27 show the velocity, course angle, and track-error tracking profiles w/ and w/o CURRENT disturbances and measurement noises, which are similar to that in the underacted case. Similarly, the desired heave velocity is not fully tracked, which is due to a competition between the heave control and vertical pitch course control. The desired heave speed can be designed in an improved manner, but the emphasize here will still lie mostly on the vertical track error, and thus, may still present such a competition.

Note that the total CURRENT disturbance rejection is smaller than that of the 4-DOF case since the 5-DOF case uses the model of ODIN UV which has smaller damping parameters, which makes it easier to be drifted by the CURRENT.

Note that the vehicle position starts at a distance away from the first waypoint, and

the program treats the distance between the initial position to the first waypoint as a zeroth waypoint, which is why is not shown on the Figures. This is same for all of the simulations.

6.5 Summary

The SELOS course control problem has been extended to 3-D in this chapter with passively-stabilized pitch and/o roll DOFs for 4 and 5-DOF scenarios, resp.. The off-track error for general 3-D PF problem has been presented with more detailed illustration. The vertical course control problem has been formulated for designing desired pitch angle with vertical-slip. The stability properties of the LOS guidance laws have been extended to vertical plane. The 3-D planar speed assignment technique was designed to allow the vehicle to track the 3-D LOS vector simultaneously in both planes. Both under and fully-actuated cases are considered, where sway is underactuated in 4-DOF and sway and heave are underactuated in 5-DOF. Simulation results show that the 3-D SELOS course control can allow the vehicle to follow the path accurately under significant CURRENT disturbances and/or measurement noises.

Chapter 7

Conclusion

This chapter provides a conclusion of the thesis, some of the implications of the results, and directions for relevant future work.

7.1 Conclusion

This thesis has contributed to the design and modeling of a novel guidance system based on LOS guidance law for PF course control of UV with a complete 3-D model of CURRENT and/or WAVE disturbances. Chapter 1 has provided a background and an application spectrum of UVs, and an introduction to the thesis with its aims and objectives, which are met accordingly.

Chapter 2 presented existing approaches on 6-DOF modeling of UVs that require a large set of hydrodynamic parameters, and the difficulty in achieving models that can accurately describe the vehicle motion and its interaction with the environment due to simplifications in actuator models, thruster-thruster and thruster hull interactions.

A comprehensive literature review has been carried out in Chapter 3 on guidance and PF control, which revealed that a large portion of research on UVs focus on the localization and navigation problem due to the unstructured and hostile environment of the ocean and the unavailability of high frequency signals underwater. The representation of the PF problem and definitions of track-errors in NED are revised and more detailed

illustrations of the PF problem were presented in this chapter.

A number of advances and improved methods regarding mathematical modeling of equations and angles of motion, and modeling and incorporation of environmental disturbances into the relative equations of motion are presented in Chapter 4. The contribution of this chapter revolves around an improved understanding of expression of motion states in reference frames. It has been shown mathematically that environmental disturbances by fluid are already present in the relative equations of motion. This implied that any amount of CURRENT and/or WAVE disturbances can be overcome by sufficiently large actuation without saturation or other limits on vehicle states (other than singularities), provided that the vehicle is not physically damaged. This has additionally shown that any fluid disturbance terms added in the relative equations of motion using linear superposition are redundant, and can only imply a non-fluid rigid-body disturbances for UVs if necessary. Ocean wave modeling is an different field on its own, and now the CURRENT and/or WAVE disturbance incorporation provides better integration between the relative equations of motion and ocean wave incorporation. This is based on an improved understanding of the FLOW reference frame and the new CURRENT and/or WAVE disturbance model. Chapter 4 has also presented an analytic method of modeling the signs of forces and moments in the equations of motion using Lyapunov stability analysis of the unforced system model. The concept of state relativity has been presented which is inspired by and provides a better understanding of Newton's 3rd Law of Motion, which helps modeling of motion systems more accurately. Finally, the formal proofs of passivity and boundedness of relative UVs have been proved under assumption of hydrostatic neutrality of the vehicle. These proofs and contributions on the understanding and modeling of FLOW and CURRENT frames can be extended to other mobile robotics where applicable and not just marine systems.

The 2-D LOS course control presented in Chapter 5 has shown the ability of the revised model and the guidance system to reject significant CURRENT disturbances. The course control problem is inherently superior in disturbance rejection over just heading

control due to its incorporation of sway velocity into the desired heading through the sideslip angle. The high level disturbance rejection is attributable to the improved modeling of the FLOW states in the relative equations of motion, new model of constant and irrotational ocean CURRENT and/or WAVE and the speed allocation, and course control. It has been shown that course control is a highly effective and simple disturbance rejection scheme. The linear and nonlinear stability results of LOS guidance laws provided with distinction between straight and curved paths that has not been looked at in the literature. The comparison made between three guidance laws using course control provide a general outlook on their advantages and disadvantages.

The SELOS guidance and horizontal course control problem has been extended to 3-D PF in 4 and 5-DOF scenarios in Chapter 6, with the general formula for the off-track error and the vertical-slip for course control in the vertical plane. The simulation results has shown that the vehicle can also follow the path under significant CURRENT and/or measurement noises in 3-D. The stability analysis has also been extended to the vertical plane. The planar speed assignment algorithm in this chapter is effective, simple and necessary to synchronize the desired speeds between horizontal and vertical planes in guidance based PF so that the vehicle tracks the 3-D LOS vector closely in both planes. The planar speed assignment methods can also be extended to 6-DOF using the right kinematic speed comparison.

The contributions in this thesis present better foundation for many future research works in dynamics modeling, kinematics and GNC that use the relative equations of motion incorporating the new CURRENT and/or WAVE disturbances. The more accurate definition of the FLOW and CURRENT velocities can now be used to achieve more accurate and thus, simulations or designs of such simulation platforms.

7.2 Future Work

Some of the specific future works are outlined in this section.

7.2.1 Drift Rate

The drift rate is a very useful technique to directly calculate the two other velocities by only knowing one through the updated relationship of relative velocities (4.4), which can be obtained in rig experiments simulating pseudo-current. This technique is particularly useful for UVs since the navigation problem is more challenging compared to above water applications. Thus, the drift rate presents an immediate experimental work that can deliver powerful results. The drift rate can be rotated to the inertial level, however, it is more suitable to be applied at the BODY level since it is essentially dominated by the geometry of the vehicle at the BODY axes.

7.2.2 Hybrid Guidance Systems

Since the guidance laws do not require high computational power and that there is no clear winner, a hybrid design would be most efficient where the vehicle can switch between the guidance laws, depending on the priorities of the current task.

The mechanism of SELOS guidance can be achieved by combining LLOS and ELOS, where ELOS is implemented first and LLOS is only activated when ELOS has no solution when $y_e > R_{min}$. When $\triangle \approx 0$, the LLOS provides a perpendicular desired heading when $y_e > R_{min}$, where exactly mimicking the action of SELOS when $y_e > R_{min}$. In addition, LLOS is simpler than the switching mechanism of SELOS, and thus is actually a better alternative than SELOS. This combination can be referred as Enclosure and Lookahed-based LOS (ELLOS).

7.2.3 Waypoint Following around Corners

The performance waypoint following system can be improved to greatly reduce the total cross-track errors by designing a system that initiates an early turning around corners, or by smoothing out the path using path parameterization. The first approahc would be similar to the work in (Nelson et al., 2005).

7.2.4 Planar Speed Assignment

The basic speed assignment technique can be similarly extended to 5 and 6-DOF PF controls since it has been shown that such a mechanism is necessary when the 3-D LOS vector is required to be tracked simultaneously in both planes. Smoother trajectories can also be generated to provide better tracking by knowing the physical constraints of the vehicle such as the turning radius.

7.2.5 PF under Time-Varying and Rotational CURRENT and/or WAVE Disturbances

The new 3-D constant and irrotational ocean CURRENT and/ow WAVE can be made time-varying and rotational. However, the CURRENT and/or WAVE in this thesis is assumed constant and irrotational relative to NED, but it is not so relative to BODY. Thus, when the vehicle moves or turns, these constant and irrotational CURRENT becomes time-varying and rotational when rotated to BODY (Børhaug & Pettersen, 2005). Therefore, the PF performances of the vehicles shown in simulations also represent the behavior of the vehicle as if the CURRENT and/or WAVE disturbances are time-varying and rotational at the BODY level. Simulating actual time-varying and irrotational CURRENT will only represent an amplification in CURRENT dynamics, and it has also been shown mathematically using the revised relative equations of motion that this increased amount of CURRENT and/or WAVE disturbances can be entirely overcome by adequate amounts of actuation and w/o limits on motion states.

7.2.6 Experimental Works

All of the simulations and future works can be further studied experimentally. However, the improved problem formulation, revised relative equations of motion and the complete model of 3-D ocean CURRENTS and/or WAVES can provide a very effective and meaningful simulations before experimental implementations.

Appendix A

Vehicle Models

A.1 Girona-500 Multipurpose AUV

Mass	$m = 140kg$	
Centre of gravity	$\boldsymbol{r}_g = [0, 0, 0.05]^T$	
Centre of buoyancy	$\boldsymbol{r}_b = [0, 0, 0]^T$	
System inertia	$I_x = 8$ $I_y = 8$ $I_z = 8$	$I_{xy} = 0$ $I_{yz} = 0$ $I_{xz} = 0$
Added mas	$X_{\dot{u}} = 109.5384$ $Y_{\dot{v}} = 237.7126$ $Z_{\dot{w}} = 519.9799$	$K_{\dot{p}} = 0$ $M_{\dot{q}} = 0$ $N_{\dot{r}} = 66.9024$
Linear damping	$X_u = 42.4181$ $Y_v = 75.7673$ $Z_w = 44.0561$	$K_p = 0$ $M_q = 0$ $N_r = 20.5833$
Quadratic damping	$X_{u\|u\|} = 125.3578$ $Y_{v\|v\|} = 447.6195$ $Z_{w\|w\|} = 325.0138$	$K_{p\|p\|} = 0$ $M_{q\|q\|} = 0$ $N_{r\|r\|} = 60.9373$

Table A.1: Girona-500 AUV Parameters.

A.2 ODIN Spherical UV

Mass	$m = 125kg$	
Centre of gravity	$\boldsymbol{r}_g = [0,0,0.05]^T$	
Centre of buoyancy	$\boldsymbol{r}_b = [0,0,0]^T$	
System inertia	$I_x = 8$ $I_y = 8$ $I_z = 8$	$I_{xy} = 0$ $I_{yz} = 0$ $I_{xz} = 0$
Added mas	$X_{\dot{u}} = 62.5$ $Y_{\dot{v}} = 62.5$ $Z_{\dot{w}} = 62.5$	$K_{\dot{p}} = 0$ $M_{\dot{q}} = 0$ $N_{\dot{r}} = 0$
Linear damping	$X_u = 0$ $Y_v = 0$ $Z_w = 0$	$K_p = 38$ $M_q = 38$ $N_r = 38$
Quadratic damping	$X_{u\|u\|} = 48$ $Y_{v\|v\|} = 48$ $Z_{w\|w\|} = 48$	$K_{p\|p\|} = 80$ $M_{q\|q\|} = 80$ $N_{r\|r\|} = 80$

Table A.2: ODIN Spherical UV Parameters.

Appendix B

Stability Proofs of LOS Guidance Laws

B.1 Horizontal SELOS Guidance Law: Curved Path

Proof. (Theorem 5.5) Stability of the system (5.41) is analyzed using the time-derivative of LFC $V_{y_e} \triangleq (1/2)y_e^2$, which is:

$$\dot{V}_{y_e} = -\frac{U_h^n}{\sqrt{R^2 + 2y_e \triangle \cos\theta_R}} y_e^2 \leq -2b(r_e)V_{y_e} \leq 0. \tag{B.1}$$

for each $r_e > 0$, all $|y_e(t)| < r_e$, and $b(r_e)$ given by:

$$b(r_e) \triangleq \frac{U_{hmin}^n}{\sqrt{R_{max}^2 + 2r_e \triangle \cos\theta_R}}, \tag{B.2}$$

First part of (B.1) means $|y_e(t)| \leq y_{e_0}$ for all $t \geq 0$. By invoking the the comparison lemma (Khalil, 2002, Lemma 3.4), the second part of (B.1) implies $y_e(t) \leq e^{-2b(r_e)} y_{e_0}$, for all $t \geq 0$. Thus, (B.1) implies that $y_e(t) \leq e^{-b(r_e)} y_{e_0}$ for $\forall t > 0$ and $y_{e_0} = y_e(0)$. Therefore, the origin $y_e = 0$ is a SGES equilibrium point of (5.41) (Loria & Panteley, 2004, Definition 2.7). □

B.2 Vertical ELOS Guidance Law with Constant R

B.2.1 Straight Path

Proof (Theorem 6.2) Stability of the vertical-track error dynamics (6.40) is analyzed using the time-derivative of LFC $V_{z_e} \triangleq (1/2)z_e^2$, which is:

$$\dot{V}_{z_e} = -\frac{U_v^n}{R_v} z_e^2 \leq -k_4 z_e^2 \leq 0. \tag{B.3}$$

on the ball $B_r = \{z_e \in \mathbb{R} | z_e \leq R_v\}$ with $0 < k_4 < U_v^n/R_v$. Since $U_v^n, R_v > 0$ are constant, and $\dot{V}_{z_e}$ is negative definite, the origin $z_e = 0$ of Eq. (6.40) is LES. The stability cannot be global since the conidition $z_e \leq R_v$ is required for real solutions. □

B.2.2 Curved Path

Proof. (Theorem 6.3) Stability of the system (6.42) is analyzed using the time-derivative of LFC $V_{z_e} \triangleq (1/2)z_e^2$, which is:

$$\dot{V}_{z_e} = -\frac{U_v^n}{\sqrt{R^2 + 2z_e \triangle_v \cos\theta_{R_v}}} z_e^2 \leq -2b(r_e)V_{z_e} \leq 0. \tag{B.4}$$

for each $r_e > 0$, all $|z_e(t)| < r_e$, and $b(r_e)$ given by:

$$b(r_e) \triangleq \frac{U_{vmin}^n}{\sqrt{R_{vmax}^2 + 2z_e \triangle_v \cos\theta_{R_v}}}, \tag{B.5}$$

First part of (B.4) means $|z_e(t)| \leq z_{e_0}$ for all $t \geq 0$. By invoking the the comparison lemma (Khalil, 2002, Lemma 3.4), the second part of (B.4) implies $z_e(t) \leq e^{-2b(r_e)} z_{e_0}$, for all $t \geq 0$. Thus, (B.4) implies that $z_e(t) \leq e^{-b(r_e)} z_{e_0}$ for $\forall t > 0$, and $z_{e_0} = z_e(0)$. Therefore, the origin $z_e = 0$ is a SGES equilibrium point of (6.42) (Loria & Panteley, 2004, Definition 2.7). □

B.3 Vertical SELOS Guidance Law

B.3.1 Straight Path

Proof. (Theorem 6.4) The stability of the system (6.46) is analyzed using the time-derivative of LFC $V_{z_e} \triangleq (1/2)z_e^2$, which is:

$$\dot{V}_{z_e} = -\frac{U_v^n z_e^2}{\sqrt{c^2 + z_e^2}} \leq -2b(r_e)V_{z_e} \leq 0. \tag{B.6}$$

for each $r_e > 0$, all $|z_e(t)| < r_e$, and $b(r_e)$ given by:

$$b(r_e) \triangleq \frac{U_{vmin}^n}{\sqrt{c_{max}^2 + r_e^2}}, \tag{B.7}$$

First part of (B.6) means $|z_e(t)| \leq z_{e_0}$ for all $t \geq 0$. By invoking the the comparison lemma (Khalil, 2002, Lemma 3.4), the second part of (B.6) implies $z_e(t) \leq e^{-2b(r_e)}z_{e_0}$, for all $t \geq 0$. Thus, (B.6) implies that $z_e(t) \leq e^{-b(r_e)}z_{e_0}$ for $\forall t > 0$ and $z_{e_0} = z_e(0)$. Therefore, the origin $z_e = 0$ is a SGES equilibrium point of (6.46) (Loria & Panteley, 2004, Definition 2.7). □

B.3.2 Curved Path

Proof. (Theorem 6.5) Stability of the system (6.47) is analyzed using the time-derivative of LFC $V_{z_e} \triangleq (1/2)z_e^2$, which is:

$$\dot{V}_{z_e} = -\frac{U_v^n}{\sqrt{R^2 + 2z_e\triangle_v \cos\theta_{R_v}}} z_e^2 \leq -2b(r_e)V_{z_e} \leq 0. \tag{B.8}$$

for each $r_e > 0$, all $|z_e(t)| < r_e$, and $b(r_e)$ given by:

$$b(r_e) \triangleq \frac{U_{vmin}^n}{\sqrt{R_{vmax}^2 + 2z_e\triangle_v \cos\theta_{R_v}}}, \tag{B.9}$$

First part of (B.8) means $|z_e(t)| \leq z_{e_0}$ for all $t \geq 0$. By invoking the the comparison lemma (Khalil, 2002, Lemma 3.4), the second part of (B.8) implies $z_e(t) \leq e^{-2b(r_e)} z_{e_0}$, for all $t \geq 0$. Thus, (B.8) implies that $z_e(t) \leq e^{-b(r_e)} z_{e_0}$ for $\forall t > 0$, and $z_{e_0} = z_e(0)$. Therefore, the origin $z_e = 0$ is a SGES equilibrium point of (6.47) (Loria & Panteley, 2004, Definition 2.7). $\square$

References

Abdurahman, B., Savvaris, A., & Tsourdos, A. (2017). A switching los guidance with relative kinematics for path-following of underactuated underwater vehicles. In *Proceedings of 20th IFAC World Congress* (Vol. 50, p. 2290-2295). Touluse, France.

Abkowitz, M. (1964). *Lectures on ship hydrodynamics – steering and maneuverability* (Tech. Rep.). Lyngby, Denmark: Stevens Institude of Technology.

Aguiar, A. P., & Hespanha, J. P. (2007). Trajectory-tracking and path-following of underactuated autonomous vehicles with parametric modeling uncertainty. *IEEE Transactions on Automatic Control*, *52*(8), 1362-1379.

Alessandretti, A., Aguiar, A. P., & Jones, C. N. (2013). Trajectory-tracking and path-following controllers for constrained underactuated vehicles using model predictive control. In *2013 european control conference (ecc)* (p. 1371-1376).

Avila, J., Décio, D., & Adamowski, J. (2013). Experimental model identification of open-frame underwater vehicles. *Ocean Engineering*, *60*, 81–94.

Bibuli, M., Caharija, W., Pettersen, K., Bruzzone, M., G. Caccia, & Zereik, E. (2014). Ilos guidance - experiments and tuning. In *Proceedings of 19th IFAC World Congress* (Vol. 47, p. 4209-4214). Cape Town, South Africa.

Blanke, M. (1981). *Ship propulsion losses related to automated steering and prime mover control* (Unpublished doctoral dissertation). The Technical University of Denmark.

Blidberg, R. (2001). *The development of autonomous underwater vehicles (auvs); a brief summary.* Online. Retrieved from `http://ausi.org/publications/ICRA_01paper.pdf`.

Breivick, M. (2003). *Nonlinear manoeuvring control of underactuated ships* (Unpublished master's thesis). Norwegian University of Science and Technology.

Breivik, M., & Fossen, T. (2004). Path following for marine surface vessels. In *MTTS/IEEE TECHNO-OCEAN '04* (p. 2282–2289). Kobe, Japan.

Breivik, M., & Fossen, T. (2005). Priciples of guidance-based path following in 2d and 3d. In *Proceedings of 44th IEEE Conference on Decision and Control and European*

Control Conference (p. 627-634). Seville, Spain.

Breivik, M., & Fossen, T. (2009). *Guidance laws for autonomous underwater vehicles* (A. Inzartsev, Ed.). InTech. Retrieved from `http://www.intechopen.com/books/underwater_vehicles/guidance_laws_for_autonomous_underwater_vehicles`

Børhaug, E., Pavlov, A., & Pettersen, K. (2008). Integral los control for path following of underactuated marine surface vessels in the presence of constant ocean currents. In *Proceedings of 47th IEEE Conference on Decision and Control* (p. 4984–4991). Cancun, Mexico.

Børhaug, E., & Pettersen, K. (2005). Cross-track control for underactuated autonomous vehicles. In *Proceedings of 44th IEEE Conference on Decision and Control* (p. 602-608). Seville, Spain.

Caccia, M., Indiveri, G., & Veruggio, G. (2000). Modeling and identification of open-frame variable configuration unmanned underwater vehicles. *IEEE Journal of Oceanic Engineering*, *25*, 227-240.

Caharija, W., Candeloro, M., Pettersen, K., & Sørensen, A. (2012). Relative velocity control and integral los for path following of underactuated surface vessels. In *Proceedings of 9th IFAC Conference on Manoeuvring and Control of Marine Craft* (Vol. 45, p. 380-385). Arenzano, Italy.

Caharija, W., Pettersen, K., Bibuli, M., Calado, P., Zereik, E., Braga, J., ... Bruzzone, G. (2016). Integral line-of-sight guidance and control of underactuated marine vehicles: Theory, simulations, and experiments. *IEEE Transactions on Control Systems Technology*, *24*(5), 1623-1642.

Caharija, W., Pettersen, K., Calado, P., & Braga, J. (2015). A comparison between the ilos guidance and the vector field guidance. In *Proceedings of 10th IFAC Conference on Manoeuvring and Control of Marine Craft* (p. 89–94). Copenhagen, Denmark.

Clark, D., & Horn, J. (1997). Estimation of hydrodynamic derivatives. In *Proceedings of 11th Ship Control Systems Symposium* (Vol. 12, p. 275–289). Southampton, UK.

Cummins, W. (1962). *The impulse response function and ship motions* (Tech. Rep.). David Taylor Model Basin, Hydrodynamics Laboratory.

David, A., & Luis, L. (2003). Adaptive identification of dynamically positioned underwater robotic vehicle. *IEEE Transactions on Control Systems Technology*, *11*, 505–515.

Davidson, K., & Schiff, L. (1946). Turning and course keeping qualities. *SNAME Transactions*, *54*, 152-200.

del Rio, F. D., Jiménez, G., Sevillano, J. L., Vicente, S., & Balcells, A. C. (1999). A generalization of path following for mobile robots. In *Proceedings of 1999 IEEE International Conference on Robotics and Automation.* Detroit, Michigan.

De luca, A., Oriolo, G., & Samson, C. (1998). *Feedback control of a nonholonomic car-like robot* (LAAS Report No. 97438). Centre National de la Recherche Scientifique.

Do, K. D., & Pan, J. (2003). Robust path following of underactuated ships using serret-frenet frame. In *Proceedings of American Control Conference.* Denver, Colorado, USA.

DRL. (2010). *Amour (autonomous modular optical underwater robot).* Online. Retrieved from `https://groups.csail.mit.edu/drl/wiki/index.php?title=AMOUR_(Autonomous_Modular_Optical_Underwater_Robot)`

Encarnação, P., & Pascoal, A. (2000a). 3D path following for autonomous underwater vehicles. In *Proceedings of 39th IEEE Conference on Decision and Control.* Sydney, Australia.

Encarnação, P., & Pascoal, A. (2000b). Path following for marine vehicles in the presence of unknown currents. In *Proceedings of 6th IFAC Conference on Robot Control* (Vol. 33, p. 507-512). Viena, Austria.

Encarnação, P., & Pascoal, A. (2001). Combined trajectory tracking and path following: an application to the coordinated control of autonomous marine craft. In *Proceedings of 40th IEEE Conference on Decision and Control* (Vol. 5, p. 964-969).

Orlando, Florida USA.

Faltinsen, O. M. (2005). *Hydrodynamics of high-speed marine vehicles*. Cambridge, England: Cambridge University Press.

Fedyaevsky, K., & Sobolev, G. (1963). *Control and stability in ship design* (Tech. Rep.). State Union Shipbuilding House.

Fossen, T. (1991). *Nonlinear modeling and control of underwater vehicles* (Unpublished doctoral dissertation). Norwegian University of Science and Technology.

Fossen, T. (1994). *Guidance and control of ocean vehicles*. Chichester, England: Wiley.

Fossen, T. (2002). *Marine control systems guidance, navigation, and control of ships, rigs and underwater vehicles*. Marine Cybernetics.

Fossen, T. (2011). *Handbook of marine craft hydrodynamics and motion control*. Chichester, England: Wiley.

Fossen, T. (2012). How to incorporate wind, waves and ocean currents in the marine craft equations of motion. In *Proceedings of 9th IFAC Conference on Manoeuvring and Control of Marine Craft* (p. 126–131). Arenzano.

Fossen, T., & Fjelstad, O. (1995). Nonlinear modelling of marine vehicles in 6 degrees of freedom. *Journal of Mathematical Modelling of Systems*, *1*(1), 17-27.

Fossen, T., & Lekkas, A. (2015). Direct and indirect integral line-of-sight path-following controllers for marine craft exposed to ocean currents. *International Journal of Adaptive Control and Signal Processing*, *31*(4), 445–463.

Fossen, T., & Pettersen, K. (2014). On uniform semiglobal exponential stability (usges) of proportional line-of-sight guidance laws. *Journal of Automatica*, *50*, 2912–2917.

Fossen, T., Pettersen, K., & Galeazzi, R. (2015). Line-of-sight path following for dubins paths with adaptive sideslip compensation of drift forces. *IEEE Transactions on Control Systems Technology*, *23*(2), 820-827.

Fossen, T. I., Breivik, M., & Skjetne, R. (2003). Line-of-sight path following of underactuated marine craft. In *Proceedings of 6th IFAC Conference in Manoeuvring and Control of Marine Craft* (Vol. 36, p. 211–216). Girona, Spain.

Fredriksen, E., & Pettersen, K. (2006). Global κ-exponential way-point maneuvering of ships: theory and experiments. *Journal of Automatica*, *42*, 677–687.

Fryxell, D., Oliveira, P., Pascoal, A., & Silvestre, C. (1994). An integrated approach to the design and analysis of navigation, guidance and control systems for auvs. In *Proceedings of IEEE Symposium on Autonomous Underwater Vehicle Technology* (p. 214–217). London, UK.

Healey, A. J., & Lienard, D. (1993). Multivariable sliding mode control for autnomous diving and steering of unmanned underwater vehicles. *IEEE Journal of Oceaning Engineering*, *18*(3), 327–339.

Humphreys, D., & Watkinson, K. (1978). *Prediction of acceleration hydrodynamic coefficients for underwater vehicle from geometric parameters* (Tech. Rep.). Naval Costal Systems Lab.

Karras, G., Bechlioulis, C., Leonetti, M., Palomeras, N., Kormushev, P., Kyriakopoulos, K., & Caldwell, D. G. (2013). On-line identification of autonomous underwater vehicles through global derivative-free optimization. In *Proceedings of 2013 IEEE/RSJ International Conference on Intelligent Robots and Systems* (p. 3859–3864). Tokyo, Japan.

Khaled, N., & Chalhoub, N. (2013). A self-tuning guidance and control system for marine surface vessels. *Journal of Nonlinear Dynamics*, *73*(1-2), 897–906.

Khalil, H. (2002). *Nonlinear systems* (3nd ed.). New Jersey, US: Prentice.

Lamb, H. (1895). *Hydrodynamics*. Cambridge, England: Cambridge University Press.

Lapierre, L., Soetanto, D., & A., P. (2003). Nonlinear path following with applications to the control of autonomous underwater vehicles. In *Proceedings of 42nd IEEE Conference on Decision and Control.* Maui, Hawaii, USA.

Lea, R., Allen, R., & Merry, S. (1999). A comparative study of control techniques for an underwater flight vehicle. *International Journal of Systems Science*, *30*(9), 947-964.

Lefeber, E. (2000). *Tracking control of nonlinear systems* (Unpublished doctoral disser-

tation). University of Twente.

Lekkas, A., & Fossen, T. (2012). A time-varying lookahead distance guidance law for path following. In *Proceedings of 9th IFAC Conference on Manoeuvring and Control of Marine Craft* (Vol. 45, p. 398-403). Arenzano, Italy.

Lekkas, A., & Fossen, T. (2013). *Line-of-sight guidance for path-following of marine vehicles* (O. Gal, Ed.). Lamber Academic Publishing.

Lekkas, M., & Fosse, T. (2014). Minimization of cross-track and along-track errors for path tracing of marine underactuated vehicles. In *2014 european control conference (ecc)* (p. 3004-3010).

Lewis, E. (1989). *Principles of naval architecture: motions in waves and controllability* (2nd ed.). SNAME.

Loria, A., & Panteley, E. (2004). *Cascaded nonlinear time-varying systems: analysis and design* (F. Lamnabhi-Lagarrigue, A. A.V. Loria, & E. Panteley, Eds.). London: Springer-Verlag.

Mainwaring, J. (2001). *Subsea inspection: The autonomous approach.* Online. Retrieved from `http://www.rigzone.com/news/oil_gas/a/120337/Subsea_Inspection_The_Autonomous_Approach`

Mark, E., Frans, H., & Chryssostomos, C. (2006). System identification of open-loop maneuvers leads to improved auv flight performance. *IEEE Journal of Oceanic Engineering*, *31*, 200–208.

Moreira, L., Fossen, T., & Soares, C. (2007). Path following control system for a tanker ship model. *Journal of Ocean Engineering*, *34*(14-15), 2074-2085.

Nelson, D. R., Barber, D. B., McLain, T. W., & Beard, R. W. (2005). Vector field path following for miniature air vehicles. *IEEE Transactions on Robotics*, *23*(3), 519 - 529.

Nomoto, K., Taguchi, T., Honda, K., & Hirano, S. (1957). *On steering qualities of ships* (Vol. 4; Tech. Rep.). International Shipbuilding Progress.

Norrbin, N. (1963). *On the design and analysis of the zig-zag test on base of quasi-linear*

frequency response (Tech. Rep. No. B 104-3). The Swedish State Shipbuilding Experimental Tank (SSPA).

Oh, S., & Sun, J. (2010). Path following of underactuated marine surface vessels using line-of-sight based model predictive control. *Ocean Engineering*, *37*(2-3), 285–295.

Park, S., Deyst, J., & How, J. (2004). A new nonlinear guidance logic for trajectory tracking. In *Aiaa guidance, navigation, and control conference and exhibit.* Providence, Rhode Island, USA.

Park, S., Deyst, J., & How, J. (2007). Performance and lyapunov stability of a nonlinear path-following guidance method. *Journal of Guidance, Navigation and Dynamics*, *30*(6), 1718-1728.

Paull, L., Saeedi, S., Seto, M., & Li, H. (2014). Auv navigation and localization: a review. *IEEE Journal of Oceanic Engineering*, *39*(1), 131–149.

Pavlov, A., Nordahl, H., & Breivik, M. (2009). Mpc-based optimal path following for underactuated vessels. In *Proceedings of 8th IFAC Conference on Manoeuvring and Control of Marine Craft* (Vol. 42, p. 340-345). Guaruja, Brazil.

Pepijin, W., Johansen, T. A., Sørensen, A. J., Flanagan, C., & Toal, D. (2007). Neural network augmented identification of underwater vehicle models. *Control Engineering Practice*, *15*(6), 715 - 725.

Pettersen, K. (2017). Lyapunov sufficient conditions for uniform semiglobal exponential stability. *Automatica*, *78*, 97-102.

Pettersen, K., & Lefeber, E. (2001). Way-point tracking control of ships. In *Proceedings of 40th IEEE Conference on Decision and Control* (p. 940-945). Orlando, Florida.

Ridao, P., Tiano, A., El-Fakdi, A., Carreras, M., & Zirilli, A. (2004). On the identification of non-linear models of unmanned underwater vehicles. *Control Engineering Practice*, *12*(12), 1483-1499.

Ross, A. (2008). *Nonlinear manoeuvring models for ships: a lagrangian approach* (Unpublished doctoral dissertation). The Technical University of Denmark.

Rysdyk, R. (2003). Uav path following for constant line-of-sight. In *Proceedings of 2nd AIAA "Unmanned Unlimitted" Systems, Technologies, and Operations - Aerospace.* San Diego, California, USA.

Sagatun, S., & Fossen, T. (1991). Langargian formulation of underwater vehicles dynamics. In *Proceedings of IEEE Internatioanl Conference on Systems, Man and Cybernetics* (Vol. 3, p. 1029–1034).

Samson, C. (1992). Path following and time-varying feedback stablization of a wheeld robot. In *Icarv.* Singapore.

Sciavicco, L., & Siciliano, B. (2000). *Modelling and control of robot manipulators* (2nd ed.). London: Springer-Verlag.

Seto, M., Paull, L., & Saeedi, S. (2013). *Introduction to autonomy for marine robots* (M. Seto, Ed.). New York: Springer.

Silvestre, C., Pascoal, A., & Kaminer, I. (2002). On the design of gain-scheduled trajectory tracking controllers. *Journal of Robust Nonlinear Control*, *12*(9), 797–839.

Skjetne, R. (2005). *The maneuvering problem* (Unpublished doctoral dissertation). Norwegian University of Science and Technology.

Skjetne, R., Fossen, T. I., & Kokotovic, P. V. (2004). Robust output maneuvering for a class of nonlinear systems. *Automatica*, *40*(3), 373-383.

SNAME. (1950). *Nomenclature for treating the motion of a submerged body through a fluid* (Technical and Research Bulletin No. 1-5). The Society of Naval Architects and Marine Engineers.

Son, K., & Nomoto, K. (1981). On the coupled motion of steering and rolling of a high-speed container ship. *Journal of Society of Naval Architects of Japan*, *150*, 73-83.

Sørensen, A., Ruth, E., & Smogeli, . (2005). Experimental validation of power and torque thruster control. In *Proceedings of the 13th Mediterranean Conference on Control and Automation* (p. 1506-1511). Limassol, Cyprus.

Sujit, P., Saripalli, S., & Sousa, J. (2014). Unmanned aerial vehicle path following: A

survey and analysis of algorithms for fixed-wing unmanned aerial vehicless. *IEEE Control Systems Magazine*, *34*(1), 42–59.

Wigg, M., Caharija, W., Krogstad, T., & Pettersen, K. (2016). Integral line-of-sight guidance of underwater vehicles without neutral buoyancy. In *Proceedings of the 10th IFAC Conference on Control Applications in Marine Systems CAMS* (Vol. 49, p. 590-597). Trondheim, Norway.

Yu, S., Li, X., Chen, H., & Allgöwer, F. (2015). Nonlinear model predictive control for path following problems. *International journal of Robust and Nonlinear Control*, *25*(8), 1168-1182.

Yuh, J. (1990). Modeling and control of underwater robotic vehicles. *IEEE Transactions on Systems, Man, and Cybernetics*, *20*(6), 1475-1483.